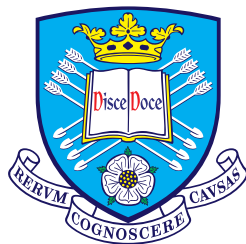


# Magneto-Acoustic Waves in the Stratified Solar Atmosphere: Single to Multi-Fluid Approach



The  
University  
Of  
Sheffield.

**James Frederick Mather**

Supervisor: Prof. Robertus Erdélyi

School of Mathematics and Statistics

University of Sheffield

This dissertation is submitted for the degree of  
*Doctor of Philosophy*

September 2017



In memory of my two exceptional Grandfathers ...



## Declaration

I hereby declare that except where specific reference is made to the work of others, the contents of this dissertation are original and have not been submitted in whole or in part for consideration for any other degree or qualification in this, or any other university. This dissertation is my own work and contains nothing which is the outcome of work done in collaboration with others, except as specified in the text and Acknowledgements. This dissertation contains fewer than 65,000 words including appendices, bibliography, footnotes, tables and equations and has fewer than 150 figures.

James Frederick Mather

September 2017



## Acknowledgements

I would like to take the time to thank my loved ones, friends, colleagues and the organisations that have helped me throughout my years as a PhD student, whether it be with the content of my thesis or just being there for support.

Firstly and most formally, I would like to thank the Science and Technologies Facilities Council (STFC) for providing me with the funding that allowed me to live whilst I completed this thesis and attend many scientific conferences around the world to help further my scientific career.

I would, wholeheartedly, like to thank my PhD supervisor Robertus Erdélyi for believing in my capabilities and providing me with the opportunity to complete a PhD. His support and supervision were always there when needed but he also provided me with enough space to work through problems myself and become a competent independent researcher. Lastly I would like to thank him for putting up with me as a tenant for two years! I would also like to thank the members of the SP2RC solar group in Sheffield for supporting me through my PhD years and lending a helping hand when necessary.

Next I would like to take the time to thank my friends and colleagues personally who have made my second stint at Sheffield University an incredible and memorable one. I thank Nabil for being my first neighbour in H23c. My time as a PhD student would have been infinitely more dull without you. Chris for guiding me with his extensive solar knowledge as well as designing and playing ball games in H23c, most notably 'name ball'. Sky for being the most enthusiastic scientist I know. Your enthusiasm was infectious. Thanks to you and Beth for being my 'roomies' and watching numerous Star Trek episodes with me. Stevie, for all your helpful discussions on mathematics, knowing you has made me a more complete mathematician. I'll miss our coffee and Harley trips. Rahul for your tireless pursuit of tea-time. Rachael for turning up to the office when 'Snakes pass' was passable and being my H23 neighbour. Mihai, Ellie and the pub for making my final years more bearable. My good friends Tim, Aaram, Alex, Tom, Marc and Jacob for providing me with an escape from PhD life. Tim (again) and Anna for providing me with a roof over my head when my funding ran out. To the rest of my friends not mentioned here, I appreciate you all.

Lastly but most certainly not least, my family. My parents for their unending support in my academic endeavours. You have undoubtedly helped me from the very beginning, spending mornings doing maths problems with me before school. My brother, George, for being a source of competition and helping me strive to become better. My two late Grandfathers, Daddy Joe a physicist turned physician and Grandpa an Accountant, clearly mathematics runs in the family. To the rest of my family, thank you for being there for me over the years in whatever capacity.

# Abstract

Mechanical waves are ubiquitous within solar plasmas, coming in the form of Magnetohydrodynamic (MHD) waves. The Sun and its atmosphere are not a single homogeneous medium and, rather, have complex structures stratified by gravity, temperature gradients, complex magnetic field structures, subject to bulk flows and even partial ionisation, with all of these affecting how oscillations propagate within the plasma.

Magneto-acoustic gravity (MAG) waves have been investigated extensively within solar physics, with three popular choices of analytical modelling for a Cartesian coordinate system: a magnetic field parallel, perpendicular, or at an angle to the gravitational field. Firstly we study the eigen-modes of bounded solar plasmas embedded in a magnetic field perpendicular to the gravitational field and their energy distribution in both single and two-layer models. We show that, indeed, modes can still be split into fast and slow MAG with stratification decreasing the magnetic energy with height and, thus, only waves with predominantly internal energy are more evenly distributed in the atmosphere. A discontinuity in temperature between layers also reflects waves but we show there is an inherent coupling between waves in both layers. Secondly we investigate the effect of a bulk flow on MAG surface waves, with the magnetic field parallel to the surface and a gravitational field perpendicular to this. We find that waves along the penumbra, where Evershed flows are present can change their direction of propagation and even the Kelvin-Helmholtz instability can occur.

Waves within solar plasmas have generally been studied in fully ionised or completely neutral media extensively and, as such, partial ionisation has not been covered much until fairly recently, meaning there is great scope for exciting studies in this sub-set of solar physics. Using single and multi-fluid methods we investigate the stability of partially ionised plasma slabs with bulk flows. We find that in the single fluid approximation that dissipative instabilities can occur for flow speeds of the internal tube speed, with a neutrals providing stability. In the two-fluid approximation our analysis confirms the existence of a mode that arises due to the shear in flow in the neutral fluid and that, in a highly collisional plasma, has a semi-resonant interaction between itself and the classical modes of incompressible or compressible magnetic slabs.



# Table of contents

<b>1</b>	<b>Introduction</b>	<b>1</b>
1.1	Introduction . . . . .	1
1.2	Structure and Dynamics of the Sun . . . . .	2
1.2.1	Solar Interior . . . . .	3
1.2.2	Solar Atmosphere . . . . .	3
1.2.3	Prominences . . . . .	6
1.3	Solar Oscillations . . . . .	7
1.4	Flows and Associated Instabilities . . . . .	10
1.4.1	Kelvin-Helmholtz . . . . .	11
1.4.2	Negative Energy Waves . . . . .	11
1.5	Fully ionised magnetohydrodynamics . . . . .	12
1.5.1	Ideal Form . . . . .	14
1.5.2	Ideal Linearised MHD . . . . .	15
1.6	Non-Ideal (Dissipative) MHD . . . . .	16
1.7	Partially Ionised Plasmas . . . . .	18
1.7.1	Two Fluid Approximation . . . . .	20
1.7.2	Single Fluid approximation . . . . .	21
1.8	Outline of Thesis . . . . .	22
<b>2</b>	<b>Magneto-acoustic Oscillations in Homogeneous Media</b>	<b>23</b>
2.1	Introduction . . . . .	23
2.2	Fully Ionised . . . . .	23
2.2.1	Alfvén Waves . . . . .	24
2.2.2	Magneto-acoustic waves . . . . .	25
2.3	Two-fluid . . . . .	29
2.3.1	Alfvén waves . . . . .	31
2.3.2	Magneto-acoustic waves . . . . .	35
2.4	Summary and Discussion . . . . .	38
<b>3</b>	<b>Magneto-Acoustic Gravity Waves in a Vertical Field: Single Layer</b>	<b>41</b>
3.1	Introduction . . . . .	41
3.2	Background Equilibrium . . . . .	42

3.3	Governing Equations . . . . .	45
3.3.1	Previous Work . . . . .	45
3.3.2	New Solutions for $\Theta = \widehat{p}/\rho$ . . . . .	47
3.4	Single Layer . . . . .	50
3.4.1	Small Wavelength Limit ( $K \rightarrow \infty$ ) . . . . .	50
3.4.1.1	Low plasma-beta . . . . .	51
3.4.1.2	High plasma-beta . . . . .	51
3.4.2	Solar Atmospheric Models . . . . .	52
3.4.2.1	Coronal Plasma . . . . .	53
3.4.2.2	Photosphere-Chromosphere . . . . .	56
3.5	Summary and Discussion . . . . .	57
<b>4</b>	<b>Magneto-Acoustic Gravity Waves in a Vertical Field: Two-Layer</b>	<b>59</b>
4.1	Introduction . . . . .	59
4.2	Background Equilibrium . . . . .	60
4.3	Solutions and Dispersion Relation . . . . .	62
4.4	Model 1: Photosphere to Upper Chromosphere . . . . .	63
4.5	Model 2: Lower Solar Atmosphere to Corona . . . . .	73
4.6	Summary and Discussion . . . . .	76
<b>5</b>	<b>Effect of Steady Flow on Magneto-Acoustic Gravity Surface Waves</b>	<b>77</b>
5.1	Introduction . . . . .	77
5.2	Governing Equation . . . . .	78
5.3	Equilibrium Model and Governing Equations . . . . .	80
5.3.1	Region with Magnetic Field . . . . .	82
5.3.2	Non-Magnetic Region with Background Flow . . . . .	82
5.4	Deriving Dispersion Relation . . . . .	83
5.4.1	Incompressible Limit . . . . .	84
5.4.2	Small Wavelength ( $k_x H_e \rightarrow \infty$ ) and Cold Plasma ( $\beta = 0$ ) Limit	86
5.4.2.1	Limit of Small Flow . . . . .	87
5.4.2.2	Limit of Small Density Ratio . . . . .	88
5.5	Numerical Solution of the Dispersion Relation . . . . .	91
5.5.1	Cut off Curves . . . . .	91
5.5.2	Numerical Results . . . . .	92
5.6	Summary and Discussion . . . . .	100
<b>6</b>	<b>Dissipative Instability in a Prominence Plasma</b>	<b>103</b>
6.1	Introduction . . . . .	103
6.2	Equilibrium and Governing Equations . . . . .	104
6.3	Dispersion Relation . . . . .	109
6.3.1	Slender Slab Limit . . . . .	112

6.3.2	Wide Slab Limit . . . . .	114
6.4	Dissipative Instability . . . . .	114
6.4.1	Negative Energy Waves . . . . .	115
6.4.2	The slender-slab limit ( $kz_0 \ll 1$ ) . . . . .	116
6.4.3	Wide Slab . . . . .	121
6.4.4	Numerical solutions . . . . .	123
6.5	Summary and Discussion . . . . .	128
<b>7</b>	<b>Resonant Flow Instabilities in the Two-Fluid Slab</b>	<b>131</b>
7.1	Introduction . . . . .	131
7.2	Linearised Two Fluid MHD Equations and Governing Equation . . .	132
7.3	Differential Equations and Solutions . . . . .	135
7.4	Derivation of Dispersion Relation . . . . .	136
7.5	Incompressible Limit . . . . .	140
7.5.1	Highly Collisional Limit . . . . .	140
7.5.2	Numerical solutions . . . . .	145
7.6	Collision-less limit . . . . .	150
7.7	Highly Collisional Limit . . . . .	154
7.8	Turbulent plumes . . . . .	158
7.9	Summary and Discussion . . . . .	161
<b>8</b>	<b>Conclusion</b>	<b>165</b>
8.1	Overview of the thesis . . . . .	165
8.2	Summary of Results . . . . .	167
8.2.1	Chapter 3 . . . . .	167
8.2.2	Chapter 4 . . . . .	168
8.2.3	Chapter 5 . . . . .	169
8.2.4	Chapter 6 . . . . .	170
8.2.5	Chapter 7 . . . . .	172
8.3	Further Work . . . . .	174
	<b>References</b>	<b>177</b>
	<b>Appendix A Chapter 3 Derivations</b>	<b>183</b>
	<b>Appendix B Chapter 7 Derivations</b>	<b>187</b>



# Chapter 1

## Introduction

### 1.1 Introduction

The Sun has been a mainstay throughout our solar system's expansive history, forming the keystone that holds it together with its massive gravitational pull on the planets and other extra-terrestrial objects. Without its energy, life as we know it would surely not exist.

In comparison to the Sun's age of 4.6 Billion years, humanity's time on this earth is but a mere moment, transcending our existence. The Sun was a great source of mythology for early humans and many ancient civilizations. Amongst many of these, in Ancient Egyptian religion, Ra/Re was believed to be the god of the Sun. With the head of a falcon and a cobra laced Sun-disk atop it, he would sail his *solar barge* across the ocean, beginning his journey with sunrise and ending it with sunset. In Ancient Greek mythology *Helios* (from which the term heliosphere derives) was the avatar of the Sun. A handsome son of the Titan *Hyperion* crowned with the shining aureole of the Sun, he rode a chariot across the sky, bringing the Sun's light to all. Many other cultures with multiple deities also worshipped Sun gods, such as the Hindu Sun god *Surya* and *Bila*, an Australian Aboriginal cannibal Sun goddess, to name but a few of the extensive list. This prevalence for mankind to explain the origin of the Sun throughout human history shows just how mysterious and wonderful it has been to humans since the beginning of sentient thought.

The Sun is comprised of a state of matter, the so called fourth state of matter, known as plasma. Plasma itself is a super hot gas in which most, if not all, the particles within it are fully ionised, that is the negatively charged electrons have separated from the positively charged nuclei and move freely. Plasma is, however, still considered globally electrically neutral. It is the most abundant state of non-exotic matter in our universe and, as such, should be considered the most 'normal' form of matter. The fact that electrons and ions can move freely means that plasma can also support currents, and therefore electric fields, as well as magnetic fields,

can be present. Due to the charged nature of the ions and electrons the magnetic field readily affects the dynamics of the plasma. Plasma, however, can be made up of a mixture of ions, electrons and neutrals, depending on the temperature and the species of atom present within it. For example, this can occur in some parts of the solar chromosphere. The neutrals within the system will not be affected by electromagnetic fields that permeate the plasma. This can lead to more interesting, but complicated, physics within the plasma. Due to this inherent complexity and rich physics, astrophysics is an astoundingly interesting area of study.

The Sun as our nearest star has always been visible to humans. Being so close means that far more detailed observations can be made of it than any other star in the universe, from Earth's perspective. Throughout the millennia, many civilizations have observed the Sun. In 2000 B.C. solar eclipses were first recorded by the Chinese. Sunspots, which are dark spots on the surface of the Sun, were first recorded by the ancient Chinese in 800 B.C. and were being observed and documented systematically by 23 B.C. so that the emperor's busy coital schedule could be organised properly. It was not until the development of the telescope that the Sun could be observed in greater detail. With this exciting new development in optics in the mid 17th century, scientists such as Galileo rediscovered and started to document sunspots again. This led to the observation of the *Maunder minimum*, where very few sunspots were present. Nowadays, large ground based telescopes (e.g. the Swedish 1-metre Solar Telescope (SST)) can view the sun in very fine detail and space based telescopes can view the sun without interference from the Earth's atmosphere. The STEREO mission can now view objects on the Sun in three dimensions by the use of two satellites working in synchronisation to create, for the first time in solar research, a 3D picture.

Observations of the Sun are only able to tell half of the story. To interpret these observations, a sound theoretical framework is needed. The observations can be used to infer the actual physics occurring within the Sun, using theory, and thus gain insight into the physical characteristics e.g. Temperature, densities etc. It is this interplay between observations and theory that can make solar physics an exciting area of study, with collaborations between theorists and observational experts vital to gain a full picture of the Sun.

## 1.2 Structure and Dynamics of the Sun

The Sun is a large spherical object, however it is hardly homogeneous. It can be split into two main regions: the *solar interior* and *solar atmosphere*. Fig. 1.1 shows a schematic representation of the Sun.

### 1.2.1 Solar Interior

The solar interior is, as the name suggests, within the Sun and it cannot be viewed directly through the surface layers. To study the interior of the Sun a branch of astrophysics called *helioseismology* has been developed to probe within it and gain insight into the physical parameters. The interior can be divided into three separate and distinct sections. Going from the centre to the surface these are: the *core*, the *radiative zone* and the *convection zone*. There is a fourth very thin layer in between the radiative zone and convection zone, called the *tacholine*, where the solar magnetic field is thought to be generated through the solar dynamo.

The solar core is where the Sun's energy is generated by the process of nuclear fusion. It uses a fairly inefficient form of fusion compared to the fusion used in tokamaks. It combines Hydrogen nuclei together to produce Helium; some mass is lost in this process and is released as energy, which can be explained by Einstein's equation relating mass and energy ( $E = mc^2$ ). The temperature of the core is about  $1.5 \times 10^7$  Kelvin with an approximate density of about  $1.6 \times 10^5 \text{ kg m}^{-3}$  and extends 0.25 solar radii within the Sun. The core is so dense that it is difficult for acoustic waves to be used to probe it by helioseismology. However gravity modes, called *g*-modes, could theoretically be used to probe the core (very low spherical degree surface gravity modes, *f*-modes, can also theoretically penetrate into the core), yet they are evanescent near the surface layers of the Sun, with amplitudes so small that they have not as of yet been reliably observed.

The radiative zone is the region of the Sun in which radiative transfer of energy takes place. It extends out to approximately 0.7 solar radii, starting from the edge of the core. The energy generated in the core is slowly leaked out through the radiative zone, with photons taking years to pass through it, being absorbed and emitted countless times.

The convection zone is just below the surface layer and is the region where the largest amount of energy transfer happens. As the name suggests, the process of energy transfer is convection. At the base of the convection zone the temperature gradient of the plasma is too large and it becomes convectively unstable. Large blobs of hot plasma rise to just below the surface of the sun where they are then able to radiate their heat once more and thus lose buoyancy and descend. This happens over and over again, creating large convection cells where bulk flows of huge amounts of plasma occur.

### 1.2.2 Solar Atmosphere

The solar atmosphere is the outer most region of the Sun and is far less dense than the interior. It is comprised of four separate regions: the *photosphere*, *chromosphere*, *transition region* and *corona*.

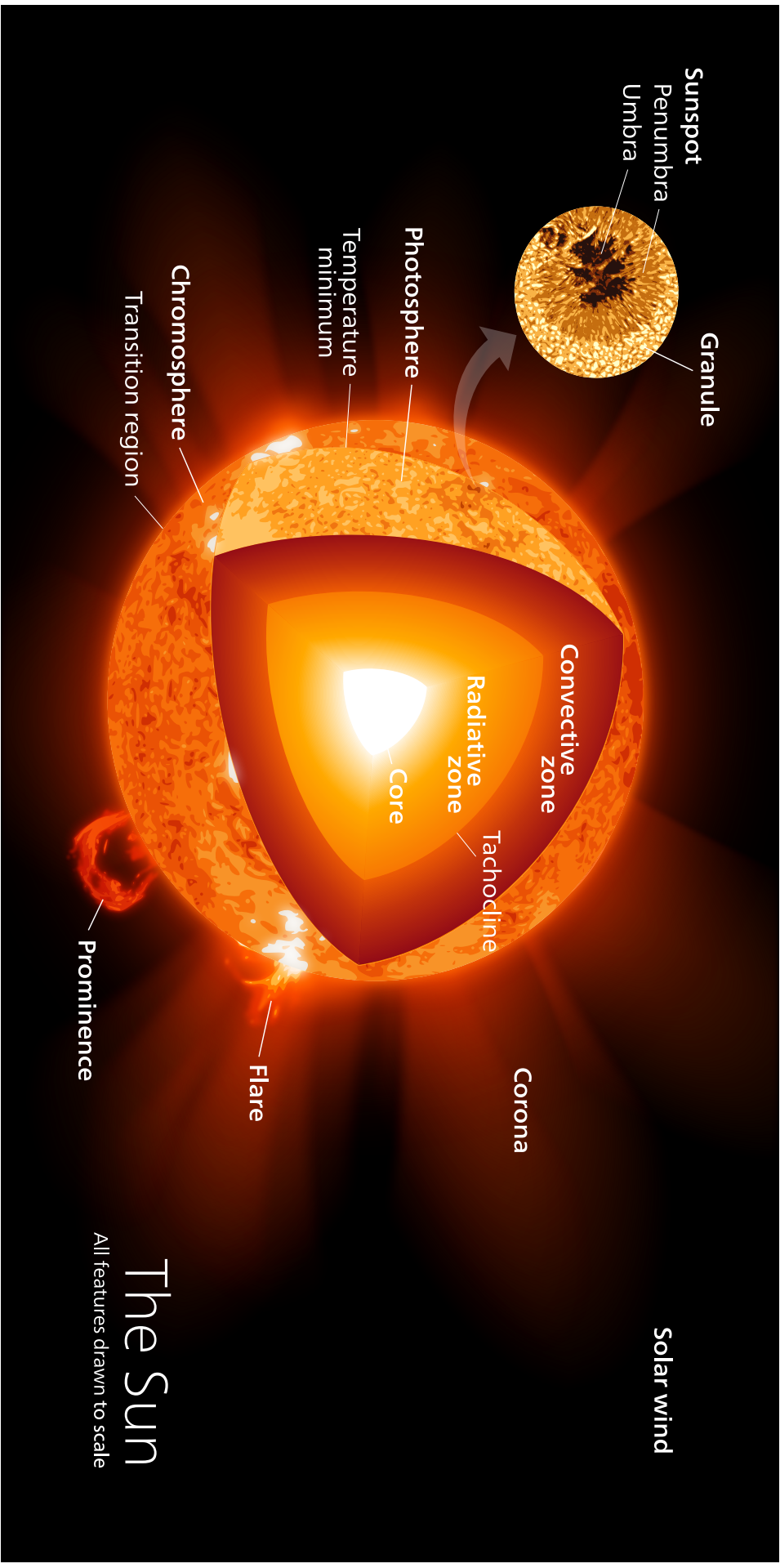


Fig. 1.1 A schematic diagram of the interior and external layers of the Sun. Also shown are several features that occur within the solar atmosphere: sunspots, granulation, flares and prominences. Image credit to [Kelvinsong \(2015\)](#).

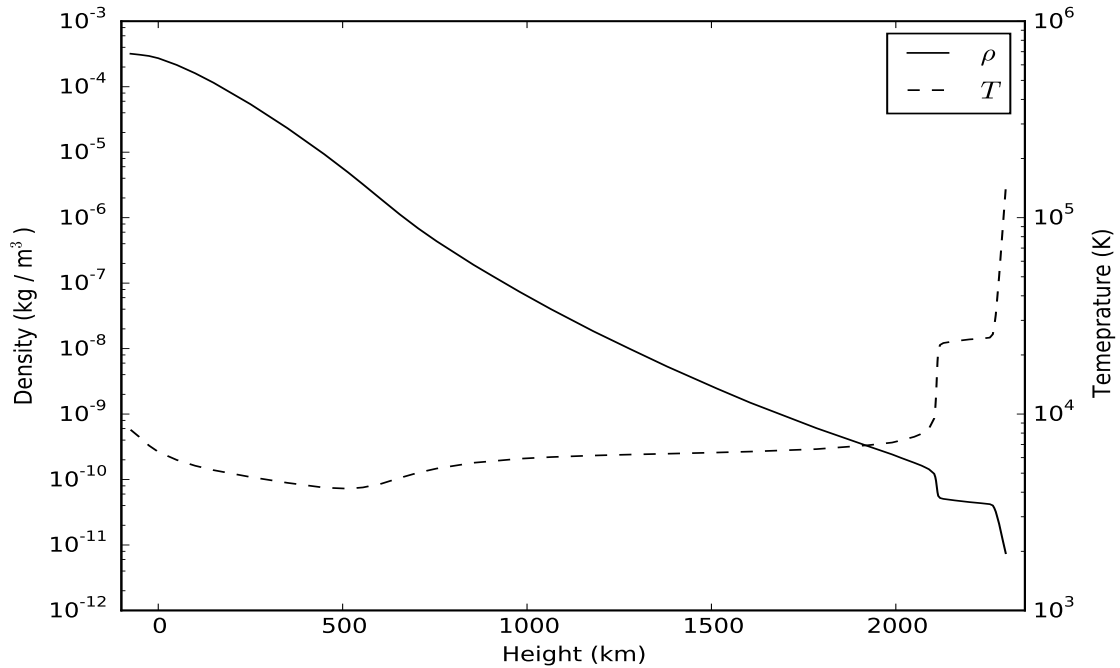


Fig. 1.2 The VAL (Vernazza *et al.*, 1981) model for the lower solar atmosphere, showing the variation of temperature and density with height above the top of the photosphere.

The photosphere is the visible surface of the Sun and is approximately 500 km in thickness, so relative to the solar radius (695,500 km) it is quite thin. Apparent on this layer are *granules*. They are the roofs of convective cells and make up a large interconnected network across the surface of the Sun, constantly changing shape and disappearing. The plasma beta (the ratio of kinetic plasma pressure to the pressure force exerted by the magnetic field) value is greater than one in the photosphere, as a whole (some intense magnetic structures will have a low plasma beta), and therefore the motions within the plasma are dominated by kinetic forces. The temperature at the base of the photosphere is around 10,000 Kelvin and slowly decreases to a minimum of about 4,400 Kelvin at the interface between the photosphere and chromosphere. The photosphere, being relatively isothermal and stratified by gravity has an almost exponential density gradient with a relatively small scale height, and decreases from about  $10^{-4} \text{ kg m}^{-3}$  to  $10^{-6} \text{ kg m}^{-3}$ . This is all according to the VAL (Vernazza *et al.*, 1981) model (shown in Fig. 1.2) which assumes thermodynamic quantities only vary with height and are stationary. In reality, the photosphere is a very dynamical region with flows, varying magnetic fields and can be highly inhomogeneous. The chromosphere sits on top of the photosphere and is around 1.5-2.5 Mm in height. It can be split into two regions; the first is the quiet chromosphere that is essentially non-magnetic and, conversely, a highly magnetic chromosphere above *active regions*. Magnetic structures can be very varied, with horizontal and vertical fields among many forms. The temperature rises slowly in the chromosphere

from the temperature minimum of 4,400 Kelvin at the base to 25,000 Kelvin at its top, i.e. the base of the transition region. These relatively low temperatures and the propensity of the plasma to consist mainly of Hydrogen atoms means that, for a reasonable amount of the chromosphere, the plasma may not be fully ionised. The plasma density decreases rapidly with height (at essentially the same rate as in the photosphere) from about  $10^{-6}$  kg m<sup>-3</sup> to  $10^{-10}$  kg m<sup>-3</sup> at 2,000 km above the solar surface.

The transition region is a very small layer in the solar atmosphere, where the temperature rises dramatically from about 25,000 K to over  $10^6$  K in the space of approximately a few hundred km, with the density falling by two orders of magnitude at the same time. In theoretical models it can be approximated as a jump region for physical quantities.

The corona is an incredibly hot ( $> 10^6$  K) plasma with a very low density. Its temperature, with a large positive gradient that exists in the transition region, is one of the major unexplained problems of solar physics. It is thought to be due to a combination of wave heating and magnetic reconnection, both of these processes dumping energy in the upper atmosphere (for comprehensive reviews on coronal heating see e.g. [Klimchuk, 2006](#), [Reale, 2010](#) and [Parnell and De Moortel, 2012](#)). The corona extends a massive distance from the Sun and by all accounts reaches far beyond the Earth. The magnetic field is mainly radial at this height, extending far into the solar system and accelerates charged particles - causing the solar wind. However, the magnetic field can also be horizontal, for example in large coronal loops connecting regions of opposite magnetic polarity together.

### 1.2.3 Prominences

As a significant portion of this thesis focusses on oscillations in solar prominences, a brief introduction to prominences is given here.

Prominences are large magnetic structures suspended within the coronal plasma. The plasma contained within the prominence, however, is more akin to chromospheric plasma, with densities and temperatures (7500-9000 K) at least two orders of magnitude smaller than that of the surrounding corona (see e.g. [Engvold, 1998](#), [Lin et al., 2005a](#), [Okamoto et al., 2007](#)). Prominences can be split into two main types: *quiescent* and *active region* prominences. Quiescent prominences are the more common type and are widespread over solar latitudes, with relatively long lifetimes of around 3 to 300 days ([Parenti, 2014](#)) compared to active region prominences' rather shorter lifetimes of hours to a day. Their magnetic field structure is mainly horizontal (relative to the surface of the Sun), which is required to support against the action of gravity which would try and push the dense and cool plasma back down. Quiescent prominences' average magnetic field strength is about 8 to 15 G but can

be as large as 80 G in some cases. The magnetic field in active region prominences is typically larger, averaging 20-70 G, although it has been reported to be as high as 600 to 700 G in some cases. The magnetic field structure is more complicated above active regions, where it is twisted into flux ropes. They are composed of dynamical fibril threads that have an average width of 200 km and heights ranging between 3500-28000 km. The sizes of prominences can vary quite a lot. For quiescent prominences their lengths range from 60-600 Mm, widths of 3 to 10 Mm and heights of 10 to 100 Mm. Active region prominences tend to be far smaller, with lengths of 10 Mm and heights of approximately 3 Mm (e.g. [Heinzel and Anzer, 2006](#) or [Lin, 2011](#) for comprehensive reviews). Due to a chromospheric origin, their temperatures at around 7500-9000 K would imply that the plasma is not fully ionised, with the ratio of ions to neutrals of Hydrogen atoms in the range of 0.2-0.9 ([Ruzdjak and Tandberg-Hanssen, 1990](#)). This could have important effects on the dynamics of the plasma, due to the interaction between the ions and neutral atoms and the fact that the neutrals are not affected by the force of the magnetic field.

Within quiescent prominences, turbulent plume structures have also been observed. These appear as dark plumes in the visible band spectra, compared to the brighter surrounding prominence plasma and are hotter as well. They are thought to be triggered by the Rayleigh-Taylor instability (see e.g. [Hillier et al., 2012](#)). The initial up-flow speed is around 20-30 km s<sup>-1</sup> and an average flow speed is around 13-17 km s<sup>-1</sup>, with life times of 300 to 1000 s ([Berger et al., 2010](#)). They exhibit turbulent profiles and even Kelvin-Helmholtz instabilities, with widths usually around 0.5-1 Mm.

Prominences are observed to be surrounded by hot (1-2 MK) elliptical coronal cavities that are much less dense than the surrounding corona (see [Gibson et al., 2010](#) and references therein). Recent observations by [Schmit and Gibson \(2013\)](#), viewed in extreme ultraviolet (EUV) along the filament line at the solar limb, have shown prominence horns that emanate into this coronal cavity. Recent simulations by [Xia et al. \(2014\)](#) gave the first model of prominences as thermally and gravitationally stratified magnetic flux ropes. The investigation confirmed the appearance of these horns.

## 1.3 Solar Oscillations

Oscillations are ubiquitous within the Sun and are observed constantly by ground and spaced based instruments. Oscillations have been used for many years in the branch of solar physics, *Helioseismology* (for extensive notes on stellar oscillations see e.g. [Christensen-Dalsgaard, 1997](#) and for recent reviews linking global to atmospheric oscillations see e.g. [Erdélyi, 2006a](#), [Erdélyi, 2006b](#) and [Pintér and Erdélyi, 2011](#)), to probe the interior of the Sun and find physical parameters such as density and

temperature etc. Cowling (1941) considered the Sun as a spherically symmetric body that was stratified by a gravitational force pointing toward the centre. He found that two types of mode can exist in such configuration namely  $p$ - and  $g$ -modes. These two types of oscillation have different properties.  $p$ -modes are acoustic, pressure driven waves modified a small amount by the strong gravitational nature of the Sun. They are essentially sound waves that one would perceive here on Earth, when one speaks, for example. On the other hand,  $g$ -modes are oscillations that are mainly driven by the buoyancy force; a perturbation displaces plasma downward from its equilibrium position which then rises back under the force of buoyancy. However, only the  $p$ -modes can readily be observed on the surface of the Sun,  $g$ -modes are evanescent within the convection zone and therefore their amplitudes are much smaller than the  $p$ -modes.  $p$ -modes were first categorically observed on the surface of the Sun by Leighton (1960). The amplitudes of the velocity are around  $15 \text{ cm s}^{-1}$  and are observed by measuring the Doppler-shift of spectral lines, with the dominant period being the familiar 5-minute oscillations.

These are, however, not the only oscillations present in the Sun. Due to its dynamo that produces large scale and long lived magnetic fields and associated structures, the Sun also exhibits magnetohydrodynamic (MHD) oscillations. An extensive theory of MHD waves has developed since the ground breaking paper that earned Hannes Alfvén his Nobel prize (Alfvén, 1942). In this one-page paper the Alfvén wave was discovered, an incompressible wave that is produced by the tension in the magnetic field lines. However, due to their incompressible nature they do not perturb the density of the plasma and have been very hard to categorically observe in the Sun, directly or indirectly (Erdélyi and Fedun, 2007a, Jess *et al.*, 2009, Mathioudakis *et al.*, 2013). Along with the Alfvén wave, electrically conducting homogeneous fluids can also support two other waves: the *slow* and *fast magneto-acoustic* (MA) waves. The fast magneto-acoustic wave is driven by a combination of the pressure from the magnetic field and the internal pressure of the plasma itself, with both of these acting in phase. A fast wave can propagate in any direction in the plasma, much like a sound wave in a gas. The slow magneto-acoustic wave is also driven by the magnetic and internal pressure but in this case they act out of phase. The slow wave propagates most of its energy only along magnetic field lines, and struggles to propagate perpendicular to the magnetic field. As their names suggest these waves move at different speeds, the fast wave being the fastest, the Alfvén being the second fastest and the slow wave the slowest (for general theory on MA waves refer to the textbooks Goedbloed and Poedts, 2004, Priest, 2014 or Chapter 5: ‘Magnetohydrodynamic Waves’ in Hasan and Banerjee, 2007).

When there is inhomogeneity in a system, the dynamics of these waves can become more complicated. For example, when a plasma is stratified by gravity, *magneto-acoustic gravity* (MAG) waves are possible. This is a very important addition with

regards to solar theory, as the Sun is highly stratified by gravity. Many studies have dealt with the problem of MAG waves, with two main geometries being extensively studied: the case when the magnetic field is parallel to the gravitational field and the other where they are perpendicular to one another. The first study of its kind was undertaken by [Ferraro and Plumpton \(1958\)](#). The magnetic field was taken to be parallel to the gravitational field and the plasma was approximated to be isothermal. In this study it was found that the Alfvén waves decoupled and could be studied alone but the slow and fast MAG waves were inherently coupled, with solutions to a fourth order ODE being found in terms of a Fröbenius series. [Zhugzhda \(1979\)](#), again, studied this same problem but found solutions in terms of the more general Meijer-G functions. With some simple asymptotic analysis it was found that, in low-beta environments, the slow waves degenerate to vertically propagating sound waves and the fast wave is evanescent. This geometry turns out to be very difficult to study due to the complexity of the functions that arise from solving the equations.

The case where the magnetic field is perpendicular to the gravitational field has been studied in far more depth ([Miles and Roberts, 1992](#), [Miles \*et al.\*, 1992](#)). In this case the Alfvén wave does not decouple from the system but a second order differential equation can be found for arbitrary stratification of magnetic field and density. Without a magnetic field, the gravitational field gives rise to a background frequency of buoyant oscillations, the *Brunt-Väisälä* frequency. In the case of a perpendicular field with a stratified magnetic field, it has been found that there can be a magnetic modification to this, with the magnetic field supporting against the gravitational field (see e.g. [Goedbloed and Poedts, 2004](#)). The stratification also gives rise to a continuous spectra of MHD oscillations due to the singular behaviour of frequencies (see e.g. [Trehan and Uberoi, 1972](#) for an example of the continuous spectra of Alfvén waves or [Cirigliano \*et al.\*, 2004](#) for an in depth exposition of continuous spectra). This singular behaviour can also lead to resonant absorption, phase mixing and then the possible dissipative processes associated with this (see e.g. [Goossens \*et al.\*, 1995](#), [Erdelyi and Goossens, 1995](#) for examples of resonant absorption, see also [Goossens \*et al.\*, 2011](#) for a recent review and [Heyvaerts and Priest, 1983](#) or [Priest, 2014](#) for examples of phase mixing).

Inhomogeneity does not always have to be a continuous transition in mathematical modelling, it can also come in the form of a sharp transition at a surface between two layers. For example, [Roberts \(1981b\)](#) investigated the case of waves both body and surface in a magnetic slab in a non-magnetic environment. It was found that two decoupled modes of oscillations existed: the symmetric *sausage* and asymmetric *kink* modes. Changing the coordinate system to that of a magnetic flux tube in cylindrical coordinates, the same modes were found by [Edwin and Roberts \(1983\)](#) as well higher order fluting harmonics. A cylindrical and slab environment are fairly good physical models of study as they appear (to an approximate extent) in the form of many solar

structures, such as coronal loops or sunspots, both of which are concentrated areas of magnetic flux. Both sausage and kink modes have been observed within the solar atmosphere, i.e. as coronal loop oscillations and in small scale magnetic structures in the photosphere (see e.g. [Verwichte, E. et al., 2005](#) for transverse kink oscillations and [Dorotovic et al., 2014](#) for sausage mode observations).

Recently, there have been models formulated to describe longitudinal oscillations observed in prominence filaments (see e.g. [Luna et al., 2014](#)). [Luna et al. \(2012\)](#) modelled a prominence filament as single flux tube surrounded by a hot corona. The main restoring force for the oscillation of the tube as a whole was found to be gravity, with a small correction due to pressure. A conclusion was drawn that large amplitude oscillations seen in prominences are due to the projected gravitational force on the flux tube, with the relatively strong curvature, due to the gravitational dips, the main contributing factor. [Luna and Karpen \(2012\)](#) investigated multiple prominence threads under the force of gravity, reaching a similar conclusion, whereby the projected gravity on the curved prominence threads was the main restoring force for large amplitude longitudinal oscillations.

## 1.4 Flows and Associated Instabilities

Flows within the Sun and its atmosphere are widespread. The solar interior is not just a spherical ball of static plasma, it is in fact highly dynamic. For one there are large scale flows at the surface of the Sun, due to e.g. its *differential rotation*. The Sun does not rotate like a solid spherical ball but rotates differentially, with some parts rotating at different speeds. The fastest rotation is at the equator with one full rotation every 26.24 days at a speed of  $1.9 \text{ km s}^{-1}$ . The poles rotate once every 36 or 37 days, therefore with much lower speeds. There is a much weaker meridional flow of about  $20 \text{ m s}^{-1}$  that flows directed toward the poles of the Sun.

In the penumbra of sunspots, along the magnetic field lines pointing radially out of the centre, *Evershed* outflow exists ([Evershed, 1909](#)). These outflows stream away from the sunspot and can be around  $2.5\text{-}6 \text{ km s}^{-1}$  in velocity (see e.g. [Montesinos and Thomas, 1997](#) or [Schlichenmaier and Schmidt, 2000](#)). However, there is a much stronger Evershed inflow that exists higher up in the chromosphere ([St. John, 1913](#)). This flow is still associated with sunspots and their magnetic field but is much farther out from the sunspot and flows back toward it along the magnetic field lines at flow speeds of around  $20 \text{ km s}^{-1}$ , although flows can be up to  $50 \text{ km s}^{-1}$ .

Bulk flows are generally present in prominences too, due to their dynamical nature. Flows of around  $10\text{-}70 \text{ km s}^{-1}$  ([Schmieder et al., 1984](#)) are observed within quiescent prominences but flows of up to  $200 \text{ km s}^{-1}$  have been observed within active region prominences. [Berger et al. \(2008\)](#) observed, in both the Ca II H-line and

H $\alpha$  band passes of Solar Orbiter Telescope (SOT), turbulent up-flows in quiescent prominences of an approximately constant speed of 20 km s<sup>-1</sup>.

Bulk flows of plasma can have a dramatic effect on the propagation of waves in fluids. Generally, from the point of an observer, the flows can either increase the speed of propagation of a wave within that medium or decrease its speed, depending on the direction of propagation relative to the flow. This phenomenon is called *Doppler shift*. When there is a shear in flow velocity between fluid layers, there are more dramatic effects on wave oscillations, with instabilities such as the *Kelvin-Helmholtz* and *negative energy wave* (NEW) instabilities occurring.

### 1.4.1 Kelvin-Helmholtz

The Kelvin-Helmholtz instability (Thomson, 1871) has a long history in the study of fluid dynamics. When a fluid exhibits a shear flow, that is two separate layers of fluid are moving at different relative speeds to one another, a surface of vortices can rapidly build up between the interface. For example, these vortices may be seen in clouds called *fluctus* which form between two shear flow layers of the atmosphere.

The Kelvin-Helmholtz instability can also occur in plasmas, again with shear flows between plasma layers necessary. However, if there is a magnetic field present, this can stabilise the surface and inhibit the Kelvin-Helmholtz instability, with the centrifugal force due to the shear flow having to overcome the stabilising magnetic tension (Ruderman *et al.*, 1996). The effect of the magnetic field is to act as somewhat analogous to that of a surface tension term in the hydrodynamic case and therefore can prevent the instability from occurring in a similar sense. In the case of a magnetic field that is parallel to the direction of the shear flow, the instability only occurs when the relative speeds of the two fluids exceeds the root mean square of the Alfvén speeds (in a uniform plasma) in the two plasma layers (Chandrasekhar, 1961). Therefore, in most solar cases, this instability can only occur at shear velocities greater than the Alfvén speed, which in the atmosphere is of a very large magnitude. It must be mentioned that, if the shear in flow is perpendicular to the magnetic field, the magnetic tension does not inhibit the Kelvin-Helmholtz instability (Chandrasekhar, 1961). However, due to the charged nature of plasmas, most background flow fields are likely parallel with the magnetic field.

### 1.4.2 Negative Energy Waves

The velocities required for the Kelvin-Helmholtz instability are rather large for a solar atmospheric context and flows of these magnitude are generally not observed apart from explosive events such as, for example, coronal mass ejections. Thus another explanation may be required to explain the instabilities observed, for example at the interfaces of prominences.

Negative Energy Waves (NEW) have been studied in both hydrodynamics and plasma physics extensively. These instabilities also occur in the presence of a shear flow but require a sink of energy from the system to exist. The reduction in the energy of the system leads to the increase in the amplitude of the wave over time. These type of waves are intimately linked to the so called dissipative instabilities, which occur when there is a reduction in the energy of the system (see e.g. [Ruderman \*et al.\*, 1996](#), [Tirry \*et al.\*, 1998](#), [Andries \*et al.\*, 2000](#), [Andries and Goossens, 2001](#), [Taroyan and Erdélyi, 2002](#)).

[Cairns \(1979\)](#) formulated a simple relation for the energy density of linear waves by discussing the linear dispersion relation and the work done in the formation of the wave, given by the following expression:

$$E = \frac{1}{4} \omega \frac{\partial D}{\partial \omega} |A_0|^2, \quad (1.1)$$

where  $E$  is the wave energy,  $\omega$  is the frequency of the wave,  $D$  is the linear dispersion relation and  $A_0$  is the amplitude of the wave.  $D$  is chosen so that when there is no flow present, all waves are of positive energy so that  $E$  is positive. With this in mind, one can see from Eq. (1.1) that the quantity  $E$  will change sign when either:  $\omega$  changes sign, that is when the flow is strong enough that it reverses the direction of the wave; or when the derivative of  $D$  changes sign, which is related to infinite group velocity of the wave ([Cairns, 1979](#)), when two waves couple together. When  $E$  is negative, a decrease in energy of the system relates to an increase in the amplitude of the wave, holding the frequency constant.

Negative energy waves were first studied in an MHD context by [Ryutova \(1988\)](#). Many other authors have followed suite. For example, [Ruderman and Wright \(1998\)](#) studied the role of negative energy surface waves in the excitation of resonant Alfvén waves at the interface between the magnetosheath and magnetosphere of the Earth (i.e. the magnetopause). It was found that backward propagating waves could become negative energy waves at shear flow speeds lower than those required for the Kelvin-Helmholtz instability (for another example of NEW related to resonant flow instabilities see e.g. [Taroyan and Erdélyi, 2002](#)).

The fact that negative energy waves can occur for flow speeds lower than those required for the Kelvin-Helmholtz instability in MHD and their link to dissipative instabilities makes them an interesting area of study in astrophysical plasmas and a possible explanation for the instabilities observed.

## 1.5 Fully ionised magnetohydrodynamics

A set of non-linear equations can be formed that relate the equations of gas dynamics and the Navier-Stokes equations of fluid dynamics to Maxwell's equations of electro-

dynamics through Ohm's law. These equations govern the dynamics of the plasma; its evolution through space and time. These equations are (in the order they will be presented): the equation of mass conservation, the equation of motion, the energy equation and the induction equation.

The mass conservation equation physically means that the changes to the density at a point in the plasma over time are due exclusively to the mass-flow in and out of that point.

$$\frac{\partial \rho}{\partial t} + \nabla \cdot (\rho \mathbf{v}) = 0, \quad (1.2)$$

where  $\rho$  is the plasma density,  $\mathbf{v}$  is the plasma velocity in 3-dimensional space and  $\nabla$  is the gradient-operator in 3-dimensional space.

The equation of motion governed by Newton's laws of motion state that the forces acting on a plasma are equal to the acceleration of the plasma. In what follows, the plasma motion is subject to a force due to the pressure gradient, the Lorentz force (a combination of the pressure and tension of the magnetic field), a constant gravitational acceleration acting on the mass and a viscous force due to the friction between the particles:

$$\rho \left( \frac{\partial}{\partial t} + \mathbf{v} \cdot \nabla \right) \mathbf{v} = -\nabla p + \mathbf{j} \times \mathbf{B} + \rho \mathbf{g} + \rho \nu \left[ \nabla^2 \mathbf{v} + \frac{1}{3} \nabla (\nabla \cdot \mathbf{v}) \right], \quad (1.3)$$

where  $p$  is the kinetic plasma pressure,  $\mathbf{B}$  is the magnetic field direction and magnitude,  $\mathbf{j}$  is the current density,  $\nu$  is the kinematic coefficient of viscosity and  $\mathbf{g}$  is the acceleration due to gravity.

The energy equation describes how the rate of increase in heat is due to the sum of all energy sinks and sources. It can be written in many forms, we opt for the following concise form:

$$\frac{\rho^\gamma}{\gamma - 1} \left( \frac{\partial}{\partial t} + \mathbf{v} \cdot \nabla \right) \left( \frac{p}{\rho^\gamma} \right) = -\mathcal{L}, \quad (1.4)$$

where  $\mathcal{L}$  is the energy loss function and  $\gamma$  is the ratio of specific heats at constant volume and pressure respectively.

The final equation governs the evolution of the magnetic field and is called the induction equation. We present this with the solenoidal condition that states that there are no sinks or sources of magnetic field, so that the only generation of magnetic field is through the induction equation and it must be true at all times.

$$\frac{\partial \mathbf{B}}{\partial t} = \nabla \times (\mathbf{v} \times \mathbf{B}) + \eta_m \nabla^2 \mathbf{B}, \quad \nabla \cdot \mathbf{B} = 0, \quad (1.5)$$

where  $\eta_m$  is the magnetic diffusivity, which is assumed constant here.

### 1.5.1 Ideal Form

Eqs. (1.2)-(1.5) form a complex system of partial differential equations relating the magnetohydrodynamic variables together. To solve these fully analytically is beyond the scope of our well-developed mathematics. The diffusive terms caused by viscosity and resistivity can often be neglected for many astrophysical objects, particularly in the Sun, where magnetic and viscous Reynolds numbers are for the most part very high.

The *Reynolds number*,  $R_e$ , is defined as

$$R_e = \frac{l_0 V_0}{\nu}, \quad (1.6)$$

where  $l_0$  is a typical length scale and  $V_0$  is a typical velocity. Eq. (1.6) gives the ratio of magnitudes of the inertial and viscous terms in Eq. (1.3). If  $R_e \gg 1$  then inertial terms dominate the viscous terms. If  $R_e \ll 1$ , then viscous forces dominate inertial forces. For the solar cases described in chapters 2-4,  $R_e \gg 1$  and thus viscous forces are neglected. Eq. (1.3) can then be written:

$$\rho \left( \frac{\partial}{\partial t} + \mathbf{v} \cdot \nabla \right) \mathbf{v} = -\nabla p + (\nabla \times \mathbf{B}) \times \frac{\mathbf{B}}{\mu} + \rho \mathbf{g}. \quad (1.7)$$

Here, we have used the fact that

$$\mu_0 \mathbf{j} = \nabla \times \mathbf{B}, \quad (1.8)$$

using Maxwell's equations and assuming non-relativistic speeds. That is,  $V_0 \ll c$ , where  $c$  is the speed of light in a vacuum. Here,  $\mu_0$  is the magnetic permeability in a vacuum.

The *magnetic Reynolds number*,  $R_m$  is defined as

$$R_m = \frac{l_0 V_0}{\eta_m}. \quad (1.9)$$

Eq. (1.9) describes how much the magnetic lines of force are tied to the movement of the plasma. If  $R_m \gg 1$ , the magnetic field is highly coupled to the plasma and moves with the flow of the plasma. If  $R_m \ll 1$ , the magnetic field is weakly coupled and diffuses away on a time-scale,  $\tau_d = l_0^2 / \eta_m$ . Again, for many astrophysical plasmas,  $R_m \gg 1$  and magnetic diffusivity can be neglected from Eq. (1.5):

$$\frac{\partial \mathbf{B}}{\partial t} = \nabla \times (\mathbf{v} \times \mathbf{B}), \quad \nabla \cdot \mathbf{B} = 0. \quad (1.10)$$

Within this thesis we will also suppose that sinks and sources of energy are very small or happen on a very large time-scale compared to the variations of the

plasma quantities. With this in mind, we can say that the energy loss function is approximately negligible, i.e.  $\mathcal{L} \approx 0$ , and thus Eq. (1.4) can be written in the following form (using Eq. (1.2)):

$$\frac{\partial p}{\partial t} + \mathbf{v} \cdot \nabla p + \gamma p \nabla \cdot \mathbf{v} = 0. \quad (1.11)$$

Eqs. (1.7)-(1.11) combined with the unchanged continuity equation, Eq. (1.2), form a closed system of non-linear partial differential equations that relate  $\mathbf{v}$ ,  $\rho$ ,  $p$  and  $\mathbf{B}$  to one another.

### 1.5.2 Ideal Linearised MHD

The non-linear ideal MHD equations above can describe the dynamics of most astrophysical plasmas fully. They are, however, still incredibly difficult to solve analytically. A simple and reasonably accurate next approximation is to assume that solar structures have a background that varies slowly in time and assume that the amplitudes of perturbations to this background are much smaller than the background quantities themselves.:

$$f(\mathbf{r}, t) = f(\mathbf{r}) + f'(\mathbf{r}, t), \quad (1.12)$$

where  $f(\mathbf{r}, t)$  denotes any of the MHD quantities, with  $f(\mathbf{r})$  a background quantity and  $f'(\mathbf{r}, t)$  a small perturbation around the background with  $|f'(\mathbf{r}, t)| \ll |f(\mathbf{r})|$ . Inserting this approximation into Eq. (1.2) and Eqs. (1.7)-(1.11) and neglecting square and cross terms both with perturbations the following set of linear MHD equations can be formed:

$$\frac{\partial \rho'}{\partial t} + \mathbf{v} \cdot \nabla \rho + \rho \nabla \cdot \mathbf{v}' = 0, \quad (1.13)$$

$$\rho \left( \frac{\partial}{\partial t} + \mathbf{v} \cdot \nabla \right) \mathbf{v}' = -\nabla p' + (\nabla \times \mathbf{B}) \times \frac{\mathbf{B}'}{\mu_0} + (\nabla \times \mathbf{B}') \times \frac{\mathbf{B}}{\mu_0} + \rho' \mathbf{g}, \quad (1.14)$$

$$\frac{\partial p'}{\partial t} + \mathbf{v} \cdot \nabla p' + \mathbf{v}' \cdot \nabla p + \gamma p (\nabla \cdot \mathbf{v}') = 0, \quad (1.15)$$

$$\frac{\partial \mathbf{B}'}{\partial t} = (\mathbf{B} \cdot \nabla) \mathbf{v}' - \mathbf{B} (\nabla \cdot \mathbf{v}') - (\mathbf{v}' \cdot \nabla) \mathbf{B} - (\mathbf{v} \cdot \nabla) \mathbf{B}' + (\mathbf{B}' \cdot \nabla) \mathbf{v}, \quad (1.16)$$

$$\nabla \cdot \mathbf{B}' = 0. \quad (1.17)$$

In this formulation we have assumed that both the background magnetic field and background flow are orientated in the same direction, with the direction of stratification perpendicular to both. The solenoidal condition still holds for the background magnetic field also. We must also maintain background momentum balance such that

$$\nabla \left( p + \frac{B^2}{2\mu_0} \right) = \rho \mathbf{g}. \quad (1.18)$$

Here  $B = |\mathbf{B}|$  is just the magnitude of the magnetic field. A convenient definition at this point is the *plasma beta* ( $\beta$ ) given by  $\beta = 2\mu_0 p / B^2$ . This quantity is a measure of the relative importance of kinetic pressure compared to the magnetic pressure. A large value indicates kinetic forces are dominating the motions of the plasma and a low value indicates that magnetic forces are dominating the plasma motions.

## 1.6 Non-Ideal (Dissipative) MHD

It was stated in 1.5.1 that within solar plasmas most non-ideal effects can be ignored due to very large viscous and magnetic Reynolds numbers. This is true in most cases, yet it is interesting to study cases where its contribution is not so small as it can lead to damping and instabilities. The forms of the Reynolds numbers suggest this occurs on reasonably small (comparatively) length scales. Within this thesis, the cases where we include dissipation are those with a low plasma beta,  $\beta \ll 1$  i.e. where magnetic forces dominate kinetic forces of the particles.

Due to the large (relative) difference in mass of protons and electrons the viscous frictional forces in a plasma are due mainly to the collisions between the protons themselves. Braginskii (1965) developed a well known representation of the viscous stress tensor. The tensor is composed of five coefficients  $\kappa_0, \dots, \kappa_4$  (see also Erdelyi and Goossens, 1995). We consider a fully ionized hydrogen plasma where the protons gyrate around the magnetic field with angular frequency  $\omega_p = |q_p \mathbf{B}| / m_p$ , where  $q_p$  is the charge of the Hydrogen ion,  $\mathbf{B}$  is the magnetic field strength and  $m_p$  is the mass of the Hydrogen ion (proton). The period of Coulomb collisions is given by  $\tau_p$ . For our purposes we shall be considering a coronal plasma so that  $\omega_p \tau_p \gg 1$  will hold true, that is the frequency of Coulomb collisions is much smaller than the gyration frequency of the protons. The stress tensor for protons,  $\pi_{ij}$  (where  $i, j = x, y, z$  are

the coordinate axes), is given by its components (Braginskii, 1965):

$$\pi_{zz} = -\kappa_0 W_{zz}, \quad (1.19)$$

$$\pi_{xx} = -\frac{\kappa_0}{2} (W_{xx} + W_{yy}) - \frac{\kappa_1}{2} (W_{xx} - W_{yy}) - \kappa_3 W_{xy}, \quad (1.20)$$

$$\pi_{yy} = \frac{\kappa_0}{2} (W_{xx} + W_{yy}) - \frac{\kappa_1}{2} (W_{yy} - W_{xx}) + \kappa_3 W_{xy}, \quad (1.21)$$

$$\pi_{xy} = \pi_{yx} = -\kappa_1 W_{xy} + \frac{\kappa_3}{2} (W_{xx} - W_{yy}), \quad (1.22)$$

$$\pi_{xz} = \pi_{zx} = -\kappa_2 W_{xz} - \kappa_4 W_{yz}, \quad (1.23)$$

$$\pi_{yz} = \pi_{zy} = -\kappa_2 W_{yz} - \kappa_4 W_{xz}, \quad (1.24)$$

where

$$W_{ij} = \frac{\partial v_i}{\partial x_j} + \frac{\partial v_j}{\partial x_i} - \frac{2\delta_{ij}}{3} \nabla \cdot \mathbf{v}, \quad (1.25)$$

where the coefficients of viscosity are given by:

$$\kappa_0 = 0.96 n_p T_p \tau_p, \quad (1.26)$$

$$\kappa_1 = \frac{3}{10} \frac{n_p T_p}{\omega_p^2 \tau_p}, \quad \kappa_2 = 4\kappa_1, \quad (1.27)$$

$$\kappa_3 = \frac{n_p T_p}{2\omega_p}, \quad \kappa_4 = 2\kappa_3. \quad (1.28)$$

Here,  $T_p$  is the proton temperature,  $n_p$  is the proton number density,  $\delta_{ij}$  is the usual Kronecker-delta function and  $i, j = x, y$  or  $z$  indicate the orthogonal directions in a Cartesian coordinate. It is also assumed here that the  $z$ -axis is aligned with the magnetic field.

What is immediately evident from this formulation is that  $\kappa_0$  is at least an order of  $\omega_p \tau_p$  larger than all the other coefficients  $\kappa_1, \dots, \kappa_4$ . These can therefore be neglected in comparison (we note that in a non-uniform plasmas at resonance locations these can, in fact, be large). The momentum equation thus has the following form

$$\begin{aligned} \rho \left( \frac{\partial}{\partial t} + \mathbf{v} \cdot \nabla \right) \mathbf{v} = & -\nabla p + \mathbf{j} \times \mathbf{B} + \rho \mathbf{g} \\ & + \rho \nu \left\{ \mathbf{b}(\mathbf{b} \cdot \nabla) - \frac{1}{3} \nabla \right\} \{ 3\mathbf{b} \cdot \nabla(\mathbf{b} \cdot \mathbf{v}) - \nabla \cdot \mathbf{v} \}, \end{aligned} \quad (1.29)$$

where  $\mathbf{b}$  is the unit vector in the direction of the magnetic field.

Within this thesis we only consider viscosity as the main dissipative effect. We neglect the energy loss function of Eq. (3.7) and neglect the resistive term of Eq. (1.5).

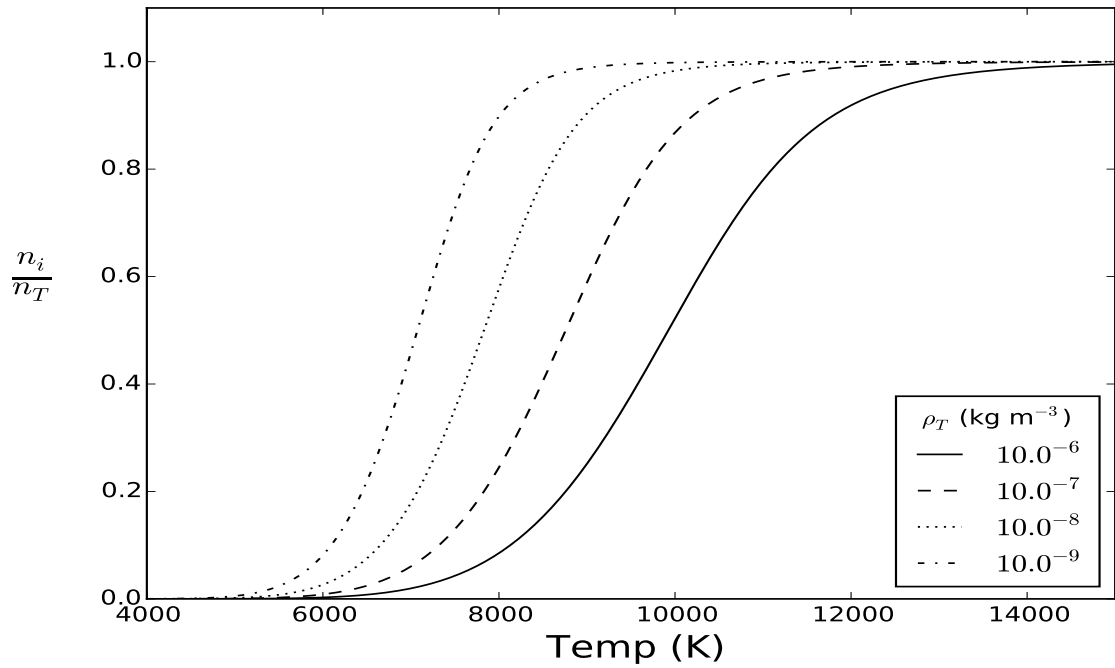
## 1.7 Partially Ionised Plasmas

The solar atmosphere is made up of many different species of atom but a great percentage of these are Hydrogen. The temperature and density of the solar atmosphere is by no means homogeneous either and, as has been stated, it can range from the temperature minimum of 4,300 K to around the  $\sim 10^6$  K mark and higher in the solar corona. The temperature of a hydrogen plasma has consequences on how ionised it is. The ionisation fraction can be described using the Saha equation (see e.g. [Goedbloed and Poedts \(2004\)](#)) which gives the ratio of the number of atoms in ionisation stage  $i + 1$  ( $N_{i+1}$ ) to those in stage  $i$  ( $N_i$ ):

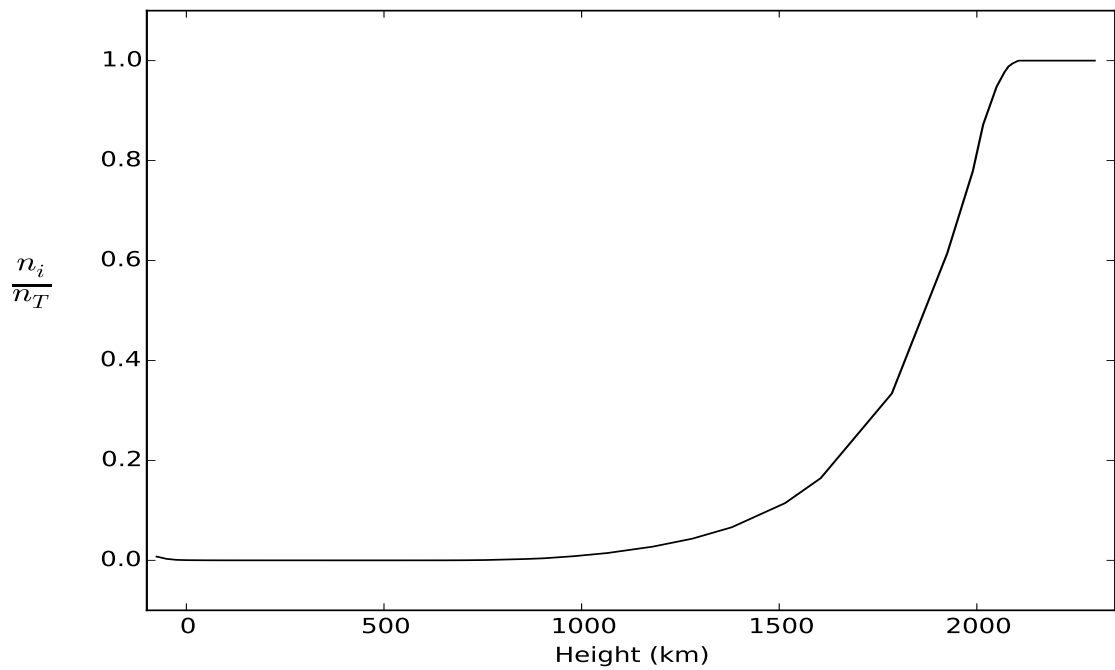
$$\frac{N_{i+1}}{N_i} = \frac{1}{n_e} \left( \frac{2\pi m_e kT}{h^2} \right)^{3/2} \exp\left(-\frac{\chi_i}{k_B T}\right), \quad (1.30)$$

where  $n_e$  is the number density of electrons not attached to an atom,  $m_e$  is the mass of an electron,  $k_B$  is the Boltzmann constant,  $T$  is the temperature of the gas,  $h$  is Planck's constant and  $\chi_i$  is the energy required to ionise an atom in ground state of stage  $i$  to ground state of stage  $i + 1$ . Fig. 1.3a plots the ionisation fraction of hydrogen given by  $n_i/n_T$ , where  $n_i$  is the number of ionised hydrogen atoms and  $n_T$  is the total number of neutral and ionised hydrogen atoms. Four values of the mass density,  $\rho_T$ , have been chosen to simulate the range of values that may occur in solar atmospheric phenomena, starting at  $\rho_T = 10^{-6}$  kg m<sup>-3</sup> at the base of the chromosphere and with a final value of  $\rho_T = 10^{-9}$  kg m<sup>-3</sup> at the top of the chromosphere ([Vernazza \*et al.\*, 1981](#)). It is evident from Fig. 1.3a that at the temperature minimum region, where the temperature is around 4,400 K and  $\rho_T \approx 10^{-6}$  kg m<sup>-3</sup>, there will be almost no ionisation of the plasma at all, with  $n_i/n_T \approx 0.05$ . However, as we climb further into the chromosphere, the temperature steadily rises but the plasma density falls dramatically and thus the ionisation of the plasma will quickly rise. At  $\rho_T = 10^{-9}$  kg m<sup>-3</sup> almost all the hydrogen plasma is ionised above 8000 K. Fig. 1.3b plots the ionisation fraction of the lower solar atmosphere (i.e. the photosphere and chromosphere) for the VAL model. What can be noted is that in the lower solar atmosphere, the ionisation fraction is quite low, that is until the high chromosphere, where the ionisation fraction starts to increase in conjunction with the rapidly increasing temperature. Therefore in the chromosphere it can be argued both that the hydrogen plasma is fully or partially ionised. Clearly, in the corona, at the  $\sim 10^6$  K temperatures the Hydrogen gas is fully ionised and only a single fluid description of the plasma is necessary.

When considering partially ionised plasmas, many different approximations can be taken. Usually one starts from the Boltzmann equations for each species within the plasma, and how these interact with the other species in the fluid. However in this thesis we will be concerned with hydrogen plasmas that are partially ionised



(a) The solution of the Saha-Boltzman equation, Eq. (1.30), for  $\rho_T = 10^{-6}, 10^{-7}, 10^{-8}, 10^{-9}$   $\text{kg m}^{-3}$ .



(b) The ionisation fraction of the solar atmosphere using the VAL (Vernazza *et al.*, 1981) model (for temperature and density plotted in Fig. 1.2) and the Saha-Boltzman equation, Eq. (1.30) for Hydrogen.

and contain the three species: hydrogen ions, neutral hydrogen atoms and electrons. We then split these into two subcategories for the purpose of this thesis: Two fluid equations and partially ionised single fluid equations.

### 1.7.1 Two Fluid Approximation

The Boltzmann kinetic equations (see e.g. [Braginskii, 1965](#) or [Goedbloed and Poedts, 2004](#)) can be used to derive ultimately as many equations as there are species of particles within a plasma. However, as a first insight that still captures the physics reasonably well, just three species are used: ions, neutrals and electrons (denoted by the subscripts  $i$ ,  $n$  and  $e$ , respectively). We would therefore have equations for all these species. For the purposes of this thesis, the equations of the electrons and ions are combined so that only a two fluid plasma is considered (for a more in depth reasoning of this see e.g. [Zaqarashvili \*et al.\*, 2011](#)). Presented below are the continuity equation, momentum equation and energy equations for the ions/electrons and neutrals respectively, the induction equation follows these:

$$\frac{\partial n_i}{\partial t} + \nabla \cdot (n_i \mathbf{v}_i) = 0, \quad (1.31)$$

$$\frac{\partial n_n}{\partial t} + \nabla \cdot (n_n \mathbf{v}_n) = 0, \quad (1.32)$$

$$m_i n_i \left( \frac{\partial \mathbf{v}_i}{\partial t} + (\mathbf{v}_i \cdot \nabla) \mathbf{v}_i \right) = -\nabla p_{ie} + \frac{1}{c} \mathbf{j} \times \mathbf{B} + \frac{\alpha_{en}}{en_e} \mathbf{j} - (\alpha_{in} + \alpha_{en}) (\mathbf{v}_i - \mathbf{v}_n), \quad (1.33)$$

$$m_n n_n \left( \frac{\partial \mathbf{v}_n}{\partial t} + (\mathbf{v}_n \cdot \nabla) \mathbf{v}_n \right) = -\nabla p_n - \frac{\alpha_{en}}{en_e} \mathbf{j} + (\alpha_{in} + \alpha_{en}) (\mathbf{v}_i - \mathbf{v}_n), \quad (1.34)$$

$$\begin{aligned} \frac{\partial p_{ie}}{\partial t} + (\mathbf{v}_i \cdot \nabla) p_{ie} + \gamma p_{ie} \nabla \cdot \mathbf{v}_i &= (\gamma - 1) \frac{\alpha_{ei}}{e^2 n_e^2} \mathbf{j}^2 \\ &+ (\gamma - 1) \alpha_{in} (\mathbf{v}_i - \mathbf{v}_n) \cdot \mathbf{v}_i + (\gamma - 1) \alpha_{en} (\mathbf{v}_e - \mathbf{v}_n) \cdot \mathbf{v}_e \\ &+ \frac{(\mathbf{j} \cdot \nabla) p_e}{en_e} + \gamma p_e \nabla \cdot \frac{\mathbf{j}}{en_e} - (\gamma - 1) \nabla \cdot (\mathbf{q}_i + \mathbf{q}_e), \end{aligned} \quad (1.35)$$

$$\begin{aligned} \frac{\partial p_n}{\partial t} + (\mathbf{v}_n \cdot \nabla) p_n + \gamma p_n \nabla \cdot \mathbf{v}_n &= -(\gamma - 1) \alpha_{in} (\mathbf{v}_i - \mathbf{v}_n) \cdot \mathbf{v}_n + (\gamma - 1) \alpha_{en} (\mathbf{v}_n - \mathbf{v}_e) \cdot \mathbf{v}_n \\ &- (\gamma - 1) \nabla \cdot \mathbf{q}_n, \end{aligned} \quad (1.36)$$

$$\begin{aligned} \frac{\partial \mathbf{B}}{\partial t} = & \nabla \times (\mathbf{v}_i \times \mathbf{B}) + \nabla \times \left( \frac{c \nabla p_e}{en_e} \right) - \nabla \times (\eta \nabla \times \mathbf{B}) \\ & - \nabla \times \left( \frac{\mathbf{j} \times \mathbf{B}}{en_e} \right) + \nabla \times \left( \frac{c \alpha_{en} (\mathbf{v}_i - \mathbf{v}_n)}{en_e} \right). \end{aligned} \quad (1.37)$$

Here,  $n_k$  is the number density,  $m_k$  is the particle mass,  $\mathbf{v}_k$  is the velocity and  $p_k$  is the kinetic pressure all for particle species  $k$ ,  $\mathbf{j}$  is the current density,  $\mathbf{B}$  is the magnetic field,  $\alpha_{kl}$  is the coefficient of friction between two particle species  $k$  and  $l$  (see [Braginskii, 1965](#)),  $e$  is the electron charge,  $\mathbf{q}_k$  is the heat flux density of the particle  $k$ ,  $c$  is the speed of light in a vacuum and  $\eta$  is the coefficient of magnetic diffusion given by

$$\eta = \frac{c^2 (\alpha_{ei} + \alpha_{en})}{4\pi e^2 n_e^2}. \quad (1.38)$$

We neglect to present Ohm's law as it forms part of the *induction* equation given by Eq. (1.37). These equations describe fully the dynamics of a two fluid collisional plasma.

### 1.7.2 Single Fluid approximation

In chapter 5, we approximate the two fluid equations as a single fluid plasma, assuming the frequency of collisions between the species to be larger enough than the frequency of the wave motions within the plasma. This is a very good approximation for wave modes with periods of 3 to 5 minutes which are the most notable for solar oscillations. The ionisation fraction is accounted for in the Cowling resistive term. We introduce the centre of mass velocity of the ions and the neutrals as

$$\mathbf{v} = \frac{\rho_i \mathbf{v}_i + \rho_n \mathbf{v}_n}{\rho_i + \rho_n}, \quad (1.39)$$

and the total density

$$\rho = \rho_i + \rho_n. \quad (1.40)$$

The continuity, momentum, and energy equations are the same as in the fully ionized case. The induction equation is where the difference lies. The plasma considered has a low plasma-beta value and we shall approximate the processes as relatively slow, we can therefore approximate the induction equation as (see e.g. [Khodachenko et al., 2004](#))

$$\frac{\partial \mathbf{B}}{\partial t} = \nabla \times [\mathbf{v} \times \mathbf{B}] + \eta \nabla^2 \mathbf{B} + (\eta_C - \eta) \frac{\nabla \times ([\nabla \times \mathbf{B}] \times \mathbf{B} \times \mathbf{B})}{B^2}, \quad (1.41)$$

where  $\eta = \frac{c^2}{4\pi\sigma}$  and  $\eta_C = \frac{c^2}{4\pi\sigma_C}$  classical Coulomb and Cowling resistivities and  $\sigma = \frac{n_e e^2}{m_e(\nu_{ei} + \nu_{en})}$  and  $\sigma_C = \frac{\xi_n^2 B^2 \sigma}{1 + \frac{\xi_n^2 B^2}{\alpha_n c^2} \sigma}$  are the Coulomb and Cowling conductivities.

Here,  $\nu_{ei}$  and  $\nu_{en}$  are the effective collisional frequencies between electrons and ions and electrons and neutrals,  $n_e$  is the electron number density,  $e$  is the electron charge,  $m_e$  is the mass of an electron,  $\xi_n = \frac{\rho_i + \rho_n}{\rho}$  is the fraction of neutrals,  $\alpha_n = \rho_e \nu_{en} + \rho_i \nu_{in}$ , where  $\nu_{en}$  is the collisional frequency between electrons and neutrals and  $\nu_{in}$  is the collisional frequency between ions and neutrals.  $B^2$  is just the magnitude of the background magnetic field.

## 1.8 Outline of Thesis

The main aim of this thesis is to investigate the modes of oscillation of the solar atmosphere. The thesis can be split into two parts: the first concerns itself with the effect of gravity on magneto-acoustic waves with and without a bulk flow and the second partial ionisation of the plasma and its effect on flow instabilities; focussing mainly on prominence plasmas.

Chapter 2 is concerned with developing the theory behind magneto-acoustic waves in both fully ionised and partially ionised plasmas. The linear oscillations of homogeneous backgrounds of both single fluid and two-fluid plasmas are investigated.

In Chapter 3, we develop a single layer bounded model for MAG waves embedded in a vertical field and study the energy density and all of its components, particularly focussing on the identification of MAG waves in a stratified medium. This leads on to Chapter 4 in which we generalise the work from Chapter 3 into a two-layer bounded model and investigate the distribution of wave energy density in two separate two-layer models of trapped waves that approximate the solar atmosphere. In Chapter 5, we study the effect of a constant bulk flow on the MAG surface waves at an interface between a magnetic and non-magnetic plasma stratified by gravity, a generalisation of previous studies.

The next chapters are focussed on instabilities arising from background flows in partially ionised plasmas. Chapter 6 investigates the effect of the Cowling resistivity in a partially ionised prominence plasma on the dissipative instability caused by a viscous corona and a constant bulk flow, modelling the prominence in a slab geometry. Chapter 7 introduces a two-fluid collisional plasma in a slab geometry with constant background flow. Instabilities due to this flow are investigated in the highly collisional case in the incompressible and compressible limits. The last Chapter summarises the work in this thesis.

# Chapter 2

## Magneto-acoustic Oscillations in Homogeneous Media

### 2.1 Introduction

The Sun is a highly dynamic, structured and stratified plasma. Its interior and atmosphere are composed mainly of Hydrogen but it does contain heavier elements such as Helium or Calcium and Iron (which can be used for observing the Sun). These elements in their base forms are neutral, but due to the large temperatures of the Sun they may be ionised such that some plasmas of the Sun can be composed of ions, electrons and neutrals.

The effects of stratification can be profound in fluids. For example, within a neutral fluid, sound waves may propagate due to a disturbance within the medium. Variations in temperature within the fluid can lead to the changing of the phase speed of the sound wave that can cause the wave to refract and eventually reflected. Stratification due to gravity leads to a buoyancy force that can modify the phase speed of acoustic waves *i.e.* p-modes.

However, when oscillations are considered more locally, for example in the WKB approximation (see *e.g.* [Bender and Orszag, 1978](#)) or when the wavelength ( $\lambda$ ) is much smaller than the scale on which background quantities vary, one can approximate the fluid to be *homogeneous*. In this chapter we introduce the linearised magneto-acoustic waves in homogeneous media. In Section 2, the case of a fully ionised plasma is considered. In Section 3, a two-fluid collisional plasma is studied. In Section 4, the results are summarised.

### 2.2 Fully Ionised

We begin from the linearised MHD equations given by Eqs. (1.13)-(1.17). However, we assume that there is no background flow so that  $\mathbf{v} = \mathbf{0}$  and that the gravitational

force is negligible i.e.  $\mathbf{g} = \mathbf{0}$ . As we are assuming homogeneous media, all background parameters are considered constant functions in space and time and only small perturbations around these vary. With these assumptions the linearised MHD equations are (we do not present the mass conservation equation as the system is fully determined by the following):

$$\rho \frac{\partial \mathbf{v}'}{\partial t} = -\nabla p' + (\nabla \times \mathbf{B}') \times \frac{\mathbf{B}}{\mu_0}, \quad (2.1)$$

$$\frac{\partial p'}{\partial t} + \gamma p (\nabla \cdot \mathbf{v}') = 0, \quad (2.2)$$

$$\frac{\partial \mathbf{B}'}{\partial t} = (\mathbf{B} \cdot \nabla) \mathbf{v}' - \mathbf{B} (\nabla \cdot \mathbf{v}'), \quad (2.3)$$

$$\nabla \cdot \mathbf{B}' = 0. \quad (2.4)$$

For simplicity, we now use a Cartesian coordinate system and assume that the background magnetic field is given by  $\mathbf{B} = (0, 0, B)$ . As the system is infinite and homogeneous in all directions, we can therefore *Fourier* decompose assuming harmonic perturbations so that:  $f'(x, y, z, t) = \hat{f} \exp(i(k_x x + k_y y + k_z z - \omega t))$ , where  $k_x, k_y, k_z$  are the wave numbers in the  $x$ -,  $y$ - and  $z$ -directions respectively and  $\omega$  is the *frequency* of the oscillation. However, as our only preferred direction is the direction in which the magnetic field points, we can rotate our coordinate system, without loss of generality, so that  $k_y = 0$ , i.e. we choose the  $x$ -direction as the direction in which the wave propagates perpendicular to the magnetic field. Inserting this approximation into Eqs. (2.1)-(2.4) and eliminating  $\mathbf{B}'$  and  $p'$  we obtain three equations for  $\hat{v}_x$ ,  $\hat{v}_y$  and  $\hat{v}_z$ :

$$\rho \omega^2 \hat{v}_x = \gamma p k_x (k_x \hat{v}_x + k_z \hat{v}_z) + \frac{B^2}{\mu} (k_x^2 + k_z^2) \hat{v}_x, \quad (2.5)$$

$$\rho \omega^2 \hat{v}_y = \frac{B^2}{\mu} k_z^2 \hat{v}_y, \quad (2.6)$$

$$\rho \omega^2 \hat{v}_z = \gamma p k_z (k_x \hat{v}_x + k_z \hat{v}_z). \quad (2.7)$$

### 2.2.1 Alfvén Waves

What can be noticed immediately from Eqs. (2.5)-(2.7) is that the velocity component in the  $y$ -direction is decoupled from the velocity components in the  $x$ - and  $z$ -directions. Eq. (2.6) describes the *Alfvén* wave (Alfvén, 1942). For non-trivial solutions ( $\hat{v}_y \neq 0$ ) we have the dispersion relation for Alfvén waves and corresponding solutions given as

$$\omega^2 = k_z^2 v_A^2, \quad \omega = \pm k_z v_A, \quad (2.8)$$

where we have introduced the Alfvén speed,  $v_A = (B^2/\rho\mu)^{1/2}$ , which is the speed at which an Alfvén wave propagates along the magnetic field lines.

The Alfvén wave is an incompressible wave that owes its existence to the tension in the magnetic fields lines, which oscillate analogously to a plucked string on a guitar. Being incompressible, they do not perturb the density of the plasma as  $\nabla \cdot \mathbf{v}' = 0$  i.e. the velocity does not diverge. To confirm the incompressibility of the wave, we note that, for an incompressible plasma, the divergence of the velocity field is equal to zero:  $\nabla \cdot \mathbf{v}' = 0$ , so that  $k_x \widehat{v}_x + k_z \widehat{v}_z = 0$ . Next, we substitute this into Eqs. (2.5)-(2.7). This results in the following set of equations:

$$\rho\omega^2 \widehat{v}_x = \frac{B^2}{\mu} (k_x^2 + k_z^2) v_x, \quad (2.9)$$

$$\rho\omega^2 \widehat{v}_y = \frac{B^2}{\mu} k_z^2 \widehat{v}_y, \quad (2.10)$$

$$\omega^2 v_z = 0. \quad (2.11)$$

Unless  $\omega = 0$ , it must be the case that  $\widehat{v}_z = 0$ . Therefore, due to  $\nabla \cdot \mathbf{v}' = 0$  or  $k_x \widehat{v}_x = -k_z \widehat{v}_z$ , we must have  $\widehat{v}_x = 0$  and as such Eqs. (2.9) and (2.11) are the trivial solution. Thus the only equation left is that for the incompressible Alfvén wave given by Eq. (2.10).

Fig. 2.1 plots the variation of the the slow and fast magneto-acoustic waves (see Section 2.2.2) and the Alfvén wave with respect to propagation angle,  $\theta$ . For now, we only refer to the Alfvén wave (green lines). Fig. 2.1a is plotted for a low plasma-beta with  $c_s/v_A = 0.5$ , Fig. 2.1b is plotted for the degenerate case  $c_s/v_A = 1.0$  and Fig. 2.1c is plotted for a high plasma-beta with  $c_s/v_A = 2.0$ . The plasma-beta value has no effect on the Alfvén wave, which always propagates at the Alfvén speed for parallel propagation. For angles of propagation further away from the magnetic field ( $\theta > 0$ ) direction the Alfvén wave decreases in phase speed until the angle of propagation is perpendicular ( $\theta = \pi/2$ ), where the Alfvén wave cannot propagate.

### 2.2.2 Magneto-acoustic waves

We now return to Eqs. (2.5) and (2.7) that relate  $\widehat{v}_x$  and  $\widehat{v}_z$  and describe the slow and fast magneto-acoustic waves. By eliminating  $\widehat{v}_z$  we find:

$$\left( \omega^4 - \omega^2 k^2 (v_A^2 + c_s^2) + k^2 k_x^2 c_s^2 v_A^2 \right) \widehat{v}_x = 0, \quad \widehat{v}_z = \frac{c_s^2 k_x k_z}{\omega^2 - k_z^2 c_s^2} \widehat{v}_x. \quad (2.12)$$

Here we have introduced the sound speed,  $c_s = (\gamma p/\rho)^{1/2}$ , and the wave number magnitude,  $k = (k_x^2 + k_z^2)^{1/2}$ . For non-trivial solutions, the bracketed term on the left hand side of Eq. (2.12) must be equal to zero, giving the dispersion relation for

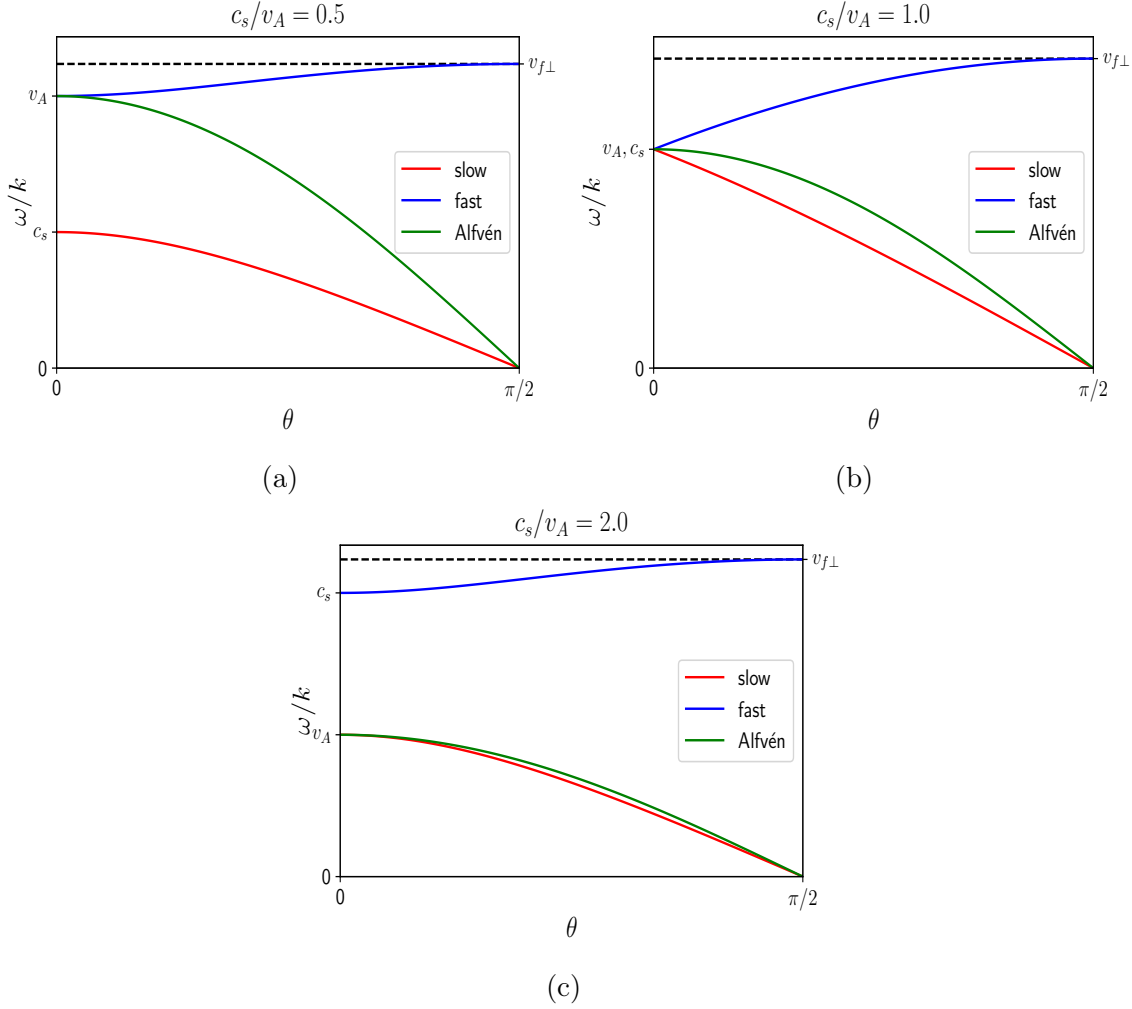


Fig. 2.1 Variation of the phase speed for the Alfvén wave given by Eq. (2.8) (green lines) and the slow (red) and fast (blue) magneto-acoustic waves given by Eqs. (2.13) with respect to the propagation angle  $\theta$  (a) is calculated for a low-beta plasma,  $c_s/v_A = 0.5$  (b) for the degenerate case of  $c_s/v_A = 1$  and (c) for a high-beta plasma,  $c_s/v_A = 2.0$ . The black dashed lines correspond to the phase speed of the fast wave for perpendicular propagation denoted  $v_{f\perp}$ .

*magneto-acoustic* waves. Eq. (2.12) can be solved for  $\omega$  to obtain:

$$\omega = \pm\omega_f, \pm\omega_s, \quad \omega_{f,s} = k \left( \frac{(v_A^2 + c_s^2)}{2} \left( 1 \pm \left( 1 - \frac{4 \cos^2(\theta) c_T^2}{(v_A^2 + c_s^2)} \right)^{1/2} \right) \right)^{1/2}, \quad (2.13)$$

where we have defined the *tube* speed as  $c_T = v_A c_s / (v_A^2 + c_s^2)^{1/2}$  and introduced the propagation angle  $\theta$  with  $k_z = k \cos(\theta)$  and  $k_x = k \sin(\theta)$ . The plus sign within the square root refers to the *fast* magneto-acoustic wave. The minus sign within the square root refers to the *slow* magneto-acoustic wave.

Some simple limits can be taken with regards to propagation angle,  $\theta$ . First, for approximately parallel propagation,  $\theta \rightarrow 0$ , the slow and fast wave frequency can be

approximated by

$$\omega_s \approx \pm k c_s \left( 1 - \frac{\theta^2 v_A^2}{v_A^2 - c_s^2} \right), \quad (2.14)$$

$$\omega_f \approx \pm k v_A \left( 1 + \frac{\theta^2 c_s^2}{v_A^2 - c_s^2} \right), \quad (2.15)$$

if  $v_A > c_s$ , and

$$\omega_s \approx \pm k v_A \left( 1 - \frac{\theta^2 c_s^2}{c_s^2 - v_A^2} \right), \quad (2.16)$$

$$\omega_f \approx \pm k c_s \left( 1 + \frac{\theta^2 v_A^2}{c_s^2 - v_A^2} \right), \quad (2.17)$$

if  $c_s > v_A$ . The degenerate case in which  $v_A = c_s$  needs more care, as a singularity appears in the perturbation methods used to derive Eqs. (2.14)-(2.17). In this case, the frequencies of the slow and the fast wave are approximated by

$$\omega_{f,s} \approx k v_A \left( 1 \pm \frac{\theta}{2} \right). \quad (2.18)$$

The approximations given by Eqs. (2.14)-(2.18) are very good approximations when compared to Fig. 2.1. Indeed, in the low-beta case of Fig. 2.1a and Eqs. (2.14) and (2.15), the phase speed of the slow wave is  $\omega_s/k = c_s$  and the phase speed of the fast wave is  $\omega_f/k = v_A$ , when  $\theta = 0$ . In the degenerate case, shown in Fig. 2.1b and given in Eq. (2.18), the slow and fast wave have equal phase speed  $\omega_{s,f}/k = v_A$  or  $c_s$  when  $\theta = 0$ . In the high-beta case of Fig. 2.1c and Eqs. (2.16) and (2.17) the phase speed of the slow wave is  $\omega_s/k = v_A$  and the phase speed of the fast wave is  $\omega_f/k = c_s$ .

For approximately perpendicular propagation,  $\theta \rightarrow \pi/2$ , the slow wave frequency becomes

$$\begin{aligned} \omega_s &\approx \pm k c_T \left( \theta - \frac{\pi}{2} \right). \\ &\approx \pm k_z c_T \end{aligned} \quad (2.19)$$

The fast wave frequency is approximated as

$$\omega_f \approx k (v_A^2 + c_s^2)^{1/2} \left( 1 - \left( \theta - \frac{\pi}{2} \right)^2 \frac{c_T^2}{v_A^2 + c_s^2} \right). \quad (2.20)$$

Again, the approximations given by Eqs. (2.19) and (2.20) are excellent when compared to Figs. 2.1a-c when  $\theta = \pi/2$ . We must first note from Eq. (2.19) that, for an almost perpendicular propagation vector, the slow wave degenerates to an

oscillation travelling only vertically at the tube speed,  $c_T$ . When the propagation vector is perpendicular to the magnetic field ( $\theta = \pi/2$ ), both Eq. (2.20) and Fig. 2.1 have a good agreement. The fast mode tends to a higher value than both the Alfvén and sound speeds, which is expected.

The plasma-beta indicates to what extent the kinetic pressure or magnetic field are influencing the motions of the plasma. We can rewrite the plasma-beta as  $\beta = 2c_s^2/\gamma v_A^2$ . In the low plasma-beta limit,  $\beta \ll 1$ , where the magnetic field is dominating the motions of the plasma,  $v_A^2 \gg c_s^2$  so that the frequency of the slow wave,  $\omega_s$ , can be approximated as

$$\omega_s \approx \pm k \cos(\theta) c_s^2, \quad (2.21)$$

and the frequency of the fast wave,  $\omega_f$ , can be approximated as

$$\omega_f \approx \pm k v_A. \quad (2.22)$$

The slow wave has deteriorated into a sound wave propagating along the magnetic field lines, whilst the fast wave propagates in any direction at the Alfvén speed.

In the high plasma beta limit,  $\beta \rightarrow \infty$ , where the motions of the plasma are dominated by kinetic effects, the frequency of the slow wave can be approximated as

$$\omega_s \approx \pm k \cos(\theta) v_A, \quad (2.23)$$

and the frequency of the fast wave is approximately

$$\omega_f \approx \pm k c_s. \quad (2.24)$$

The slow wave again propagates along the magnetic field lines but at the Alfvén speed. The fast wave is essentially just a sound wave that can propagate in any direction as kinetic effects are dominant. The reason for this behaviour is that for the fast wave the magnetic pressure and kinetic pressure are acting in phase but for the slow wave they are out of phase so that the slow wave is just a remnant of both.

To further illustrate the effect of plasma-beta on the slow and fast magneto-acoustic modes, we introduce the *wave energy density*,  $E_T$ , (see *e.g.* Bray and Loughhead, 1974) that consists of the kinetic energy density,  $KE$ , magnetic energy density,  $ME$ , internal energy density,  $IE$ , and gravitational energy density,  $GE$ . However, as there is no gravitational force acting within the homogeneous system we neglect  $GE$ . Therefore, we write:

$$E_T = KE + IE + ME, \quad KE = \frac{1}{2}\rho(\widehat{v}_x^2 + \widehat{v}_z^2), \quad IE = \frac{\widehat{p}^2}{2\rho c_s^2}, \quad ME = \frac{1}{2\mu}(\widehat{B}_x^2 + \widehat{B}_z^2). \quad (2.25)$$

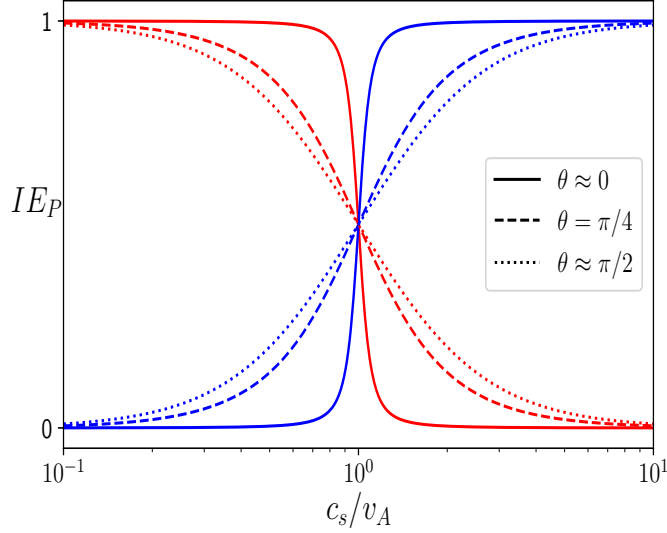


Fig. 2.2 The variation of the proportion of internal energy  $IE_P$  with respect to the parameter  $c_s/v_A$  for the slow (red) and fast (blue) waves with almost parallel ( $\theta \approx 0$ , solid lines), oblique ( $\theta = \pi/4$ , dashed lines) and almost perpendicular ( $\theta \approx \pi/2$ , dotted lines) propagation.

We now define the quantity,

$$IE_P = \frac{IE}{IE + ME}, \quad (2.26)$$

to study whether the mode is of an acoustic nature or magnetic nature.

Fig. 2.2 plots the variation of  $IE_P$  with respect to  $c_s/v_A$  for almost parallel ( $\theta \approx 0$ ), oblique ( $\theta = \pi/4$ ) and almost perpendicular ( $\theta \approx \pi/2$ ) propagation. As  $c_s/v_A \rightarrow 0$  the slow mode is essentially driven by the internal energy whereas the fast mode is driven by the magnetic energy. On the other hand, as  $c_s/v_A \rightarrow \infty$ , the fast wave is driven by the internal energy and the slow wave is driven by the magnetic energy. When  $c_s/v_A \rightarrow 1$ , from either side, we see that the slow and fast wave both have an equal share of internal and magnetic energy driving them, in agreement with Fig. 2.1 and Eq. (2.18). As the propagation angle departs further from parallel to the magnetic field, there is a greater share of magnetic and internal energy for both the slow and fast modes.

## 2.3 Two-fluid

We now consider a two-fluid collisional plasma in which we only study the effects of collisions between ion and neutral fluids. We once again use a Cartesian coordinate system where the background fluids are infinite and homogeneous, permeated by a magnetic field that is chosen in the  $z$ -direction i.e.  $\mathbf{B} = (0, 0, B)$ . We linearise Eqs. (1.31)-(1.37) around this background plasma and neglect magnetic diffusion in the

induction equations for simplicity, as well as collisions between electrons and neutrals in the momentum equations and any heating terms in the energy equations (see [Zaqarashvili \*et al.\*, 2011](#) for more details):

$$\rho_i \frac{\partial \mathbf{v}'_i}{\partial t} = -\nabla p'_i + (\nabla \times \mathbf{B}') \frac{B}{\mu} - \rho_n \nu_{in} (\mathbf{v}'_i - \mathbf{v}'_n), \quad (2.27)$$

$$\rho_n \frac{\partial \mathbf{v}'_n}{\partial t} = -\nabla p'_n + \rho_n \nu_{in} (\mathbf{v}'_i - \mathbf{v}'_n), \quad (2.28)$$

$$\frac{\partial p'_i}{\partial t} + \gamma p_i \nabla \cdot \mathbf{v}'_i = 0, \quad (2.29)$$

$$\frac{\partial p'_n}{\partial t} + \gamma p_n \nabla \cdot \mathbf{v}'_n = 0, \quad (2.30)$$

$$\frac{\partial \mathbf{B}'}{\partial t} = \nabla \times (\mathbf{v}'_i \times \mathbf{B}). \quad (2.31)$$

Here, we have introduced the collisional frequency,  $\nu_{in}$  between two species when both species have the same temperature ([Soler \*et al.\*, 2012](#)):

$$\nu_{in} = \frac{\alpha_{in}}{\rho_n}, \quad (2.32)$$

where  $\alpha_{in}$  is the coefficient of friction between ions and neutrals given by ([Braginskii, 1965](#)):

$$\alpha_{in} = n_i n_n m_{in} \sigma_{in} \frac{4}{3} \sqrt{\frac{8kT}{\pi m_{in}}}. \quad (2.33)$$

Here,  $n_i$  and  $n_n$  are the number densities of the ion and neutral species  $m_i$  and  $m_n$  are the masses of the ion and neutral molecules,  $m_{in} = m_i m_n / (m_i + m_n)$  is the reduced mass and  $\sigma_{in} = \pi(r_i + r_n)^2 = 4\pi r_i^2$  is the collisional cross section between ions and neutrals assuming the same radius,  $r_i = r_n$ , of the molecules.

Like the fully ionised case we now Fourier decompose in space and time assuming harmonic perturbations of the form  $f'(x, y, z, t) = \widehat{f} \exp(i(k_x x + k_y y + k_z z - \omega t))$ . Again, as the only preferred direction in the system is in the direction of the magnetic field, we can rotate our coordinate system so that  $k_y = 0$ , without loss of generality. Inserting these assumptions into Eqs. (2.27)-(2.28) we form a set of equations for the components of both the ion and neutral velocities in the  $x$ ,  $y$  and  $z$ -directions,

respectively:

$$\rho_i \omega^2 \widehat{v}_{xi} = \gamma p_i k_x (k_x \widehat{v}_{xi} + k_z \widehat{v}_{zi}) + \frac{B^2}{\mu} (k_x^2 + k_z^2) \widehat{v}_{xi} - i\omega \rho_n v_{in} (\widehat{v}_{xi} - \widehat{v}_{xn}), \quad (2.34)$$

$$\rho_i \omega^2 \widehat{v}_{yi} = \frac{B^2}{\mu} k_z^2 \widehat{v}_{yi} - i\omega \rho_n v_{in} (\widehat{v}_{yi} - \widehat{v}_{yn}), \quad (2.35)$$

$$\rho_i \omega^2 \widehat{v}_{zi} = \gamma p_i k_z (k_x \widehat{v}_{xi} + k_z \widehat{v}_{zi}) - i\omega \rho_n v_{in} (\widehat{v}_{zi} - \widehat{v}_{zn}). \quad (2.36)$$

$$\rho_n \omega^2 \widehat{v}_{xn} = \gamma p_n k_x (k_x \widehat{v}_{xn} + k_z \widehat{v}_{zn}) + i\omega \rho_n v_{in} (\widehat{v}_{xi} - \widehat{v}_{xn}), \quad (2.37)$$

$$\rho_n \omega^2 \widehat{v}_{yn} = i\omega \rho_n v_{in} (\widehat{v}_{yi} - \widehat{v}_{yn}), \quad (2.38)$$

$$\rho_n \omega^2 \widehat{v}_{zn} = \gamma p_n k_z (k_x \widehat{v}_{xn} + k_z \widehat{v}_{zn}) + i\omega \rho_n v_{in} (\widehat{v}_{zi} - \widehat{v}_{zn}). \quad (2.39)$$

Immediately evident is the number of equations in comparison to the fully ionised case, six in total compared to three. The ion and neutral velocity components are only coupled to one another through the collisions between them in the momentum equation

### 2.3.1 Alfvén waves

Just as in the fully ionised case, the velocity perturbations in the y-direction have decoupled from the other perturbations. By eliminating  $\widehat{v}_{yn}$  between Eqs. (2.35) and (2.38) we find

$$\left( \tilde{\omega}^2 - k_z^2 v_A^2 \right) v_{yi} = 0, \quad \tilde{\omega}^2 = \omega^2 \left( 1 + \frac{i\chi v_{in}}{\omega + i v_{in}} \right). \quad (2.40)$$

Here, we have introduced the parameter  $\tilde{\omega}^2$  as in [Kumar and Roberts \(2003\)](#) and  $\chi = \rho_n/\rho_i$  that measures the ionisation of the plasma. If  $\chi \rightarrow 0$  the fluid is almost fully ionised, if  $\chi \rightarrow \infty$  the fluid is almost completely neutral and an intermediate value e.g.  $\chi = 1$  means the plasma consists of an even amount of neutrals and ions.

The bracketed term on the left hand side of Eq. (2.40) gives the dispersion relation for Alfvén waves in a two fluid plasma. The formulation in Eq. (2.40) is useful as we can see the physics very nicely. For example, if  $v_{in} \ll \omega$ , i.e. the collision-less limit, the solution is approximately

$$\omega \approx k_z v_A, \quad (2.41)$$

just like the fully ionised case because the ionised fluid is not interacting with the neutral fluid. On the other hand, if  $\omega \ll v_{in}$ , the highly collisional limit, the solution is approximately

$$\omega \approx k_z \tilde{v}_A, \quad \tilde{v}_A = \left( \frac{B^2}{(\rho_i + \rho_n) \mu} \right)^{1/2} \quad (2.42)$$

where  $\tilde{v}_A$  is the Alfvén speed with the ion and neutral fluid acting as a single fluid, due to the high amount of collisions between them.

In reality Eq. (2.40) is a third order polynomial

$$\omega^3 + i\nu_{in}(1 + \chi)\omega^2 - k_z^2 v_A^2 \omega + i\nu_{in} k_z^2 v_A^2 = 0 \quad (2.43)$$

The analytical expression for the roots of Eq. (2.43) are reasonably cumbersome. We therefore follow the same procedure as in Soler *et al.* (2013) and study the discriminant of this third order polynomial to see what type of solutions are produced. Firstly, a more convenient dimensionless form for this study appears to be

$$\tilde{\phi}^3 + \tilde{\phi}^2 + \frac{s^2}{1 + \chi}\tilde{\phi} + \frac{s^2}{(1 + \chi)^2} = 0. \quad (2.44)$$

Here, we have introduced the dimensionless variables

$$\tilde{\phi} = \frac{\omega}{i\nu_{in}(1 + \chi)}, \quad s = \frac{k_z \tilde{v}_A}{\nu_{in}}. \quad (2.45)$$

Eq. (2.44) is a third-order polynomial with real coefficients and thus its discriminant,  $\Delta$ , is given by

$$\Delta = -\frac{s^2}{(1 + \chi)^4} \left[ 4s^4(1 + \chi) - s^2(\chi^2 + 20\chi - 8) + 4(1 + \chi)^2 \right] \quad (2.46)$$

We have three cases for the discriminant  $\Delta$ :

- If  $\Delta > 0$ , there are three distinct imaginary roots of Eq. (2.43).
- If  $\Delta = 0$ , Eq. (2.43) has multiple purely imaginary roots.
- If  $\Delta < 0$ , Eq. (2.43) has one purely imaginary root and two complex roots.

For propagating waves, we require that  $\Delta < 0$ . We set  $\Delta = 0$  to see at what values of  $s$  there is a change in behaviour.

$$s = \left[ \frac{\chi^2 + 20\chi - 8}{8(1 + \chi)} \pm \frac{\chi^{1/2}(\chi - 8)^{3/2}}{8(1 + \chi)} \right]^{1/2}. \quad (2.47)$$

We specify that  $s$  must be real. With this in mind, when  $\chi < 8$ , we have that  $s$  would be complex and thus only complex solutions of  $s$  satisfy  $\Delta = 0$  and, therefore, all solutions are oscillatory. If  $\chi > 8$  we have to consider positive and negative signs of Eq. (2.47). For  $\chi > 8$  all solutions to Eq. (2.47) are positive, which we denote  $r_1$  and  $r_2$ , where  $r_1 > r_2$ . Within the interval  $r_2 < s < r_1$  the discriminant changes sign and is positive and thus oscillatory solutions are not possible in that region.

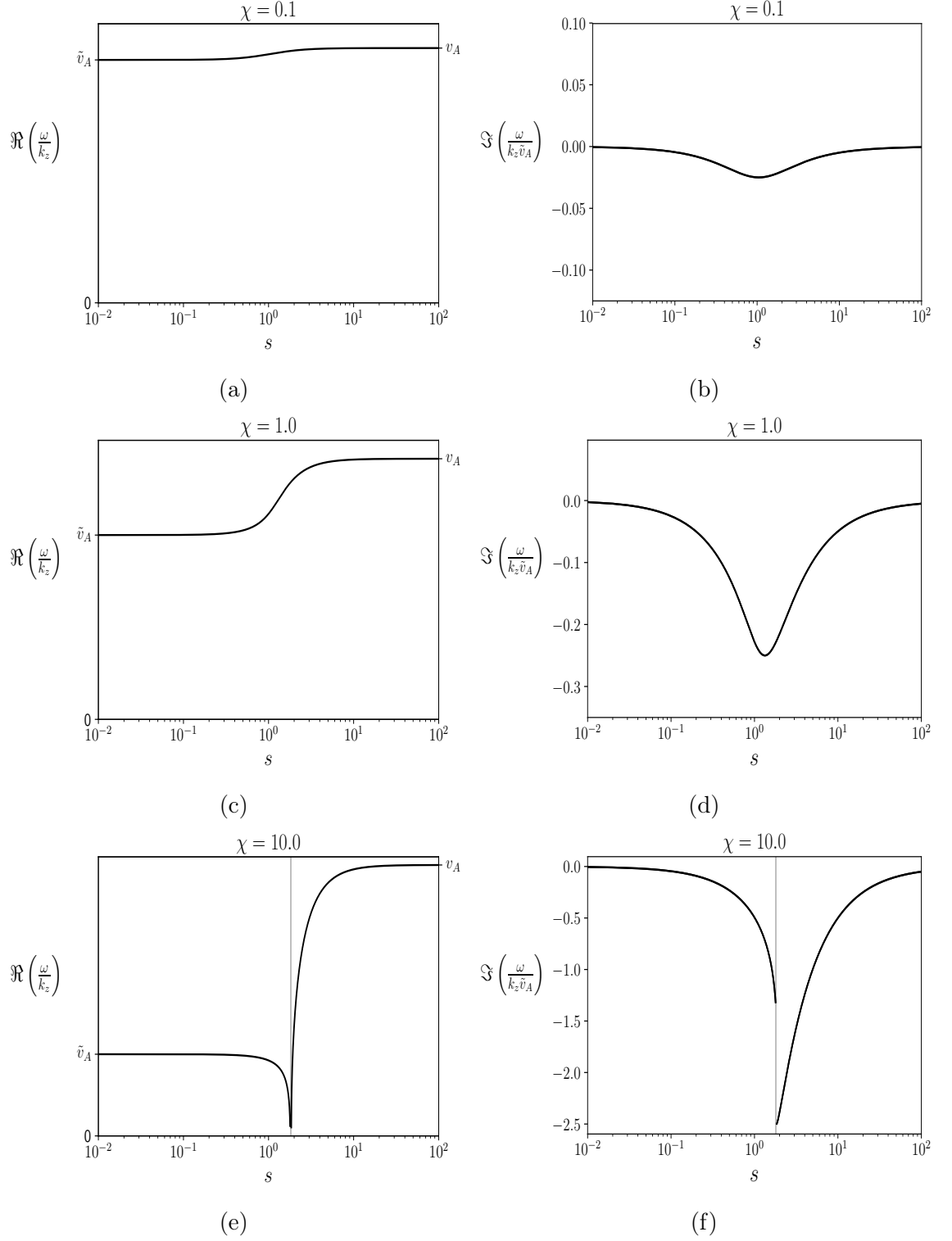


Fig. 2.3 The variation of the real part of the phase speed,  $\omega/k_z$ , and imaginary parts of the dimensionless frequency,  $\omega/k_z \tilde{v}_A$ , with respect to the dimensionless parameter  $s$  given by solutions to Eq. (2.43). Panels (a) and (b) are plotted for  $\chi = 0.1$ , (c) and (d) are for  $\chi = 1.0$  and (e) and (f) are for  $\chi = 10.0$ . The grey regions indicate the cut-off regions given by Eq. (2.47).

Figs. 2.3a-f plot the solutions,  $\omega/k\tilde{v}_A$ , of Eq. (2.43) for  $\chi = 0.5, 4$  and  $100$  with respect to the dimensionless quantity,  $s$ , that measures the size of the collisional frequency compared to the external Alfvén frequency,  $\tilde{v}_A$ ; a large value of  $s$  corresponds to a low collisional frequency (periods of oscillations are shorter than the time-scale that collisions between neutrals and ions occur on) and a low value of  $s$  to a high collisional frequency (periods of oscillations are far longer than the time-scale that collisions between neutrals and ions occur on).

Figs. 2.3a, c and e plot the real parts of the solution and Figs. 2.3b, d and f plot the imaginary parts of the solution. In all cases, for a high collisional frequency, the real part of the dimensionless phase speed,  $\omega/k_z = \tilde{v}_A$ , which is expected, as in that limit the phase speed tends to  $\tilde{v}_A$  i.e. the total Alfvén speed defined previously. However, when  $s \approx 1$ , the real part of the frequency starts to be affected. In Fig. 2.3a when  $\chi = 0.5$ , i.e. there are twice as many ions and neutrals, we see that as  $s \rightarrow \infty$ , that is in the collision-less limit,  $|\omega/k_z|$  tends to the ion Alfvén speed,  $v_A$ . Again, in Fig. 2.3c, when  $\chi = 4.0$ , i.e. there are 4 times as many neutrals as ions, we see that  $\omega/k_z$  tends to the ion Alfvén speed once more.

In Fig. 2.3e there is a slight difference to the the previous figures. We see that, somewhere between  $s = 1$  and  $10$ ,  $\Re(\omega/k_z) = 0$ , and we reach the cut-off region described in Eq. (2.47). However, when the cut-off region indicated by the grey area is navigated, as  $s \rightarrow \infty$  again, we see  $\omega/k_z$  tends to  $v_A$  again.

The more interesting behaviour is largely for the imaginary parts of the solutions. In Figs. 2.3b,d and f, in the limit as  $s \rightarrow 0$ , the imaginary part of the frequency tends to 0 and, in the limit as  $s \rightarrow \infty$ , again, the imaginary part of the frequency tends to 0. This is expected for the highly collisional limit and collision-less limit. When  $s \approx 1$ , the imaginary part of the frequency becomes more negative (i.e. the modes are damped more), peaking around this value. In Fig. 2.3b,  $\chi = 0.5$ , the peak value is around  $\Im(\omega/k_z\tilde{v}_A) \approx 0.15$  whereas, when  $\chi = 4.0$  in Fig. 2.3d the peak is even higher at around  $\Im(\omega/k_z\tilde{v}_A) \approx 1$ . When  $\chi = 100$  in Fig. 2.3f, the peak value is around  $\Im(\omega/k_z\tilde{v}_A) \approx 10$ .

Clearly very interesting behaviour can occur for Alfvén waves in a two-fluid plasma. If the collisional frequency between ions and neutrals is much larger than the frequency of the waves, we may as well consider the single fluid approximation. However, if the collisional frequency is much smaller than the frequency of Alfvén waves, we can consider the ion and neutral fluids to not interact at all.

### 2.3.2 Magneto-acoustic waves

By rewriting Eqs. (2.34), (2.36), (2.37) and (2.39) we can write the following set of equations:

$$\left(\omega^2 - k_x^2 c_i^2 - k^2 v_A^2 + i\omega\chi v_{in}\right) \widehat{v}_{xi} = c_i^2 k_x k_z \widehat{v}_{zi} + i\omega\chi v_{in} \widehat{v}_{xn}, \quad (2.48)$$

$$\left(\omega^2 - k_z^2 c_i^2 + i\omega\chi v_{in}\right) \widehat{v}_{zi} = c_i^2 k_x k_z \widehat{v}_{xi} + i\omega\chi v_{in} \widehat{v}_{zn}, \quad (2.49)$$

$$\left(\omega^2 - k_x^2 c_n^2 + i\omega v_{in}\right) \widehat{v}_{xn} = c_n^2 k_x k_z \widehat{v}_{zn} + i\omega v_{in} \widehat{v}_{xi}, \quad (2.50)$$

$$\left(\omega^2 - k_z^2 c_n^2 + i\omega v_{in}\right) \widehat{v}_{zn} = c_n^2 k_x k_z \widehat{v}_{xn} + i\omega v_{in} \widehat{v}_{zi}. \quad (2.51)$$

Here, we have defined the ion sound speed as  $c_i = (\gamma p_i / \rho_i)^{1/2}$  and the neutral sound speed as  $c_n = (\gamma p_n / \rho_n)^{1/2}$ . The system of equations given by Eqs. (2.48)-(2.51) can be written as a matrix, the determinant of which, after some algebra, provides the dispersion relation (Zaqarashvili *et al.*, 2011):

$$\begin{aligned} & \left(\omega^2 - \omega_f^2\right) \left(\omega^2 - \omega_s^2\right) \omega \left(\omega^2 - k^2 c_n^2\right) \\ & + i v_{in} \left[ \omega^4 (1 + \chi) \left(\omega^2 - k^2 \tilde{c}_i^2\right) \right. \\ & \quad \left. + \left(\omega^2 - k^2 c_n^2\right) \left( \left(\omega^2 - \omega_s^2\right) \left(\omega^2 - \omega_f^2\right) + \chi \omega^2 \left(\omega^2 - k^2 (c_i^2 + v_A^2)\right) \right) \right] \\ & - v_{in}^2 \omega (1 + \chi)^2 \left(\omega^2 - \tilde{\omega}_f^2\right) \left(\omega^2 - \tilde{\omega}_s^2\right) = 0. \end{aligned} \quad (2.52)$$

Here, we have defined the *total* sound speed,  $\tilde{c}_i = \gamma(p_i + p_n) / (\rho_i + \rho_n)$  and total fast (subscript *f*) and slow (subscript *s*) frequencies

$$\tilde{\omega}_{f,s} = k \left( \frac{(\tilde{v}_A^2 + \tilde{c}_i^2)}{2} \left( 1 \pm \left( 1 - \frac{4k_z^2 \tilde{c}_T^2}{k^2 (\tilde{v}_A^2 + \tilde{c}_i^2)} \right)^{1/2} \right) \right)^{1/2}, \quad (2.53)$$

where the *total* tube speed is  $\tilde{c}_T = \tilde{v}_A \tilde{c}_i / (\tilde{v}_A^2 + \tilde{c}_i^2)^{1/2}$ .

Again, Eq. (2.52) has been written in a useful form so that limits may be taken easily. Firstly, taking the collision-less limit ( $\omega \gg v_{in}$ ), Eq. (2.52) reduces to

$$\left(\omega^2 - \omega_f^2\right) \left(\omega^2 - \omega_s^2\right) \left(\omega^2 - k^2 c_n^2\right) = 0, \quad (2.54)$$

which has solutions

$$\omega \approx \pm k c_n, \quad \omega \approx \pm \omega_{f,s}. \quad (2.55)$$

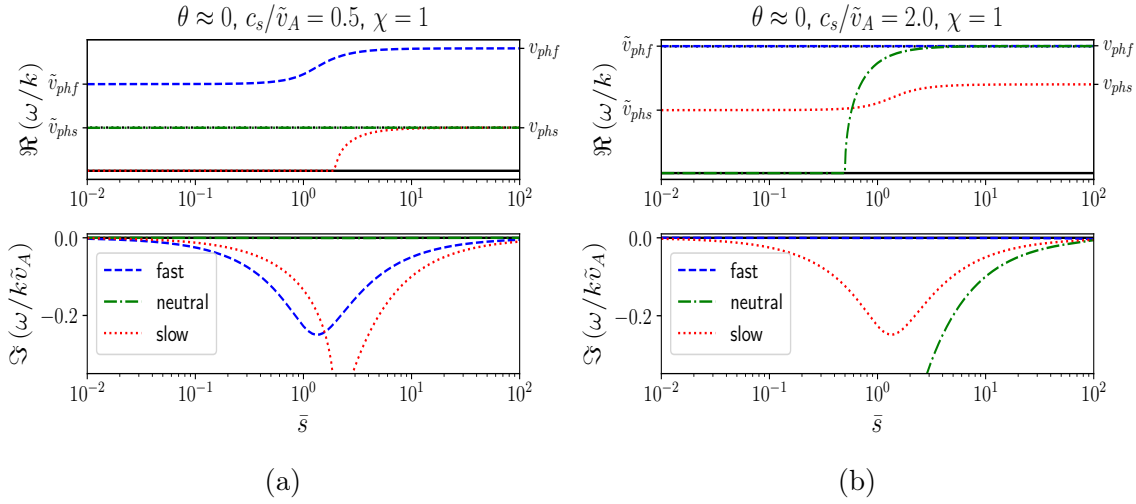


Fig. 2.4 Variation of the real part of the phase speed (upper panels),  $\Re(\omega/k)$  and imaginary part of the dimensionless frequency (lower panels),  $\Im(\omega/k\tilde{v}_A)$ , with respect to the dimensionless parameter  $\bar{s}$  for the slow (red dotted), fast (blue dashed) and neutral (green dot-dashed) solutions of Eq. 2.52 for approximately perpendicular propagation ( $\theta \approx 0$ ) (a) for a low-beta plasma ( $c_s/\tilde{v}_A = 0.5$ ) (b) for a high-beta plasma ( $c_s/\tilde{v}_A = 2$ ). Noted on the right hand axes of the top panels are the phase speeds of the slow ( $v_{phf}$ ) and fast ( $v_{phs}$ ) waves in the collision-less limit (Eq.) and on the left hand axis the phase speeds of the slow ( $\tilde{v}_{phf}$ ) and fast ( $\tilde{v}_{phs}$ ) waves in the highly collisional limit. Both (a) and (b) are evaluated for  $\chi = 1$ .

It is clear from these solutions that, due to the weak interaction between the ion and neutral fluids, the ion and neutral fluids oscillate alone so that in the neutral fluid there are just sound waves propagating at the neutral sound speed and in the ion fluid the slow and fast magneto-acoustic waves propagate.

Next, we may take the highly collisional limit ( $\omega \ll \nu_{in}$ ) of Eq. (2.52), which then reduces to

$$\left(\omega^2 - \tilde{\omega}_f^2\right)\left(\omega^2 - \tilde{\omega}_s^2\right) = 0, \quad \omega \approx \pm\tilde{\omega}_{f,s}. \quad (2.56)$$

Eq. (2.56) has solutions given by Eq. (2.53). The collisions between the neutral and ion fluids are so regular that they effectively behave as a single fluid with density  $\rho = \rho_i + \rho_n$ , and pressure,  $p = p_i + p_n$ .

Figs. 2.4-2.6 plot the variation of the real part (upper panel) of the phase speed,  $\omega/k$ , and the imaginary part (lower panel) of the dimensionless frequency,  $\omega/k\tilde{v}_A$ , with respect to the dimensionless parameter,  $\bar{s} = k\tilde{v}_A/\nu_{in}$  (this measures the size of the collisional frequency in comparison to the mode frequency) for the solutions of Eq. (2.52).

Figs. 2.4a and b are plotted for almost parallel propagation (parallel to the magnetic field) with  $\theta = 0.1$ , Figs. 2.5a and b for oblique propagation,  $\theta = \pi/4$ , and Figs. 2.6a and b for almost perpendicular propagation,  $\theta = \pi/2 - 0.1$ . Figs. 2.4a-2.6a are plotted for a moderately low plasma-beta,  $c_s/\tilde{v}_A = 0.5$ , and Figs. 2.4b-2.6b are

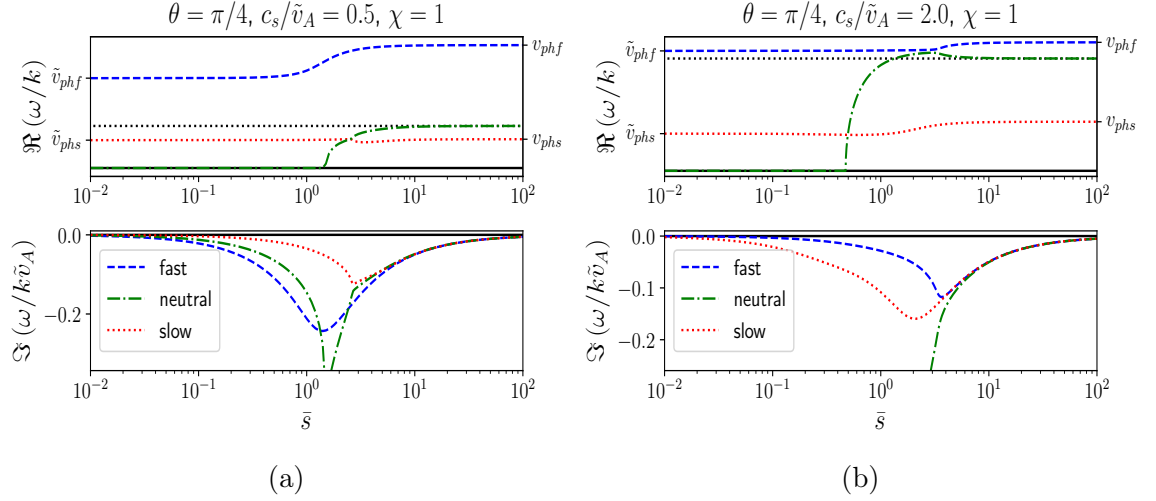


Fig. 2.5 Same as Fig. 2.4 but for oblique propagation ( $\theta = \pi/4$ ).

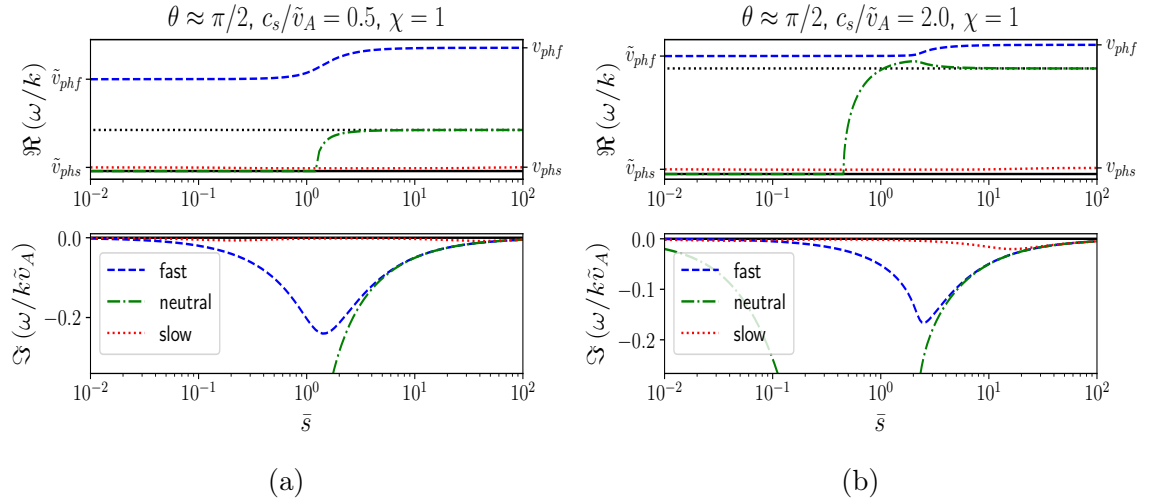


Fig. 2.6 Same as Fig. 2.4 but for approximately perpendicular propagation ( $\theta \approx \pi/2$ ).

plotted for a moderately high plasma-beta,  $c_s/\tilde{v}_A = 2.0$ . Noted on the panels showing the real part of the phase speed, are the phase speeds of the slow and fast wave in the highly collisional limit ( $\tilde{v}_{phf,s} = \tilde{\omega}_{f,s}/k$ ) on the left hand side and the phase speeds of the slow and fast wave in the collision-less limit ( $v_{phf,s} = \omega_{f,s}/k$ ) on the right-hand side. All have an equal amount of neutral and ionised fluids i.e.  $\chi = 1$ .

In the highly collisional limit are two modes that tend toward the slow and fast phase speeds solutions given by Eq. (2.53), in the highly collisional limit i.e. when  $\bar{s} \rightarrow 0$ . Conversely, in the collision-less limit ( $\bar{s} \rightarrow \infty$ ), we now pick out three modes, two that tend towards the slow and the fast phase speeds of the ionised fluid, given by Eq. (2.13) and another that propagates at the sound speed of the neutral fluid (the dotted black line indicates this speed). In the low-beta plasma (Figs. 2.4a-2.6a) the slow phase speed and neutral sound speed are approximately the same for approximately parallel propagation (Fig. 2.4a) for oblique propagation (Fig. 2.5a) the phase speed of the slow mode is lowered even more and becomes much lower

for almost perpendicular propagation (Fig. 2.6a). In the high beta plasma (Figs. 2.4b-2.6b), the fast phase speed and the neutral sound speed are almost the same for approximately parallel propagation (Fig. 2.4b) but for oblique and perpendicular propagation it is slightly higher (Figs. 2.5b and 2.6b, respectively). Departing from the limits, we can see that the greatest damping rates for the slow and fast modes occur when  $\bar{s} \approx 1$  and the greatest difference to the phase speeds of the highly collisional and collision-less limits occurs here. As mentioned in Zaqarashvili *et al.* (2011), there is a new neutral acoustic mode that appears with the phase speed of the neutral sound speed as  $\bar{s} \rightarrow \infty$ . However, when  $\bar{s}$  gets to a low enough value, the neutral acoustic mode frequency becomes a non-oscillatory, completely imaginary and damped vortex mode (see Zaqarashvili *et al.*, 2011).

It is evident from Figs. 2.4-2.6 that if the frequency of the oscillation is much lower than the frequency of collisions between the ions and neutrals, we may use single fluid theory and if the frequency of the oscillations is much larger than the frequency of collisions, we may consider the fully ionised plasma and neutral plasmas to be decoupled. The main effect of partial ionisation comes when the frequency of the waves and the collisions are approximately of the same order.

## 2.4 Summary and Discussion

In this chapter, we have introduced the magneto-acoustic waves in homogeneous media, in both fully ionised and two-fluid plasmas.

In a fully ionised homogeneous plasma, three waves exist: the slow and fast magneto-acoustic waves and Alfvén wave. The Alfvén wave owes its presence to the tension in the magnetic field lines and only propagates along magnetic field lines. The slow wave propagates mainly along magnetic field lines but in a low beta atmosphere it propagates with the sound speed and in a high beta atmosphere with the Alfvén speed. The propagation angle has important effects on the Alfvén and slow waves, for example if the propagation angle is completely perpendicular, neither will propagate. On the other hand, the fast wave was found to propagate in any direction, with greatest phase speed when the propagation angle was perpendicular to the magnetic field. In the degenerate case, when  $c_s = v_A$ , the phase speeds of the slow, fast and Alfvén waves were the same when the propagation angle was parallel to the magnetic field.

In a two-fluid plasma, matters are complicated more due to the collisions between the ion and neutral fluids. The slow and fast magneto-acoustic and Alfvén waves still appear, but are modified somewhat. The collisional frequency, as compared to the frequency of the oscillation, profoundly affects the behaviours of these waves. For all of these waves, if the frequency of the oscillation is much smaller than the collisional frequency, the neutral and ion fluids essentially act as a single fluid and

behave like the fully ionised magneto-acoustic waves. However, if the frequency of the oscillation is much greater than the frequency of collisions between ions and neutrals, the ion and neutral fluids act as separate fluids, where the magneto-acoustic waves propagate in the ion fluid and sound waves propagate in the neutral fluid. The greatest divergence from this is when the oscillation and collision frequency are of similar sizes, in which the modes see the greatest damping due to collisions. The appearance of a cut-off region, where no propagation can occur, is also seen for Alfvén waves when enough neutrals are present in the system.



# Chapter 3

## Magneto-Acoustic Gravity Waves in a Vertical Field: Single Layer

### 3.1 Introduction

Magnetic fields within the solar atmosphere are incredibly varied. The field may be collected in tubular-like magnetic flux structures such as coronal loops, which appear from the photosphere and extend high into the corona connecting two regions of opposite polarity. On a more global scale, the magnetic field may be grouped into two main categories: a vertical field (radially pointing out of the Sun) and a horizontal field perpendicular to the radial direction, although magnetic fields of the Sun are generally far more complex than these two situations. Within the solar atmosphere the stratification of the plasma, caused by the gravitational field, can be very important, with the pressure and density scale heights being in the region of 400 km. This means that the medium is clearly inhomogeneous and, therefore, inhomogeneity of the plasma must be considered as a next approximation. In this chapter we consider the case of a background magnetic field that is parallel to the gravitational field, considering also the plasma to be isothermal for simplicity. This case happens to be a far harder analytical study in comparison to the horizontal case due to the complexities of the solutions.

As was already mentioned in the introduction, [Ferraro and Plumpton \(1958\)](#) were the first authors to study the case of a vertical field aligned parallel with gravity in an isothermal atmosphere, assuming a static background [Zhugzhda \(1979\)](#) extended this work to find the solutions for the horizontal velocity component in terms of the more general Meijer-G functions. Performing some simple asymptotic analysis it was found, for propagating waves, that the fast waves are evanescent in a low-beta plasma, whilst the slow waves degenerate to sound waves travelling along the magnetic field line. [Wang \(1986\)](#) found hypergeometric solutions for the horizontal as well as vertical velocity components. [Cally \(2001\)](#) extended these studies further. Using

simple asymptotic expansions for these hypergeometric functions (for asymptotic limits of many generalized hypergeometric functions see e.g. [Luke, 1975](#)) in the high plasma-beta regime, it was found that the solutions naturally contained the acoustic-gravity modes of an un-magnetized plasma, with also a magnetic contribution that represented the slow mode.

The solar atmosphere is highly and complexly structured. For example, the lower solar atmosphere can be approximated to be one continuous isothermal layer (see e.g. [1.2](#)) with a lower boundary the solar interior and an upper reflection point the transition region. [Abdelatif \(1990\)](#) studied the case of a plasma that was bounded above and below by perfectly reflecting boundaries i.e. line-tying. For various different cases the wave energy density distribution of the solutions were studied, mainly around the so-called *avoided crossings* where two solution paths of the  $\omega - k$  dispersion graph come very close to meeting and then separate each mode swapping behaviour. [Hasan and Christensen-Dalsgaard \(1992\)](#) studied the same case of a one layer system with perfectly reflecting boundaries but considered the asymptotic expansion of their derived governing equation in the high plasma-beta limit. This expansion was used to find the first-order corrections to the  $p$ - and  $g$ -modes and the magnetic mode. [Banerjee et al. \(1995\)](#) studied the same case but with different boundary conditions in which a gravity-Lamb mode also occurred.

In this chapter we study the effect of a vertical magnetic field on the modes of oscillations in an isothermal stratified plasma. We derive a new governing equation for the new variable  $\Theta = p'/\rho$ , where  $p'$  is the kinetic pressure perturbation and  $\rho$  is the background density function. This new formulation is used to find the vertical velocity component,  $v'_z$ , in terms of hypergeometric functions as well as the horizontal velocity component. A dispersion relation is then derived for the case of two perfectly reflecting boundaries and asymptotic limits for the small wavelength limit and a high-beta plasma are calculated. The dispersion relation is then solved numerically for the cases of a low-beta coronal plasma and secondly for a plasma mimicking the transition from high to low plasma-beta in the lower solar atmosphere. The wave energy density of the wave modes is considered, to aid in their classification as well as giving a brief consideration of avoided crossings. We note that the work in this chapter is based on the work completed in [Mather and Erdélyi \(2016\)](#).

## 3.2 Background Equilibrium

We consider an ideal plasma that is perfectly conducting and acts as an ideal gas. By assuming relatively small wavelengths in comparison to the curvature of the Sun, we may use a Cartesian coordinate system. There are no sources or sinks of heating and the plasma is considered to be *adiabatic* and *isothermal* and therefore has a constant temperature,  $T$ , throughout the equilibrium plasma. Background

flows are supposed small compared to the characteristic background speeds of waves in the plasma *i.e.*  $\mathbf{v} = 0$ . The variation of background quantities compared to the characteristic wave motions is considered to be negligible so that the time derivative of background quantities is also negligible as a consequence *i.e.*

$$\frac{\partial}{\partial t} \sim 0.$$

The medium is infinite and homogeneous in the  $x$ - and  $y$ -directions, parallel to the solar surface. The background magnetic field is vertical (perpendicular to the solar surface),  $z$ -direction, and is given as  $\mathbf{B} = B\hat{\mathbf{z}}$ , where  $\hat{\mathbf{z}}$  is the unit vector in the  $z$ -direction. The plasma is stratified by a constant gravitational force in the negative  $z$ -direction and takes the form  $\mathbf{g} = -g\hat{\mathbf{z}}$ . Background momentum conservation gives the following relationship between kinetic pressure and density

$$\frac{dp}{dz} = -\rho g. \quad (3.1)$$

Density, pressure and temperature are also linked by the ideal gas law:

$$p = \rho RT. \quad (3.2)$$

The gas constant for fully ionized Hydrogen plasma is  $R = R_0/\tilde{\mu}$ , where  $R_0 = 8.3143 \text{ J K}^{-1} \text{ mol}^{-1}$  is the *universal molar gas constant* and  $\tilde{\mu}$  is the mean molar mass of a fully ionised Hydrogen plasma. Equations (3.1) and (3.2) lead to the conclusion that both the density and pressure are only functions of  $z$  *i.e.*  $p = p(z)$  and  $\rho = \rho(z)$ . The background pressure can be eliminated between Eqs. (3.1) and (3.2) to give the following differential equation for  $\rho(z)$ :

$$-\rho g = \frac{d\rho}{dz} RT. \quad (3.3)$$

Equation (3.3) can be solved using separation of variables to give the following exponential form for density and, in turn, the same exponential distribution for pressure (see *e.g.* Figure 3.1):

$$\rho(z) = \rho(0) \exp\left(-\frac{z}{H}\right), \quad p(z) = p(0) \exp\left(-\frac{z}{H}\right), \quad H = \frac{c_s^2}{\gamma g}. \quad (3.4)$$

Here,  $H$  is the pressure and density *scale height* (the characteristic length for the density and pressure to decrease by a factor of  $e \approx 2.718$ , Euler's number),  $\gamma$  is the *adiabatic index* and  $c_s$  is the background speed of a sound wave in the medium. Two

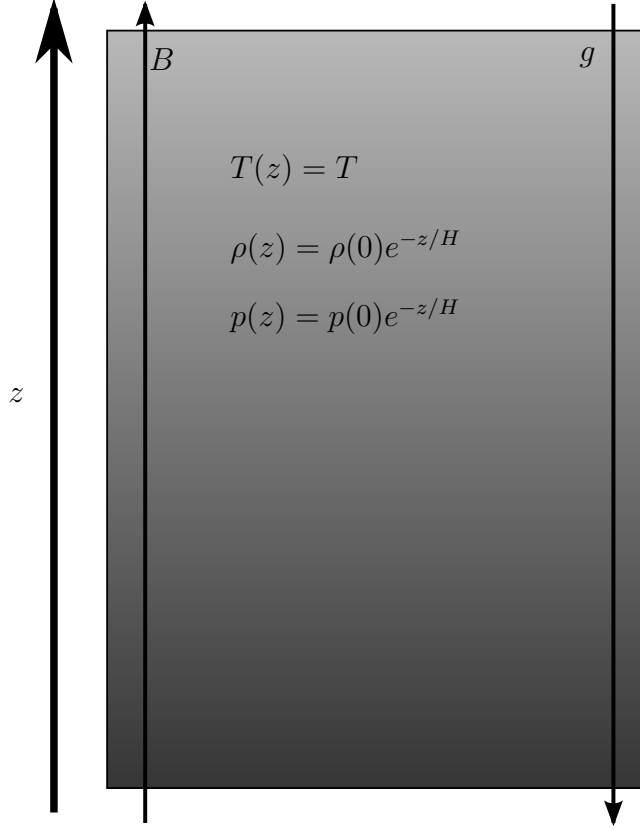


Fig. 3.1 The equilibrium background plasma analysed in this section. The greyscale depicts the density and pressure decrease with increasing height.

characteristic speeds that often appear for wave motions are:

$$c_s^2 = \frac{\gamma p}{\rho} = \text{const}, \quad v_A^2 = \frac{B^2}{\mu_0 \rho} = v_{A0}^2 e^{z/H}. \quad (3.5)$$

Here,  $\mu_0$  is the magnetic permeability of free space and  $v_A$  is the Alfvén speed. The linearised ideal MHD equations are assumed to hold if one takes small perturbations around this background plasma. These governing equations are presented below:

$$\frac{\partial \rho'}{\partial t} + (\mathbf{v}' \cdot \nabla) \rho + \rho (\nabla \cdot \mathbf{v}') = 0, \quad (3.6)$$

$$\frac{\partial p'}{\partial t} + (\mathbf{v}' \cdot \nabla) p + \gamma p (\nabla \cdot \mathbf{v}') = 0, \quad (3.7)$$

$$\rho \frac{\partial \mathbf{v}'}{\partial t} = -\nabla p' + (\nabla \times \mathbf{B}') \times \frac{\mathbf{B}}{\mu} - \rho' g \hat{\mathbf{z}}, \quad (3.8)$$

$$\frac{\partial \mathbf{B}'}{\partial t} = \nabla \times (\mathbf{v}' \times \mathbf{B}), \quad \nabla \cdot \mathbf{B}' = 0. \quad (3.9)$$

## 3.3 Governing Equations

### 3.3.1 Previous Work

Because the background is homogeneous in the  $x$ - and  $y$ -directions, the perturbed variables can, therefore, be Fourier decomposed and written in the form  $f'(x, y, z, t) = \widehat{f}(z)e^{i(k_x x + k_y y - \omega t)}$ . Since the only preferred direction in the system is the  $z$ -direction, the co-ordinate system can be rotated such that  $k_y = 0$  (without loss of generality), then  $f'(x, z, t) = \widehat{f}(z)e^{i(k_x x - \omega t)}$ . The linearised MHD equations take the form of three equations for the variables  $\widehat{v}_x$ ,  $\widehat{v}_y$  and  $\widehat{v}_z$ , respectively:

$$v_A^2(z) \frac{d^2 \widehat{v}_x}{dz^2} + (\omega^2 - k_x^2 (c_s^2 + v_A^2(z))) \widehat{v}_x = ik_x g \widehat{v}_z - ik_x c_s^2 \frac{d \widehat{v}_z}{dz}, \quad (3.10)$$

$$v_A^2(z) \frac{d^2 \widehat{v}_y}{dz^2} + \omega^2 \widehat{v}_y = 0, \quad (3.11)$$

$$c_s^2 \frac{d^2 \widehat{v}_z}{dz^2} - \gamma g \frac{d \widehat{v}_z}{dz} + \omega^2 \widehat{v}_z = i(\gamma - 1) g k_x \widehat{v}_x - i c_s^2 k_x \frac{d \widehat{v}_x}{dz}. \quad (3.12)$$

Taking the limit  $k_x = 0$ , Eq. (3.10) and Eq. (3.12) form the well-known equations (see e.g., [Hasan and Christensen-Dalsgaard, 1992](#)),

$$v_A^2(z) \frac{d^2 \widehat{v}_x}{dz^2} + \omega^2 \widehat{v}_x = 0, \quad (3.13)$$

$$c_s^2 \frac{d^2 \widehat{v}_z}{dz^2} - \gamma g \frac{d \widehat{v}_z}{dz} + \omega^2 \widehat{v}_z = 0. \quad (3.14)$$

It is easy to see that Eq. (3.13) governs a ‘magnetic’ wave and Eq. (3.14) governs an ‘acoustic’ wave. In addition, the velocity components,  $\widehat{v}_x$  and  $\widehat{v}_z$  have been decoupled from one another. Eqs. (3.13) and (3.14) permit the following solutions for  $\widehat{v}_x$  and  $\widehat{v}_z$ , respectively:

$$\widehat{v}_x = C_1 J_0(2\psi) + C_2 Y_0(2\psi), \quad (3.15)$$

$$\widehat{v}_z = C_3 \psi^{-1+2i\sqrt{\sigma^2/\gamma-1/4}} + C_4 \psi^{-1-2i\sqrt{\sigma^2/\gamma-1/4}}, \quad (3.16)$$

where  $J_0$  and  $Y_0$  are Bessel's functions of the first and second kind of zeroth order, respectively. Here, dimensionless variables have been introduced and are given below:

$$\psi = \frac{\omega H}{v_A(z)}, \quad \widehat{\sigma} = \frac{\omega H \sqrt{\gamma}}{c_s}, \quad K = kH.$$

In the limit  $k_x \rightarrow \infty$ , Eqs. (3.10) and (3.12) reduce to a second-order differential equation governing the propagation of vertically propagating slow magneto-acoustic waves (see *e.g.* Hasan and Christensen-Dalsgaard, 1992, Roberts, 2006 or Hague and Erdélyi, 2016):

$$\frac{d^2 \widehat{v}_z}{dz^2} - \frac{1}{H} \frac{c_T^2}{c_s^2} \frac{d \widehat{v}_z}{dz} + \frac{1}{H^2} \frac{c_s^2}{c_T^2} \left( \widehat{\sigma}^2 - \frac{c_T^2}{v_A(z)^2} \left( \widehat{N}^2 + \frac{c_T^2}{\gamma c_s^2} \right) \right) \widehat{v}_z = 0. \quad (3.17)$$

Considering the more general case for arbitrary values of  $k_x$ , Eq. (3.10) and Eq. (3.12) can be used to derive a dimensionless differential equation for  $\widehat{v}_x$  (see *e.g.* Zhugzhda, 1979):

$$\begin{aligned} & \psi^4 \frac{d^4 \widehat{v}_x}{d\psi^4} + 4\psi^3 \frac{d^3 \widehat{v}_x}{d\psi^3} + \psi^2 \left[ \psi^2 + 1 + 4 \left( \frac{\widehat{\sigma}^2}{\gamma} - K^2 \right) \right] \frac{d^2 \widehat{v}_x}{d\psi^2} \\ & + \psi \left[ 3\psi^2 - 1 + 4 \left( \frac{\widehat{\sigma}^2}{\gamma} + K^2 \right) \right] \frac{d \widehat{v}_x}{d\psi} \\ & + 16 \left[ \left( \frac{\widehat{\sigma}^2}{\gamma} + K^2 \left( \frac{\widehat{N}}{\widehat{\sigma}^2} - 1 \right) \right) \psi^2 - \frac{4K^2 \widehat{\sigma}^2}{\gamma} \right] \widehat{v}_x = 0. \end{aligned} \quad (3.18)$$

Eq. (3.18) can be solved with hypergeometric solutions, see *e.g.* Eq. (8) in Cally (2001). The solution to Eq. (3.18) is given below as

$$\begin{aligned} \widehat{v}_x = & A_1 \psi^{2K} {}_2F_3 \left[ \begin{matrix} \frac{1}{2} - iq_z + K, \frac{1}{2} + iq_z + K; \\ 1 + 2K, \frac{1}{2} - iq_0 + K, \frac{1}{2} + iq_0 + K \end{matrix} \middle| -\psi^2 \right] \\ & + A_2 \psi^{-2K} {}_2F_3 \left[ \begin{matrix} \frac{1}{2} + iq_z - K, \frac{1}{2} - iq_z - K; \\ 1 - 2K, \frac{1}{2} - iq_0 - K, \frac{1}{2} + iq_0 - K \end{matrix} \middle| -\psi^2 \right] \\ & + A_3 \psi^{1+i2q_0} {}_2F_3 \left[ \begin{matrix} 1 + iq_0 - iq_z, 1 + iq_0 + iq_z; \\ 1 + 2iq_0, \frac{3}{2} + iq_0 + K, \frac{3}{2} + iq_0 - K \end{matrix} \middle| -\psi^2 \right] \\ & + A_4 \psi^{1-i2q_0} {}_2F_3 \left[ \begin{matrix} 1 - iq_z - iq_0, 1 + iq_z - iq_0; \\ 1 - 2iq_0, \frac{3}{2} - iq_0 + K, \frac{3}{2} - iq_0 - K \end{matrix} \middle| -\psi^2 \right]. \end{aligned} \quad (3.19)$$

The quantities  $q_z$  and  $q_0$  are defined as

$$q_z = \sqrt{\frac{\widehat{\sigma}^2}{\gamma} - \frac{(\widehat{\sigma}^2 - \widehat{N}^2)K^2}{\widehat{\sigma}^2} - \frac{1}{4}}, \quad q_0 = \sqrt{\frac{\widehat{\sigma}^2}{\gamma} - \frac{1}{4}}, \quad \widehat{N}^2 = \frac{\gamma - 1}{\gamma}.$$

Here,  $\widehat{N}$  is the dimensionless Brunt-Väisälä frequency in an isothermal plasma (the frequency at which a fluid parcel would oscillate around its equilibrium position).

### 3.3.2 New Solutions for $\Theta = \widehat{p}/\rho$

It has already been stated that solutions have been found for  $\widehat{v}_x$ . Next, the vertical velocity component can be written in terms of derivatives of  $\widehat{v}_x$  up to third order in  $\psi$ . In this article, we aim to show that, by defining a new and suitably chosen auxiliary variable, a single hypergeometric function solution can be derived for  $\widehat{v}_z$  as was found in Wang (1986). Let us introduce  $\Theta = \widehat{p}/\rho$ , as the equations connecting  $\widehat{v}_x$  and  $\Theta$ , as well as  $\widehat{v}_z$  and  $\Theta$ , will be substantially simpler. By eliminating the divergence between Eqs. (3.6) and (3.7) we obtain:

$$\frac{\widehat{p}}{\rho} = \frac{\Theta}{c_s^2} - \frac{N^2}{g} \frac{\widehat{v}_z}{i\omega}, \quad (3.20)$$

where  $N = \left(\frac{(\gamma-1)g^2}{c_s^2}\right)^{1/2}$  is the *Brunt-Väisälä frequency* of an isothermal plasma. Eq. (3.20) is then substituted into the vertical component of Eq. (3.8) to obtain

$$(\omega^2 - N^2)\widehat{v}_z = -i\omega \left( \frac{d\Theta}{dz} - \frac{N^2}{g}\Theta \right). \quad (3.21)$$

The vertical velocity component,  $\widehat{v}_z$ , is eliminated from Eq. (3.7), using Eq. (3.21), to obtain a relation for  $\widehat{v}_x$  in terms of derivatives of  $\Theta$ :

$$c_s^2(\omega^2 - N^2)k_x\widehat{v}_x = \omega \left( c_s^2 \frac{d^2\Theta}{dz^2} - \frac{c_s^2}{H} \frac{d\Theta}{dz} + \omega^2\Theta \right), \quad (3.22)$$

Finally, from the horizontal component of Eq. (3.8), an equation relating  $\Theta$  to derivatives of  $\widehat{v}_x$  is found:

$$k_x\omega\Theta = v_A^2 \frac{d^2\widehat{v}_x}{dz^2} + (\omega^2 - v_A^2 k_x^2)\widehat{v}_x, \quad (3.23)$$

By eliminating  $\widehat{v}_x$  between Eq. (3.22) and Eq. (3.23), a fourth order differential equation for  $\Theta$  is acquired:

$$\begin{aligned} c_s^2 v_A^2 \frac{d^4 \Theta}{dz^4} - \frac{v_A^2 c_s^2}{H} \frac{d^3 \Theta}{dz^3} + [(v_A^2 + c_s^2)\omega^2 - k_x^2 v_A^2 c_s^2] \frac{d^2 \Theta}{dz^2} \\ - \frac{c_s^2}{H} [\omega^2 - v_A^2 k_x^2] \frac{d\Theta}{dz} + [\omega^4 - k_x^2 (v_A^2 + c_s^2)\omega^2 + k_x^2 c_s^2 N^2] \Theta = 0. \end{aligned} \quad (3.24)$$

Eq. (3.24) can be transformed, with  $\psi$  as a new independent variable, to:

$$\begin{aligned} \psi^4 \frac{d^4 \Theta}{d\psi^4} + 8\psi^3 \frac{d^3 \Theta}{d\psi^3} + \psi^2 \left[ 4\psi^2 + 13 + 4 \left( \frac{\widehat{\sigma}^2}{\gamma} - K^2 \right) \right] \frac{d^2 \Theta}{d\psi^2} \\ + \psi \left[ 12\psi^2 + 3 + 4 \frac{\widehat{\sigma}^2}{\gamma} - 12K^2 \right] \frac{d\Theta}{d\psi} + 16 \left[ \left( \frac{\widehat{\sigma}^2}{\gamma} + K^2 \left( \frac{\widehat{N}^2}{\widehat{\sigma}^2} - 1 \right) \right) \psi^2 - \frac{K^2 \widehat{\sigma}^2}{\gamma} \right] \Theta = 0. \end{aligned} \quad (3.25)$$

This is clearly very similar to (3.18). However, as can be seen by Eqs. (3.21) and (3.22), the expressions for  $\widehat{v}_x$  and  $\widehat{v}_z$  are simple and are found by taking up to second order derivatives in  $z$  of  $\Theta$ , whereas the relationship between  $\widehat{v}_x$  and  $\widehat{v}_z$  is a third order  $z$  derivative expression. Using the Fröbenius method, solutions to Eq. (3.25) can be written as infinite series. These series solutions can then be written as *hypergeometric functions*:

$$\begin{aligned} \Theta = C_1 \psi^{2K} {}_2F_3 \left[ \begin{matrix} a_{11}, a_{12}; \\ b_{11}, b_{12}, b_{13} \end{matrix} \middle| -\psi^2 \right] + C_2 \psi^{-2K} {}_2F_3 \left[ \begin{matrix} a_{21}, a_{22}; \\ b_{21}, b_{22}, b_{23} \end{matrix} \middle| -\psi^2 \right] \\ + C_3 \psi^{-1+i2q_0} {}_2F_3 \left[ \begin{matrix} a_{31}, a_{32}; \\ b_{31}, b_{32}, b_{33} \end{matrix} \middle| -\psi^2 \right] + C_4 \psi^{-1-i2q_0} {}_2F_3 \left[ \begin{matrix} a_{41}, a_{42}; \\ b_{41}, b_{42}, b_{43} \end{matrix} \middle| -\psi^2 \right]. \end{aligned} \quad (3.26)$$

We note an arbitrary hypergeometric function of the variable  $-\psi^2$  can be written as

$${}_pF_q \left[ \begin{matrix} a_1, \dots, a_p; \\ b_1, \dots, b_q \end{matrix} \middle| -\psi^2 \right] = \sum_{n=0}^{\infty} \frac{(a_1)_n \dots (a_p)_n (-\psi^2)^n}{(b_1)_n \dots (b_q)_n n!},$$

where the *Pochhammer* symbol,  $(a)_n$ , is defined as

$$(a)_n = (a)(a+1)\dots(a+(n-1)), \quad (a)_0 = 1, \quad \forall a \in \mathbb{C},$$

with  $\mathbb{C}$  denoting the set of complex numbers. Solutions for both  $\widehat{v}_x$  and  $\widehat{v}_z$  can then be found in a straightforward way using the relationships between  $\Theta$ ,  $\widehat{v}_x$  and  $\widehat{v}_z$ , respectively. Detailed derivations and definitions of  $a_{ij}, b_{ij}$  ( $i, j = 1, \dots, 4$ ) can be found in Appendix A. The solutions for  $\widehat{v}_x$  and  $\widehat{v}_z$  are presented below:

$$\begin{aligned} \widehat{v}_x = & C_1 \psi^{2K} S^{(1)} {}_2F_3 \left[ \begin{matrix} a_{11}, a_{12}; \\ b_{11}, b_{12} - 1, b_{13} - 1 \end{matrix} \middle| -\psi^2 \right] \\ & + C_2 \psi^{-2K} S^{(2)} {}_2F_3 \left[ \begin{matrix} a_{21}, a_{22}; \\ b_{21}, b_{22} - 1, b_{23} - 1 \end{matrix} \middle| -\psi^2 \right] \\ & - C_3 \psi^{1+2iq_0} S^{(3)} {}_2F_3 \left[ \begin{matrix} a_{31} + 1, a_{32} + 1; \\ b_{31}, b_{32} + 1, b_{33} + 1 \end{matrix} \middle| -\psi^2 \right] \\ & - C_4 \psi^{1-2iq_0} S^{(4)} {}_2F_3 \left[ \begin{matrix} a_{41} + 1, a_{42} + 1; \\ b_{41}, b_{42} + 1, b_{43} + 1 \end{matrix} \middle| -\psi^2 \right], \end{aligned} \quad (3.27)$$

$$\widehat{v}_z = iK \left\{ \begin{aligned} & C_1 \psi^{2K} R^{(1)} {}_3F_4 \left[ \begin{matrix} a_{11}, a_{12}, a_{13}; \\ b_{11}, b_{12}, b_{13}, b_{14} \end{matrix} \middle| -\psi^2 \right] \\ & + C_2 \psi^{-2K} R^{(2)} {}_3F_4 \left[ \begin{matrix} a_{21}, a_{22}, a_{23}; \\ b_{21}, b_{22}, b_{23}, b_{24} \end{matrix} \middle| -\psi^2 \right] \\ & + C_3 \psi^{-1+2iq_0} R^{(3)} {}_3F_4 \left[ \begin{matrix} a_{31}, a_{32}, a_{33}; \\ b_{31}, b_{32}, b_{33}, b_{34} \end{matrix} \middle| -\psi^2 \right] \\ & + C_4 \psi^{-1-2iq_0} R^{(4)} {}_3F_4 \left[ \begin{matrix} a_{41}, a_{42}, a_{43}; \\ b_{41}, b_{42}, b_{43}, b_{44} \end{matrix} \middle| -\psi^2 \right] \end{aligned} \right\}. \quad (3.28)$$

Note that  $S^{(i)}$ ,  $R^{(i)}$ ,  $a_{ij}$  and  $b_{ij}$  are given in Appendix A. Eq. (3.27) is none other than the solution given by Eq. (3.19). The solution for  $\widehat{v}_z$ , given by Eq. (3.28), does not differ in essence from the solution given in Leroy and Schwartz (1982) and is the same as in Wang (1986). Generalised hypergeometric functions have been well studied and various asymptotic expansions have been derived for large and small arguments (see e.g. Luke, 1975). With these asymptotic relations we can see the physics of the problem more readily than could be seen solely with the Fröbenius series.

### 3.4 Single Layer

A single atmospheric plasma layer model, for a vertical magnetic field, has been addressed in several different ways by e.g. [Hasan and Christensen-Dalsgaard \(1992\)](#) or [Abdelatif \(1990\)](#). The boundary conditions that are imposed are line-tying at the boundaries (perfect reflection), i.e.  $\widehat{v}_x = \widehat{v}_z = 0$  at  $z = 0, L$ . These ensure that no magnetic energy nor kinetic energy passes through the boundaries. The four boundary conditions permit four linearly independent equations that may be written as a matrix equation to determine the coefficients  $C_1, C_2, C_3$  and  $C_4$ :

$$\begin{pmatrix} \widehat{v}_{x(0)}^{(1)} & \widehat{v}_{x(0)}^{(2)} & \widehat{v}_{x(0)}^{(3)} & \widehat{v}_{x(0)}^{(4)} \\ \widehat{v}_{x(L)}^{(1)} & \widehat{v}_{x(L)}^{(2)} & \widehat{v}_{x(L)}^{(3)} & \widehat{v}_{x(L)}^{(4)} \\ \widehat{v}_{z(0)}^{(1)} & \widehat{v}_{z(0)}^{(2)} & \widehat{v}_{z(0)}^{(3)} & \widehat{v}_{z(0)}^{(4)} \\ \widehat{v}_{z(L)}^{(1)} & \widehat{v}_{z(L)}^{(2)} & \widehat{v}_{z(L)}^{(3)} & \widehat{v}_{z(L)}^{(4)} \end{pmatrix} \begin{pmatrix} C_1 \\ C_2 \\ C_3 \\ C_4 \end{pmatrix} = 0. \quad (3.29)$$

Note that, here,  $\widehat{v}_{x(a)}^{(j)}$  and  $\widehat{v}_{z(a)}^{(j)}$  ( $a = 0, L$  and  $j = 1, 2, 3, 4$ ) refer to the functions multiplying the constants of integration,  $C_j$ . Here,  $L$  is the height of the upper boundary of the atmosphere. To obtain non-trivial solutions, the determinant of the matrix on the left is taken to obtain the full dispersion relation for standing waves in a bounded plasma with a vertical field that is stratified by a vertical gravitational force. Before studying dispersion relation (3.29) numerically, certain limits can be taken to obtain analytic information.

#### 3.4.1 Small Wavelength Limit ( $K \rightarrow \infty$ )

Taking the limit of the determinant of Eq. (3.29) as  $K \rightarrow \infty$ , where we assume also that  $H \gg L$  does not hold true. To take the limits of the hypergeometric functions as  $K \rightarrow \infty$  we use the general limit:

$$\lim_{|r| \rightarrow \infty} \frac{(r)_n}{r^n} \rightarrow 1, \quad r \in \mathbb{C}.$$

With this limit the functions  $\widehat{v}_{z(0,L)}^{(3)}$  and  $\widehat{v}_{z(0,L)}^{(4)}$  can be written as

$$\widehat{v}_{z(0,L)}^{(3)} = \psi_{(0,L)}^{-1+2iq_0} R^{(3)} {}_1F_2 \left[ \begin{matrix} a_{33}; \\ b_{31}, b_{34} \end{matrix} \middle| -\frac{(\widehat{\sigma}^2 - \widehat{N}^2)\psi_{(0,L)}^2}{\widehat{\sigma}^2} \right], \quad (3.30)$$

$$\widehat{v}_{z(0,L)}^{(4)} = \psi_{(0,L)}^{-1-2iq_0} R^{(4)} {}_1F_2 \left[ \begin{matrix} a_{43}; \\ b_{41}, b_{44} \end{matrix} \middle| -\frac{(\widehat{\sigma}^2 - \widehat{N}^2)\psi_{(0,L)}^2}{\widehat{\sigma}^2} \right]. \quad (3.31)$$

Next, the determinant of Eq. (3.29) is expanded and the largest term as  $K \rightarrow \infty$  is found and given by:

$$K^4 \exp(KL/H) \left( \widehat{v}_{z(0)}^{(3)} \widehat{v}_{z(L)}^{(4)} - \widehat{v}_{z(L)}^{(3)} \widehat{v}_{z(0)}^{(4)} \right) = 0 \quad (3.32)$$

The term outside the brackets in Eq.(3.32) cannot be equal to zero, therefore the dispersion relation is given by the terms within the brackets:

$$\widehat{v}_{z(0)}^{(3)} \widehat{v}_{z(L)}^{(4)} - \widehat{v}_{z(L)}^{(3)} \widehat{v}_{z(0)}^{(4)} = 0. \quad (3.33)$$

It is well known that taking this limit in Eqs. (3.10) and (3.12) removes the fast mode (see e.g. [Moreno-Insertis and Spruit, 1989](#), [Roberts, 2006](#) or [Hague and Erdélyi, 2016](#)). To study this further we take the limit of both high and low plasma-beta separately of Eq. (3.33).

#### 3.4.1.1 Low plasma-beta

For a small plasma-beta value, that is  $\beta \ll 1$ , the parameter  $\psi^2 \ll 1$ . Therefore, the hypergeometric function  ${}_1F_2 \left[ ; -\frac{(\widehat{\sigma}^2 - \widehat{N}^2)\psi_{(0,L)}^2}{\widehat{\sigma}^2} \right] \approx 1$ , and Eq. (3.33) becomes

$$\sin(q_0 L/H) = 0, \quad \frac{q_0 L}{H} = m\pi, \quad m \in \mathbb{N}. \quad (3.34)$$

Transforming back to dimensional quantities,

$$\frac{\omega^2}{c_s^2} = \frac{m^2 \pi^2}{L^2} + \frac{1}{4H^2}. \quad (3.35)$$

Dispersion relation (3.35) shows that the slow mode has degenerated to a vertically propagating sound wave, along the field lines. Eq. (3.35) also reveals that the atmosphere has a cut-off frequency of  $\omega_{ac}^2 = c_s^2/4H^2$ , otherwise called the *acoustic cut-off frequency*. Any frequencies below this threshold are evanescent and therefore cannot satisfy the dispersion relation given by Eq. (3.35).

#### 3.4.1.2 High plasma-beta

The limit of large plasma-beta ( $\beta \gg 1$ ) is suitable as an approximation of the lower solar atmosphere. Therefore, taking the limit of large plasma-beta in Eq. (3.33) (assuming  $L = -D^2$ , where  $D \in \mathbb{R}$ ), the asymptotic expansions of the hypergeometric functions are taken as  $\psi^2 \rightarrow \infty$  ([Luke, 1975](#)). Therefore, to lowest order in  $\psi^{-1}$ ,

Eq. (3.31) can be written,

$$v_{(0,L)}^{(3)} = \frac{\Gamma(1 + 2iq_0)}{2\sqrt{\pi}} \psi_{(0,L)}^{(-1/2)} \begin{bmatrix} e^{-i\frac{\pi}{4}} e^{q_0} e^{-2i\sqrt{(\widehat{\sigma}^2 - \widehat{N}^2)/\widehat{\sigma}^2}} \psi_{(0,L)} \\ + e^{i\frac{\pi}{4}} e^{-q_0} e^{2i\sqrt{(\widehat{\sigma}^2 - \widehat{N}^2)/\widehat{\sigma}^2}} \psi_{(0,L)} \end{bmatrix},$$

$$v_{(0,L)}^{(4)} = \frac{\Gamma(1 - 2iq_0)}{2\sqrt{\pi}} \psi_{(0,L)}^{(-1/2)} \begin{bmatrix} e^{-i\frac{\pi}{4}} e^{-q_0} e^{-2i\sqrt{(\widehat{\sigma}^2 - \widehat{N}^2)/\widehat{\sigma}^2}} \psi_{(0,L)} \\ + e^{i\frac{\pi}{4}} e^{q_0} e^{2i\sqrt{(\widehat{\sigma}^2 - \widehat{N}^2)/\widehat{\sigma}^2}} \psi_{(0,L)} \end{bmatrix},$$

Here,  $\Gamma(x)$  is the well-known gamma-function. Substituting these expressions into Eq. (3.33) the dispersion relation reduces to

$$\sin \left( 2\widehat{\psi} \sqrt{(\widehat{\sigma}^2 - \widehat{N}^2)/\widehat{\sigma}^2} \right) = 0, \quad \widehat{\psi} = \psi_L - \psi_0. \quad (3.36)$$

Clearly, for this to be zero, we require,

$$2\widehat{\psi} \sqrt{(\widehat{\sigma}^2 - \widehat{N}^2)/\widehat{\sigma}^2} = m\pi, \quad m \in \mathbb{N}, \quad (3.37)$$

$$\widehat{\sigma}^2 = \widehat{N}^2 + \frac{m^2 \pi^2}{2s^2 \beta}, \quad s = 1 - e^{-D^2/2}.$$

It is interesting to note that Eq. (3.37) agrees with the counterpart derived, in a completely different way, by [Hasan and Christensen-Dalsgaard \(1992\)](#). These authors took the limit  $k_x \rightarrow \infty$  of the wave equations and the high-beta limit, directly implemented in the governing equation. From there, they applied boundary conditions on the solutions and again found asymptotic expansions for  $\beta \gg 1$ . The solution in Eq. (3.37) has two different interpretations: the first being for low harmonics, where the solutions are the  $g$ -modes modified by the magnetic field. However, for larger harmonics, the contribution from the Brunt-Väisälä frequency becomes negligible, thus the modes are of a far more magnetic nature. Also noting the completely hydrodynamic limit,  $\beta \rightarrow \infty$ , we see that all modes tend to the Brunt-Väisälä frequency, i.e, the limit of  $g$ -modes as  $k_x \rightarrow \infty$  in an isothermal bounded plasma (see e.g. [Goedbloed and Poedts, 2004](#)).

### 3.4.2 Solar Atmospheric Models

In this section, Eq. (3.29) is numerically solved for dimensionless parameters that approximate the physical parameters of the solar atmosphere. We investigate two models: the first being analogous to a plasma that describes the solar corona and the other approximates the transition from the solar photosphere to the upper

chromosphere. Both these models are important to consider as the models will be connected together across a discontinuity in Chapter 3.

In what follows, we use the useful relation for the *wave energy density* of MAG waves derived in Bray and Loughhead (1974) (the relation can also be found in Goedbloed and Poedts, 2004). The total wave energy density is comprised of the kinetic energy density (KE) and the potential energy density (PE). The potential energy density can be split into gravitational potential (GE), internal (IE) and magnetic energy (ME) density. The total energy density is given as:

$$E_T = KE + ME + IE + GE, \quad (3.38)$$

where,

$$KE = \frac{1}{2}\rho(\widehat{v}_x^2 + \widehat{v}_z^2), \quad IE = \frac{\widehat{p}^2}{2\rho c_s^2}, \quad GE = \frac{\rho N^2 \widehat{v}_z^2}{2\omega^2}, \quad ME = \frac{1}{2\mu}(\widehat{B}_x^2 + \widehat{B}_z^2).$$

### 3.4.2.1 Coronal Plasma

The first model corresponds to a low-beta plasma which decreases further with increasing height. The representative parameters for the first model are:

$$z = [0, D_2], \quad \frac{D_2}{H} = 3, \quad \beta|_{z=0} = 0.1.$$

The scale height,  $H$ , is approximately 50 Mm so that  $D_2 = 150$  Mm. In a low-beta homogeneous plasma, the phase speed,  $\omega/k_x$ , of the slow wave is approximately equal to the sound speed of the background plasma i.e.  $\omega/k_x \approx c_s$ . In an opposite manner, the phase speed of the fast wave is approximately equal to the background Alfvén speed of the plasma i.e.  $\omega/k_x \approx v_A$ . This leads to the conclusion that the main component of the ‘slow’ waves’ energy density will be due to the internal energy density (IE) and the main component of the fast waves’ energy density will be due to the magnetic energy density (ME). This will help us characterise the modes given in this model.

For a given mode that satisfies Eq. (3.29) we calculate the internal energy density and magnetic energy density integrated from  $z = 0$  to  $z = D_2$

$$IE_T = \int_0^{D_2} IE(z, \widehat{\sigma}, K) dz, \quad ME_T = \int_0^{D_2} ME(z, \widehat{\sigma}, K) dz. \quad (3.39)$$

To investigate the proportion of magnetic and internal energy in a mode we define the quantity

$$IE_P = \frac{IE_T}{IE_T + ME_T}, \quad (3.40)$$

as the proportion of the total internal energy of the mode compared to the total internal and magnetic energy of the mode. If  $IE_P > 0.5$  then the mode is pressure dominated and if  $IE_P < 0.5$  the mode is magnetically dominated.

Fig. 3.2 plots the dispersion diagram for the model described here, with  $\hat{\omega}$  against  $K$ . The colour bar shows the value of  $IE_P$  for each solution. From both Figs. 3.2a and c one can see that there are, almost, two distinct modes. One mode has a very large proportion of magnetic energy and as such the solution line is blue. We thus characterise this as the ‘fast’ mode. One can see that the fast mode is largely non-dispersive with respect to the dimensionless wave number,  $K$ , as would be expected in an homogeneous medium also. The second distinct mode has a large proportion of internal energy, as can be noted from the solution lines’ deep red colour. We therefore can characterise this mode as the ‘slow’ wave. Due to the frequency,  $\hat{\omega}$ , of the wave staying relatively constant with respect to  $K$ , the slow wave is clearly quite dispersive with respect to the horizontal wave number. However, each harmonic of the slow wave is, approximately, a set frequency apart. We conclude, that the slow wave is not dispersive due to the vertical wave number, i.e. the wave number in the direction of the magnetic field. Again, these are all characteristics of the slow wave in a homogeneous medium.

Although there are two distinct modes in one sense, on a closer inspection of Figs. 3.2a and c one can see that the two solution paths do not cross and instead actually ‘avoid’ one another. These phenomena are referred to as ‘avoided-crossings’ (see e.g. Abdelatif, 1990). Figs. 3.2b and d show zoomed in portions of Figs. 3.2a and c (indicated by the rectangles) respectively. The solution paths do not actually cross but avoid each other smoothly, with both lines changing their initial path to the path of the other. What is noticeable is that the proportion of internal energy changes rapidly around these avoided crossings. So, for example, in Fig. 3.2b the solution path that starts off with a high proportion of internal energy, i.e. a slow wave, then becomes closer to the avoided crossing where the proportion of internal energy then drops quickly and the solution path then continues on the path of the fast-mode, with  $IE_P \approx 0$ . Oppositely the fast mode, that had a high proportion of magnetic energy, reaches the avoided crossing and then takes on the path of the slow mode. The proportion of internal energy of the mode then increases rapidly and  $IE_P \approx 1$ . Comparing Figs. 3.2b and d and looking at Figs. 3.2, it may then also be noted that, as  $K$  increases, the transition of the internal energy proportion is more smooth. The fast mode has a higher proportion of internal energy for a larger

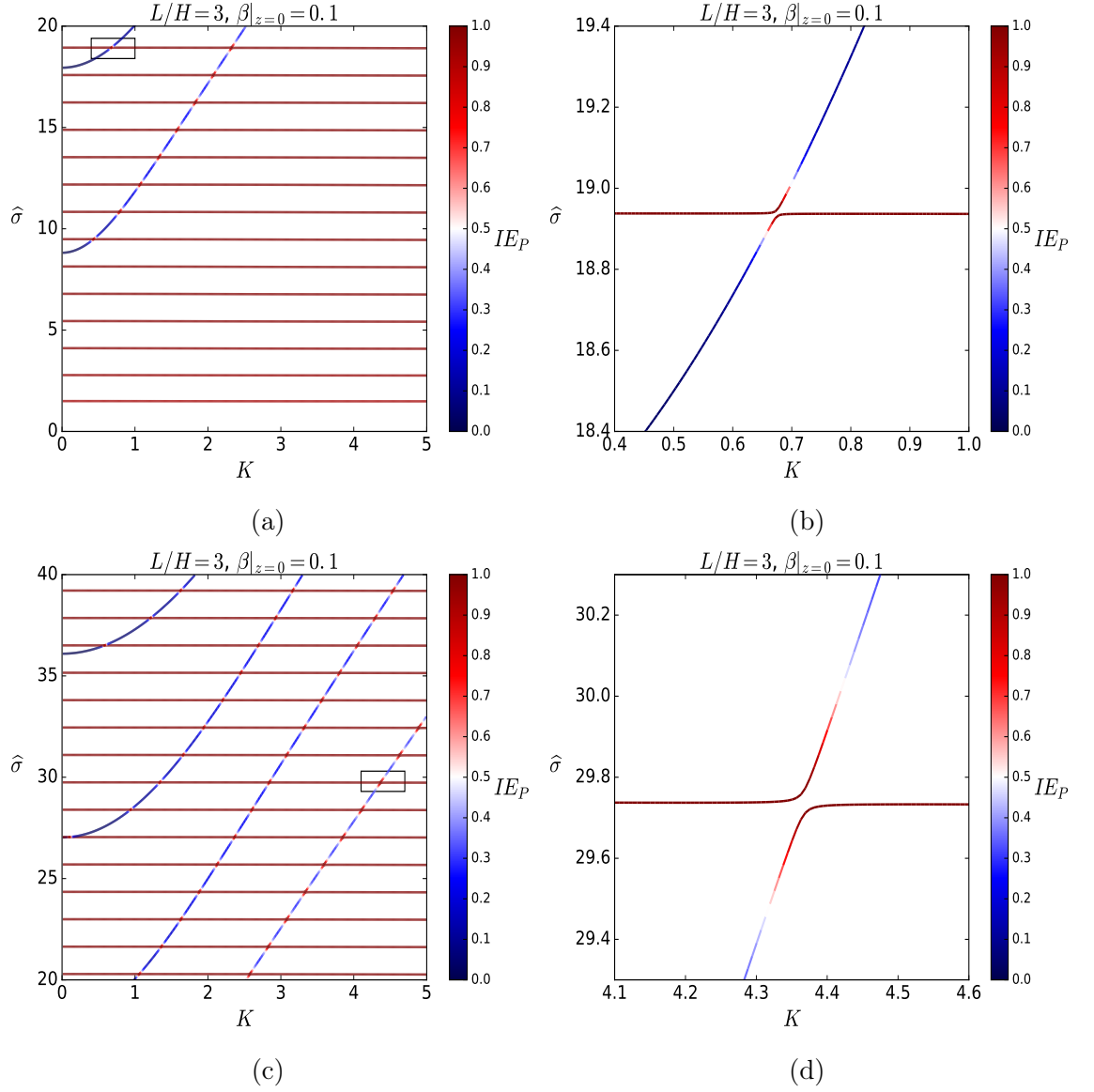


Fig. 3.2 Variation of the dimensionless frequency,  $\hat{\sigma}$ , with respect to the dimensionless wave number,  $K$ , (a value of  $K = 1$  relates to a horizontal wavelength,  $\lambda$ , of approximately 50 Mm with a scale height of 50 Mm) for the model of a low beta coronal plasma. Panel (a) is the dispersion graph for  $\hat{\sigma} = 0 - 20$  (this gives an angular frequency range of  $0 - 3 \times 10^{-3} \text{ s}^{-1}$ ), with panel (b) is the zoomed-in portion represented by the outline of a box in panel (a). Panel (c) is the dispersion graph for  $\hat{\sigma} = 20 - 40$  (this gives an angular frequency range of  $3 \times 10^{-3} - 6 \times 10^{-3} \text{ s}^{-1}$ ), with panel (d) is the zoomed-in portion represented by the outline of a box in panel (c). The lines are given colours that correspond to the colour bar which indicates the proportion of internal energy density compared to the sum of this and the magnetic energy density,  $IE_P$ .

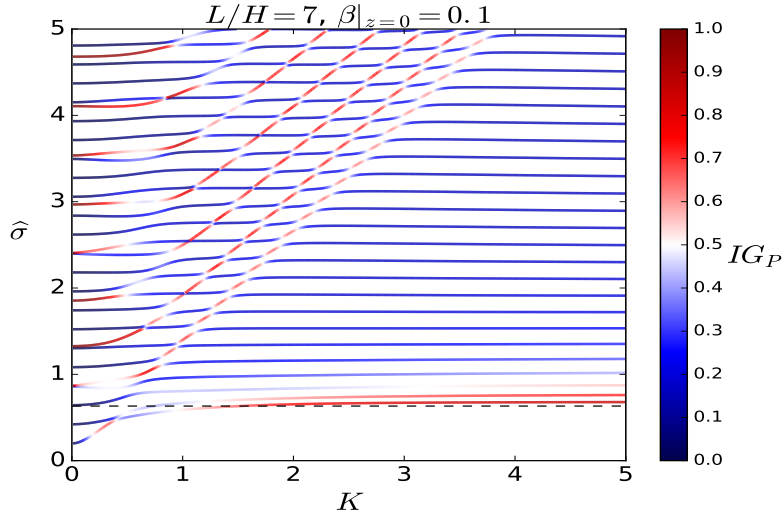


Fig. 3.3 Variation of  $\hat{\sigma}$  ( $\hat{\sigma} = 1$  corresponds to an angular frequency,  $\omega$ , of  $6.4 \times 10^{-2} \text{ s}^{-1}$ ) with respect to  $K$  ( $K = 1$  corresponds to a horizontal wavelength,  $\lambda$ , of 125 km) for the photosphere/chromosphere model. Again, the lines are coloured, using the colourbar on the right, to represent  $IG_P$ . The black dashed line represents the horizontal  $\hat{\sigma} = \hat{N}$ .

interval of  $K$  values. This supports the asymptotic analysis resulting in Eq. (3.35) for a low beta atmosphere, where there are only vertically propagating sound waves i.e. slow-modes; the fast wave is decoupled.

### 3.4.2.2 Photosphere-Chromosphere

The second solar atmospheric model is one transitioning from a high-beta plasma to a low-beta plasma as height increases, analogous to a basic model of the real solar atmosphere. Typical parameters for this particular model are:

$$z = [-D_1, 0], \quad \frac{D_1}{H} = 7, \quad \beta|_{z=0} = 0.1.$$

In this model, it is harder to separate the modes, as there are modes near the Brunt-Väisälä frequency that have a more gravitational character, along with the magnetic and acoustic modes. We therefore opt to use the full compliment of the potential energy density, that is  $IE$ ,  $ME$  and  $GE$ . For a given mode that satisfies Eq. (3.29) we calculate the internal energy density, magnetic energy density and

gravitational energy density integrated (numerically) over  $z = -D_1$  to  $z = 0$ :

$$\begin{aligned} IE_T &= \int_{-D_1}^0 IE(z, \hat{\sigma}, K) dz, & ME_T &= \int_{-D_1}^0 ME(z, \hat{\sigma}, K) dz, \\ GE_T &= \int_{-D_1}^0 GE(z, \hat{\sigma}, K) dz. \end{aligned} \quad (3.41)$$

To investigate the proportion of magnetic and internal energy in a mode we define the quantity

$$IG_P = \frac{IE_T + GE_T}{IE_T + ME_T + GE_T}, \quad (3.42)$$

Fig. 3.3 plots the dispersion diagram for the model described above i.e for  $\hat{\sigma}$  against  $K$ . We first consider the modes around the dimensionless Brunt-Väisälä frequency,  $\hat{N}$ . The modes below  $\hat{N}$  are either: predominantly magnetic in nature hence the blue colouring or gravitational in nature, hence the red colouring. One can note as  $K$  is increased, that the modes around  $\hat{N}$  are highly gravitational in nature. However, staying at  $K \approx 5$ , the higher harmonics start to become far more magnetic in nature. This can be explained, somewhat, by Eq. (3.37) in the limit as  $K \rightarrow \infty$  and  $\beta \rightarrow \infty$ . The equation shows that the first modes would be around the Brunt-Väisälä frequency and would therefore have most potential energy due to gravitational potential energy. However as the harmonics increase and  $\hat{N}^2 \ll m^2 \pi^2 / 2s^2 \beta$ , i.e. the frequencies become noticeably larger than the Brunt-Väisälä frequency, the modes are now far more magnetic in nature and as such would have a higher proportion of magnetic potential energy. This is evident in Fig. 3.3 for the higher harmonics for frequencies becoming much larger than the Brunt-Väisälä frequency.

## 3.5 Summary and Discussion

In this chapter, we have presented the basic static background equilibrium for an isothermal fully ionised plasma in a magnetic field parallel to a constant gravitational field. The fully ionized MHD equations from chapter 1 were then used to linearise around this background plasma. Eqs. (3.23)-(3.21) were used to form a fourth order differential equation given by Eq. (3.25) for the variable  $\Theta = \hat{p}/\rho$ . The Fröbenius method was used to find four linearly independent solutions for  $\Theta$ . Equation (3.25) is the first governing equation found for the variable  $\Theta$ , in this regime.

The simple relation between  $\hat{v}_z$  and  $\Theta$  was used to find the solutions for  $\hat{v}_z$  which was in the form of an infinite series solution which then was found to actually be 4 linearly independent hypergeometric functions as in Wang (1986). Schwartz and

Leroy (1982) found solutions for  $\widehat{v}_z$  as well but these were described as an infinite series and not as the well defined and fairly well studied hypergeometric functions. These new solutions were then used to study the single plasma layer case (bounded above and below). A dispersion relation was found that was fairly complicated. Using well known asymptotic expansions of the hypergeometric functions, we were able to study the short wavelength limit, taking high-beta and low beta approximations. It was found, as expected, the modes degenerate into the slow modes, which is well known (see e.g. Erdélyi and Fedun, 2006 or Hague and Erdélyi, 2016). In the high-beta case, the modes had, for low harmonics, more of a gravitational nature but for higher harmonics they were simply magnetic modes. This was in full agreement with the relation given in Hasan and Christensen-Dalsgaard (1992) which was found by taking the small wavelength limit on the governing equation. The low beta limit of this equation shows that the slow modes are essentially vertically propagating sound waves.

The next part of this chapter concerned itself with the numerical solutions to Eq. (3.29). The first case considered was a coronal type low beta plasma. The expected behaviour using the homogeneous theory (see e.g. Goedbloed and Poedts, 2004) was that the fast modes would be of a highly magnetic nature, propagating at the Alfvén speed in any direction. On the other hand, the slow modes were expected to be driven by internal pressure variations, propagating at approximately the sound speed but mainly along the magnetic fields lines. It was found that this was just the case, as the modes shown in Figs. 3.2a-d were shown to have their potential energy density either being magnetic or internal energy density. However, this was shown to not hold around avoided crossings, where the modes changed nature and had more of an even composition of both the energies. These avoided crossings were very small and sharp indeed though.

Fig. 3.3 plotted the dispersion graph for a solar atmospheric model transitioning from a high to a low plasma-beta plasma. In this case the slow modes were now of a magnetic nature, but near the Brunt-Väisälä frequency they also had a strong gravitational potential energy component. The fast modes were pressure driven acoustic modes. Around the avoided crossings the modes had a more reasonable share of magnetic and internal pressure energy.

# Chapter 4

## Magneto-Acoustic Gravity Waves in a Vertical Field: Two-Layer

### 4.1 Introduction

As discussed in the introduction the solar atmosphere can be split into separate regions, on a global scale. One could treat the lower solar atmosphere as a single layer with perfectly reflecting boundaries at the lower and upper limits due to the rapidly changing densities at these points. However, sharp discontinuities still do not trap all energy within their bounds. It is therefore important to see how MAG waves react to these discontinuities and how the energy of these waves is distributed in multilayer models.

[Scheuer and Thomas \(1981\)](#) considered a three layer model of a sunspot, extending down into the convection zone of the Sun, modelling this using a poly-tropic temperature profile and with an interface at the photosphere. The next layer was considered isothermal to approximate the lower solar atmosphere with another interface at the boundary between the corona and lower solar atmosphere. Solving this system numerically it was found that, for both forced and free oscillations, a resonant ‘fast’ mode was possible with a period of around 153 seconds, with most of the wave energy reflected before even reaching the transition region. [Leroy and Schwartz \(1982\)](#) studied a two layer atmosphere, a photospheric/chromospheric plasma layer with a semi-infinite homogeneous coronal plasma above this. Boundary conditions were derived for the case of a contact discontinuity which were then solved numerically for the case of sunspots and coronal holes in the companion paper [Schwartz and Leroy \(1982\)](#). The wave energy density of forced oscillations was considered and it was concluded that along with the effects of stratification, causing the Alfvén speed to increase, and that there would be partial transverse propagation, it was unlikely that MAG waves would transmit significant energy into the coronal plasma. [Yelles Chaouche and Abdelatif \(2005\)](#) studied a two layer atmosphere, again

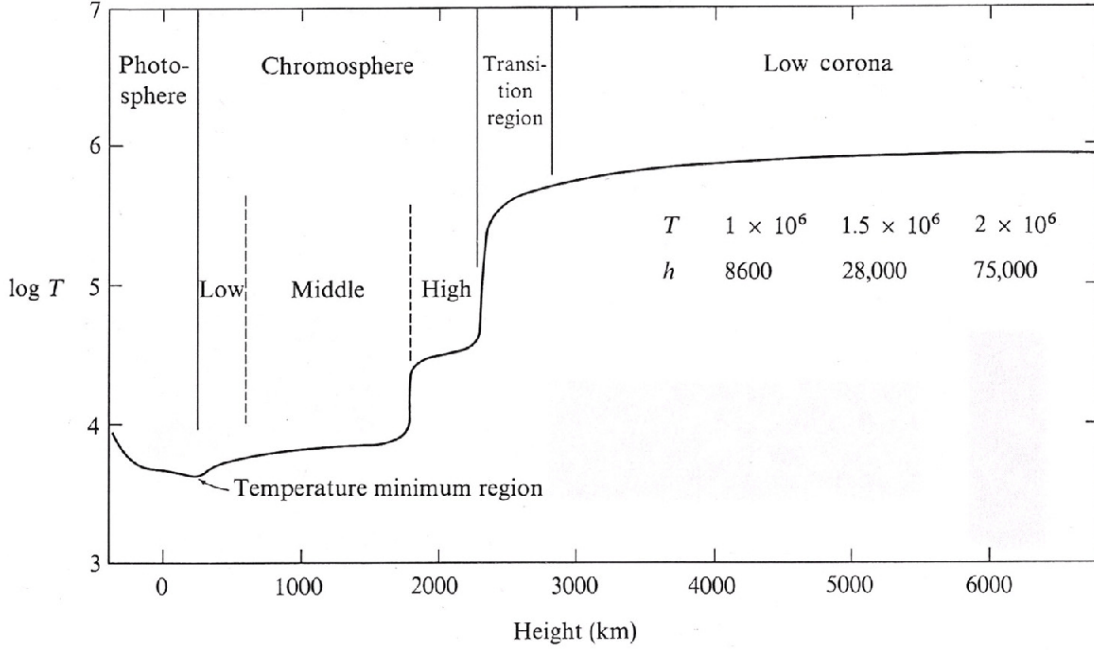


Fig. 4.1 The VAL ([Vernazza et al., 1981](#)) model of temperature distribution in the solar atmosphere. Image credit to [Athay \(1976\)](#)

for a lower solar atmosphere and coronal two-layer model. The emphasis in this study was on the damping of the waves as they propagated across the magnetic field.

In this chapter, a two layer bounded atmosphere is considered, with perfectly reflecting boundaries at the base and the top. Using the solutions formulated in Chapter 3, two models are studied: one that represents the jump from the lower chromosphere to the upper chromosphere bounded above by the corona. The second represents a model of the lower solar atmosphere and the corona, with the interface between representing the sharp change due to the transition region. We explore the numerical solutions to the dispersion relations and study the distributions of the wave energy density, along with their components. This chapter is based on work completed in our published paper [Mather and Erdélyi \(2016\)](#).

## 4.2 Background Equilibrium

Let us now consider a two-layer, gravitationally stratified plasma embedded in a uniform vertical magnetic field. The ideal forms of the linearised MHD equations are used i.e. Eqs. (3.6)-(3.9). We also neglect the spherical shape of the Sun that gives an upper limit of the horizontal wavelength. The model is outlined in Fig. 4.2. The lower layer is bounded by  $z \in [-D_1, 0]$ . The top layer is described within the bounds  $z \in [0, D_2]$ . Both layers are isothermal and, as such, have constant temperature in both the upper (subscript '0') and lower (subscript 'e') layers given, respectively, by  $T_0$  and  $T_e$ . In general there is a temperature discontinuity between the two media

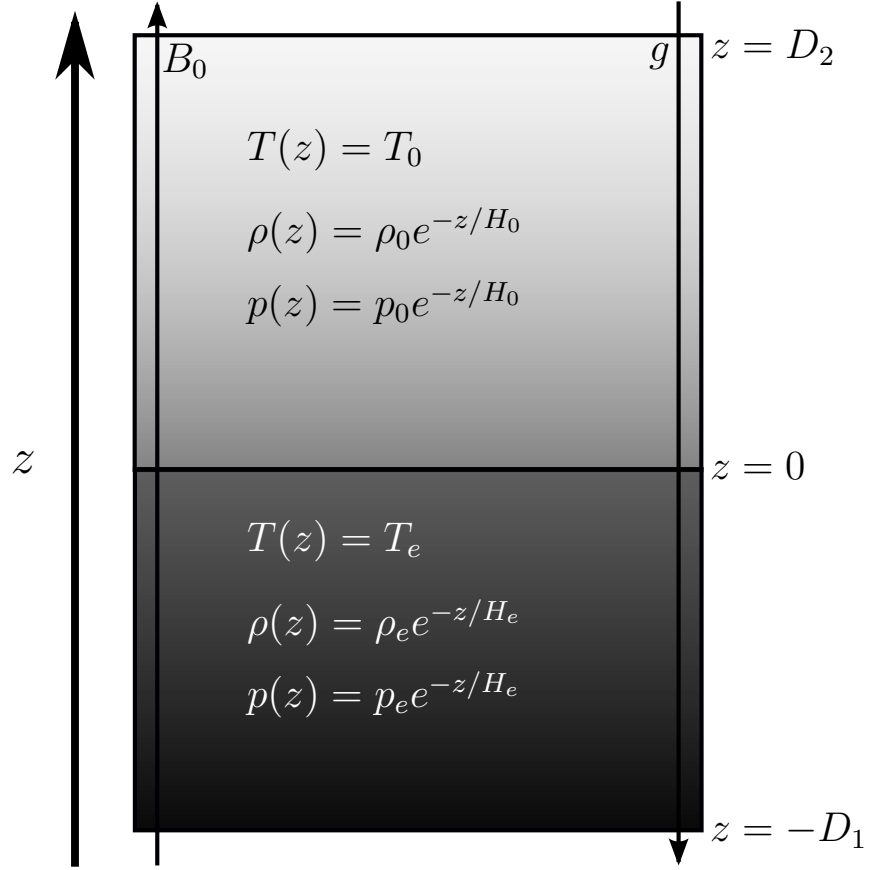


Fig. 4.2 The background: A two-layer gravitationally stratified model of the global solar atmosphere.

and, therefore, a density discontinuity. The lighter plasma is on top (upper) and the relatively heavy plasma in the bottom (lower) and as such the Rayleigh-Taylor instability is not studied. The plasma-beta ( $\beta$ ) is continuous across the discontinuity at  $z = 0$ . We introduce the quantity  $\rho_r = \rho_0/\rho_e$  to denote the density ratio between the lower and upper layers. The solutions in the two separate layers are only different due to the difference in the parameters:

$$\begin{aligned}
 K_e &= K_0 \rho_r, & \widehat{\sigma}_e &= \widehat{\sigma}_0 \rho_r, & \psi_e(z) &= \frac{\omega H_e}{v_{Ae}(0)} e^{-z/H_e}, \\
 \psi_0(z) &= \frac{\omega H_0}{v_{A0}(0)} e^{-z/H_0}, & \frac{H_e}{H_0} &= \rho_r,
 \end{aligned} \tag{4.1}$$

where,

$$K_l = k_x H_l, \quad \widehat{\sigma}_l = \frac{\omega H_l \sqrt{\gamma}}{c_{sl}}, \quad v_{Al}^2(0) = \frac{B_0^2}{\mu \rho_l}, \quad c_{sl} = \frac{\gamma p_l}{\rho_l}, \quad l := 0, e. \tag{4.2}$$

### 4.3 Solutions and Dispersion Relation

To study global standing waves we use the boundary conditions  $v_z = v_x = 0$  at the heights  $z = -D_1, D_2$ . The solutions must also be connected across the discontinuity. [Schwartz and Leroy \(1982\)](#) derived the boundary conditions for a magnetic field across an interface by studying the stress across the boundary and continuity of the magnetic flux across the interface. These led to the conditions that:  $\widehat{v}_x, \widehat{v}_z$  and their derivatives are continuous across the boundary at  $z = 0$ . We define the velocity perturbations,  $\widehat{v}_x$  and  $\widehat{v}_z$  below:

$$\widehat{v}_z(z) = \sum_{j=1,5}^{4,8} C_j v_z^{(j)}(z), \quad \widehat{v}_z^{(j)}(z) = A_j^{(z)}, \quad \widehat{v}_x(z) = \sum_{j=1,5}^{4,8} C_j \widehat{v}_x^{(j)}(z), \quad \widehat{v}_x^{(j)}(z) = B_j^{(z)}. \quad (4.3)$$

Note that when  $j \in \{1, 2, 3, 4\}$ , all parameters are given by the values in the lower layer and when  $j \in \{5, 6, 7, 8\}$ , all parameters are given by their corresponding values for the upper layer. The derivatives of  $\widehat{v}_x$  and  $\widehat{v}_z$  are denoted with a dash e.g.  $A_j^{(z)}$ ,  $B_j^{(z)}$ . Evaluating  $\widehat{v}_x, \widehat{v}_z$  and their derivatives using the boundary and continuity conditions, eight equations are obtained that can be cast as a matrix equation as below,

$$\begin{pmatrix} A_1^{(-D_1)} & A_2^{(-D_1)} & A_3^{(-D_1)} & A_4^{(-D_1)} & 0 & 0 & 0 & 0 \\ B_1^{(-D_1)} & B_2^{(-D_1)} & B_3^{(-D_1)} & B_4^{(-D_1)} & 0 & 0 & 0 & 0 \\ 0 & 0 & 0 & 0 & A_5^{(D_2)} & A_6^{(D_2)} & A_7^{(D_2)} & A_8^{(D_2)} \\ 0 & 0 & 0 & 0 & B_5^{(D_2)} & B_6^{(D_2)} & B_7^{(D_2)} & B_8^{(D_2)} \\ A_1^{(0)} & A_2^{(0)} & A_3^{(0)} & A_4^{(0)} & -A_5^{(0)} & -A_6^{(0)} & -A_7^{(0)} & -A_8^{(0)} \\ B_1^{(0)} & B_2^{(0)} & B_3^{(0)} & B_4^{(0)} & -B_5^{(0)} & -B_6^{(0)} & -B_7^{(0)} & -B_8^{(0)} \\ A_1^{(0)} & A_2^{(0)} & A_3^{(0)} & A_4^{(0)} & -A_5^{(0)} & -A_6^{(0)} & -A_7^{(0)} & -A_8^{(0)} \\ B_1^{(0)} & B_2^{(0)} & B_3^{(0)} & B_4^{(0)} & -B_5^{(0)} & -B_6^{(0)} & -B_7^{(0)} & -B_8^{(0)} \end{pmatrix} \begin{pmatrix} C_1 \\ C_2 \\ C_3 \\ C_4 \\ C_5 \\ C_6 \\ C_7 \\ C_8 \end{pmatrix} = 0. \quad (4.4)$$

For non-trivial solutions to this equation, the determinant must be equal to zero. The determinant of the matrix on the left-hand side of Eq. (4.4) is regarded from now on as a function of  $\omega$  and  $k_x$ , say  $g(\omega, k_x)$ . We, therefore, look for the roots of  $g(\omega, k_x) = 0$  numerically. In what follows, we now introduce, and use, the dimensionless frequency,  $\widehat{\omega}$  and wave-number,  $\widehat{k}_x$ ,

$$\widehat{\omega} = \frac{\omega(D_1 + D_2)}{c_{s0}}, \quad \widehat{k}_x = k_x(D_1 + D_2), \quad (4.5)$$

along with the dimensionless Brunt-Väisälä frequencies in the lower and upper layers, respectively:

$$\widehat{N}_e^2 = \frac{\gamma - 1}{\gamma^2 \rho_r} \left( \rho_r \frac{D_1}{H_e} + \frac{D_2}{H_0} \right)^2, \quad \widehat{N}_0^2 = \frac{\gamma - 1}{\gamma^2} \left( \rho_r \frac{D_1}{H_1} + \frac{D_2}{H_0} \right)^2. \quad (4.6)$$

## 4.4 Model 1: Photosphere to Upper Chromosphere

We now solve Equation (4.4) for a solar atmospheric model that is analogous to the transition from photosphere/lower-mid chromosphere to the high chromosphere. We choose a model similar to the jump in temperature from the mid chromosphere to the high chromosphere, shown in Fig. 4.1. However, both the lower and upper regions are considered isothermal due to the constraints caused by the analytic solutions, we therefore flatten the temperature profile of the lower region and consider this constant without a temperature minimum region. The plasma is bounded below, at  $z = -D_1$ , by the solar interior and above, at  $z = D_2$  by the large jump in temperature of the transition region. The discontinuity in temperature occurs at  $z = 0$ . The typical values of the parameters can be given as:

$$\frac{D_1}{H_e} = 8, \quad \frac{D_2}{H_0} = 2, \quad \beta|_{z=D_2} = 0.1, \quad \rho_r = \frac{1}{2}.$$

The sound speed in the lower layer is taken to be  $7.9 \text{ km s}^{-1}$  and thus the sound speed in the upper layer is approximately  $11.17 \text{ km s}^{-1}$ , due to the temperature increase of a factor of 2. The gravitational acceleration in the solar atmosphere is approximately  $274 \text{ m s}^{-2}$ . This gives the lower layer scale height,  $H_e = 137 \text{ km}$ . The scale height in the upper layer is,  $H_0 = 300 \text{ km}$ . Therefore  $D_1 \approx 1.1 \text{ Mm}$  and  $D_2 \approx 0.6 \text{ Mm}$ .

Fig. 4.3 shows the dispersion relation for this model with the dimensionless frequency,  $\widehat{\omega}$  plotted against the dimensionless wave-number,  $\widehat{k}_x$ . Noted in the diagram are the frequencies corresponding to the 3-minute and 5-minute oscillation periods that are ubiquitous in the Sun. Again, as in Chapter 3, avoided-crossings between modes are present. A zoomed-in section is noted to emphasise that these solution paths do not cross. The same approach, that of studying the components of the wave energy, is used as in Chapter 3.

$$E_T = KE + ME + IE + GE, \quad (4.7)$$

where,

$$KE = \frac{1}{2} \rho_0 (v_x^2 + v_z^2), \quad IE = \frac{p_1^2}{2 \rho_0 v_s^2}, \quad GE = \frac{\rho_0 N^2 v_z^2}{2 \omega^2}, \quad ME = \frac{1}{2 \mu} (B_x^2 + B_z^2).$$

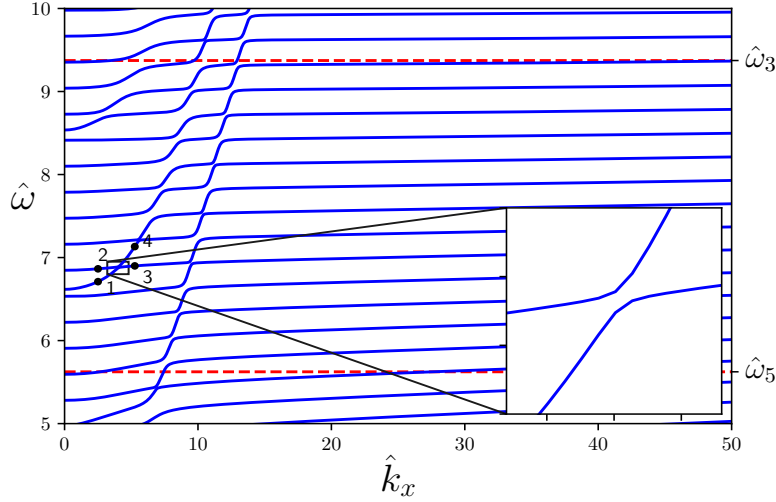


Fig. 4.3 Variation of dimensionless frequency,  $\hat{\omega}$  ( $\hat{\omega} = 1$  corresponds to an angular frequency of  $\omega = 6.9 \times 10^{-3} \text{ s}^{-1}$ ), and wave-number,  $\hat{k}_x$  ( $\hat{k}_x = 10$  corresponds to a wavelength,  $\lambda = 1.07 \text{ Mm}$ ) for the solution of Eq. (4.4) for model one. The red dotted lines indicate the five-minute,  $\hat{\omega}_5$ , and three-minute  $\hat{\omega}_3$  periods of waves. A zoomed-in box indicates that the solution paths do not cross, even they may seem like they do on a larger scale. 1, 2, 3 and 4 annotate the wave solution points that correspond to the eigenfunctions plotted in Figs. 4.6-4.9

Abdelatif (1990) studied the components of the wave energy for a bounded one-layer plasma. He showed that close to the avoided crossing the two solutions took on similar characteristics, slowly changing their character as the avoided crossing was traversed. To study the wave energy distribution in each layer, the integral of the total wave energy over the whole cavity and the integral of the total wave energy in the upper layer are introduced:

$$E_{T_I} = \int_{-D_1}^{D_2} E_T(z, \hat{\omega}, \hat{k}_x) dz, \quad E_{T_L} = \int_{-D_1}^0 E_T(z, \hat{\omega}, \hat{k}_x) dz. \quad (4.8)$$

Here,  $E_{T_I}$  is the total wave energy integrated across both layers.  $E_T$  is the total wave energy as a function of height, frequency and horizontal wave number and  $E_{T_L}$  is the total wave energy integrated from  $z = -D_1$  to  $z = 0$ .

Fig. 4.4a plots the dispersion graph again but in the interval  $0 \leq \hat{\omega} \leq 10$ . However, the solution paths use a colourmap to describe the proportion of the total wave energy density integrated over the lower plasma layer,  $E_{T_L}$ , compared to the total wave energy density integrated over both layers,  $E_{T_I}$ . The lower plasma layer's Brunt-Väisälä frequency is plotted as the red-dashed line. Firstly, it can be immediately noted that for almost all modes the largest proportion of the wave energy density is within the lower plasma layer. The modes that lie below the Brunt-Väisälä frequency have almost no energy within the upper plasma layer, which can be seen by the dark black shade of the line, where  $E_{T_L}/E_{T_I} \approx 1$ . Figs. 4.4b,c and d plot the proportion of

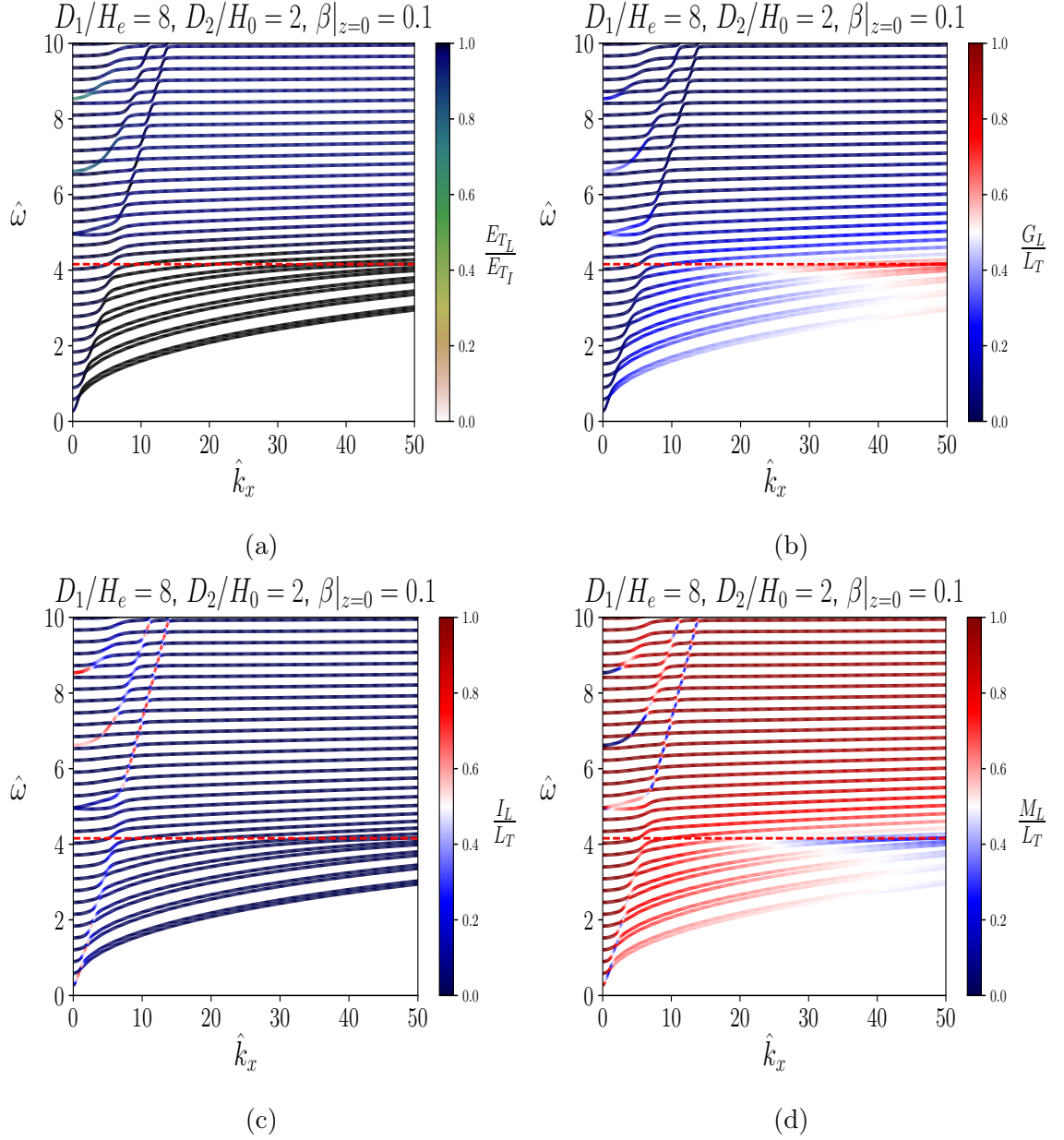


Fig. 4.4 Variation of the dimensionless frequency,  $\hat{\omega}$ , with respect to the dimensionless wave-number,  $\hat{k}_x$ , for model 1. Panel (a) shows the proportion of  $E_{TL}$  to  $E_{TI}$  in the colorbar. Panel (b) depicts the proportion of  $G_L$  to  $L_T$  in the colorbar. Panel (c) is the proportion of  $I_L$  to  $L_T$ . Panel (d) shows the proportion of  $M_L$  in  $L_T$ . The red dashed line represents the dimensionless Brunt-Väisälä frequency of the lower layer,  $\tilde{N}_e$ . The plasma-beta value at the interface has a value of 0.1. From the interface the lower layer descends by eight scale-heights and the upper layer ascends by two scale-heights.

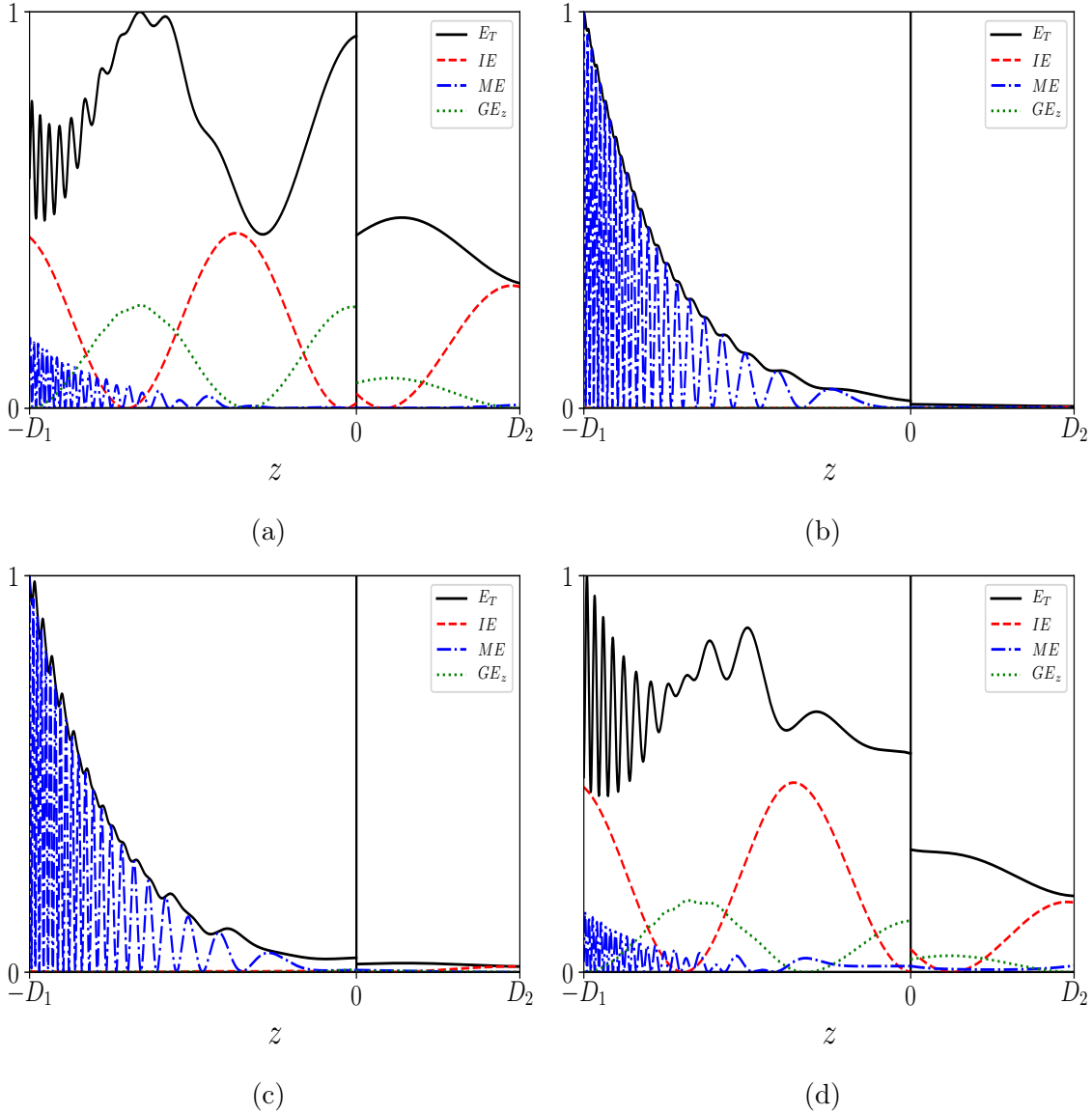


Fig. 4.5 Variation of the components of the potential energy density,  $IE$  (red dashed),  $ME$  (blue dash-dot) and  $GE$  (green dotted) and the total energy density,  $E_T$  with height  $z$ . Panel (a) is evaluated for the point 1 ( $\omega = 0.046 \text{ s}^{-1}$  and wavelength,  $\lambda = 4.3 \text{ Mm}$ ) Fig. 4.3, (b) for point 2 ( $\omega = 0.047 \text{ s}^{-1}$  and wavelength,  $\lambda = 4.3 \text{ Mm}$ ), (c) for point 3 ( $\omega = 0.048 \text{ s}^{-1}$  and wavelength,  $\lambda = 2.0 \text{ Mm}$ ) and (d) for point 4 ( $\omega = 0.049 \text{ s}^{-1}$  and wavelength,  $\lambda = 2.0 \text{ Mm}$ ).

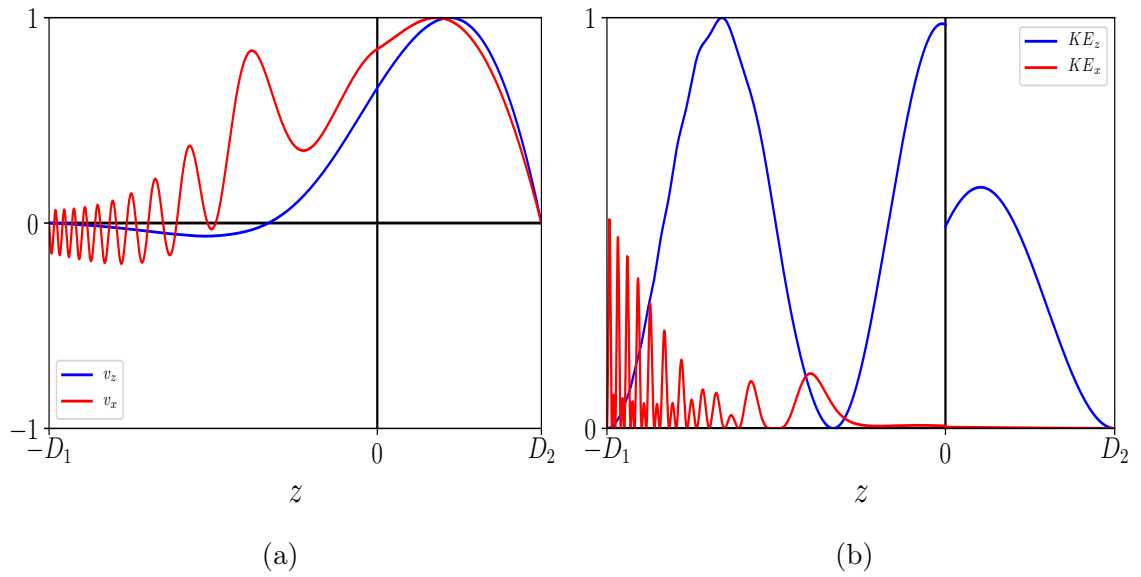


Fig. 4.6 For point 1 in Fig. 4.3, panel (a) the variation of  $v_x$  (red line) and  $v_z$  (blue line), normalised against themselves, with respect to  $z$  and (b) the variation of the horizontal kinetic energy density ( $KE_x$  in red) and vertical kinetic energy density ( $KE_z$  in blue) with height.

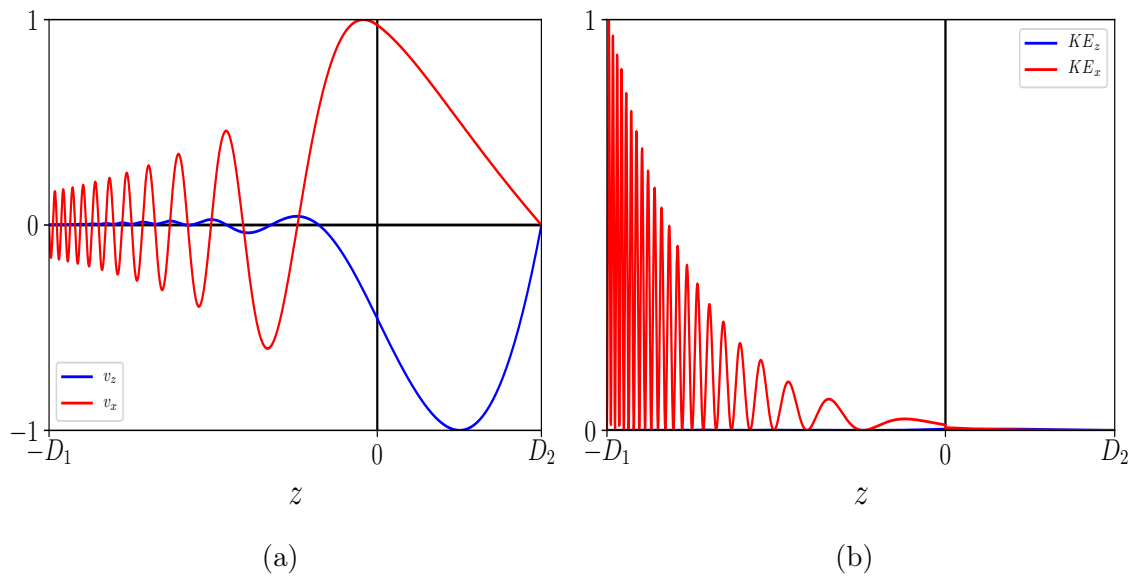


Fig. 4.7 Same as Fig. 4.6 but for point 2 of Fig. 4.3.

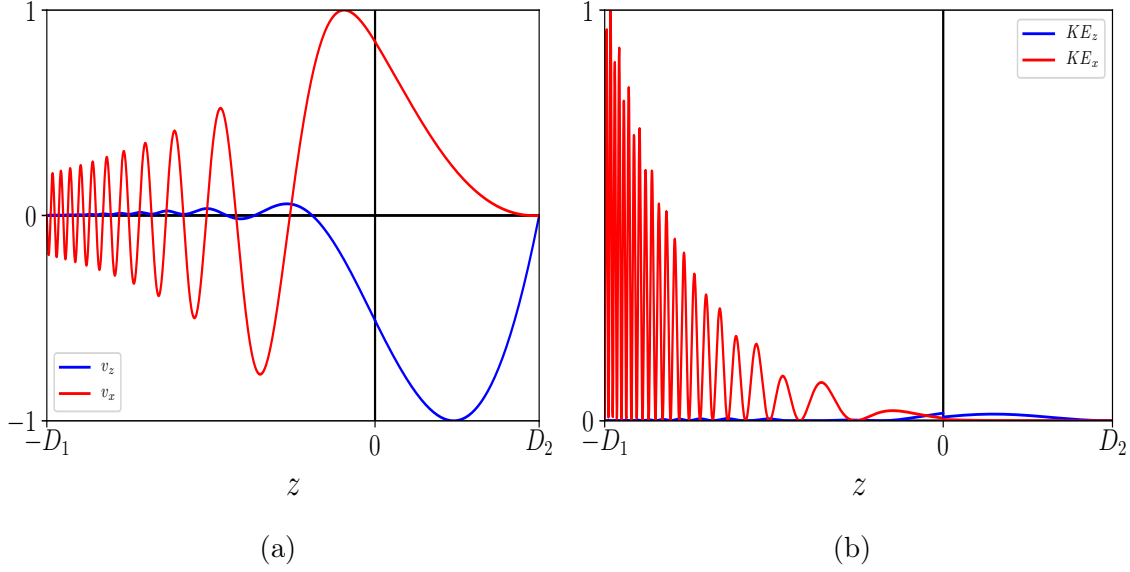


Fig. 4.8 Same as Fig. 4.6 but for point 3 of Fig. 4.3.

the total gravitational ( $G_L$ ), internal ( $I_L$ ) and magnetic ( $M_L$ ) energy density in the lower layer, respectively, as compared to the sum of all three,  $L_T$  all of which are given below:

$$G_L = \int_{-D_1}^0 GE(z, \hat{\omega}, \hat{k}_x) dz, \quad I_L = \int_{-D_1}^0 IE(z, \hat{\omega}, \hat{k}_x) dz, \quad M_L = \int_{-D_1}^0 ME(z, \hat{\omega}, \hat{k}_x) dz, \quad (4.9)$$

$$L_T = G_L + I_L + M_L. \quad (4.10)$$

The modes below the Brunt-Väisälä frequency have very little energy trapped in the upper layer. These modes are comprised mainly of gravitational and magnetic energy density. It is well known  $g$ -modes become evanescent as the height within the atmosphere increases. There is also the fact that the Alfvén speed of the system is increasing with height, which will act to reflect the propagating waves that form the standing waves of our system and thus energy will be trapped further down in the cavity. This remark also holds well for all the modes comprised mainly of magnetic energy density. Referring to Fig. 4.4c we can see that the ‘fast’ (acoustic) modes are comprised primarily of internal energy density and comparing this to Fig. 4.4a the modes that have energy within the upper layer (signified by their aqua hue on the diagram) are these modes but only for low wave-numbers,  $\hat{k}_x$ . These ‘acoustic’ modes still will have reflection of energy at the interface between the lower and upper layers due to the discontinuity in density and, therefore, temperature (as a consequence of maintaining pressure balance).

To further illustrate this, Figs. 4.5a-d show the components of the potential and total wave energy densities as a function of height,  $z$ , for the points 1, 2, 3 and 4, respectively, indicated on Fig. 4.3. These four points are chosen purposefully near

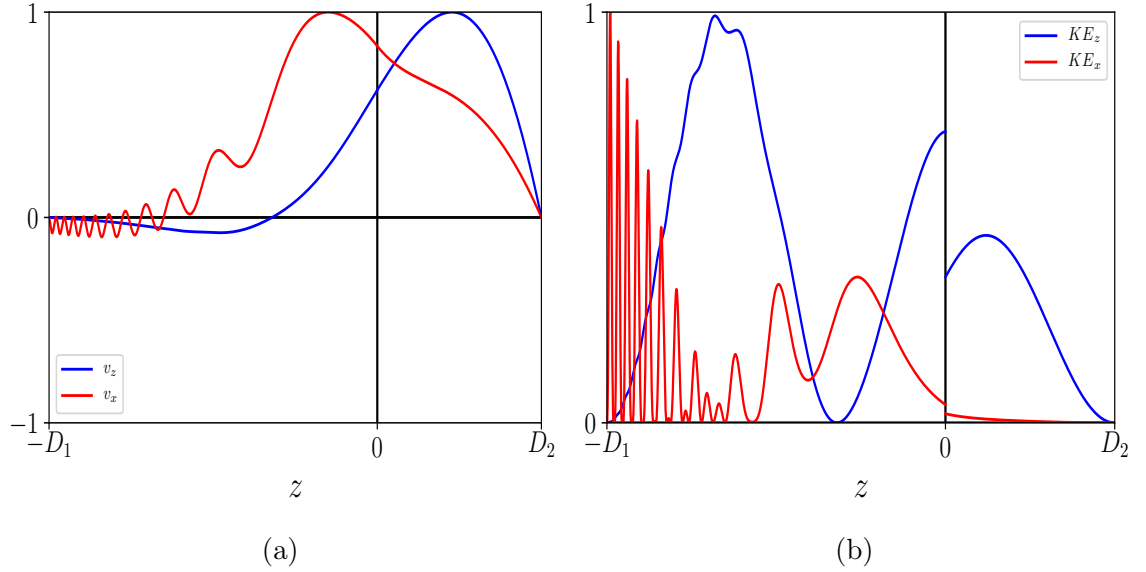


Fig. 4.9 Same as Fig. 4.6 but for point 4 of Fig. 4.3.

to an avoided crossing to show how a solution curve transitions from one mode to another. The eigen-functions for  $\widehat{v}_x$  and  $\widehat{v}_z$  (normalised against themselves) for these points are shown in Figs. 4.6a-4.9a along with their normalised kinetic energy density components in the  $x$ - and  $z$ -directions in Figs. 4.6b-4.9b.

Figs. 4.5a and b plot the potential energy densities for the solution line that passes through the points 1 and 3 in Fig. 4.3. Comparing Figs. 4.5a and b, it is evident that the behaviour of the solution has changed along the solution line. In Fig. 4.5a point 1 is an acoustic gravity mode, however when the solution line gets to point 3 the mode is clearly a purely magnetic mode. The transition of the modes is further evident from Figs. 4.6a and 4.7a in which the eigen-modes appear very different and the kinetic energy density has switched from mainly being vertical in Fig. 4.6b, to being almost purely horizontal in Fig. 4.7b. Figs. 4.5c and d plot the potential energy densities for the solution line that passes through the points 2 and 4 in Fig. 4.3. If these are compared, it is observed that point 2 is essentially a purely magnetic mode, however as the solution line is traversed to point 4 it is seen that the mode has become an acoustic gravity mode. Again, analysing the eigen-modes and kinetic energy densities of the modes in Figs. 4.8 and 4.9, respectively, we see, that, from being dominated by horizontal motions for point 3 shown in Fig. 4.8, when the solution line lies on point 4 in Fig. 4.9, the mode is dominated by vertical motions.

Another important point to note is whether the previous solutions are preserved along the line. We compare the potential energy densities of the points 1 and 4 by comparing Figs. 4.5a and 4.5d. The modes are very similar in terms of their potential energy structure. Indeed, in the lower layer, below the line  $z = 0$ , we see very many similarities in the structure of the gravitational energy (GE) and the internal energy (IE). The main difference between the modes is the amount of total

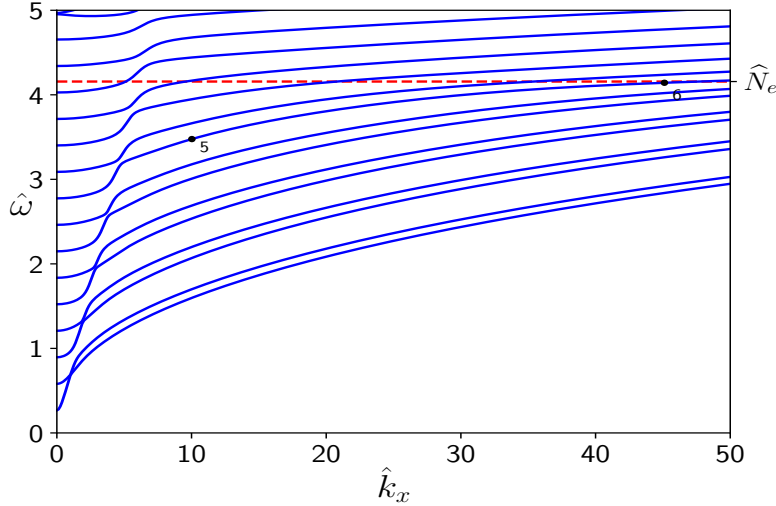


Fig. 4.10 The variation of the dimensionless frequency,  $\hat{\omega}$ , with respect to the dimensionless wave-number,  $\hat{k}_x$ . The dimensionless frequency lies in the range,  $\omega = 0$  to 5. The red dashed line indicates the dimensionless Brunt-Väisälä frequency of the lower layer,  $\hat{N}_e$ . The points '5' and '6' have been indicated on one of the solution curves.

energy trapped in the upper layer. Less total energy is trapped for the mode of Fig. 4.5d than for the mode of Fig. 4.5a. This is probably due to the increase in horizontal wave-number in which an incident wave would be reflected more at the surface. If the points 2 and 3 are compared using Figs. 4.5b and c, one can see that both modes are purely magnetic modes. These modes lose energy very quickly with height and hardly any energy is trapped in the upper layer. Evidently, from our analysis, we see that, when avoided crossings are traversed, modes maintain a fairly similar structure, as if there was no avoided crossing there.

Fig. 4.10 shows the dispersion diagram for  $\hat{\omega} = 0$  to 5. The points '5' and '6' are indicated as selected modes. Both these points lie below the Brunt-Väisälä frequency of the lower atmosphere. Point '5' has a larger proportion of magnetic potential energy, whereas point '6' has a larger proportion of gravitational potential energy, which can be evidenced in Fig. 4.5. Figs. 4.11a and b plot the potential energy of the points '5' and '6' respectively. By studying Figs. 4.11a and b it is evident that the mode at point '5' is mainly of magnetic in nature, whereas '6' is gravitational. From both of these we can see that all the energy is mostly trapped in the lower layers of chromosphere. Our results agree well with those found in [Vigeesh \*et al.\* \(2017\)](#) in which the internal gravity modes are coupled to the slow MA waves and all energy is trapped in the lower chromosphere and photosphere.

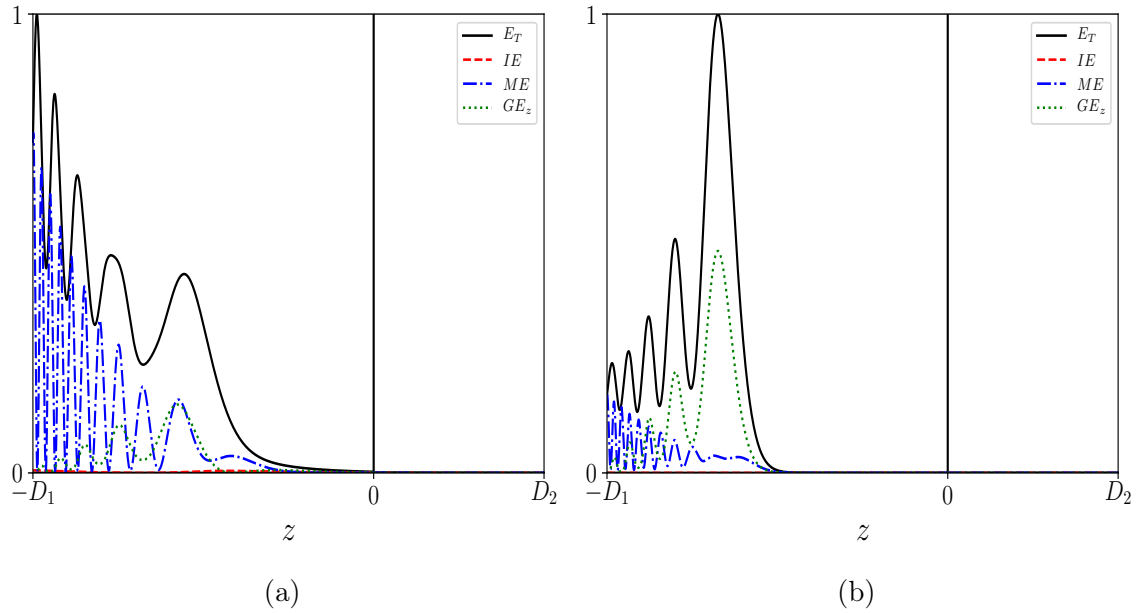


Fig. 4.11 Variation of the total wave energy density,  $E_T$ , along with the components of the potential energy density,  $IE$ ,  $ME$ ,  $GE$ , with respect to height,  $z$  for the points (a) ‘5’ and (b) ‘6’ shown in Fig. 4.10.

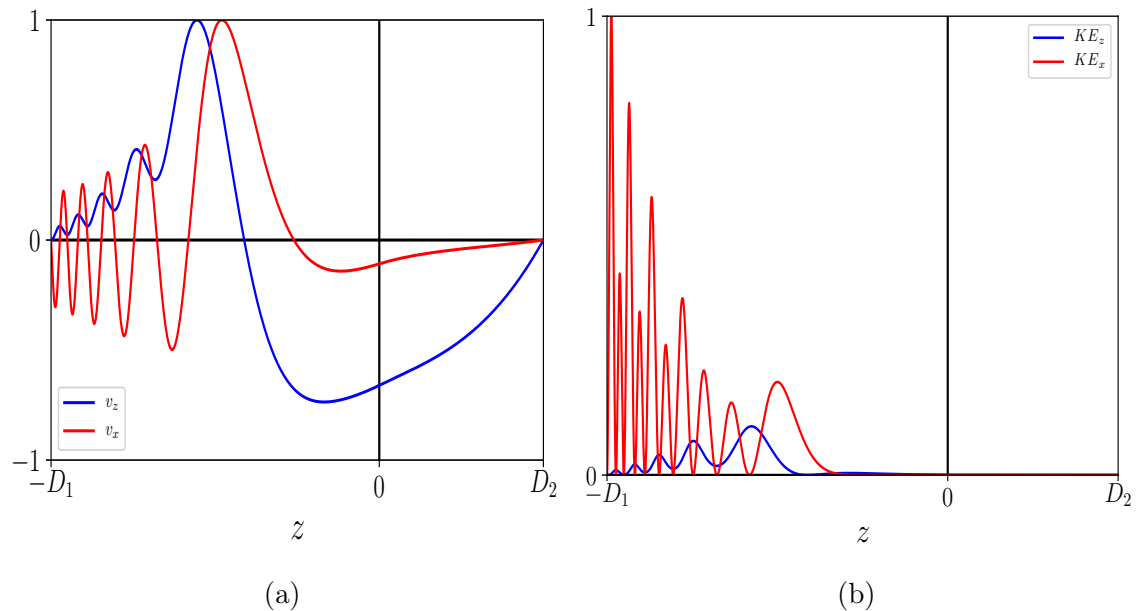


Fig. 4.12 For point ‘5’ in Fig. 4.10 panel (a) the variation of  $v_x$  and  $v_z$  normalised against themselves with respect to height,  $z$  (b) the variation of the horizontal,  $KE_x$ , and vertical,  $KE_z$ , components of the kinetic energy density,  $KE$ , with respect to  $z$ .

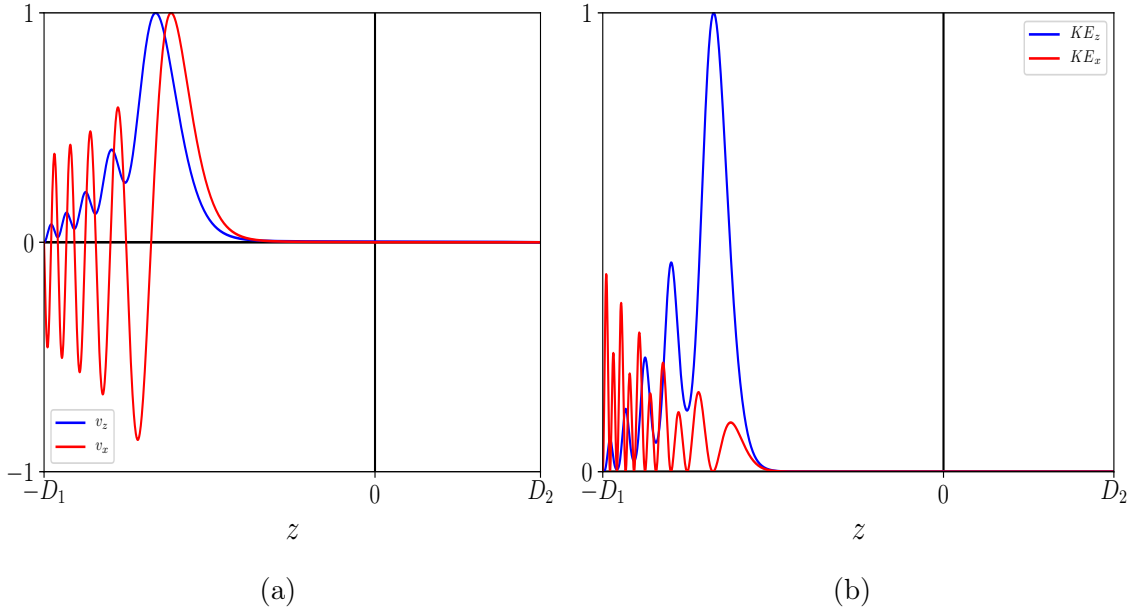


Fig. 4.13 Same as Fig. 4.12 but for point ‘6’ in Fig. 4.10.

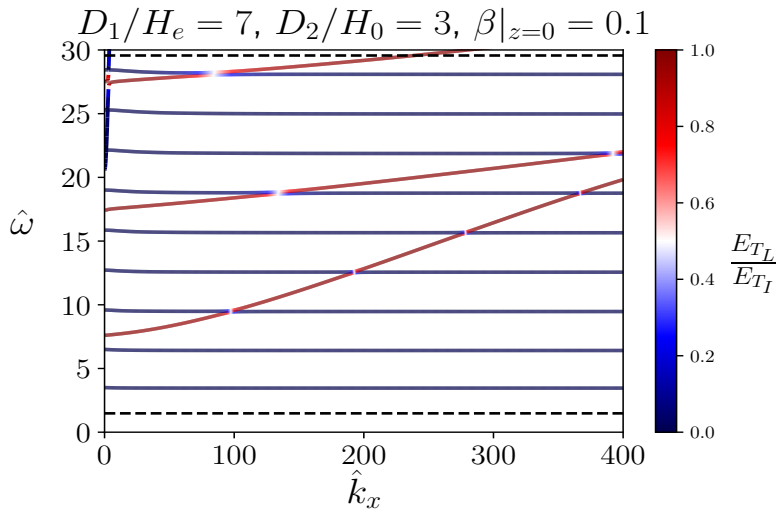


Fig. 4.14 The dispersion diagram,  $\hat{\omega} - \hat{k}_x$ , for model 2. The colour bar represents the proportion of the total energy density in the lower layer,  $E_{TL}$  compared to the total energy density integrated over both layers,  $E_{T1}$ . The plasma beta at the interface has a value of 0.1. From the interface, the lower layer descends by 7 scale heights and the upper layer ascends by 3 scale heights. The black dashed lines indicate the dimensionless Brunt-Väisälä frequencies of the upper ( $\hat{N}_0$ ) and lower ( $\hat{N}_e$ ) layers respectively, with the lower frequency being the upper layer and the larger the lower layer.

## 4.5 Model 2: Lower Solar Atmosphere to Corona

The second model is analogous to the temperature jump from the lower atmosphere to the corona. The upper turning point is, physically, considered to be when the solar wind flow speed growth is greater than the local Alfvén speed. The parameters for this model are given below:

$$\frac{D_1}{H_e} = 7, \quad \frac{D_2}{H_0} = 3, \quad \beta|_{z=0} = 0.1, \quad \rho_r = \frac{1}{400}.$$

The lower layer sound speed is taken as  $7.9 \text{ km s}^{-1}$  again with the sound speed in the upper coronal plasma  $158 \text{ km s}^{-1}$ . Assuming a gravitational acceleration, again, of  $274 \text{ m s}^{-2}$  gives  $H_e = 137 \text{ km}$  and  $H_0 = 54.7 \text{ Mm}$ . Therefore  $D_1 \approx 0.96 \text{ Mm}$  and  $D_2 \approx 164.1 \text{ Mm}$ .

Fig. 4.14 plots the dispersion diagram of  $\hat{\omega}$  against  $\hat{k}_x$  for the model described above. Again, as in Fig. 4.3, there is a colormap that is represented by the colorbar of Fig. 4.14 showing the proportion of total wave energy density within the bottom layer  $E_{T_L}$  as compared to the total wave energy density integrated in both the layers,  $E_{T_I}$ . Extremely evident in this plot is that the modes either only have energy trapped within the top layer i.e. when the line is blue or conversely energy trapped within the bottom layer i.e. when the line is red. The only ‘sharing’ of energy is around the avoided crossings between the modes indicated by the change of color of the mode smoothly around these points, as one mode takes on the characteristics of the other. To accentuate this point, we have plotted in Figs. 4.15a-d the lower layer and upper layer solutions given in Chapter 3 for the photosphere to chromosphere and coronal models over the the solutions of the corresponding two-layer dispersion diagram. We have also plotted the change in the total wave energy density for the bottom layer as a proportion of the total wave energy integrated over both layers.

One can see from Figs. 4.15 a-d that the large density discontinuity acts as a physical barrier that traps the wave energy. This is evidenced in both Figs. 4.15c and d where the energy is mainly trapped in either the upper or lower layer. The dispersion relation is therefore rather similar to that of a single-layer plasma. However, at an avoided crossing, the nature of each mode switches; the modes are inherently coupled together. It is also possible to see from Fig. 4.15a and b that the lower layer solutions are shifted slightly in frequency for  $\hat{k}_x$  up to approximately a value of 200 which corresponds to a small  $K_e$  value, the discontinuity seems to lower the frequency of these modes slightly. It is possible to find an approximation for this frequency shift analytically for  $\hat{k}_x = 0$ . Using the solutions of Eqs. (3.13) and (3.14) and applying the boundary conditions as described before, two distinct dispersion relations can be found for  $\hat{v}_x$  and  $\hat{v}_z$  respectively. The dispersion relation for  $\hat{v}_x$  is highly transcendental and analytic study is to our best knowledge not possible.

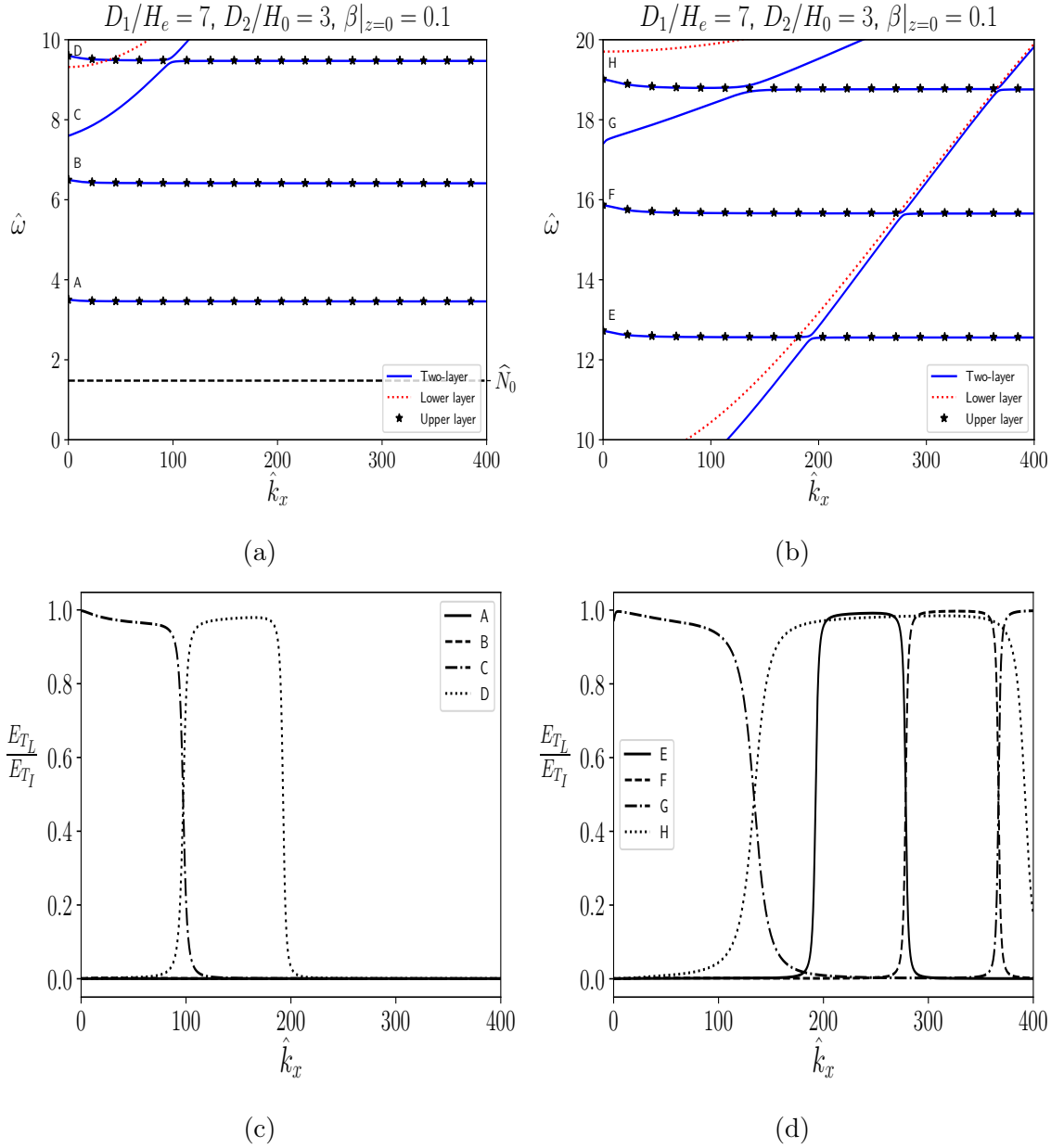


Fig. 4.15 Panels (a) and (b) show the dispersion diagrams for model 2 with the dispersion diagrams from models 1 and 2 of Chapter 3 plotted as well, indicated by the red dotted line for the lower layer and by the ‘star’ (★) markers for the upper layer. Panels (c) and (d) show the ratio of total energy density in the lower layer,  $E_{TL}$ , to total energy density in both layers,  $E_T$ , for the lines A, B, C, D, E, F, G and H from panels (a) and (b).

However, the dispersion relation for  $\hat{v}_z$  is much simpler and is presented below:

$$\begin{aligned} \sin(q_{0e}\hat{D}_1)\sin(q_{00}\hat{D}_2)(1-\rho_r) + 2\sin(q_{0e}\hat{D}_1)\cos(q_{00}\hat{D}_2)q_{00}\rho_r \\ + 2\sin(q_{00}\hat{D}_1)\cos(q_{0e}\hat{D}_1)q_{0e} = 0. \end{aligned} \quad (4.11)$$

Here,  $\hat{D}_1 = D_1/H_e$  and  $\hat{D}_2 = D_2/H_0$ . Due to the very large temperature increase between the two layers,  $\rho_r$  is a small parameter so that the approximation,  $\rho_r^{1/2} \ll 1$ , can be made. Therefore any terms of order  $(\rho_r)^{1/2}$  or higher order can be neglected resulting in the following dispersion relation

$$\sin(q_{00}\hat{D}_2)\left(\tan(q_{0e}\hat{D}_1) + 2q_{0e}\right) \approx 0. \quad (4.12)$$

The first term just refers to sound waves trapped in the upper layer, reflected by the temperature discontinuity. The second term refers to sound waves in the lower layer with a correction due to the discontinuity. If we denote  $\delta = 2/\hat{D}_1$  and suggest that this is a small quantity, it is possible to use a perturbation method to find an approximation of the frequencies

$$\hat{\omega}^2 \approx \frac{(\rho_r\hat{D}_1 + \hat{D}_2)^2}{\rho_r} \left( \frac{1}{4} + \frac{m^2\pi^2}{\hat{D}_1^2} \left(1 - \delta + \delta^2 + O(\delta^3)\right)^2 \right) \quad (4.13)$$

Taking the lowest order approximation in  $\delta$  of Eq. (4.13), it can be seen that the frequencies are slightly lower when compared to that of the single layer (SL) which is shown below as a comparison

$$\hat{\omega}_{SL}^2 = \frac{(\rho_r\hat{D}_1 + \hat{D}_2)^2}{\rho_r} \left( \frac{1}{4} + \frac{m^2\pi^2}{\hat{D}_1^2} \right). \quad (4.14)$$

Therefore, to the lowest order in  $\delta$ , the frequency shift,  $\Delta\hat{\omega}^2$ , is given by

$$\Delta\hat{\omega}^2 = -4 \frac{(\rho_r\hat{D}_1 + \hat{D}_2)^2}{\rho_r} \frac{m^2\pi^2}{\hat{D}_1^3}. \quad (4.15)$$

This result agrees with those plotted Fig. 4.15a and b that the frequency of the lower layer is reduced (for small wave-numbers) due to having some continuity across the layer, while the frequency of the upper layer solution seems to be almost identical. Physically, due to the huge discontinuity in density, almost all the energy of an incident wave will be reflected however, some will be transmitted as the boundary does let energy through, regardless of how small that is. This changes the exact location of the node and in turn lowers the frequency.

## 4.6 Summary and Discussion

In this section we considered two-layer bounded models. A two-layer model was suggested by Yelles Chaouche and Abdelatif (2005) but with an upper boundary condition of finite energy density as  $z \rightarrow \infty$ . The wavenumber was found to have an imaginary component. In a two-layer bounded atmosphere this was not seen to occur. Two different model atmospheres were considered. The first was analogous to the temperature jump between the photosphere/low chromosphere to the high chromosphere. Eigen-frequencies were found within the band of 3-minute and 5-minute oscillations for viable physical parameters. The larger the wave-number,  $\hat{k}_x$ , the less energy of the wave was contained in the upper layer. The energy of the so-called ‘magnetic’ modes was found to decrease rapidly with height. This physically is caused by the change in the Alfvén speed with height and therefore the wave is reflected. However, it was shown for certain modes e.g. as a typical example, for point 1 of Fig. 4.3 when  $\omega = 0.046 \text{ s}^{-1}$  and  $\lambda = 4.3 \text{ Mm}$ , an ‘acoustic-gravity’ mode was seen to share wave energy relatively equally between the lower atmosphere and the upper atmosphere (with a small drop in total wave energy across the discontinuity). This distribution of wave energy, along with dissipative processes, could lead to heating in the higher solar atmosphere.

The second model considered a transition in temperature reminiscent of that between the lower solar atmosphere and the corona; a factor of 400 increase in temperature was implemented in the equilibrium. It was found that solutions to the dispersion relation were practically those of the upper and lower single layer atmospheres. Physically, this just shows that the large density discontinuity acts as a physical barrier to reflect waves incident on this surface. However, it was also found that around the avoided crossings there would always be some inherent coupling where the solutions change character between the upper and lower layer solutions, with the transition sometimes smooth. This coupling is important as it allows wave energy to *leak* from one layer to another. Given the huge change (i.e. drop) in inertia of going from the chromosphere to the corona, even a small leakage may have considerable effects on the oscillations in the corona.

# Chapter 5

## Effect of Steady Flow on Magneto-Acoustic Gravity Surface Waves

### 5.1 Introduction

Surface waves are ubiquitous in nature, the most obvious example being the waves seen on the surface of the ocean. Surface waves have been explored to a large extent in a solar physics/MHD context. The classic paper by [Roberts \(1981a\)](#) studied the surface waves at a magnetic interface, with non-dispersive slow and fast MA surface waves present. [Roberts \(1981b\)](#) then studied surface waves in a symmetrical magnetic slab, showing that the famous *sausage* and *kink* modes existed in this context, along with dispersion being present due to the thickness of the slab compared to the wave number of the oscillation. This case was extended to a slab in a magnetic environment ([Edwin and Roberts, 1982](#)) and to cylindrical co-ordinate system ([Edwin and Roberts, 1983](#)).

However, none of these cases considered the effect of gravitational stratification on the propagation of surface modes which leads to dispersion. [Miles and Roberts \(1992\)](#) considered the case of an isothermal, stratified plasma with an exponentially decreasing magnetic field above a non magnetic isothermal plasma of higher density. The exponentially decreasing magnetic field led to a constant Alfvén speed. The stratification was not only responsible for the introduction of dispersion but also led to *cut-off* curves where modes with finite energy density could not exist. In some cases, the fast-mode does not exist regardless of the wave-number combination. [Miles et al. \(1992\)](#) extended this work to the case of a uniform magnetic field, so that now the Alfvén speed was not constant. This would lead to singularities at which resonance can occur, however, their study did not consider this. Due to the varying Alfvén speed not only surface modes are present but also body modes.

The Sun does not only have different surface structures but also can exhibit flows on both small and large scales, as was discussed in Chapter 1. The differential rotation of the Sun can act as a shear flow situation between the solar atmosphere and the solar interior, although the shear is rather low in comparison to the phase speeds of the waves. The Evershed flow, found above sunspots flowing away from them or further away towards them, is another situation where shear flows occur in the solar atmosphere, however the flow velocities in this situation can be much larger (Evershed, 1909). Flows, in wave theory, can lead to Doppler shifts in the frequencies of the waves in a single uniform medium. In systems with interfaces and shear flows it is possible that waves are decelerated or accelerated, depending on the direction of wave propagation relative to the flow. It can even reverse wave directions, leading to phenomena such as negative energy wave instabilities or the Kelvin-Helmholtz instability.

The work in this chapter is the natural extension to and generalisation of the work in Miles and Roberts (1992) with the addition of a uniform flow in the lower non-magnetic region and is taken from the work in Erdélyi and Mather (2017). A governing equation is derived for both separate regions. A dispersion relation for wave propagation is then derived and the limiting case of small wavelength is taken, along with the case of a small density ratio and small flow velocity. The cut-off curves of wave propagation are considered along with how the flow affects these. The dispersion relation is then solved numerically and dispersion diagrams are plotted.

## 5.2 Governing Equation

Consider a plane-parallel background plasma stratified by gravity in the negative  $z$ -direction i.e.  $\mathbf{g} = -g\hat{\mathbf{z}}$ , where  $\hat{\mathbf{z}}$  is the unit vector in the  $z$ -direction. A magnetic field, perpendicular to the gravitational field (the  $z$ -axis), is embedded within the plasma, and arbitrarily varies in the  $z$ -direction i.e.  $\mathbf{B}(z) = (B(z), 0, 0)$ . The kinetic pressure,  $p(z)$  and plasma density,  $\rho(z)$ , are both in general functions of  $z$  along with a horizontal equilibrium flow  $\mathbf{v} = (u(z), 0, 0)$ . For magneto-hydrostatic balance, from the momentum equation given by Eq. (1.7), the following condition must be satisfied:

$$\frac{d}{dz} \left( p(z) + \frac{B^2(z)}{2\mu_0} \right) = -g\rho(z). \quad (5.1)$$

Considering small perturbations (denoted by subscript 1 throughout this chapter) around this background equilibrium, the Equations (1.13)-(1.17) reduce to the following

$$\frac{\partial \rho'}{\partial t} + (\mathbf{v}(z) \cdot \nabla) \rho' + (\mathbf{v}' \cdot \nabla) \rho(z) + \rho(z)(\nabla \cdot \mathbf{v}') = 0, \quad (5.2)$$

$$\frac{\partial p'}{\partial t} + (\mathbf{v}(z) \cdot \nabla) p' + (\mathbf{v}' \cdot \nabla) p(z) + \gamma p(z)(\nabla \cdot \mathbf{v}') = 0, \quad (5.3)$$

$$\rho(z) \left( \frac{\partial \mathbf{v}'}{\partial t} + (\mathbf{v}(z) \cdot \nabla) \mathbf{v}' \right) = -\nabla p' + (\nabla \times \mathbf{B}') \times \frac{\mathbf{B}(z)}{\mu_0} + (\nabla \times \mathbf{B}(z)) \times \frac{\mathbf{B}'}{\mu_0} - \rho' g \hat{\mathbf{z}}, \quad (5.4)$$

$$\begin{aligned} \frac{\partial \mathbf{B}'}{\partial t} &= (\mathbf{B}(z) \cdot \nabla) \mathbf{v}' - \mathbf{B}(z) (\nabla \cdot \mathbf{v}') - (\mathbf{v}' \cdot \nabla) \mathbf{B}(z) \\ &\quad - (\mathbf{v}(z) \cdot \nabla) \mathbf{B}' + (\mathbf{B}' \cdot \nabla) \mathbf{v}(z), \end{aligned} \quad (5.5)$$

$$\nabla \cdot \mathbf{B}' = 0. \quad (5.6)$$

In a compressible ideal plasma, two-dimensional, linear, isentropic disturbances about the equilibrium take the form

$$\boldsymbol{\xi}(x, z, t) = (\widehat{\xi}_x(z), 0, \widehat{\xi}_z(z)) e^{i(k_x x - \omega t)}. \quad (5.7)$$

Here the *Lagrangian displacement*,  $\boldsymbol{\xi}$ , has been introduced and is given by the relation

$$\boldsymbol{\xi} = \frac{i\mathbf{v}'}{\Omega(z)}, \quad (5.8)$$

where,

$$\Omega(z) = \omega - u(z)k_x, \quad (5.9)$$

is the Doppler-shifted wave frequency. The Alfvén wave has been decoupled (perturbations lying solely in the y-direction) and, as such, two coupled equations relating  $\widehat{\xi}_z$  and the divergence of the velocity perturbation,  $\Delta = \nabla \cdot \mathbf{v}'$ , can be formed

$$\frac{i\Delta(z)}{\Omega(z)} = \frac{\widehat{\xi}_z(z)' \Omega^2(z) - \widehat{\xi}_z(z) k_x^2 g}{\Omega^2(z) - k^2 c_s^2(z)}, \quad (5.10)$$

$$\begin{aligned} -\rho(z) \left( \Omega^2(z) - k_x^2 v_A^2(z) \right) \widehat{\xi}_z &= \left( \widehat{\xi}_z p(z)' - \frac{\Delta c_s^2(z) \rho(z)}{i\Omega(z)} \right)' + \left( \frac{\mathbf{B}(z)}{\mu} (\xi_z(z) \mathbf{B}(z))' \right)' \\ &\quad + \frac{i\rho(z)\Delta(z)}{\Omega(z)} g + \widehat{\xi}_z(z) \rho(z)' g. \end{aligned} \quad (5.11)$$

The divergence can then be eliminated between Equations (5.10) and (5.11) to obtain a second-order ordinary differential for  $\widehat{\xi}_z$  that governs MAG waves in an arbitrarily

stratified medium with an incompressible flow:

$$\begin{aligned} & \frac{d}{dz} \left[ \frac{\rho(z)(c_s^2(z) + v_A^2(z))(\Omega^2(z) - c_T^2(z)k_x^2)}{\Omega^2(z) - c_s^2(z)k_x^2} \frac{d\widehat{\xi}_z(z)}{dz} \right] \\ & + \left[ \rho(z)(\Omega^2(z) - v_A^2(z)k_x^2) \right. \\ & \quad \left. - \frac{g^2 k_x^2 \rho(z)}{\Omega^2(z) - c_s^2(z)k^2} - \frac{d}{dz} \left( \frac{g k_x^2 \rho(z) c_s^2(z)}{\Omega^2(z) - c_s^2(z)k^2} \right) \right] \widehat{\xi}_z(z) = 0, \end{aligned} \quad (5.12)$$

where  $\gamma = 5/3$  is the adiabatic index, and  $\mu_0$  is the magnetic permeability of free-space. Here,

$$v_A(z) = \frac{B(z)}{(\mu_0 \rho(z))^{1/2}} \quad (5.13)$$

is the Alfvén speed, and

$$c_T(z) = \frac{c_s(z)v_A(z)}{(c_s^2(z) + v_A^2(z))^{1/2}} \quad (5.14)$$

is the tube speed. Equation (5.12) can in essence be derived from the more general differential equation, given in [Goedbloed \*et al.\* \(2010\)](#), by setting  $k_y = 0$  and  $B_y = 0$ .

### 5.3 Equilibrium Model and Governing Equations

In this section, we describe the equilibrium of a two layer system of plasmas, connected across an interface between them at  $z = 0$ , stratified by gravity. The upper region ( $z > 0$ ) is approximated to be isothermal, with temperature,  $T_0$ . An exponentially decreasing (with height) magnetic field,  $B_0(z)$ , is embedded within the plasma, with the requirement that the Alfvén speed ( $v_A$ ) is constant. The lower plasma region ( $z < 0$ ) is also approximated to be isothermal, with temperature,  $T_e$ . From now on, quantities above the interface (in  $z > 0$ ) are denoted by the subscript ‘0’, and quantities below (in  $z < 0$ ) by the subscript ‘e’ (see [Figure 5.1](#)). The ideal gas law relates the temperature, pressure and density together and is given by

$$p(z) = \frac{k_B}{m_{av}} \rho(z) T(z), \quad (5.15)$$

where  $k_B$  is Boltzmann’s constant, and  $m_{av}$  the mean particle mass of the plasma. Eq. (5.15), along with the assumptions that both plasmas are isothermal and the background momentum balance, given by Eq. (5.4), leads to exponential pressure,

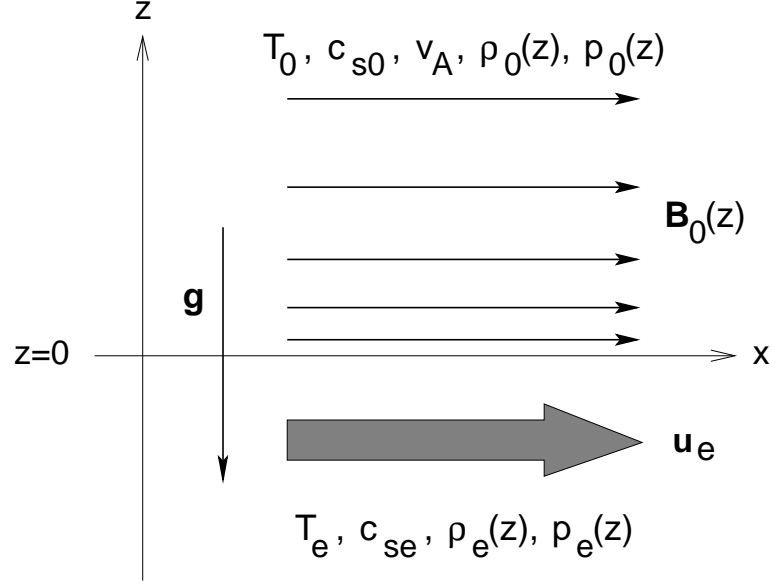


Fig. 5.1 Equilibrium model of a single magnetic interface at  $z = 0$  in a gravitationally stratified atmosphere, with an exponentially decreasing horizontal magnetic field,  $B_0(z)$ , in  $z > 0$  and a horizontal constant equilibrium flow,  $u_e$ , in  $z < 0$ . The temperatures  $T_0$  and  $T_e$  either side of the interface are approximated as isothermal.

density and magnetic field (for the upper region,  $z > 0$ ) profiles

$$p(z), \rho(z), B(z) = \begin{cases} p_0 e^{-z/H_B}, & \rho_0 e^{-z/H_B}, & B_0 e^{-z/2H_B}, & z > 0, \\ p_e e^{-z/H_e}, & \rho_e e^{-z/H_e}, & 0, & z < 0. \end{cases} \quad (5.16)$$

Here,  $H_B = c_{s0}^2/\Gamma g$  and  $H_e = c_{se}^2/\gamma g$  are the isothermal density/pressure scale-heights above and below the interface, respectively, and

$$\Gamma = \frac{2\gamma\beta}{\gamma + 2\beta}. \quad (5.17)$$

is the magnetically modified adiabatic exponent with  $\beta = c_{s0}^2/v_A^2$ . We note that in the limit of zero magnetic field  $\Gamma = \gamma$  and  $H_B = H_0 = c_{s0}^2/\gamma g$ . Here,  $c_{s0} = (\gamma p_0/\rho_0)^{1/2}$  and  $v_A = B_0/(\mu_0 \rho_0)^{1/2}$  are the sound and Alfvén speeds in the magnetic atmosphere, respectively, and  $c_{se} = (\gamma p_e/\rho_e)^{1/2}$  is the sound speed in the field-free region. The following notations have been made:  $\rho_0 = \rho_0(0_+)$ ,  $\rho_e = \rho_e(0_-)$ ,  $p_0 = p_0(0_+)$ ,  $p_e = p_e(0_-)$ , and  $B_0 = B_0(0_+)$ . The exponential profiles for the density, pressure and magnetic field lead to constant sound and Alfvén speeds above and below the interface. The profiles for the temperature, sound speed, Alfvén speed and background flow speed are given below:

$$T(z), c_s(z), v_A(z), u(z) = \begin{cases} T_0, & c_{s0}, & v_A, & 0, & z > 0, \\ T_e, & c_{se}, & 0, & u_e, & z < 0, \end{cases} \quad (5.18)$$

where  $T_0$ ,  $T_e$ ,  $c_{s0}$ ,  $c_{se}$ ,  $v_A$  and  $u_e$  are all constants.

### 5.3.1 Region with Magnetic Field

Using Eq. (5.12) and inserting background equilibrium of the upper region ( $z > 0$ ) into this returns a second-order homogeneous ODE:

$$\frac{d^2 \widehat{\xi}_z(z)}{dz^2} - \frac{1}{H_B} \frac{d \widehat{\xi}_z(z)}{dz} + A_B \widehat{\xi}_z(z) = 0, \quad z > 0, \quad (5.19)$$

where

$$A_B = \frac{(\Gamma - 1)g^2 k_x^2 + (\omega^2 - k_x^2 c_{s0}^2)(\omega^2 - k_x^2 v_A^2)}{(c_{s0}^2 + v_A^2)(\omega^2 - k_x^2 c_T^2)}. \quad (5.20)$$

Eq. (5.19) has constant coefficients and possesses the general solution:

$$\widehat{\xi}_z(z) = d_1 e^{\left(\frac{1}{2H_B} + M_0\right)z} + d_2 e^{\left(\frac{1}{2H_B} - M_0\right)z}, \quad z > 0, \quad (5.21)$$

where

$$M_0 = \frac{\sqrt{1 - 4A_B H_B^2}}{2H_B}, \quad (5.22)$$

and  $d_1$  and  $d_2$  are arbitrary constants.

### 5.3.2 Non-Magnetic Region with Background Flow

Using background equilibrium quantities in the lower region ( $z < 0$ ) with the bulk flow and inserting these into Eq. (5.12) gives the following second-order homogeneous ODE

$$\frac{d^2 \widehat{\xi}_z(z)}{dz^2} - \frac{1}{H_e} \frac{d \widehat{\xi}_z(z)}{dz} + A_e \widehat{\xi}_z(z) = 0, \quad z < 0, \quad (5.23)$$

where

$$A_e = \frac{(\gamma - 1)g^2 k_x^2 + \Omega^2(\Omega^2 - k_x^2 c_{se}^2)}{\Omega^2 c_{se}^2}, \quad (5.24)$$

with

$$\Omega = \omega - k_x u_e. \quad (5.25)$$

Equation (5.23) possesses the general solution

$$\widehat{\xi}_z(z) = d_3 \exp\left(\frac{1}{2H_e} + M_e\right)z + d_4 \exp\left(\frac{1}{2H_e} - M_e\right)z, \quad z < 0, \quad (5.26)$$

where

$$M_e = \frac{\sqrt{1 - 4A_e H_e^2}}{2H_e}, \quad (5.27)$$

and  $d_3$  and  $d_4$  are arbitrary constants.

## 5.4 Deriving Dispersion Relation

There are four solutions to Eqs. (5.19) and (5.23), given by Eqs. (5.21) and (5.26), therefore there are four unknown constant of integration:  $d_1$ ,  $d_2$ ,  $d_3$ , and  $d_4$ . This requires four *physical* boundary conditions, needed to derive a dispersion relation for this model and eliminate the constants.

The first two of these boundary conditions are that the total of the kinetic [ $\rho(z)\widehat{v}_z^2(z)$ ] and magnetic [ $B_0(z)B'_0(z)\widehat{v}_z(z) + B_0^2(z)d\widehat{v}_z(z)/dz$ ] energy density remains finite as  $|z| \rightarrow \infty$ . It is also assumed that the conditions  $4A_B H_B^2 < 1$  and  $4A_e H_e^2 < 1$  are held so that only MAG surface waves are studied here, as  $M_0$  and  $M_e$  are then both real and the eigenfunctions do not oscillate in space, this will be discussed in more detail in Section 5.5.1. Here,

$$\widehat{v}_{1z}(z) = \frac{i\widehat{\xi}_z(z)}{\Omega(z)}. \quad (5.28)$$

Application of these boundary conditions reveal that for physically meaningful solutions,  $d_1 = d_4 = 0$ . The eigenfunction,  $\widehat{\xi}_z(z)$  can then be written for the upper and lower plasma regions as

$$\widehat{\xi}_z(z) = \begin{cases} d_2 \exp\left(\frac{1}{2H_B} - M_0\right)z, & z > 0, \\ d_3 \exp\left(\frac{1}{2H_e} + M_e\right)z, & z < 0. \end{cases} \quad (5.29)$$

It is simple to see from Eq. (5.29) that  $\widehat{\xi}_z(z) \rightarrow 0$  as  $z \rightarrow -\infty$ . However, for  $z > 0$   $\widehat{\xi}_z(z)$  is exponentially decreasing with height only if  $A_B < 0$  (Eq. 5.22) and is otherwise exponentially increasing with height. The total kinetic and magnetic energy density still remains finite, even for this case.

The remaining solutions must be connected across the interface at  $z = 0$ , this requires two extra boundary conditions. The first is the continuity of the Lagrangian displacement across the interface. The second is the continuity of the total (gas plus magnetic) Lagrangian pressure perturbation across the interface at  $z = 0$ :

$$\left\{\widehat{\xi}_z(z)\right\}_{z=0} = 0, \quad (5.30)$$

$$\left\{\widehat{p}_{T1}(z) - \rho(z)g\widehat{\xi}_z(z)\right\}_{z=0} = 0, \quad (5.31)$$

where

$$\begin{aligned} \widehat{p}_{T1}(z) = & -\rho(z) \frac{(c_s^2(z) + v_A^2(z))(\Omega^2(z) - k_x^2 c_T^2(z))}{\Omega^2(z) - k_x^2 c_s^2(z)} \frac{d\widehat{\xi}_z(z)}{dz} \\ & + \frac{\Omega^2(z)g\rho(z)}{\Omega^2(z) - k_x^2 c_s^2(z)} \widehat{\xi}_z(z), \end{aligned} \quad (5.32)$$

is the Eulerian perturbation of total pressure. The two boundary conditions, Eqs. (5.30) and (5.31), are applied to the solutions given by Eq. (5.29). This results in the dispersion relation:

$$\begin{aligned} & \frac{\rho_0(c_{s0}^2 + v_A^2)(\omega^2 - c_T^2 k_x^2)}{\omega^2 - c_{s0}^2 k_x^2} \left( M_0 - \frac{1}{2H_B} \right) + \frac{\rho_0 g k_x^2 c_{s0}^2}{\omega^2 - c_{s0}^2 k_x^2} \\ & = \frac{\rho_e c_{se}^2}{\Omega^2 - c_{se}^2 k_x^2} \left[ g k_x^2 - \left( \frac{1}{2H_e} + M_e \right) \Omega^2 \right], \end{aligned} \quad (5.33)$$

where  $c_T = c_{s0} v_A / (c_{s0}^2 + v_A^2)^{1/2}$  is the tube speed in the magnetic atmosphere. Eq. (5.33) governs the parallel (to magnetic field) propagation of MAG surface waves at a magnetic interface in a gravitationally stratified atmosphere, with an upper isothermal magnetic region and a lower non-magnetic isothermal region moving under a constant bulk motion.

#### 5.4.1 Incompressible Limit

To explore the effect of the flow on the surface waves given by Eq. (5.33) we take the incompressible limit of the dispersion relation. To illuminate the derivation of the incompressible limit, Eq. (5.33) can be written in a form similar to that found in Miles and Roberts (1992):

$$\begin{aligned} \frac{\omega^2}{k_x^2} &= \frac{\rho_0}{\rho_0 + \rho_e} \frac{(M_e + 1/2H_e) m_0}{(M_0 - 1/2H_B) m_e} v_A^2 \\ & \quad - \frac{\frac{\rho_0 c_{s0}^2}{(\omega^2 - c_{s0}^2 k_x^2)} - \frac{\rho_e c_{se}^2}{(\Omega^2 - c_{se}^2 k_x^2)}}{\rho_0 \frac{(M_0 - 1/2H_B)}{m_0} + \rho_e \frac{(M_e + 1/2H_e)}{m_e}}, \end{aligned} \quad (5.34)$$

where

$$m_0 = \frac{(\omega^2 - v_A^2 k_x^2) (\omega^2 - c_{s0}^2 k_x^2)}{(c_{s0}^2 + v_A^2) (\omega^2 - c_T^2 k_x^2)}, \quad (5.35)$$

and

$$m_e = \frac{(\Omega^2 - c_{se}^2 k_x^2) \omega^2}{c_{se}^2 \Omega^2}. \quad (5.36)$$

The incompressible limit of Eq. (5.34) is taken, in which we assume that the sound speeds in both regions tend to infinity compared to the phase speed ( $\omega/k_x$ ) of the waves i.e.  $c_{se}, c_{s0} \rightarrow \infty$ . For further analytic progress it is assumed that  $\rho_0(z) = \rho_0$  and  $\rho_e(z) = \rho_e$ . Therefore  $m_e \rightarrow -k_x^2 \omega^2 / \Omega^2$ ,  $m_0 \rightarrow -k_x^2$  and  $M_e, M_0 \rightarrow k_x$ . Eq. (5.34)

then reduces to the following second order polynomial for the phase speed,  $\omega/k_x$ :

$$\left(\frac{\omega}{k_x}\right)^2 - \frac{2u_e}{1+\rho_r} \frac{\omega}{k_x} + \left(\frac{u_e^2}{1+\rho_r} - \frac{v_A^2 \rho_r}{1+\rho_r} + \frac{g}{k_x} \left(\frac{1-\rho_r}{1+\rho_r}\right)\right) = 0. \quad (5.37)$$

Here,  $\rho_r = \rho_0/\rho_e$ . When we solve Equation (5.37), the solution for the phase speed can be written as

$$\frac{\omega}{k_x} = \frac{u_e}{1+\rho_r} \left[ 1 \pm \left\{ \rho_r \left( \frac{(1+\rho_r) \left( v_A^2 \rho_r + \frac{g}{k_x} (1-\rho_r) \right)}{\rho_r u_e^2} - 1 \right) \right\}^{1/2} \right]. \quad (5.38)$$

Immediately, it is evident from Eq. (5.38) that, when the quantity within the square root is less than zero, there is a damped wave as well as an amplified wave. This can be written in the form of an inequality,

$$(1+\rho_r) \left( v_A^2 + \frac{g}{k_x} \frac{(1-\rho_r)}{\rho_r} \right) < u_e^2. \quad (5.39)$$

The critical wave number (denoted  $k_c$ ) for the Kelvin-Helmholtz instability is given by

$$k_c = \frac{(1-\rho_r)(1+\rho_r)g}{\rho_r (u_e^2 - v_A^2(1+\rho_r))}. \quad (5.40)$$

The Rayleigh-Taylor instability is not studied here, the density of the upper plasma,  $\rho_0$ , is lower than the density in the lower plasma,  $\rho_e$ , so that  $k_c$  is always a positive number. We can conclude from Eq. (5.39) that the presence of gravity acts to increase the threshold for the Kelvin-Helmholtz instability. We introduce the following notation

$$\bar{k} = \frac{k_x v_A^2}{g}, \quad \bar{u}_e = \frac{u_e}{v_A}. \quad (5.41)$$

Here,  $\bar{k}$  is a dimensionless wave number and  $\bar{u}_e$  is the dimensionless flow speed. The critical flow speed,  $u_{e,c}$ , is when Eq. (5.39) is taken as an equality. Fig. 5.2 plots the variation  $\bar{u}_{e,c}$  against  $\bar{k}$ . It is immediately evident from Fig. 5.2 that as  $\bar{k}$  increases  $u_{e,c}$  decreases, although this reaches a limit as  $\bar{k} \rightarrow \infty$ , which is essentially the limit of zero gravity. The limit taking  $\bar{k} \rightarrow 0$  results in  $\bar{u}_{e,c} \rightarrow \infty$ . There are two separate effects of increasing  $\rho_r$ . The first is for small  $\bar{k}$  where the increase appears to decrease  $\bar{u}_{e,c}$ . However, the second effect is for large  $\bar{k}$ . The increase of  $\rho_r$  increases  $\bar{u}_{e,c}$ .

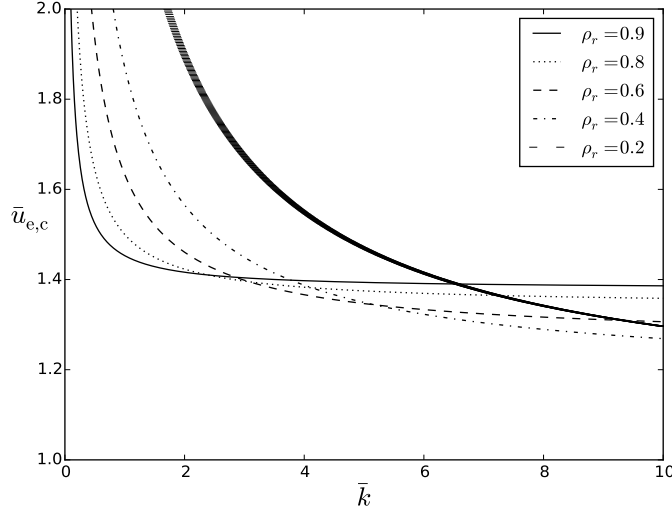


Fig. 5.2 Variation of the dimensionless critical flow speed,  $\bar{u}_{e,c}$ , with respect to the dimensionless wave number,  $\bar{k}$ .

#### 5.4.2 Small Wavelength ( $k_x H_e \rightarrow \infty$ ) and Cold Plasma ( $\beta = 0$ ) Limit

We take the limit as  $k_x H_e \rightarrow \infty$  of Equation (5.33). This reduces to the following equation:

$$\rho_r^2 \frac{(\omega^2 - k_x^2 v_A^2)(\omega^2 - k_x^2 c_T^2)(c_{s0}^2 + v_A^2)}{\omega^2 - k_x^2 c_{s0}^2} = \frac{\Omega^4}{\Omega^2 - k_x^2 c_{se}^2}. \quad (5.42)$$

We note that Eq. (5.42) may have spurious roots as it is derived by squaring terms. Clearly, Eq. (5.42) is still insoluble, as it is essentially a sixth order polynomial that has no analytic solution. Therefore, for further analytic progress the *cold plasma* limit ( $\beta = 0$ ) is taken. This is equivalent to setting  $c_{s0} = 0$  in Eq. (5.42) and so the slow surface mode is not present in this limit and only the fast surface mode can be studied. Eq. (5.42) then reduces to the following fourth-order polynomial in  $\widehat{\Omega}$ :

$$\begin{aligned} \widehat{\Omega}^4 \left(1 - \frac{2\rho_r}{\gamma}\right) - \frac{4\rho_r \widehat{u}_e}{\gamma} \widehat{\Omega}^3 - \widehat{\Omega}^2 \left(\frac{2\rho_r}{\gamma} \widehat{u}_e^2 - \frac{4}{\gamma^2} - \frac{2\rho_r}{\gamma}\right) \\ + \frac{4\rho_r \widehat{u}_e}{\gamma} \widehat{\Omega} + \left(\frac{2\rho_r \widehat{u}_e^2}{\gamma} - \frac{4}{\gamma^2}\right) = 0. \end{aligned} \quad (5.43)$$

Here, we have introduced the two following dimensionless quantities

$$\widehat{\Omega} = \frac{\Omega}{k_x c_{se}}, \quad \widehat{u}_e = \frac{u_e}{c_{se}}. \quad (5.44)$$

Due to background pressure balance, along with the cold plasma approximation (where essentially  $p_0 = 0$ ) the following relation is found:  $v_A^2 = 2c_{se}^2/\rho_r\gamma$ . Eq. (5.43) is a fourth-order polynomial and does possess a completely analytic solution. However these solutions are large and unwieldy and we therefore opt to use a perturbation method to find approximate solutions to it. The two approximations are:

1. the limit of small flow *i.e.*  $\widehat{u}_e = \epsilon$ , where  $\epsilon \ll 1$ ;
2. a large discontinuity in density *i.e.*  $\rho_r = \epsilon$ , where  $\epsilon \ll 1$ .

#### 5.4.2.1 Limit of Small Flow

In this limit, we assume a regular perturbation series for  $\widehat{\Omega}$  of the form (with  $\widehat{u}_e = \epsilon$ )

$$\widehat{\Omega} = \widehat{\Omega}_0 + \epsilon\widehat{\Omega}_1 + \dots \quad (5.45)$$

Inserting this approximation into Eq. (5.43) we obtain for the order  $\epsilon^0$  balance:

$$\widehat{\Omega}_0^4 \left(1 - \frac{2\rho_r}{\gamma}\right) + \widehat{\Omega}_0^2 \left(\frac{4}{\gamma^2} + \frac{2\rho_r}{\gamma}\right) - \frac{4}{\gamma^2} = 0. \quad (5.46)$$

The balance for  $\epsilon^1$  gives the following equation:

$$\widehat{\Omega}_1 = \frac{\rho_r (\widehat{\Omega}_0^2 - 1)}{\gamma \left( \widehat{\Omega}_0^2 \left(1 - \frac{2\rho_r}{\gamma}\right) + \frac{2}{\gamma^2} + \frac{\rho_r}{\gamma^2} \right)}. \quad (5.47)$$

Eq. (5.46) is a quadratic in  $\widehat{\Omega}_0^2$  and can thus be easily solved by conventional means to obtain a solution for  $\widehat{\Omega}_0$

$$\widehat{\Omega}_0^2 = \frac{2 + \rho_r\gamma}{\gamma(2\rho_r - \gamma)} \left( 1 - \left( 1 + \frac{4\gamma(\gamma - 2\rho_r)}{(2 + \rho_r\gamma)^2} \right)^{1/2} \right). \quad (5.48)$$

In general, there should be four solutions to a fourth order polynomial, two of the solutions have been discarded as they are purely imaginary and have been introduced by squaring the dispersion relation. The frequency is then approximated as

$$\frac{\omega}{k_x c_{se}} = \pm \widehat{\Omega}_0 + \frac{u_e}{c_{se}} \frac{\gamma (\widehat{\Omega}_0^2 (\gamma - \rho_r) + \rho_r)}{((\gamma\rho_r - 2)^2 + 4\gamma^2)^{1/2}} + O(\widehat{u}_e^2), \quad (5.49)$$

Equation (5.49) must satisfy the following conditions for surface waves to exist:

$$(1) \quad \omega^2 < k_x^2 v_A^2, \quad (2) \quad \Omega^2 < k_x^2 c_{se}^2.$$

Since there is gravity in the system, the density ratio is constrained between the values of zero and one, *i.e.*  $0 \leq \rho_r \leq 1$ , so that we do not study the Rayleigh-Taylor instability. We, therefore, have a minimum value of the Alfvén speed  $v_A^2 = 2c_{se}^2/\gamma$ . Therefore  $v_A > c_{se}$  (taking the value of the adiabatic index,  $\gamma$ , to be 5/3), and therefore we only need to fulfil condition (2) above when  $u_e = 0$ . We find that solutions do not exist for  $\widehat{\Omega}_0^2 = 1$  (*i.e.*  $\Omega^2 = k_x^2 c_{se}^2$ ) and that the function  $\widehat{\Omega}_0^2(\rho_r)$ , from Equation (5.48), is continuous (this is confirmed by considering the Taylor expansion around the point  $\gamma - 2\rho_r = 0$ ). If a value for  $\widehat{\Omega}_0^2$  can be found that is lower than one, then all values of  $\widehat{\Omega}_0^2$  must be lower than one. In the limit  $\rho_r \rightarrow 0$ ,

$$\begin{aligned} \widehat{\Omega}_0^2 &= -\frac{2}{\gamma^2} \left(1 - (1 + \gamma^2)^{1/2}\right) \\ &\approx 0.68. \end{aligned} \tag{5.50}$$

Therefore  $\Omega^2 < k_x^2 c_{se}^2$  and surface waves exist in this limit, and therefore surface waves must exist everywhere for  $\widehat{u}_e = 0$ . As is expected, Eq. (5.50) agrees with the work of Roberts (1981a) in which MA surface waves were studied with  $v_A \gg c_{se}, c_{s0}$  and no background flow, which is the situation here as:  $k_x H_e \rightarrow \infty$ , we study the cold plasma approximation ( $v_A \gg c_{s0}$ ),  $\rho_r \rightarrow 0$  ( $v_A \gg c_{se}$ ) and to zeroth order there is no background flow.

Eq. (5.48) shows that  $\widehat{\Omega}_0$  is a function of  $\rho_r$ . We find that the derivative of  $\widehat{\Omega}(\rho_r)$  with respect to  $\rho_r$  is negative when  $\rho_r = 0$ . We also find that there are no turning points of this function. Therefore, the dimensionless frequency is bounded above by 0.86 at  $\rho_r = 0$ , so that the phase speed of the wave is at most 0.82 times the sound speed in the lower layer,  $c_{se}$ .

The upper panel of Fig. 5.3 plots the dimensionless frequencies for the backward propagating waves, given by Eq. (5.49), as  $\rho_r$  varies. The lower panel shows the dimensionless frequency shift,  $\Delta\omega/k_x u_e$ , computed from Eq. (5.47). The upper panel is plotted for dimensionless flow speeds of  $\widehat{u}_e = 0.0, 0.01, \text{ and } 0.1$ . One can see from the upper panel that increasing the dimensionless flow speed increases the frequency shift. The lower panel shows that the frequency shift is largest for  $\rho_r = 1$ . We therefore conclude that, the closer the densities, the larger the frequency shift is when flow is present.

#### 5.4.2.2 Limit of Small Density Ratio

In the limit of a small density ratio, we now take as the small parameter,  $\epsilon = \rho_r$ , where  $\epsilon \ll 1$ . We, again, use the perturbations series of the form

$$\widehat{\Omega} = \widehat{\Omega}_0 + \epsilon \widehat{\Omega}_1 + \dots \tag{5.51}$$

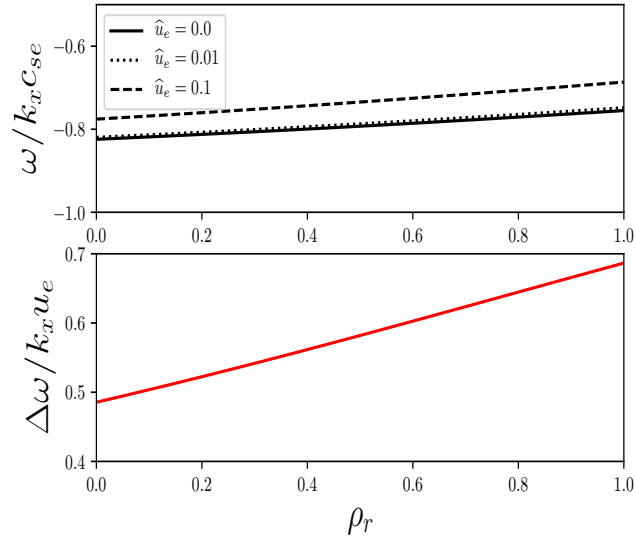


Fig. 5.3 Upper panel: the dimensionless frequency,  $\omega/k_x c_{se}$  computed from Eq. (5.49) varying with respect to the density ratio  $\rho_r$ . Lower panel: the dimensionless frequency shift,  $\Delta\omega/k_x u_e$ , computed from Eq. (5.47), varying with respect to  $\rho_r$  once again. The legend indicates the solutions that correspond to the values  $\hat{u}_e = 0.0, 0.01,$  and  $0.1$ . The adiabatic index,  $\gamma$ , is taken to be  $5/3$ .

If this approximation is inserted into Eq. (5.43) and powers of  $\epsilon$  are collected, we have for the  $\epsilon^0$  balance the equation

$$\widehat{\Omega}_0^4 + \widehat{\Omega}_0^2 \frac{4}{\gamma^2} - \frac{4}{\gamma^2} = 0. \quad (5.52)$$

Eq. (5.52) is a quadratic in  $\widehat{\Omega}_0^2$  and can be solved easily with solutions given by

$$\widehat{\Omega}_0^2 = \frac{2 \left( -1 \pm (1 + \gamma^2)^{1/2} \right)}{\gamma^2}. \quad (5.53)$$

It is interesting to note that this equation agrees with that derived by Roberts (1981a) for  $v_A \gg c_{s0}, c_{se}$  which is in essence the cold plasma approximation here with a low density ratio. In that paper the frequency was derived for surface waves at a magnetic interface, without stratification or flow. Here, we take the limit of Eq. (5.33) as  $k_x H_e \rightarrow \infty$ , which is equivalent to approximating that there is no gravitational force, as the wavelengths of the waves are small compared to the change in background quantities, meaning that the stratification has little effect on the waves. Therefore, the case considered here and the one considered in Roberts (1981a) are the same and thus it is natural they produce the same answer.

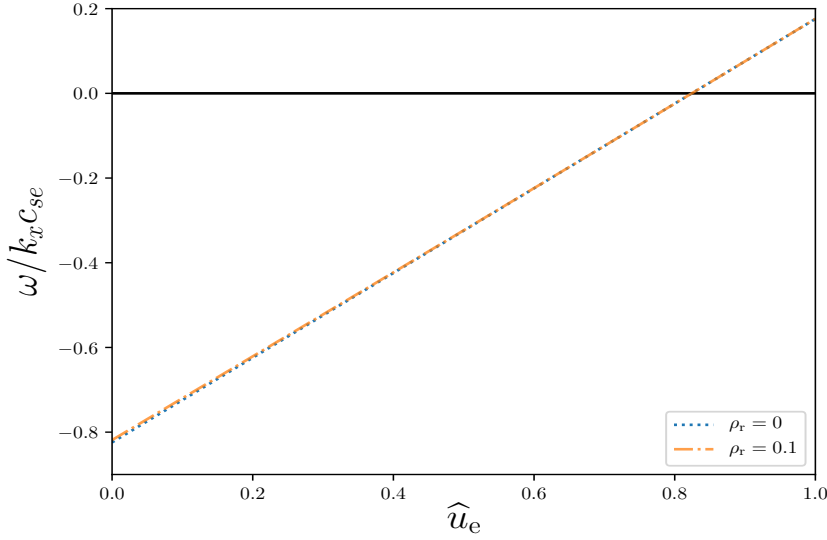


Fig. 5.4 Variation of the dimensionless frequency,  $\omega/k_x c_{se}$ , against dimensionless flow speed,  $\hat{u}_e$ , for the backward-propagating solution for  $\rho_r = 0$  (blue dotted line) and 0.1 (orange dash-dotted line).

The balance for the next order term ( $\epsilon^1$ ) results in the following equation:

$$\hat{\Omega}_1 = \frac{(\hat{\Omega}_0^2 - 1)(\hat{\Omega}_0 + \hat{u}_e)^2}{2\hat{\Omega}_0(2\hat{\Omega}_0^2 + \rho_r^2 \hat{v}_A^4)}. \quad (5.54)$$

Using both Eqs. (5.53) and (5.54) the dimensionless frequency can be written as

$$\frac{\omega}{k_x c_{se}} = (\pm \hat{\Omega}_0 + \hat{u}_e) \left( 1 \pm \rho_r \frac{\gamma(\hat{\Omega}_0^2 - 1)(\pm \hat{\Omega}_0 + \hat{u}_e)}{4\hat{\Omega}_0(\pm(1 + \gamma^2)^{1/2})} \right). \quad (5.55)$$

Eq. (5.55) shows that the change in frequency is due overwhelmingly to the change in the flow speed and increases linearly with an increase in flow. Considering the zeroth order solution,  $\hat{\Omega}_0$ , which is the Doppler shifted frequency, we find that

$$\hat{\Omega}_0^2 \approx 0.68, \quad (5.56)$$

and thus the surface wave condition  $\hat{\Omega} < 1$  is satisfied in the zeroth order approximation. Now the other condition is that  $\omega^2 < k_x v_A^2$ . This is always satisfied because as  $\rho_r \rightarrow 0$ ,  $v_A/c_{se} \rightarrow \infty$  and to zeroth order  $\omega/k_x c_{se} \approx \pm 0.82 + \hat{u}_e$  which, unless the flow speed is of the order of the Alfvén speed, will satisfy the surface wave condition.

Fig. 5.4 plots the variation of the dimensionless frequency,  $\omega/k_x c_{se}$  for the backward propagating solutions given by Eq. (5.55) for  $\rho_r = 0$  and 0.1. Clearly there is a linear increase in  $\omega/k_x c_{se}$  with respect to  $\hat{u}_e$ . The gradient is unaffected

by a small increase in  $\rho_r$ . If the flow is greater than the phase speed of the wave in the static atmosphere, the direction of propagation is switched and the oscillation transitions from a backward to a forward propagating wave.

## 5.5 Numerical Solution of the Dispersion Relation

### 5.5.1 Cut off Curves

The dispersion relation, Equation (5.33) is to be solved subject to the constraints that  $\omega \neq \pm k_x c_{s0}$ ,  $\omega \neq k_x(u_e \pm c_{se})$  and that

$$1 - 4A_B H_B^2 > 0 \quad \text{and} \quad 1 - 4A_e H_e^2 > 0. \quad (5.57)$$

These two latter constraints are required for surface wave solutions, *i.e.* evanescent (non-propagating) modes in the  $z$  direction. This means that in the  $\omega - k_x$  plane these constraints (where both are fulfilled) determine those permitted regions of the  $(\omega, k_x)$  parameter space of propagation where magnetoacoustic-gravity surface modes given by Equation (5.33) may propagate. The boundary curves to these regions represent cut-off curves (cut-off frequencies) for the modes. Outside these regions, where either  $(1 - 4A_B H_B^2)$  or  $(1 - 4A_e H_e^2)$  is negative, spatially oscillating leaky-modes arise in which we are not interested.

The condition  $1 - 4A_e H_e^2 > 0$  gives rise to the cut-off curves  $R_1, R_2, R_3$  and  $R_4$  given by

$$R_{1,2} = u_e/c_{se} + P_{1,2}, \quad R_{3,4} = u_e/c_{se} - P_{2,1}, \quad (5.58)$$

where

$$P_{1,2}^2 = \frac{1 + 4k_x^2 H_e^2 \mp \sqrt{(1 + 4k_x^2 H_e^2)^2 - 64 \frac{\gamma-1}{\gamma^2} k_x^2 H_e^2}}{8k_x^2 H_e^2}. \quad (5.59)$$

We note that  $P_2 > P_1 > 0$ . The regions where  $1 - 4A_e H_e^2 > 0$  is satisfied are defined by either

$$R_1 < \frac{\omega}{k_x c_{se}} < R_2 \quad (5.60)$$

or

$$R_3 < \frac{\omega}{k_x c_{se}} < R_4. \quad (5.61)$$

The other condition,  $1 - 4A_B H_B^2 > 0$ , generates the cut-off curves  $R_5, R_6$ , which satisfy the equation

$$\frac{4 \frac{c_{s0}^4}{c_{se}^4}}{\Gamma^2} \left[ \frac{\Gamma - 1 + \gamma^2 k_x^2 H_e^2 \left( R_{5,6}^2 - \frac{c_{s0}^2}{c_{se}^2} \right) \left( R_{5,6}^2 - \frac{v_A^2}{c_{se}^2} \right)}{\left( \frac{c_{s0}^2}{c_{se}^2} + \frac{v_A^2}{c_{se}^2} \right) \left( R_{5,6}^2 - \frac{c_T^2}{c_{se}^2} \right)} \right] = 1, \quad (5.62)$$

(note that  $R_6 > R_5 > 0$ ) and the regions where  $1 - 4A_B H_B^2 > 0$  is met are either

$$R_6 < \frac{\omega}{k_x c_{se}} < \frac{c_T}{c_{se}}, \quad (5.63)$$

$$-\frac{c_T}{c_{se}} < \frac{\omega}{k_x c_{se}} < -R_6, \quad (5.64)$$

$$\max\left(-\frac{c_T}{c_{se}}, -R_5\right) < \frac{\omega}{k_x c_{se}} < \min\left(\frac{c_T}{c_{se}}, R_5\right), \quad (5.65)$$

$$\max\left(\frac{c_T}{c_{se}}, R_5\right) < \frac{\omega}{k_x c_{se}} < R_6, \quad (5.66)$$

or

$$-R_6 < \frac{\omega}{k_x c_{se}} < \min\left(-\frac{c_T}{c_{se}}, -R_5\right). \quad (5.67)$$

We note that both positive and negative phase speed ( $\omega/k_x$ ) solutions of the dispersion relation are allowed. Now, considering the phase speed regions determined by Equations (5.60)-(5.61) and (5.63)-(5.67), we can easily deduce the permitted regions where the two constraints written in Equation (5.57) are fulfilled.

In the limit  $k_x H_e \rightarrow \infty$  (which is equivalent to  $g \rightarrow 0$ ), we obtain

$$R_1 \rightarrow \frac{u_e}{c_{se}}, \quad R_2 \rightarrow \frac{u_e}{c_{se}} + 1, \quad (5.68)$$

$$R_3 \rightarrow \frac{u_e}{c_{se}} - 1, \quad R_4 \rightarrow \frac{u_e}{c_{se}}, \quad (5.69)$$

$$R_5 \rightarrow \min\left(\frac{c_{s0}}{c_{se}}, \frac{v_A}{c_{se}}\right), \quad R_6 \rightarrow \max\left(\frac{c_{s0}}{c_{se}}, \frac{v_A}{c_{se}}\right). \quad (5.70)$$

The cut-off curves are illustrated in the next section.

## 5.5.2 Numerical Results

We now solve the dispersion relation, Eq. (5.33), numerically and study the modes that are found. The goal is to examine the results of increasing the background flow,  $u_e$ , on the surface modes.

A magnetic interface may support one or two surface modes, when it is static and gravity is neglected (depending on the relative strengths of the magnetic fields and the temperatures on either side). These modes are the slow and fast MA surface waves (Roberts, 1981a). The fast mode only occurs when both  $v_A > c_{s0}$  and  $c_{se} > c_{s0}$  (*i.e.* the field-free region is hotter than the magnetic region). Both the slow and fast waves have sub Alfvénic phase speeds if these conditions are met.

When gravity is included in the system, MAG surface modes arise. They are the modification of the fast and slow MA surface waves by gravity (see e.g. Miles and Roberts, 1992). However when the upper, magnetic region is cooler than the lower

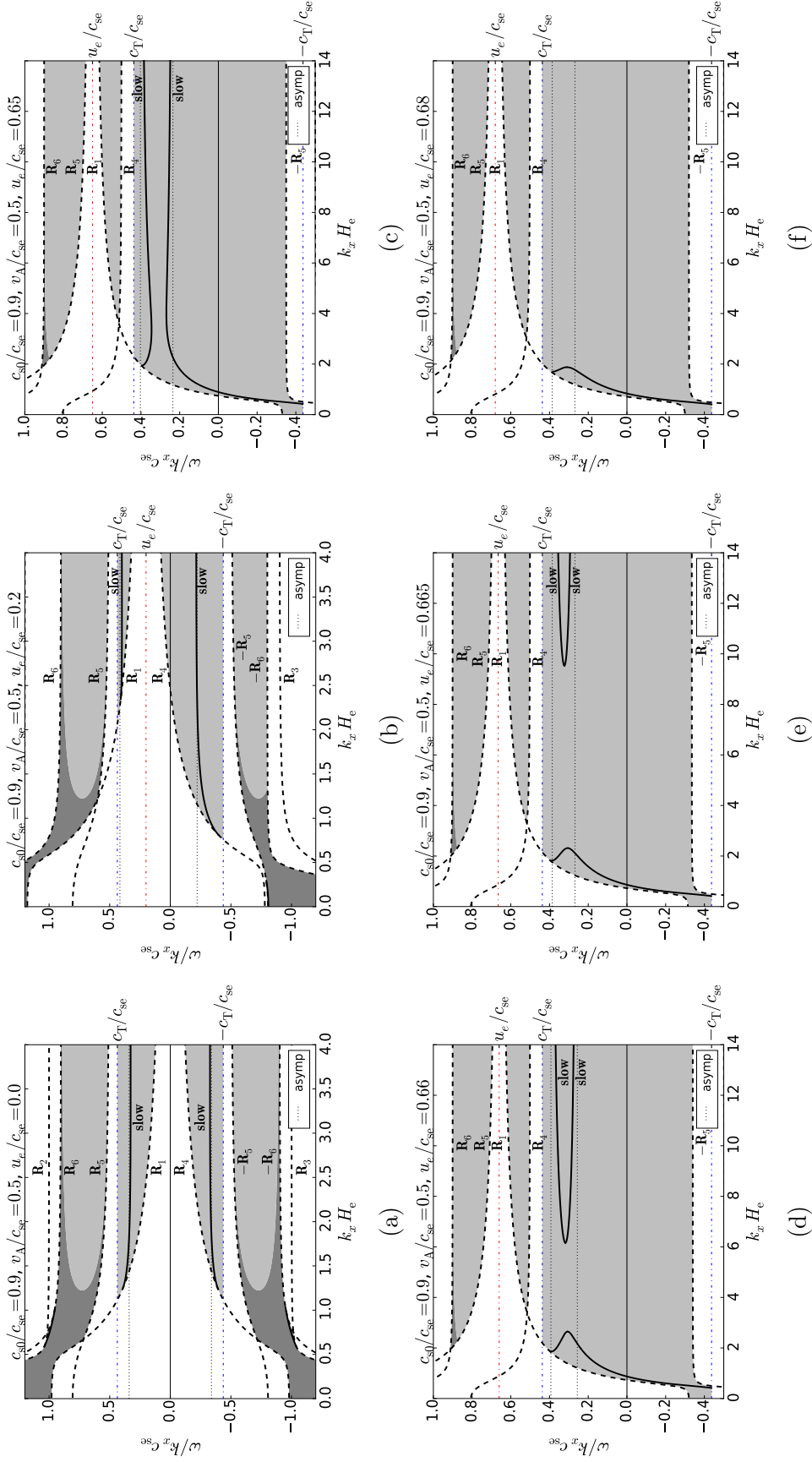


Fig. 5.5 The dimensionless phase speed of MAG surface waves as a function of the dimensionless horizontal wavenumber for  $c_{s0}/c_{se} = 0.9$ ,  $v_A/c_{se} = 0.5$  and (a)  $u_e/c_{se} = 0.0$ , (b)  $u_e/c_{se} = 0.2$ , (c)  $u_e/c_{se} = 0.65$ , (d)  $u_e/c_{se} = 0.66$ , (e)  $u_e/c_{se} = 0.665$ , (f)  $u_e/c_{se} = 0.68$ . The grey regions bounded by the cutoff curves  $R_1, R_2, R_3, R_4, R_5, \pm R_6$ ,  $\pm R_6$ ,  $\pm R_6$  are regions where surface waves can propagate. Dark grey regions contain modes for which the vertical velocity component is exponentially growing with height in the  $z > 0$  region. In the light grey regions modes have decreasing vertical velocities with height  $z$ . The asymptotes to which the modes tend in the short-wavelength limit ( $k_x H_e \rightarrow \infty$ ) are shown as well.

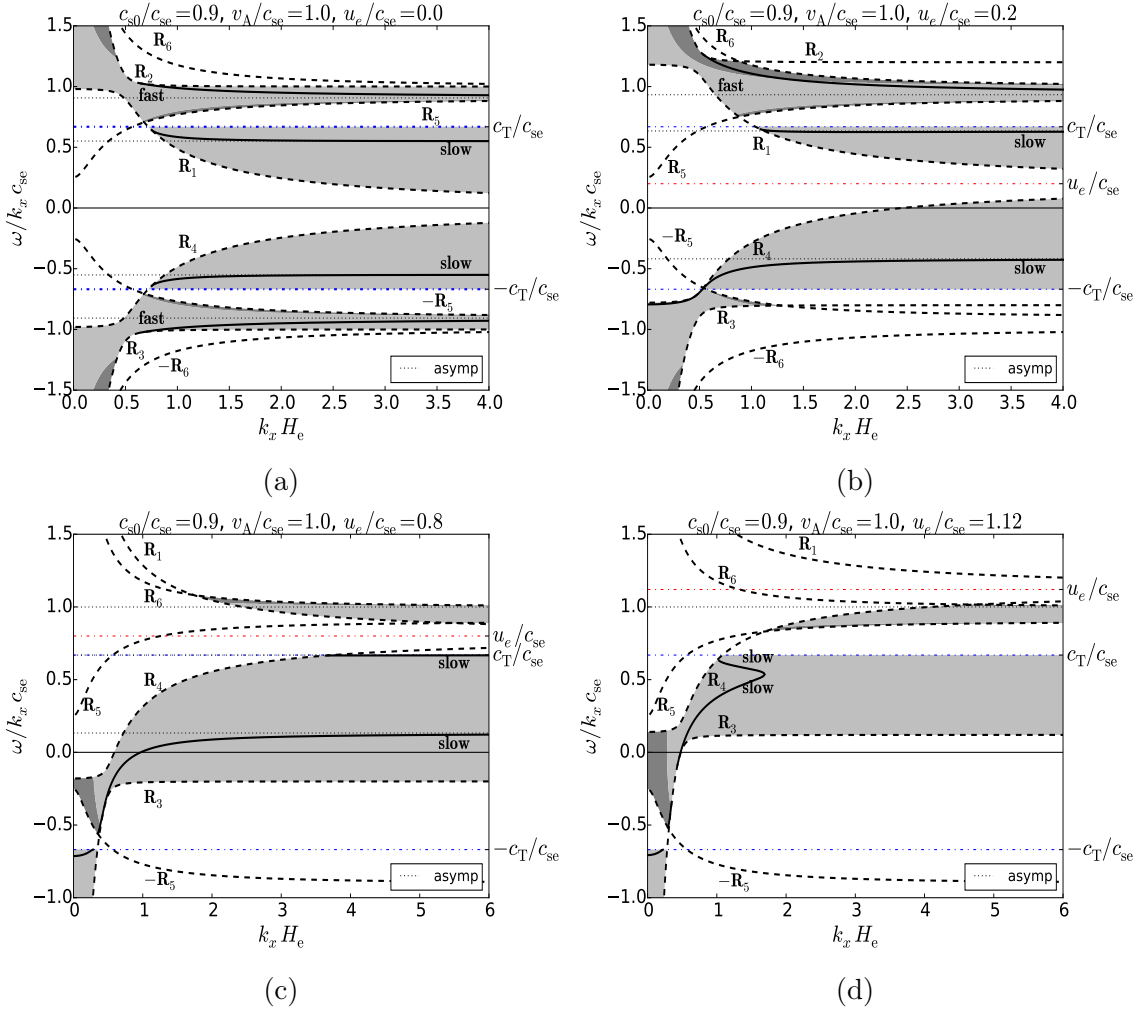


Fig. 5.6 The dimensionless phase speed of MAG surface waves versus dimensionless horizontal wavenumber for  $c_{s0}/c_{se} = 0.9$ ,  $v_A/c_{se} = 1.0$  and (a)  $u_e/c_{se} = 0.0$ , (b)  $u_e/c_{se} = 0.2$ , (c)  $u_e/c_{se} = 0.8$ , (d)  $u_e/c_{se} = 1.12$ . The permitted regions of propagation for surface waves are shaded grey. The effect of increasing flow on the fast and slow magnetoacoustic-gravity modes can be seen.

field free plasma, ( $c_{se} > c_{s0}$ ), the  $f$ -mode, modified by the magnetic field, may also propagate, although for a limited range of the dimensionless horizontal wave-number,  $k_x H_e$ . It was shown by Miles and Roberts (1992) that the  $f$ -mode becomes the fast mode as the strength of the magnetic field is increased. In addition, the fast MAG surface mode merges with the fast MA wave of the non-stratified ( $g = 0$ ) medium when  $k_x H_e \rightarrow \infty$  and  $v_A > c_{s0}$ . If the field-free region is cooler than the upper magnetic region, the  $f$ -mode is replaced by a surface gravity wave.

In what follows, we investigate the influence of increasing the background equilibrium flow on the modes considered above. We solve the dispersion relation, Eq. (5.33), numerically and plot the dimensionless horizontal phase speed,  $\omega/k_x c_{se}$ , as a function of the dimensionless horizontal wavenumber,  $k_x H_e$ . We set  $\gamma = 5/3$  throughout.

Figure 5.5 is plotted for  $c_{se} > c_{s0}$  (specifically  $c_{s0}/c_{se} = 0.9$ ), and  $v_A < c_{s0}$  (specifically  $v_A/c_{se} = 0.5$ ), for six different values of the dimensionless flow speed,

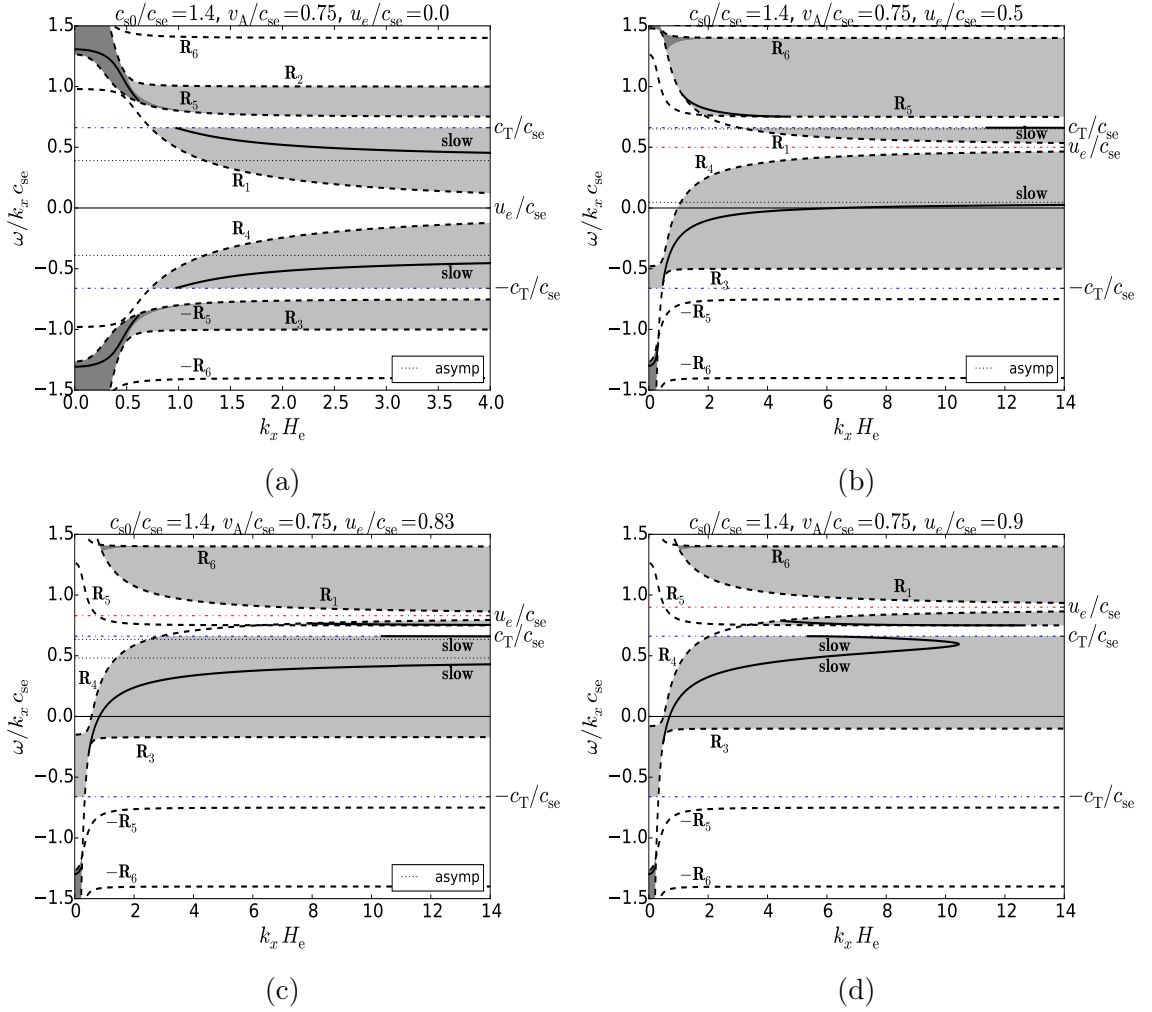


Fig. 5.7 The dimensionless phase speed of surface MAG waves as a function of the dimensionless horizontal wavenumber for  $c_{s0}/c_{se} = 1.4$ ,  $v_A/c_{se} = 0.75$  and (a)  $u_e/c_{se} = 0.0$ , (b)  $u_e/c_{se} = 0.5$ , (c)  $u_e/c_{se} = 0.83$ , (d)  $u_e/c_{se} = 0.9$ . The permitted regions of propagation for surface waves are shaded grey. The effect of increasing flow on the slow magnetoacoustic-gravity mode can be seen.

$u_e/c_{se}$ , ascending from zero (Figures 5.5a-f). The plasma-beta value is approximately 0.98, with a density ratio ( $\rho_0/\rho_e$ ) of 0.98. These parameters can approximate the temperature minimum region in the solar photosphere embedded in an overlying horizontal magnetic field (*e.g.* in the higher parts of the penumbra).

The permitted regions of propagation for surface modes (see Section 5.5.1) bounded by the cut-off curves  $R_1$ ,  $R_2$ ,  $R_3$ ,  $R_4$ ,  $\pm R_5$ , and  $\pm R_6$  (shown as dashed lines) are shaded grey. The dot-dashed line represents the curve  $A_B = 0$  (see Equation (5.20)) and divides the region of evanescence in the upper medium ( $z > 0$ ) into a region (shaded dark grey) where the vertical velocity component is exponentially growing with height,  $z$ , (here  $A_B > 0$ ), from a region (shaded light grey) where it decreases with height (here  $A_B < 0$ ). We note again that in the lower region,  $z < 0$ , the vertical velocity component always becomes smaller with height.

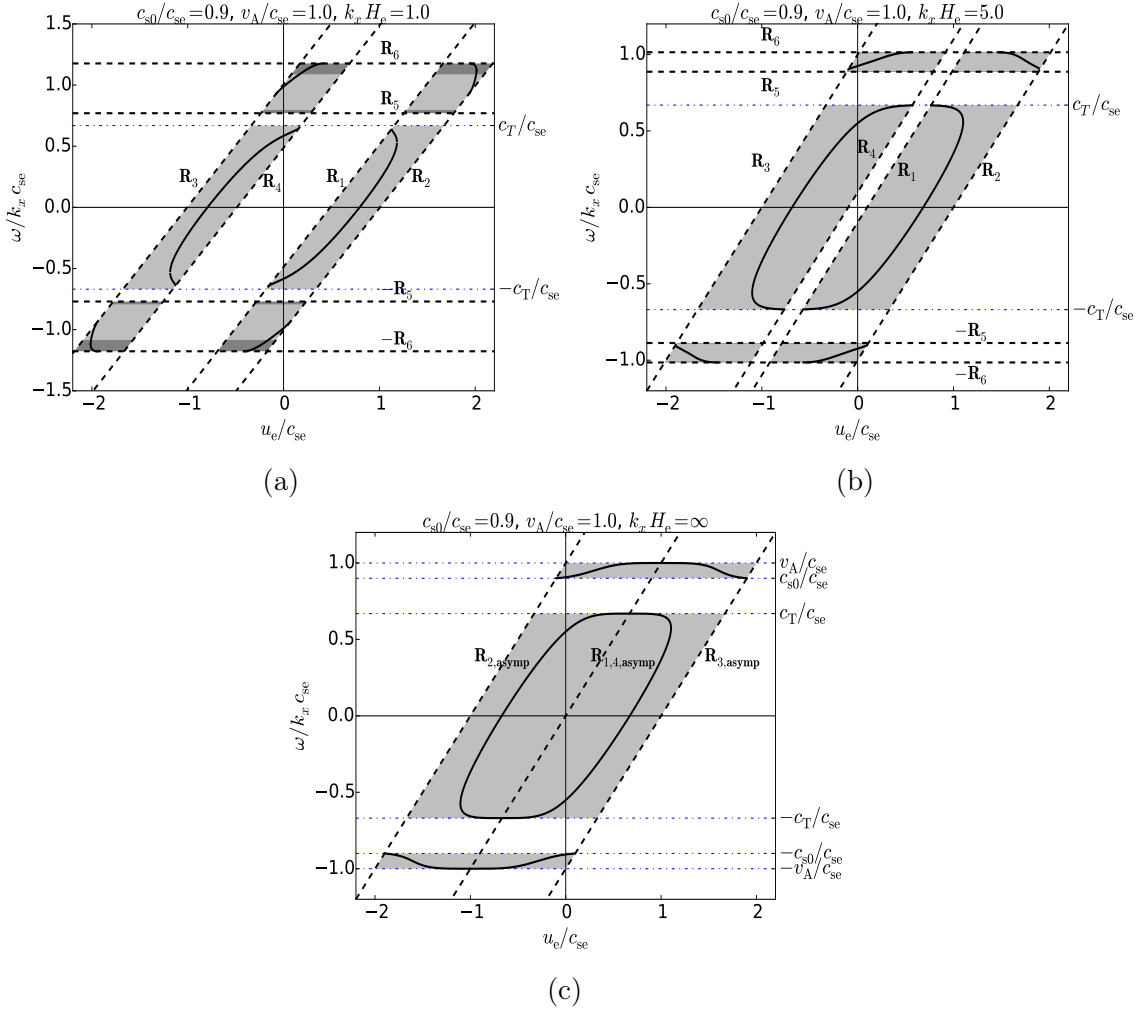


Fig. 5.8 The variation of the dimensionless phase speed of surface MAG waves as a function of the dimensionless flow velocity at a given wavenumber for  $c_{s0}/c_{se} = 0.9$ ,  $v_A/c_{se} = 1.0$ . Cases are: (a)  $k_x H_e = 1.0$ , (b)  $k_x H_e = 5.0$  and (c)  $k_x H_e = \infty$ . The permitted regions of propagation for surface waves are shaded grey. The effect of increasing the overall magnitude of the flow on the fast and slow magnetoacoustic-gravity modes can be seen. The modes shown here are the same fast and slow MAG surface modes as those displayed in Figure 5.6.

The dot-dashed horizontal lines in Figure 5.5 correspond to  $\omega = \pm k_x c_T$  and the dotted horizontal lines correspond to the asymptotes to which the MAG surface modes tend as  $k_x H_e \rightarrow \infty$ . The limit  $k_x H_e \rightarrow \infty$  is equivalent to  $g \rightarrow 0$ , where the asymptotes can be determined by solving the non-gravity dispersion relation that is obtained from the dispersion relation (5.33) in the limit of zero gravity.

We note that with the parameters chosen as  $c_{s0}/c_{se} = 0.9$  and  $v_A/c_{se} = 0.5$ , only the slow surface mode can propagate in the zero-gravity limit and therefore for large  $k_x H_e$ . Thus, in Figure 5.5a (which corresponds to the static background case) we show that the slow MAG mode (the fast mode is absent) is only present within the light grey region ( $A_B < 0$ ). At lower wave numbers (for a limited range of wave numbers) the  $f$ -mode (modified by the magnetic field) is visible. It lies entirely

within the dark grey region ( $A_B > 0$ ) and therefore has a growing vertical velocity in the upper medium ( $z > 0$ ).

Modes with negative phase speeds correspond to waves propagating in the opposite, backwards, direction. Here, in the static case, forward- (positive phase speed) and backward-propagating (negative phase speed) waves are symmetrical counterparts to the  $\omega/(k_x c_{se}) = 0$  axis. In the remaining figures, we examine the effect of increasing the equilibrium flow on the symmetrical modes of the static equilibrium.

The cut-off curves  $R_1, R_2, R_3$ , and  $R_4$  are shifted upwards as the flow increases (see Equation (5.58)), but the curves  $\pm R_5, \pm R_6$  (Equation (5.62)) and  $A_B = 0$  (Equation (5.20)) do not change their position. This results in a similar upward shift of the permitted regions of wave propagation as well as in the deformation of their shape. We may observe that permitted regions may disappear together with the modes propagating in them as, for example, in Figures 5.5b,c where the  $f$ -modes vanish. New permitted regions may also appear but it does not necessarily follow that new modes also appear (see Figure 5.5c where the permitted regions bounded by the curves  $R_1$  and  $R_6$  and  $R_5$  and  $R_4$  appear without new modes).

The flow also modifies the frequency (and the phase speed) of the modes. However, frequency shifts of various modes may differ in magnitude. In the series of panels from Figure 5.5a-f, the backward-propagating slow mode shifts together with the flow and even changes its direction of propagation, thus becoming a forward-propagating (in the same direction as the flow) mode (see Figure 5.5c).

On the other hand, the forward-propagating slow mode mainly retains its position (*i.e.* its phase speed), while the permitted regions “pass through” it as the flow changes. The permitted region that originally contains this mode (bounded by the curves  $R_1$  and  $c_T/c_{se}$ ) gradually disappears as the flow increases (see Figures 5.5a,b), and in the end, the mode is transferred to the permitted region containing the other slow mode “travelling upward” with the flow (Figure 5.5c).

In what follows, the slow mode with lower phase speed continuously approaches the upper slow mode as the flow increases, and finally, when the flow reaches a critical value, it couples to the upper mode. The coupled slow modes form two branches, and the gap between them continues to expand with further growing equilibrium flows (Figures 5.5d and e). Meanwhile, the two asymptotes to which the slow modes tend become closer until they merge with each other and cancel out, leaving behind only the lower branch of the coupled modes (Figure 5.5f). A further increase of the flow gradually causes this mode to disappear.

Figure 5.6 shows solutions of the dispersion relation (5.33), still taking  $c_{s0}/c_{se} = 0.9$  but with  $v_A/c_{se} = 1.0$ , for four increasing values of the flow,  $u_e/c_{se}$  starting from zero (Figures 5.6a-d). These parameters again describe a plasma that is slightly hotter in the lower region similar to the case in Figure 5.5. However, the difference here is that the plasma-beta value is approximately 0.98 and the density ratio between the layers

is 0.61. This situation is applicable to the region of the upper chromosphere. In case of these parameters, both the fast and slow MAG surface modes can propagate as is visible in Figure 5.6a (which corresponds to the static case), both lying entirely within the light grey region ( $A_B < 0$ ) where the modes have declining vertical velocities in the upper medium ( $z > 0$ ).

The upward shift of the permitted regions and of the modes (as a result of the increasing flow) results in the disappearance of the backward-propagating fast mode (Figure 5.6b). The upper permitted region containing the forward-propagating fast mode is deformed as a result of the upward shift of the curve  $R_2$ . This causes the lower part of the mode to be transferred to a region (shaded dark grey) where the mode has a growing vertical velocity with height  $z$  (Figure 5.6b). Next, at higher flow values, the mode, while slowly shifting upward together with the asymptote to which it tends, can only propagate at increasing wavenumbers (as shown by their absence in the range  $0 \leq k_x H_e \leq 6$  in Figures 5.6c and d).

The forward- and backward-propagating slow modes behave similarly to the case depicted in Figure 5.5. The forward propagating slow mode, whilst keeping its relatively constant position, is transferred to the permitted region containing the other slow mode (Figure 5.6c). Meanwhile, the backward-propagating slow mode carried away by the flow continues to shift upwards, and thus changes its direction of propagation (Figure 5.6c) and approaches the upper slow mode. Just before the asymptotes - to which the slow modes tend - reach each other, the slow modes couple and form two branches like in Figures 5.5d and e (this is not visible here). After the connection and cancellation of the asymptotes, only the lower branch of the coupled modes remains (Figure 5.6d), which gradually disappears as the flow increases.

Finally, in Figure 5.7 we show solutions of the dispersion relation (5.33) taking  $c_{s0}/c_{se} = 1.4$  and  $v_A/c_{se} = 0.75$ . These parameters may model a situation where the upper plasma is hotter than the lower plasma. The plasma-beta value is approximately 4.18 and the density ratio is 0.41. We use these parameters for a direct comparison to the model used in Miles *et al.* (1992). For these parameters only the slow MA mode may propagate in the limit of no gravity ( $k_x H_e \rightarrow \infty$ ). Thus, in Figure 5.7a (the static case), the slow MAG mode is visible. The mode is split into two parts, the upper curve (in the dark grey region) has a growing vertical velocity, while the lower part (in the light grey region) has a velocity decreasing in the  $z > 0$  region.

Taking the case when the equilibrium flow increases, the modes in the dark grey regions behave differently: the backward-propagating mode disappears, while its forward-propagating counterpart slips out from the dark grey region into the light grey region (Figure 5.7b) and later (at higher flow velocities) is transferred to the permitted region bounded by the cut-off curves  $R_4$  and  $R_5$  (Figures 5.7c and d). The slow modes behave similarly to the previous cases: the backward-propagating slow mode shifts together with the flow (Figure 5.7b), changes its direction of propagation

(Figure 5.7c), and finally reaches and couples to the forward propagating slow mode (Figure 5.7d). The coupled modes gradually disappear as the flow increases further. It is of interest to deduce how the phase speed of a mode varies with the increasing flow magnitude at a specific wavenumber.

In Figure 5.8 we show the variation of the dimensionless phase speed,  $\omega/k_x c_{se}$ , of surface MAG waves as a function of the dimensionless flow velocity,  $u_e/c_{se}$ . The parameters were set to  $c_{s0}/c_{se} = 0.9$ ,  $v_A/c_{se} = 1.0$ , and we chose three different values for the dimensionless wavenumber: (a)  $k_x H_e = 1.0$ , where the horizontal wavelength and the scale on which the (lower) equilibrium changes are comparable, (b)  $k_x H_e = 5.0$ , where the equilibrium varies on a scale lower than the wavelength and (c)  $k_x H_e = \infty$ , where the length of a wave is far smaller than the change in equilibrium conditions, *i.e.* stratification is unimportant. From the choice of parameters the modes shown here are the same fast and slow MAG surface modes as those displayed in Figure 5.6. The permitted regions of propagation for surface waves are shaded grey. The  $k_x H_e = \infty$  case is equivalent to the gravity-free case and therefore Figure 5.8c shows the behaviour of the fast and slow MAG surface modes that correspond to the asymptotes of the modes in Figure 5.6.

It is visible in all three figures that as the flow starts to increase from zero the phase speeds of all modes increase. The backward-propagating fast mode vanishes in all three cases. A forbidden gap where surface modes are not allowed to propagate, bounded by the  $R_1$  and  $R_4$  cut-off curves. This causes the forward-propagating fast and slow modes to exist in two separate flow intervals below and above the gap (Figures 5.8a,b). However, with increasing wavenumber the width of the gap decreases, eventually disappearing in the  $k_x H_e \rightarrow \infty$  limit (Figure 5.8c). See Equations (5.68)-(5.70) for the asymptotic values of the cut-off curves  $R_1, R_2, R_3, R_4, R_5$ , and  $R_6$ .

The phase speeds of the forward-propagating fast and slow modes clearly change little with flow speed. For lower flow velocities they increase, and for higher flow velocities they decrease with growing flow. On the other hand, the phase speed of the backward-propagating slow mode changes substantially with flow speed, being carried away by the flow (see the parts in Figure 5.8 where the phase speed increases together with the flow with unit slope). It is also easily observable that the backward-propagating slow mode changes the direction of propagation and couples to the other slow mode.

For flows in the negative direction, the opposite behaviour occurs. The forward-propagating slow modes are decelerated by this counter-flow and even reverse their direction of propagation. The backward-propagating fast and slow mode phase speeds are barely changed by the increase in the magnitude of the negative flow. This is due to the property of the dispersion relation (5.33) that it is symmetric for the Doppler shifted frequency ( $\Omega$ ) in the lower layer.

## 5.6 Summary and Discussion

In this chapter, we studied the effect of a steady uniform flow on the MAG surface waves described in Miles and Roberts (1992). With respect to the solar atmosphere this situation can model the Evershed flow seen in sunspot canopies or, for lower shear flow velocities, the meridional flows of the interior of the Sun compared to the overlying solar atmosphere.

The addition of flow to this problem was shown to have some fairly distinct effects, on the propagation of the surface waves. Firstly the regions, where surface modes were allowed to propagate were shifted, this was especially evident in Eqs. (5.68) and (5.69). This can be held responsible for the fact that the fast wave disappears (see e.g. Fig. 5.6). It was also shown that the background flow would affect the propagation of the surface waves. In Figs. 5.5-5.7 we plotted the backward and forward propagating waves and increased the flow steadily. It was seen (for the slow mode) in all of the graphs that increasing the flow decelerated the backward propagating wave, whilst leaving the forward propagating wave relatively untouched. Eventually, if the flow was large enough the direction of propagation could be changed. This may have implications for observations of waves. A wave that is observed may seem to have a relatively slow phase speed when, in fact, if the coordinate system is transformed so that the flow is static the wave has the expected phase speed. For shear flow velocities larger than the Alfvén speed, the Kelvin-Helmholtz instability also occurred. However, the effect of gravity is important, as  $k_x H_e$  becomes smaller, larger flow velocities are required to change the direction of propagation and, therefore, this also inhibits the Kelvin-Helmholtz instability. The effect of flow on the forward propagating wave was more apparent when fixing the dimensionless wave number,  $k_x H_e$ . In Figs. 5.8a-c it was seen that the forward propagating mode, upon increasing the flow, would be accelerated slightly but then remain fairly constant and eventually be decelerated, finally coupling to the backward propagating wave for the Kelvin-Helmholtz instability.

The modes of oscillation that have changed their direction can possibly be unstable to the Negative energy wave instability. This is of interest as there is a possibility that energy can transfer between a positive and negative energy wave (Ryutova, 1988), resonant absorption (Ruderman and Wright, 1998, Tirry *et al.*, 1998 and Erdélyi and Taroyan, 2003) or explosive instabilities (Joarder *et al.*, 1997).

Meridional flows of the interior of the Sun are very slow, up to  $0.2 \text{ km s}^{-1}$ . We take this value as  $u_e$  and the sound speed as  $7 \text{ km s}^{-1}$  such that  $u_e/c_{se} = 0.03$  for the model proposed for Figure 5.5. It is clear from this value that this type of velocity shear will only have a modest effect on the propagation of MAG surface waves in the proposed model. However, this type of velocity shear is not the only possible shear for the model described in Figure 5.5. Velocity shears between the two layers could also

be attributed to differential rotation of the Sun. If we take a high differential rotation velocity of  $2.0 \text{ km s}^{-1}$  i.e.  $u_e/c_{se} = 0.29$ , then the ratio is higher, but as shown in Figure 5.5, the flow speed is not high enough for backward-propagating waves to reverse their direction. Therefore no negative energy waves nor the Kelvin-Helmholtz instability will occur.

Evershed flows in sunspots can reach up to  $6 \text{ km s}^{-1}$ . Applying this to Figure 5.6 and taking  $c_{se} = 7 \text{ km s}^{-1}$  and  $u_e = 6 \text{ km s}^{-1}$  and thus  $u_e/c_{se} = 0.86$ , it can be seen from Figures 5.6 and 5.8 that this flow speed is high enough for the backward-propagating waves to reverse their direction of propagation. Thus, some running penumbral waves (RPW) may become negative energy waves. This could also have implications for interpreting the observations of RPW, as some may have very slow phase speed because they are backward-propagating waves.



# Chapter 6

## Dissipative Instability in a Prominence Plasma

### 6.1 Introduction

The fully ionised description of plasmas can be appropriate for many cases within the Sun and the solar atmosphere. However, as was stated in the introduction, at chromospheric temperatures or below the plasma may not be fully ionised. Prominences are magnetic structures, supported against gravity by the magnetic field, made up of chromospheric material at around 7500-9000 K (Engvold, 1998, Lin *et al.*, 2005b) suspended within a surrounding coronal plasma. Therefore a partially ionised description of them may be more appropriate.

Being such dynamic objects, prominences also exhibit plasma flows. Bulk flows of around 10-70 km s<sup>-1</sup> are observed within quiescent prominences (Schmieder *et al.*, 1984). Berger *et al.* (2008) observed turbulent up-flows of around 20 km s<sup>-1</sup> in both the Ca II H-line and H $\alpha$  band passes of the Solar Orbiter Telescope (SOT). Flows of up to 200 km s<sup>-1</sup> have even been observed in active region prominences, most probably due to their formation.

Given that flows are so abundant, flow instabilities are likely to occur within prominences. For instance, at the region of transition between the corona and prominence turbulent eddies have been observed (Ryutova *et al.*, 2010, Berger *et al.*, 2010). There could be various reasons for these instabilities. One obvious example would be the Kelvin-Helmholtz instability (see e.g. Soler *et al.* (2012)), however, flows of the velocities required for the Kelvin-Helmholtz instability are not regularly observed. Therefore, another description is probably required to explain these instabilities. Negative energy wave (NEW) instabilities, linked to the dissipative instability, are a possible candidate as they occur at flow speeds generally lower than the Kelvin-Helmholtz instability.

In terms of structure, prominences have been modelled in slab, cylindrical and interface geometries. Soler *et al.* (2012) studied the Kelvin-Helmholtz instability in a two fluid incompressible plasma in the cylindrical coordinate system. Soler *et al.* (2012) modelled a prominence as a cylinder using a two fluid description of the plasma, studying mainly the kink mode and how it was effected by changing the collisional frequency between ions and neutrals. Ballai *et al.* (2015) modelled the interface between a coronal and prominence plasma using the single fluid incompressible description, studying the effect of a viscous corona and a partially ionised prominence plasma (through the Cowling resistivity) on wave modes. It was found that the viscosity could cause a NEW dissipative instability but the introduction of neutrals caused the Cowling resistivity to have more importance and would eventually stabilise the plasma. Ballai *et al.* (2017b) studied the same idea but this time modelling the plasma as a slab, coming to the same conclusion as Ballai *et al.* (2015). The work in this chapter is the natural extension and generalisation to Ballai *et al.* (2017b), but considering a compressible plasma, the dissipative instability caused by the effect of a viscous corona, and, how that is affected by the partially ionised prominence plasma.

In this chapter, we first present the background equilibrium and then the governing equations for both the coronal and prominence plasmas. Solutions to these are connected via appropriate boundary conditions and a dispersion relation is formed, considering weak non-ideal effects. The slender slab limit is used to investigate the onset of the dissipative instability. For a complete study, numerical solutions of the dispersion relation are taken and the variation of the dimensionless wave-number is taken into account. This work has been submitted to Astronomy and Astrophysics and is currently in the last stages of review.

## 6.2 Equilibrium and Governing Equations

We consider a magnetised plasma slab of width  $2z_0$  with boundaries at  $z = -z_0$  and  $z = z_0$  (see Figure 1), situated between to semi-infinite planes. The magnetic field in the three regions is uniform and parallel with the  $x$ -axis such that,  $\mathbf{B} = B\hat{\mathbf{x}}$ , where  $\hat{\mathbf{x}}$  is the unit vector in the  $x$ -direction. A uniform background flow is present within the slab environment, parallel to the  $x$ -axis, i.e.  $\mathbf{v} = u_0\hat{\mathbf{x}}$ . The equilibrium temperatures, densities and pressures are assumed to vary on a scale that is much larger than the wavelength of the waves studied and are therefore considered constant functions in  $z$ , i.e.

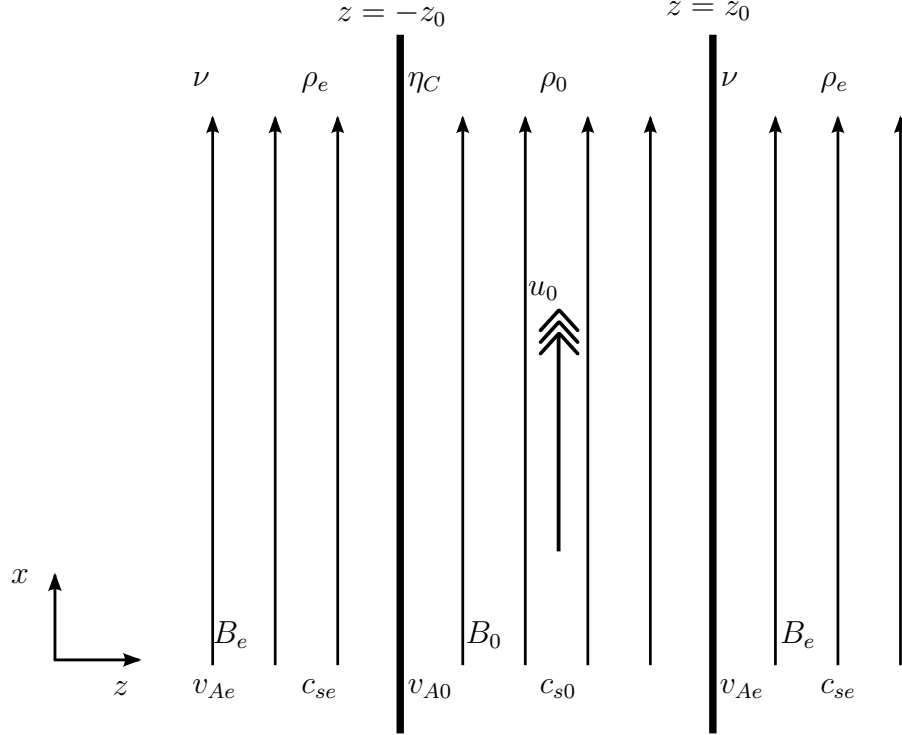


Fig. 6.1 The equilibrium configuration for the magnetic slab and its surrounding magnetic environment.

$$\begin{aligned}
 \left. \begin{array}{l} T(z), \quad c_s(z), \\ v_A(z), \quad c_T(z), \quad u(z) \end{array} \right\} = \begin{cases} T_e, \quad c_{se} & |z| > z_0, \\ v_{Ae}, \quad c_{Te}, \quad 0, & \\ T_0, \quad c_{s0}, & |z| < z_0, \\ v_{A0}, \quad c_{T0}, \quad u_0, & \end{cases} \quad (6.1)
 \end{aligned}$$

where the indices 0 and  $e$  denote internal and external quantities of the slab, respectively, and  $T_l$ ,  $c_{sl}$ ,  $v_{Al}$ ,  $c_{Tl}$ ,  $u_l$  ( $l = 0, e$ ) are the temperature, sound speed, Alfvén speed, tube speed ( $c_{Tl} = c_{sl}v_{Al}/(c_{sl}^2 + v_{Al}^2)^{1/2}$ ), and background equilibrium bulk-flow speed inside the slab.

In our model, we approximate the entire prominence by a slab and, therefore, the solar corona constitutes the external environment. Given the high probability that prominences are of chromospheric origin (although they may be cooling material from the corona [Xia et al., 2014](#)), we assume that their temperature does not reach the threshold where hydrogen is fully ionised. In contrast, the surrounding corona, with its million degree temperature, is fully ionised. In partially ionised plasmas, the concept of transport mechanisms has to be treated differently, as the way momentum and energy is transported and dissipated is distinct from the formalism used in fully ionised plasmas. The reason for this is that the presence of neutrals and the collisions between heavy particles may change the nature and magnitude of these mechanisms

(for a detailed discussion on the possible transport mechanisms in partially ionised plasmas see e.g. [Khodachenko \*et al.\*, 2004](#) or [Zaqarashvili \*et al.\*, 2011](#)). Here, we assume that the ion-neutral collisional frequency is much larger than the harmonic motions of waves. Therefore the dynamics in the partially ionised plasma can be described within the framework of a single-fluid MHD. In addition, we assume that there is strong thermal coupling between the ions, electrons and neutrals. Among all possible dissipative mechanisms, we concentrate on the processes that appear in the generalised Ohm's law, in particular, we deal with the classical and Cowling resistivity. The effects of these two resistivities are very different. The classical Spitzer resistivity is due to electrons and generates the dissipation of currents along magnetic field. Contrastingly, the Cowling resistivity is due to ions and creates a magnetic resistivity of currents that flow perpendicular to the ambient magnetic field.

With these considerations, the dynamics in the partially ionised prominence is given by the system of linearised MHD equations

$$\frac{\partial p'}{\partial t} + (\mathbf{v} \cdot \nabla) p' + \gamma p (\nabla \cdot \mathbf{v}') = 0, \quad (6.2)$$

$$\rho \left( \frac{\partial \mathbf{v}'}{\partial t} + (\mathbf{v} \cdot \nabla) \mathbf{v}' \right) = -\nabla p' + (\nabla \times \mathbf{B}') \times \frac{\mathbf{B}}{\mu_0}, \quad (6.3)$$

$$\begin{aligned} \frac{\partial \mathbf{B}'}{\partial t} + (\mathbf{v} \cdot \nabla) \mathbf{B}' &= (\mathbf{B} \cdot \nabla) \mathbf{v}' - \mathbf{B} (\nabla \cdot \mathbf{v}') + \eta \nabla^2 \mathbf{B}' \\ &+ \frac{\eta_C - \eta}{|\mathbf{B}|^2} \nabla \times \{[(\nabla \times \mathbf{B}') \times \mathbf{B}] \times \mathbf{B}\}, \end{aligned} \quad (6.4)$$

$$\nabla \cdot \mathbf{B}' = 0, \quad (6.5)$$

where all quantities with subscript 1 denote small perturbations of background quantities. Note that the diamagnetic current that would be present in Eq. (6.4) is neglected due to the plasma that we consider having a low plasma-beta value with a strong magnetic field ([Khodachenko \*et al.\*, 2004](#)). Here,  $\rho = \rho_i + \rho_n$  so that the total background density,  $\rho$ , is always constant, with the ion density  $\rho_i$  and the neutral density changing, depending on how ionised the plasma is. For a completely ionised plasma  $\rho_i = \rho$  and for a fully neutral plasma  $\rho_n = \rho$ .

We assume all perturbations to be of the form

$$f' = \widehat{f}(z) \exp[i(kx - \omega t)],$$

where  $\widehat{f}(z)$  is the amplitude of perturbations and the frequency,  $\omega$ , may be a complex quantity. Since the plasma is unbounded in the  $x$  direction, we Fourier analyse the perturbations. In addition, instead of velocity components in the momentum equation (6.3), we use the Lagrangian displacement,

$$\mathbf{v}' = \left( \frac{\partial}{\partial t} + \mathbf{v} \cdot \nabla \right) \boldsymbol{\xi}.$$

Here,  $\boldsymbol{\xi} = (\widehat{\xi}_x(z), \widehat{\xi}_y(z), \widehat{\xi}_z(z)) \exp[i(kx, -\omega t)]$ . Equations (6.2)-(6.5) along with Eq. (6.1) can be then reduced to a second order differential equation governing the Lagrangian displacement in the  $z$ -direction

$$\frac{d^2 \widehat{\xi}_z(z)}{dz^2} - \bar{M}_0^2 \widehat{\xi}_z(z) = 0, \quad \bar{M}_0^2 = - \frac{(\Omega^2 - k^2 c_{s0}^2) (\Omega^2 - k^2 \bar{v}_{A0}^2)}{(c_{s0}^2 + \bar{v}_{A0}^2) (\Omega^2 - k^2 \bar{c}_{T0}^2)}, \quad (6.6)$$

where the quantity  $\bar{M}_0$  is the magnetoacoustic parameter,  $\bar{v}_{A0}^2 = v_{A0}^2 (1 - i\eta_C k^2 / \Omega)$  is the modified Alfvén speed, while  $\bar{c}_{T0}^2 = c_{s0}^2 \bar{v}_{A0}^2 / (c_{s0}^2 + \bar{v}_{A0}^2)$  is the associated cusp speed. Here,  $v_{A0} = (B_0^2 / \mu_0 \rho_0)^{1/2}$  is the Alfvén speed and  $c_{s0} = (\gamma p_0 / \rho_0)^{1/2}$  is the sound speed of the internal medium, where  $\gamma = 5/3$  is the adiabatic index and  $\mu_0$  is the magnetic permeability of free space. In the above equation,  $\Omega = \omega - ku_0$  is the Doppler-shifted frequency.

The solutions inside the slab must be matched, at the boundaries of the slab with the solutions outside the slab. These boundaries must be stable to perturbations, i.e. any displaced fluid element on (or near) the boundary will not be advected by perturbations. This can be achieved only by assuming that the transversal component of the Lagrangian displacement is continuous and any other stresses that act in the perpendicular direction of the boundaries are matched by stresses on the other side of the boundary. That is why it is essential to use the Reynolds-Maxwell stress tensor to calculate the transversal stress component that is given by

$$S_z = -\rho_0 \frac{(\bar{v}_{A0}^2 + c_{s0}^2) (\Omega^2 - k^2 \bar{c}_{T0}^2)}{\Omega^2 - k^2 c_{s0}^2} \frac{d\widehat{\xi}_z(z)}{dz}. \quad (6.7)$$

Let us now consider the dynamics in the surrounding coronal plasma. Due to the high temperatures of the corona ( $> 10^6 \text{ K}$ ), the plasma is fully ionised. Following on from the work by Ballai *et al.* (2017b), we consider that the dominant dissipative mechanism acting upon modifying the amplitude of waves is the viscosity. Given that the dynamics in the solar corona are driven mainly by magnetic forces, the viscosity is anisotropic and its value is given by the Braginskii's tensor present in the momentum equation. This tensor has five components, but by far the leading term (by about five orders of magnitude) is the first component (also called compressional viscosity) that is due to ions (see, e.g. Braginskii, 1965, Erdelyi and Goossens, 1995,

Erdélyi, 1996, Ruderman *et al.*, 1996). Therefore, the dynamics in the solar corona is described with the help of the linearised MHD equations

$$\frac{\partial p'}{\partial t} + \gamma p_e (\nabla \cdot \mathbf{v}') = 0, \quad (6.8)$$

$$\begin{aligned} \rho_e \frac{\partial \mathbf{v}'}{\partial t} = & -\nabla p' + (\nabla \times \mathbf{B}') \times \frac{\mathbf{B}_e}{\mu_0} \\ & + \rho_e \nu \left\{ \mathbf{b}(\mathbf{b} \cdot \nabla) - \frac{1}{3} \nabla \right\} \{ 3\mathbf{b} \cdot \nabla(\mathbf{b} \cdot \mathbf{v}') - \nabla \cdot \mathbf{v}' \}, \end{aligned} \quad (6.9)$$

$$\frac{\partial \mathbf{B}'}{\partial t} = (\mathbf{B}_e \cdot \nabla) \mathbf{v}' - \mathbf{B}_e (\nabla \cdot \mathbf{v}'), \quad \nabla \cdot \mathbf{B}' = 0, \quad (6.10)$$

where  $\mathbf{b} = \mathbf{B}_e/B_e$  is the unit vector in the direction of the equilibrium magnetic field,  $\nu = \kappa_0/\rho_e$  is the kinematic viscosity, and  $\kappa_0$  is the viscosity coefficient and its approximative value is given by

$$\kappa_0 = \frac{\rho_e k_B T_e \tau_p}{m_p},$$

where  $T_e$  is the temperature of the external medium,  $k_B$  is the Boltzmann constant,  $\tau_p$  is the proton-proton collision time, and  $m_p$  is the proton mass. For typical coronal values we can obtain that  $\kappa_0 \approx 5 \times 10^{-2} \text{ kg m}^{-1} \text{ s}^{-1}$  (see, e.g. Hollweg, 1985 or Erdélyi, 1996).

In a similar way to the prominence plasma derivation, the MHD equations can be reduced to a single equation that describes the evolution of the transverse component of the Lagrangian displacement as

$$\frac{d^2 \widehat{\xi}_z(z)}{dz^2} - M_e^2 N_e^2 \widehat{\xi}_z(z) = 0, \quad \text{with } M_e^2 = -\frac{(\omega^2 - k^2 c_{se}^2)(\omega^2 - k^2 v_{Ae}^2)}{(c_{se}^2 + v_{Ae}^2)(\omega^2 - k^2 c_{Te}^2)}, \quad (6.11)$$

and

$$N_e^2 = 1 + \frac{i\nu\omega}{3} \frac{(\omega^2 - 3k^2 c_{se}^2)^2}{(c_{se}^2 + v_{Ae}^2)(\omega^2 - k^2 c_{Te}^2)(\omega^2 - k^2 c_{se}^2)}. \quad (6.12)$$

Here,  $v_{Ae} = (\mathbf{B}_e^2/\mu_0\rho_e)^{1/2}$  is the Alfvén speed,  $c_{se} = (\gamma p_e/\rho_e)^{1/2}$  is the sound speed of the external medium and  $c_{Te}^2 = c_{se}^2 v_{Ae}^2/(c_{se}^2 + v_{Ae}^2)^2$  is the external tube speed. In order to ensure that the interface between various regions is stable, the stress across the interfaces must be continuous, which now in the external region takes the form

$$S_z = -\rho_e \frac{(v_{Ae}^2 + c_{se}^2)(\omega^2 - k^2 c_{Te}^2)}{\omega^2 - k^2 c_{se}^2} \frac{d\widehat{\xi}_z(z)}{dz} + \rho_e \frac{i\nu\omega}{3} \frac{(\omega^2 - 3k^2 c_{se}^2)^2}{(\omega^2 - k^2 c_{se}^2)^2} \frac{d\widehat{\xi}_z(z)}{dz}, \quad (6.13)$$

where  $\widehat{\xi}_z(z)$  is the solution of Eq. (6.11).

### 6.3 Dispersion Relation

To study the waves and how the viscosity and Cowling resistivity affect the propagation of linear MA waves we derive a dispersion relation. We, first, require that  $\widehat{\xi}_z(z)$  is finite as  $|z| \rightarrow \infty$ . Therefore the general solutions inside and outside of the slab are

$$\widehat{\xi}_z(z) = \begin{cases} C_1 \exp(-M_e N_e(z - z_0)) & z > z_0, \\ C_2 \sinh(\bar{M}_0 z) + C_3 \cosh(\bar{M}_0 z) & |z| < z_0, \\ C_4 \exp(M_e N_e(z + z_0)) & z < -z_0. \end{cases} \quad (6.14)$$

The solutions in the regions  $z < -z_0$  and  $z > z_0$  must be connected to the solutions within the slab,  $|z| < z_0$ . The constants of integration  $C_1 \dots C_4$  can be found by four boundary conditions these are:

- $\widehat{\xi}_z(z)$  is continuous at  $z = -z_0$  and  $z = z_0$ ;
- The stress on the boundary is continuous at  $z = -z_0$  and  $z = z_0$ .

Applying these boundary conditions to the solutions given in Eq. (6.14) we recover two distinct and separate solutions. One describes the symmetric sausage modes and the other describes the antisymmetric kink modes (see e.g. Roberts, 1981b). There are two roots: the *kink* mode, described by the coth function; and the *sausage* mode, described by the tanh function. The dispersion relation is given below:

$$\rho_e M_e N_e \left( \frac{D_{Ae}}{M_e^2} - i \frac{v\omega}{3} \frac{D_{3se}^2}{D_{se}^2} \right) \begin{Bmatrix} \coth(M_0 z_0) \\ \tanh(M_0 z_0) \end{Bmatrix} + \rho_0 \frac{\bar{D}_{A0}}{\bar{M}_0} = 0. \quad (6.15)$$

Below we introduce for ease of use ( $l = 0, e$ ):

$$\begin{aligned} D_{sl} &= \Omega_l^2 - c_{sl}^2 k^2, & D_{Al} &= \Omega_l^2 - v_{Al}^2 k^2, \\ D_{Tl} &= \left( c_{sl}^2 + v_{Al}^2 \right) \left( \Omega_l^2 - c_{Tl}^2 k^2 \right), \\ D_{3sl} &= \Omega_l^2 - 3c_{sl}^2 k^2, & D_{ml} &= \Omega_l^4 - 2k^2 D_{Tl}, \\ \Omega &= \omega - ku_0 \end{aligned} \quad (6.16)$$

We note that the bar in Eq. (6.15) refers to the fact that the Alfvén speed is of the form  $\bar{v}_{A0}^2 = v_{A0}^2 (1 - i\eta_C k^2 / \Omega)$  as opposed to just  $v_{A0}^2$ . Even though Eq. (6.15) describes these waves fully, we now use a perturbation method so that the dispersion relation can be written in terms of a real part for the ideal effects and an imaginary part

for the non-ideal effects. We therefore consider  $\eta_C k^2 / \Omega \ll 1$  and  $\frac{i\nu\omega}{3} \frac{D_{3se}^2}{D_{Te} D_{se}} \ll 1$ . These assumptions are essentially the same as saying  $R \gg 1$  and  $R_m \gg 1$ . With these assumption we derive the following dispersion relations

$$F(\omega, k) = F_0(\omega, k) + iF_1(\omega, k) = 0, \quad (6.17)$$

where

$$F_0(\omega, k) = \rho_e \frac{D_{Ae}}{M_e} \left\{ \begin{array}{c} \coth \\ \tanh \end{array} \right\} (M_0 z_0) + \rho_0 \frac{D_{A0}}{M_0}, \quad (6.18)$$

is the real part of the dispersion relation, while the imaginary part is written as

$$\begin{aligned} F_1 = & \rho_e M_e \frac{\nu\omega}{6} \frac{D_{3se}^2}{D_{se}^2} \left\{ \begin{array}{c} \coth \\ \tanh \end{array} \right\} (M_0 z_0) \\ & + \eta_C \frac{k^2 v_{A0}^2}{2\Omega} \left[ \rho_0 M_0 \frac{D_{m0}}{D_{s0} D_{A0}} + \rho_e \frac{D_{Ae}}{M_e} \frac{\Omega^4}{D_{A0} D_{T0}} \left( 1 - \left\{ \begin{array}{c} \coth^2 \\ \tanh^2 \end{array} \right\} (M_0 z_0) \right) M_0 z_0 \right]. \end{aligned} \quad (6.19)$$

Due to the high viscous and magnetic Reynolds numbers the imaginary part of Eq. (6.17) is considered to be far smaller than the real part i.e.  $F_0 \gg F_1$  for both the kink and sausage modes. Eq. (6.18) is identical to the dispersion relation derived by Nakariakov and Roberts (1995). To find an approximate solution to dispersion relation (6.17) we expand the dispersion relation around the solution to

$$F_0(\omega_0, k) = 0, \quad (6.20)$$

where  $\omega_0$  is the frequency solution to the ideal part of the dispersion relation. We now assume that  $\omega \approx \omega_0 + i\omega'$ , where  $\omega_0 \gg \omega'$  and use the Taylor expansion of Eq. (6.17) around  $\omega_0$

$$F(\omega, k) \approx F_0(\omega_0, k) + iF_1(\omega_0, k) + \frac{\partial F(\omega_0, k)}{\partial \omega} (\omega - \omega_0). \quad (6.21)$$

Since both  $F(\omega, k) = 0$  and  $F_0(\omega_0, k) = 0$  and  $\omega - \omega_0 = i\omega'$

$$\omega' \approx -\frac{F_1(\omega_0, k)}{\partial F(\omega_0, k) \partial \omega}, \quad (6.22)$$

$$\omega' \approx -\frac{F_1(\omega_0, k)}{\partial F_0(\omega_0, k) \partial \omega}. \quad (6.23)$$

Here,

$$\begin{aligned} \frac{\partial F_0(\omega, k)}{\partial \omega} = & -\rho_0 \frac{\Omega^3 (\Omega^2 - 2k^2 c_{T0}^2)}{D_{s0}(\Omega^2 - k^2 c_{T0}^2) M_0} \left( M_0 z_0 \frac{1 - \left\{ \frac{\tanh^2}{\coth^2} \right\} (M_0 z_0)}{\left\{ \frac{\tanh}{\coth} \right\} (M_0 z_0)} \right), \\ & -\rho_0 \frac{\Omega D_{mc0}}{D_{T0} D_{s0} M_0} - \rho_e \frac{\omega D_{mce}}{M_e D_{Te} D_{se}} \left\{ \frac{\coth}{\tanh} \right\} (M_0 z_0), \end{aligned} \quad (6.24)$$

and

$$D_{mcl} = (c_{sl}^2 + v_{Al}^2) \Omega_l^4 - 2k^2 c_{sl}^2 D_{Tl}. \quad (6.25)$$

The assumption was that amplitudes of waves vary in time like  $\sim \exp(-i\omega t)$ . This can be split up into a real exponential that either increases or decreases with time multiplied by another that varied harmonically in time i.e  $\sim \exp(-i\omega_0 t) \exp(\omega' t)$ . It is therefore simple to see that if  $\omega' < 0$  waves decrease exponentially in time i.e. they are *damped*. If  $\omega' > 0$  waves increase exponentially in time i.e. the wave is *unstable*.

Both Eqs.(6.19) and (6.24) can be re-written due to the zeroth order relation of Eq. (6.20). We therefore have

$$\begin{aligned} F_1(\omega_0, k) = & -\frac{\rho_0 D_{A0}}{M_0} \frac{M_e^2 v \omega_0 D_{3se}^2}{6 D_{Ae} D_{se}^2} \\ & -\frac{\rho_0 D_{A0}}{M_0} \frac{\eta_c k^2 v_{A0}^2}{D_{A0} D_{T0} 2\Omega_0} \left( D_{m0} + \Omega_0^4 \left( M_0 z_0 \frac{1 - \left\{ \frac{\tanh^2}{\coth^2} \right\} (M_0 z_0)}{\left\{ \frac{\tanh}{\coth} \right\} (M_0 z_0)} \right) \right), \end{aligned} \quad (6.26)$$

and

$$\begin{aligned} \frac{\partial F_0(\omega_0, k)}{\partial \omega} = & -\rho_0 \frac{\Omega_0^3 (\Omega_0^2 - 2k^2 c_{T0}^2)}{D_{s0}(\Omega_0^2 - k^2 c_{T0}^2) M_0} \left( M_0 z_0 \frac{1 - \left\{ \frac{\tanh^2}{\coth^2} \right\} (M_0 z_0)}{\left\{ \frac{\tanh}{\coth} \right\} (M_0 z_0)} \right) \\ & -\rho_0 \frac{\Omega_0 D_{mc0}}{D_{T0} D_{s0} M_0} + \rho_0 \frac{\omega_0 D_{mce} D_{A0}}{M_0 D_{Te} D_{se} D_{Ae}}. \end{aligned} \quad (6.27)$$

Eq. (6.18) is cannot be solved analytically. It is therefore necessary to find approximate solutions.

### 6.3.1 Slender Slab Limit

The slender slab limit is a relatively simple approximation to take such that analytic progress can be made. We take the limit of Eq. (6.18) as  $kz_0 \rightarrow 0$  and find an approximate solutions. Key to this approximation is supposing  $M_0 z_0 \rightarrow 0$  as  $kz_0 \rightarrow 0$  (see e.g. Edwin and Roberts, 1982 or Nakariakov and Roberts, 1995). Eq. (6.18) then reduces to the following equation for the sausage modes

$$\rho_e D_{Ae} M_0^2 z_0 + \rho_0 D_{A0} M_e = 0. \quad (6.28)$$

We use the method of dominant balance (we compare and balance orders of  $kz_0$ ) on Eq. (6.28) to find a regular perturbation series representation of the solution. In this limit, the real part of the dispersion relation admits wave solutions that can, in general, be either surface ( $M_0 > 0$ ) or body ( $M_0 < 0$ ) modes depending on values of background quantities (Edwin and Roberts, 1982). In our study, we use the term *pseudo-body* for one of the modes that has a peculiar behaviour inside the slab, in the sense it does not have a spatially oscillatory structure in the  $z$ -direction but is a body mode as it satisfies the condition:  $M_0 < 0$  (for more information on these modes see e.g. Zhugzhda and Goossens, 2001, Ruderman, 2005, Erdélyi and Fedun, 2006 or Erdélyi and Fedun, 2007b). In addition, there are also spatially oscillating body-modes inside the slab which we term  $n = 1, 2..$  body modes. The real solutions of the dispersion relation are

$$\omega_0 \approx \pm k c_{se} \left\{ 1 + \frac{\rho_e^2 c_{se}^2 (v_{Ae}^2 - c_{se}^2) [(c_{se} - u_0)^2 - c_{s0}^2]^2}{\rho_0^2 2 (c_{s0}^2 + v_{A0}^2)^2 [(c_{se} - u_0)^2 - c_{T0}^2]^2} (kz_0)^2 \right\}, \quad (6.29)$$

$$\omega_0 \approx u_0 k \pm k c_{T0} \left\{ 1 + \frac{\rho_e [v_{Ae}^2 - (\pm c_{T0} + u_0)^2] (c_{s0}^2 - c_{T0}^2)}{\rho_0 \hat{M}_e (c_{s0}^2 + v_{A0}^2) c_{T0}^2} kz_0 \right\}, \quad (6.30)$$

where the upper signs describe the forward propagating waves, while the lower ones describe the backward propagating waves. In the above relation the parameter  $\hat{M}_e$  is defined as

$$\hat{M}_e^2 = - \frac{[(\pm c_{T0} + u_0)^2 - c_{se}^2] [(\pm c_{T0} + u_0)^2 - v_{Ae}^2]}{(c_{se}^2 + v_{Ae}^2) [(\pm c_{T0} + u_0)^2 - c_{Te}^2]}. \quad (6.31)$$

The quantity  $\hat{M}_e^2$  must be positive for non-leaky modes and this will impose a restriction on the domain of flows where our study is valid. A simple analysis would

reveal that waves will be able to propagate in the slab provided  $|u_0 \pm c_{T0}| < c_{Te}$  or

$$\min(c_{se}, v_{Ae}) < |u_0 \pm c_{T0}| < \max(c_{se}, v_{Ae}).$$

We now apply the same limit  $kz_0 \rightarrow 0$  to the kink mode solution of Eq. (6.18) which then reduces to

$$\rho_e D_{Ae} + \rho_0 D_{A0} M_e z_0 = 0. \quad (6.32)$$

Again, using the method of dominant balance we find two surface wave solutions which are given as

$$\omega_0 \approx \pm k v_{Ae} \left( 1 - \left( \frac{\rho_0}{\rho_e} \right)^2 \frac{\left( (\pm v_{Ae}^2 - u_0)^2 - v_{A0}^2 \right)^2 (v_{Ae}^2 - c_{se}^2)}{2v_{Ae}^6} (kz_0)^2 \right), \quad (6.33)$$

and

$$\omega_0 \approx \pm k c_{Te} \left( 1 - \left( \frac{\rho_0}{\rho_e} \right)^2 \frac{\left( (\pm c_{Te}^2 - u_0)^2 - v_{Ae}^2 \right)^2 (c_{Te}^2 - c_{se}^2)}{2c_{Te}^2 v_{Ae}^4} (kz_0)^2 \right). \quad (6.34)$$

We now apply the slender slab limit to Eq. (6.26). We first find for the sausage mode

$$F_1(\omega_0, k) \approx -\frac{\rho_0 D_{A0}}{M_0} \left( \frac{M_e^2 v \omega_0 D_{3se}^2}{6D_{Ae} D_{se}^2} + \frac{\eta_c k^2 v_{A0}^2 D_{s0}}{D_{T0} \Omega_0} \right), \quad (6.35)$$

and secondly for the kink mode

$$F_1(\omega_0, k) \approx -\frac{\rho_0 D_{A0}}{M_0} \left( \frac{M_e^2 v \omega_0 D_{3se}^2}{6D_{Ae} D_{se}^2} - \frac{\eta_c k^4 v_{A0}^2}{D_{A0} \Omega_0} \right). \quad (6.36)$$

Next, we apply the slender slab limit to Eq. (6.27). Again, we first find for the sausage mode

$$\frac{\partial F_0(\omega_0, k)}{\partial \omega} = -2\rho_0 \frac{\Omega_0 k^2 c_{s0}^4 D_{A0}}{D_{T0} D_{s0} M_0} + \rho_0 \frac{\omega_0 D_{mce} D_{A0}}{M_0 D_{Te} D_{se} D_{Ae}}. \quad (6.37)$$

and then for the kink mode

$$\frac{\partial F_0(\omega_0, k)}{\partial \omega} = -2\rho_0 \frac{\Omega_0}{M_0} + \rho_0 \frac{\omega_0 D_{mce} D_{A0}}{M_0 D_{Te} D_{se} D_{Ae}}. \quad (6.38)$$

### 6.3.2 Wide Slab Limit

The wide slab limit assumes that  $kz_0 \gg 1$ , that is the width of the slab is far greater than the wavelength (see e.g. [Roberts, 1981b](#)). There are two ways to look at the problem. By assuming  $M_0z_0 \rightarrow \infty$  as  $kz_0 \rightarrow \infty$  Eq. (6.18) becomes:

$$\rho_e \frac{D_{Ae}}{M_e} + \rho_0 \frac{D_{A0}}{M_0}. \quad (6.39)$$

Eq. (6.39) represents the dispersion relation of a single interface ([Roberts, 1981a](#)). However, as there can also be body modes, assuming that  $M_0z_0 \rightarrow \infty$  as  $kz_0 \rightarrow \infty$  is incorrect. We follow the steps in [Roberts \(1981b\)](#) but assume that  $v_{A0} > c_{s0}$ . By assuming a perturbation expansion of  $\omega_0$ , we find for the sausage body modes:

$$\omega_0 \approx (u_0 \pm c_{s0})k \mp c_{s0}k \frac{c_{s0}^2 \pi^2 \left(j - \frac{1}{2}\right)^2}{\left(v_{A0}^2 - c_{s0}^2\right) (kz_0)^2} \left( \frac{1}{2} - \rho_r \frac{\left(v_{Ae}^2 - (u_0 \pm c_{s0})^2\right)}{\left(v_{A0}^2 - c_{s0}^2\right) \hat{M}_e k z_0} \right). \quad (6.40)$$

Here,  $j = 1, 2, 3, \dots$ , represents the separate harmonics. We note, that, the factor  $\pi(j - 1/2)/kz_0$  must be of a sufficiently low value for the perturbation expansion to be valid. If we take  $u_0 = 0$  and assume that there is no external magnetic field so that  $v_{Ae} = 0$ , Eq. (6.40) agrees with the result in [Roberts \(1981b\)](#) up to first order. The next order in the perturbation series has been added, as it is needed to calculate the imaginary part of the solution.

We now wish to approximate the imaginary part of the solution. Inserting the approximation given by Eq. (6.40) into Eq. (6.23), we find after some algebra and retaining only the lowest order terms

$$\omega' \approx \mp \frac{kc_0^3 \pi^2 \left(j - \frac{1}{2}\right)^2}{\left(v_{A0}^2 - c_{s0}^2\right)^2 (kz_0)^2} \left( \rho_r \frac{k v (u_0 \pm c_{s0}) \left((u_0 \pm c_{s0})^2 - 3c_{se}^2\right)^2}{6\hat{M}_e \left((u_0 \pm c_{s0})^2 - c_{se}^2\right)^2 kz_0} \pm \frac{\eta_C k v_{A0}^2}{2c_{s0}^2} \right). \quad (6.41)$$

From Eq. (6.41), it is evident that  $\omega' \propto 1/(kz_0)^2$  if  $\eta_C \neq 0$  and  $\omega' \propto 1/(kz_0)^3$  if  $\eta_C = 0$ .

## 6.4 Dissipative Instability

In this section, we wish to focus on the dissipative instability due to the presence of a shear flow. It is well known that the Kelvin-Helmholtz instability can occur in astrophysical plasmas. The flow speeds required usually exceed the maximum Alfvén speed for the system; this is usually greater than the flow speeds observed in solar plasmas. The concept of negative energy waves has been used to find flow

speeds lower than those required for the onset of the Kelvin-Helmholtz instability. According to Cairns (1979), NEW's can occur in the presence of a flow, when the sign of the frequency,  $\omega$ , changes i.e. when the direction of propagation of a wave changes. Negative energy waves are characterised by the fact that the energy of the system must be decreased and this reduction of energy leads the amplitude of the wave to increase. This leads nicely onto the dissipative instability that is studied here. Clearly if there is some form of dissipation this leads to the energy of the system decreasing. In our system we have two forms of dissipation: viscous forces in the external part of the slab for the loss of energy due to collisions between ions and the Cowling resistivity within the slab, which takes into account how the ratio of neutrals to ions affects the magnitude. We use Eq. (6.23) to study the sign of the imaginary part of the frequency.

### 6.4.1 Negative Energy Waves

Before we investigate how the addition of neutrals to the system affects the stability of the interface, we make a quick note on how NEW's are related to the dissipative instability. The criteria from Cairns (1979) for negative energy waves to occur is given when the quantity  $E$  given below changes sign:

$$E = \alpha \omega_0 \frac{\partial F_0(\omega_0, k)}{\partial \omega}. \quad (6.42)$$

Here,  $\alpha$  is chosen to be positive or negative so that  $E$  is positive when there is no flow present. It is fairly evident that this quantity will change sign when either  $\omega_0$  changes sign or  $\partial F_0(\omega_0, k)/\partial \omega$  changes sign. To relate this to the dissipative instability we look to the sign of the imaginary part of the frequency given by Eq. (6.23). We know that a negative energy wave is possible if there is dissipation in the system but the wave is growing in amplitude. As was discussed in Ruderman *et al.* (1996), when there is dissipation on both sides of an interface it is extremely hard to determine the choice of coordinate system so that the sign of  $E$  can be determined. We therefore set  $\eta_C = 0$  so that we only consider the viscous effects in relation to negative energy waves.

Considering the sign of Eq. (6.23) now, we only need to find when  $F_1(\omega_0, k)$  changes sign. When  $\eta_C = 0$  Eq. (6.19) becomes

$$F_1(\omega_0, k) = \rho_e M_e \frac{\nu \omega_0}{6} \frac{D_{3se}^2}{D_{se}^2} \left\{ \begin{array}{c} \coth \\ \tanh \end{array} \right\} (M_0 z_0). \quad (6.43)$$

It is obvious that Eq. (6.43) changes sign when  $\omega_0$  changes sign. All waves, when there is no flow, are damped so that the negative energy wave occurs when the flow is strong enough to change the direction of propagation of the surface wave. One can

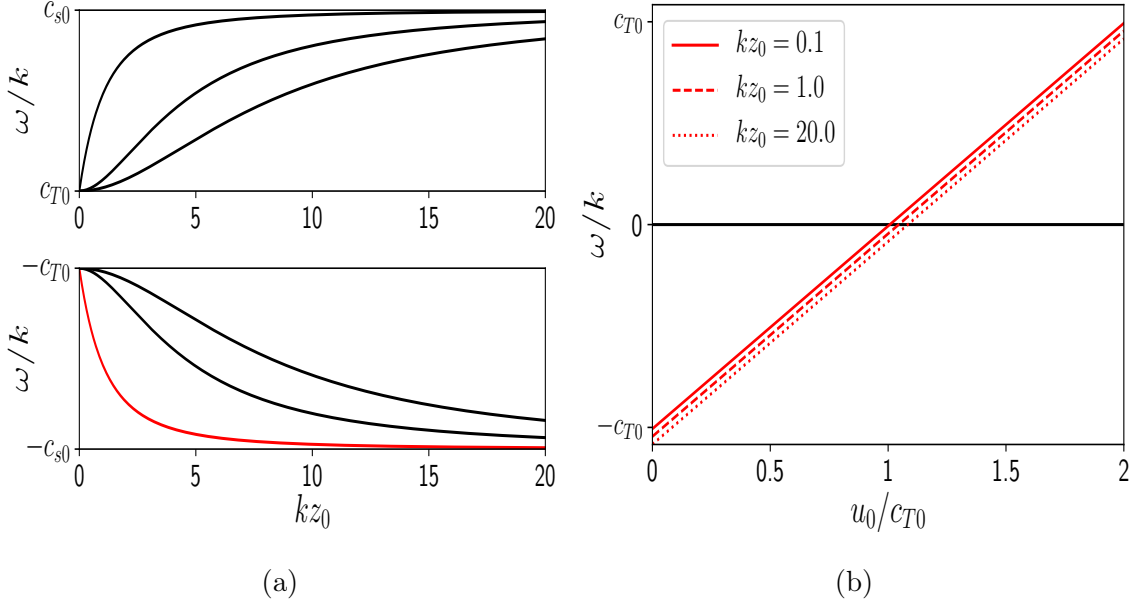


Fig. 6.2 (a) Variation of the phase speed,  $\omega/k$ , for forward (upper panel) and backward (lower panel) propagating body waves in the bounds  $c_{T0} < |\omega/k| < c_{s0}$  with respect to  $kz_0$  (b) variation of  $\omega/k$  with respect to  $u_0/c_{T0}$  for the mode indicated in red in panel (a) for  $kz_0 = 0.1, 1.0$  and  $20.0$ . The background speeds satisfy:  $v_{Ae} > c_{se} > c_{T0} > v_{A0} > c_{s0} > c_{T0}$ .

see from the slender slab limits given by Eqs. (6.29)-(6.34) that only the solution for the sausage mode, given by Eq. (6.30), can change sign and does so when  $u_0 \approx c_{T0}$  for the backward propagating wave and  $u_0 \approx -c_{T0}$  for the forward propagating wave. In Fig 6.2a we have plotted the slow body wave solutions, both backward and forward propagating. Taking the backward propagating body mode highlighted in red, Fig. 6.2b plots the variation of  $\omega/k$  for  $kz_0 = 0.1, 1, 20$  with respect to  $u_0/c_{T0}$ . There is clearly a linear relationship and the sign of  $\omega/k$  changes at approximately  $u_0 = c_{T0}$ . Having noted this, when the sign of the frequency does change, we then have a positive value for  $\omega'$  and the wave grows in amplitude. We can therefore see that in this case the dissipative instability is in fact a negative energy wave instability, with the dissipation caused by viscosity.

#### 6.4.2 The slender-slab limit ( $kz_0 \ll 1$ )

The slender slab limit is a useful tool to analyse the modes and the dissipative instabilities that occur in our system. Referring to Eqs. (6.29), (6.30), (6.33) and (6.34), it can be noted that only the mode described by Eq. (6.30) is affected by the background flow and is thus the only mode that is likely to change its direction of propagation as the magnitude of the flow is increased. We therefore focus our attention on this mode as it is the only candidate for which the dissipative instability may be present, in the slender slab limit. Inserting the approximate root given by

Eq. (6.30) into Eq. (6.23), whilst using the approximate forms given by Eqs. (6.35) and (6.37), we find an approximate equation for  $\omega'$ :

$$\omega' = \mp \left[ \rho_r \frac{c_{s0}^4 k^2 v (\pm c_{T0} + u_0) [(\pm c_{T0} + u_0)^2 - 3c_{se}^2]^2}{12 [(\pm c_{T0} + u_0)^2 - c_{se}^2]^2 c_{T0} (v_{A0}^2 + c_{s0}^2)^2} \hat{M}_e k z_0 \right. \\ \left. \pm \frac{\eta_C v_{A0}^2 c_{s0}^4 k^2}{2c_{T0}^2 (v_{A0}^2 + c_{s0}^2)^2} \right]. \quad (6.44)$$

Here,  $\rho_r = \rho_e/\rho_0$  is the relative density of our equilibrium and the Cowling resistivity,  $\eta_C$ , is given by

$$\eta_C = \frac{v_{A0}^2 m_n (2\mu - 1)}{2\rho_0 (1 - \mu) \Sigma_{in}} \sqrt{\frac{\pi m_p}{k_B T_0}}, \quad (6.45)$$

where  $m_n$  is the mass of neutral atom,  $\Sigma_{in} = 5 \times 10^{-15} \text{ cm}^2$  is the ion-neutral collisional cross section and  $\mu$  is the ionisation degree of the plasma given by:

$$\mu = \frac{\rho_0}{2\rho_i + \rho_n},$$

with  $\mu = 0.5$  corresponding to a fully ionised plasma and  $\mu = 1.0$  a completely neutral plasma. In our calculations, we assume that  $\rho_0 = 5 \times 10^{-11} \text{ kg m}^{-3}$ . Using prominence parameters we can estimate the *Magnetic Reynolds number*,  $R_m$  for this particular set up. We define

$$\hat{\eta}_C = \frac{v_{A0}^2 m_n}{2\rho_0 \Sigma_{in}} \sqrt{\frac{\pi m_p}{k_B T_0}}, \quad \eta_C = \hat{\eta}_C \frac{2\mu - 1}{1 - \mu}. \quad (6.46)$$

We then have, using a length scale of approximately  $10^7 \text{ m}$  and typical prominence wave speeds of  $10^4 \text{ m s}^{-1}$ ,

$$R_m \approx 10^4 \frac{1 - \mu}{2\mu - 1}. \quad (6.47)$$

The sign of the imaginary part of the frequency will determine whether a wave will be damped or amplified due to instabilities. According to the ansatz used in the present paper,  $\omega' > 0$  would mean that the wave is amplified, while waves will be damped in the opposite case i.e. when  $\omega' < 0$ .

Eq. (6.44) can be used to find the critical flow speed required for the dissipative instability to occur, although it would result in finding a solution to a sixth order polynomial which cannot be done analytically. The case we study is that of a relatively cold chromospheric slab surrounded by hot coronal material with similar magnetic fields and, as such, the density ratio is small i.e.  $\rho_r \ll 1$ . All the characteristic background speeds within the slab are therefore much smaller than outside the

slab. In this limit, the imaginary part of the frequency given by Eq. (6.44) can be approximated as

$$\omega' \approx \mp \frac{c_{s0}^4 k^2 \left[ \frac{3}{2} \rho_r v (\pm c_{T0} + u_0) k z_0 \pm \frac{\eta_C v_{A0}^2}{c_{T0}} \right]}{2 c_{T0} (v_{A0}^2 + c_{s0}^2)^2}, \quad (6.48)$$

where the two signs denote the forward and backward propagating wave. The straight-forward result that is obvious from Eq. (6.48) is that  $\omega'$  for the forward propagating wave (corresponding to the upper sign) is always negative, and, therefore, the forward propagating wave is always subject to damping. In contrast, the backward propagating wave (corresponding to the lower sign) is damped only for a particular combination of values, but it may become positive for flows that are larger than the critical value

$$u_{0c} = c_{T0} + \frac{2\eta_C v_{A0}^2}{3\nu\rho_r k z_0 c_{T0}}. \quad (6.49)$$

In the absence of Cowling resistivity ( $\eta_C = 0$ , i.e. the plasma is fully ionised), the instability occurs at flow speeds equal to  $c_{T0}$ . When neutrals are present in the system (i.e.  $\eta_C \neq 0$ ) and the plasma is less ionised, the Cowling resistivity tends to stabilise the system by increasing the threshold where instability can appear. In the limit of an incompressible plasma, (i.e.  $c_{s0} \rightarrow \infty$ ), the critical flow speed becomes

$$u_{0c} = v_{A0} + \frac{2\eta_C v_{A0}}{3\nu\rho_r k z_0}, \quad (6.50)$$

and, therefore, modes might become unstable for super-Alfvénic flows. This result suggests that once compressibility is taken into account, the plasma can become unstable at lower flow speeds ( $c_{T0} < v_{A0}$ ) (a lower critical flow speed is needed for the dissipative instability to occur), so compressibility tends to destabilise the plasma.

As specified earlier, the whole partially ionised prominence is modelled here by a slab that is surrounded by the fully ionised corona. In general, the width of prominences varies between approximately 1-30 Mm (Lin, 2011). Observations of waves in prominences show that typical wave-numbers are between  $10^{-8}$  and  $10^{-6}$   $\text{m}^{-1}$ , meaning that the slender slab limit is justified to a large extent. However, this does not cover the whole spectrum of possible values.

We consider a slab width of  $\approx 1$  Mm, so that the set value of  $k z_0 = 0.01$  corresponds to a wave-number of  $k = 2 \times 10^{-7}$   $\text{m}^{-1}$ , while the dimensionless quantity  $k z_0 = 0.02$ , corresponds to the wave-number  $k = 4 \times 10^{-7}$   $\text{m}^{-1}$ . We assume that the temperature of the prominence is  $T_i = 10^4$  K that corresponds to a sound speed of  $c_{s0} = 11.7$   $\text{km s}^{-1}$ . Assuming an Alfvén speed of  $v_{A0} = 28.0$   $\text{km s}^{-1}$  results in a

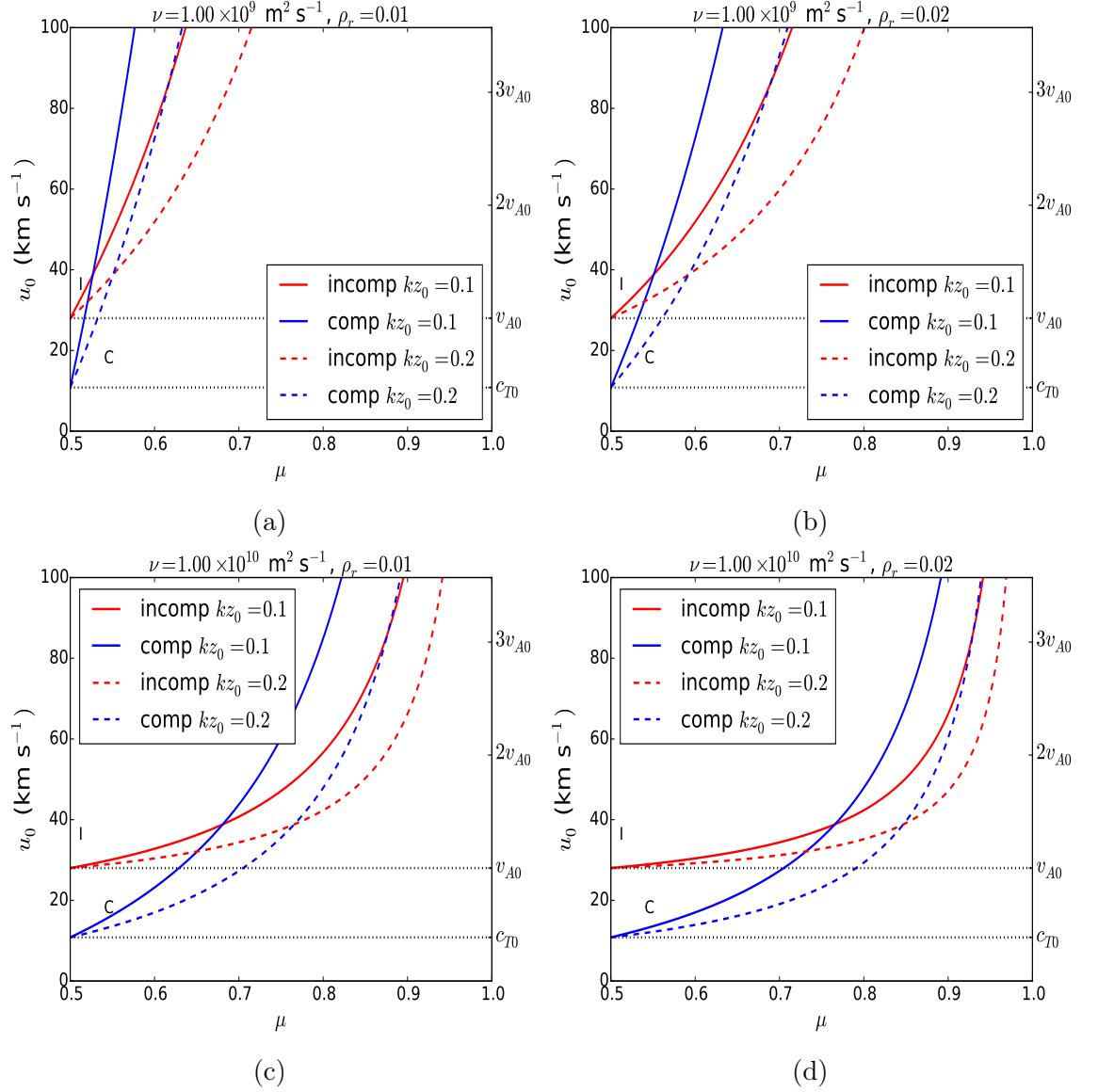


Fig. 6.3 The variation of the critical flow speed with respect to ionisation degree,  $\mu$ , for the compressible case (blue lines), given by Eq. (6.49), and the incompressible case (red lines), given by Eq. (6.50): (a) and (b) both with  $\nu = 10^9 \text{ m}^2 \text{ s}^{-1}$  but with  $\rho_r = 0.01$  and  $\rho_r = 0.02$  respectively and (c) and (d) both with  $\nu = 10^{10} \text{ m}^2 \text{ s}^{-1}$  but with  $\rho_r = 0.01$  and  $\rho_r = 0.02$  respectively. In each the solid lines (—) indicate  $kz_0 = 0.1$  and the dashed lines (- - -) indicate  $kz_0 = 0.2$ . The regions under the curves correspond to the stable regime.

tube speed of  $c_{T0} = 10.8 \text{ km s}^{-1}$ . When  $\rho_r = 0.02$  the coronal characteristic speed are (assuming the same magnetic field strength in all regions):  $v_{Ae} = 198.0 \text{ km s}^{-1}$ ,  $c_{se} = 83.0 \text{ km s}^{-1}$  and  $c_{Te} = 76.5 \text{ km s}^{-1}$ . When  $\rho_r = 0.01$  the coronal characteristic speeds become  $v_{Ae} = 280.0 \text{ km s}^{-1}$ ,  $c_{se} = 117.0 \text{ km s}^{-1}$  and  $c_{Te} = 108.0 \text{ km s}^{-1}$ .

The variation of the critical flow speed with the ionisation degree for a compressible (based on Eq. 6.49) and incompressible (based on Eq. 6.50) plasma is shown in Figure 6.3. The top two panels correspond to a viscosity coefficient of  $\nu = 10^9 \text{ m}^2\text{s}^{-1}$  that leads to a viscous Reynolds number of  $R \approx 10^4$  with typical length scales of  $10^7 \text{ Mm}$  and typical velocities of  $10^5\text{-}10^6 \text{ m s}^{-1}$ . The variation of the critical speed is studied for two distinct values of the density ratio between the corona and chromosphere ( $\rho_r = 0.01$  and  $\rho_r = 0.02$ ). The bottom two panels show the variation of the critical flow speed for a viscosity coefficient of  $\nu = 10^{10} \text{ m}^2\text{s}^{-1}$  (corresponding to a Reynolds number of  $R \approx 10^3$ ), for the same density ratios as before. In these plots, the ionisation degree,  $\mu$ , varies between 0.5 (fully ionised plasma) to 1 (fully neutral fluid) and for different values of the dimensionless quantity  $kz_0$ .

These figures clearly show that, in the case of a fully ionised plasma, the instability occurs at flows speeds that have realistic values and the critical value of the flow for compressional plasma ( $u_{0c} = c_{T0}$ ) is approximately half of the flow necessary to induce an instability in an incompressible plasma ( $u_{0c} = v_{A0}$ ). When the concentration of neutrals is increased, there is a critical value of this ionisation degree after which the critical flow corresponding to the incompressible plasma is lower. At this point the curves representing the critical flows intersect. When either  $kz_0$  or  $\rho_r$  are increased the value of  $\mu$  at which the solutions cross is increased and the gradients of the flow with respect to  $\mu$  decrease. It is possible to find the critical value,  $\mu_c$ , when the solution paths cross, by equating Eqs. (6.49) and (6.50)

$$\mu_c = \frac{1 + \frac{2\hat{\eta}_C}{3\nu\rho_r kz_0} \frac{v_{A0}}{c_{T0}}}{1 + \frac{4\hat{\eta}_C}{3\nu\rho_r kz_0} \frac{v_{A0}}{c_{T0}}}. \quad (6.51)$$

It has to be borne in mind that this relation only applies for the plasma stated above and only sausage modes and is not a universal relation.

It is evident from Figs. 6.3a-d that viscosity has a destabilising effect for the backward propagating waves when the plasma is not completely ionised. Conversely, as we have explained above, the neutrals present in the plasma serve to stabilise the prominence. Comparing Figs. 6.3a and c, one can see that the steepness of the curves is reduced when the viscosity coefficient is increased from  $\nu = 10^9 \text{ m}^2\text{s}^{-1}$  to  $\nu = 10^{10} \text{ m}^2\text{s}^{-1}$ . This is also evident when comparing Figs. 6.3b and d. This can be explained easily from Eqs. (6.49) and (6.50) as when the viscous coefficient is increased in comparison to  $\eta_C$  this will reduce  $u_{0c}$  for both the incompressible

and compressible cases. Comparing Figs. 6.3a and b and Figs. 6.3c and d, the increase in the density ratio,  $\rho_r$  serves to decrease  $u_{0c}$  for both the compressible and incompressible cases as well, again obvious from Eqs. (6.49) (6.50). Interesting also is that the increase in  $kz_0$  decreases  $u_{0c}$ , this motivates using the numerical solutions to Eq. (6.23) to study the effect of increasing  $kz_0$  on this threshold for  $u_{0c}$ .

Figs. 6.4a-d show a contour plot for the variation of the imaginary part of the frequency,  $\omega'$  with respect to the background flow,  $u_i$ , and the ionisation degree,  $\mu$ . Figs. 6.4a and b are plotted for the values  $\rho_r = 0.01$ ,  $kz_0 = 0.1$  and  $k = 2 \times 10^{-7} \text{ m}^{-1}$  but with  $\nu = 10^9 \text{ m}^2\text{s}^{-1}$  and  $\nu = 10^{10} \text{ m}^2\text{s}^{-1}$  respectively. Figs. 6.4c and d we used  $\rho_r = 0.02$ ,  $kz_0 = 0.2$  and  $k = 4 \times 10^{-7} \text{ m}^{-1}$  along with  $\nu = 10^9 \text{ m}^2\text{s}^{-1}$  and  $\nu = 10^{10} \text{ m}^2\text{s}^{-1}$  respectively. Again, it is evident from the  $\omega' = 0$  contour and by comparing Figs. 6.4a and c and Figs. 6.4b and d that increasing  $kz_0$  and  $\rho_r$  decreases the speed  $u_0$  at which the imaginary part of the frequency,  $\omega'$ , changes sign and instability ensues. We can also see from this how the neutrals play a role. By increasing  $\mu$ , which is equivalent to increasing the number of neutrals in the system, and holding every other variable constant,  $\omega'$  decreases in line with this. Comparing Figs. 6.4a and b and Figs. 6.4c and d we can see that increasing the value of the kinematic viscosity coefficient,  $\nu$ , serves to increase the value of  $\omega'$  and thus increases the magnitude of  $\omega'$ . The increase in  $\nu$  also decreases the threshold at which the instability occurs as has been discussed. What must be noted is that this is the slender slab limit and is therefore very restrictive and as such the actual time-scales shown for the amplification and damping rates are very large, on the order of  $10^6 - 10^7 \text{ s}$ . The slender slab limit only gives a guide as to when the instability occurs and the physics involved. This is why a numerical approach must be taken to ascertain whether this instability can occur on the time-scale of the life time of prominences.

### 6.4.3 Wide Slab

Having studied the slender slab limit, we make a mention of the wide slab limit. Exactly as in the slender slab limit, we are considering an interface between two plasmas in which  $\rho_r \ll 1$ , with equal magnetic fields in and outside the slab. Therefore, all the characteristic background speeds within the slab are much smaller than outside the slab. We can thus further approximate  $\omega'$  from Eq. (6.41) to

$$\omega' \approx \mp \frac{k^2 c_0^3 \pi^2 \left(j - \frac{1}{2}\right)^2}{2 \left(v_{A0}^2 - c_{s0}^2\right)^2 (kz_0)^2} \left( \rho_r \frac{3\nu(u_0 \pm c_{s0})}{kz_0} \pm \frac{\eta c v_{A0}^2}{c_{s0}} \right). \quad (6.52)$$

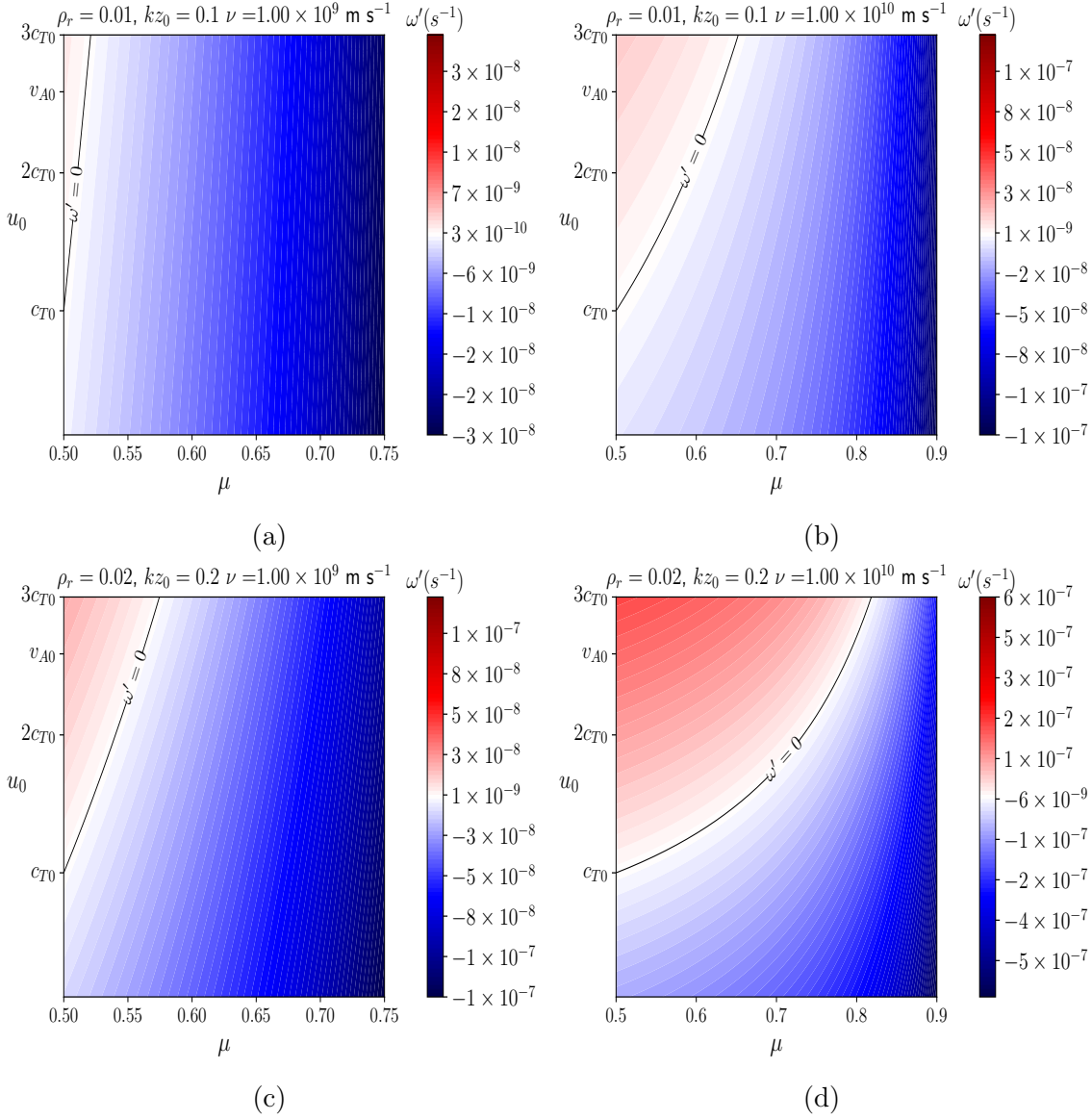


Fig. 6.4 Contour plots showing the variation of  $\omega'$  with respect to the internal background flow speed,  $u_0$ , and the ionisation degree  $\mu$ . Red indicates a positive value of  $\omega'$  (amplification) and blue indicates a negative value of  $\omega'$  (damping). The color bar shows the numerical value of  $\omega'$  and the contour labelled  $\omega' = 0$  indicates the transition between amplification and damping of the wave. Panels (a) and (b) are both constructed by using the parameters  $\rho_r = 0.01$ ,  $k z_0 = 0.1$  and  $k = 2 \times 10^{-7} \text{ m}^{-1}$  but with  $\nu = 10^9 \text{ m}^2 \text{ s}^{-1}$  and  $\nu = 10^{10} \text{ m}^2 \text{ s}^{-1}$ , respectively. In panels (c) and (d) we used  $\rho_r = 0.02$ ,  $k z_0 = 0.2$  and  $k = 4 \times 10^{-7} \text{ m}^{-1}$  along with  $\nu = 10^9 \text{ m}^2 \text{ s}^{-1}$  and  $\nu = 10^{10} \text{ m}^2 \text{ s}^{-1}$ , respectively.

For amplification to occur  $\omega' > 0$ . As in the slender slab limit, it is possible to find an approximate speed at which amplification occurs. We therefore set the numerator of Eq. (6.52) to zero to find the critical flow speed,  $u_{0c}$ , for marginal stability.

$$|u_{0c}| = c_{s0} \left( 1 + \frac{\eta C k z_0 v_{A0}^2}{3 \nu \rho_r c_{s0}^2} \right). \quad (6.53)$$

We have used a modulus sign here as, if the wave is forward propagating, the critical flow speed will be negative and positive for a backward propagating wave. From Eq. (6.53) it is clear that the wider the prominence the more stable it is when neutrals are present.

The slender and wide slab limits only gives a guide as to if an instability occurs, as well as the physics involved. This is why a numerical approach must be undertaken to ascertain whether this instability can occur on the time-scale of prominence life-times.

#### 6.4.4 Numerical solutions

The analysis using the slender slab limit is very useful as a guide towards understanding the nature and behaviour of the modes present in the system. However, this limit is restrictive due to the size of prominences, for which the condition  $kz_0 \ll 1$  is not satisfied. Therefore, it is instructive to solve numerically Eq. (6.18) and approximate the imaginary part of the frequency using Eq. (6.23) for the sausage waves i.e. the tanh solution. Figures 6.5 and 6.8 show the variation of the imaginary part of the frequency ( $\omega'$ ), with respect to the dimensionless wave-number,  $kz_0$ , for three different values of the ionisation degree and the same viscosity coefficient. In both figures, the top panels correspond to a density ratio of  $\rho_r = 0.01$ , while the bottom panels were obtained for  $\rho_r = 0.02$ . The value of the background flow was chosen to be  $u_0 = 16 \text{ km s}^{-1}$  (just above the internal tube speed,  $c_{T0}$ , in the left-hand side panels) and  $u_0 = 28 \text{ km s}^{-1}$  (close to the internal Alfvén speed,  $v_{A0}$ , in right-hand side panels), respectively. The variation of the damping/amplification rate is plotted against the dimensionless quantity  $kz_0$ , keeping  $k = 5 \times 10^{-6} \text{ m}^{-1}$  and allowing the width of the slab  $2z_0$ , to vary, see Fig. 6.5). In Fig. 6.8, we plot the same quantity, but now the width of the slab is maintained constant at  $2z_0 = 4 \text{ Mm}$  (Fig. 6.5) and  $k$  is allowed to vary. In all cases, a horizontal line is drawn at the  $\omega' = 0$  level in order to clearly identify the behaviour of the rate of change of the amplitude.

Figure 6.5 shows that at flow speeds just above the internal tube speed of the prominence, the pseudo-body mode and the  $n = 1$  body modes are unstable when  $\mu = 0.5$ , i.e. when the prominence is fully ionised. Increasing the ionisation fraction (i.e. more neutrals are taken into account), all modes become stable and their amplitudes are damped, with the pseudo-body mode being the most damped. This

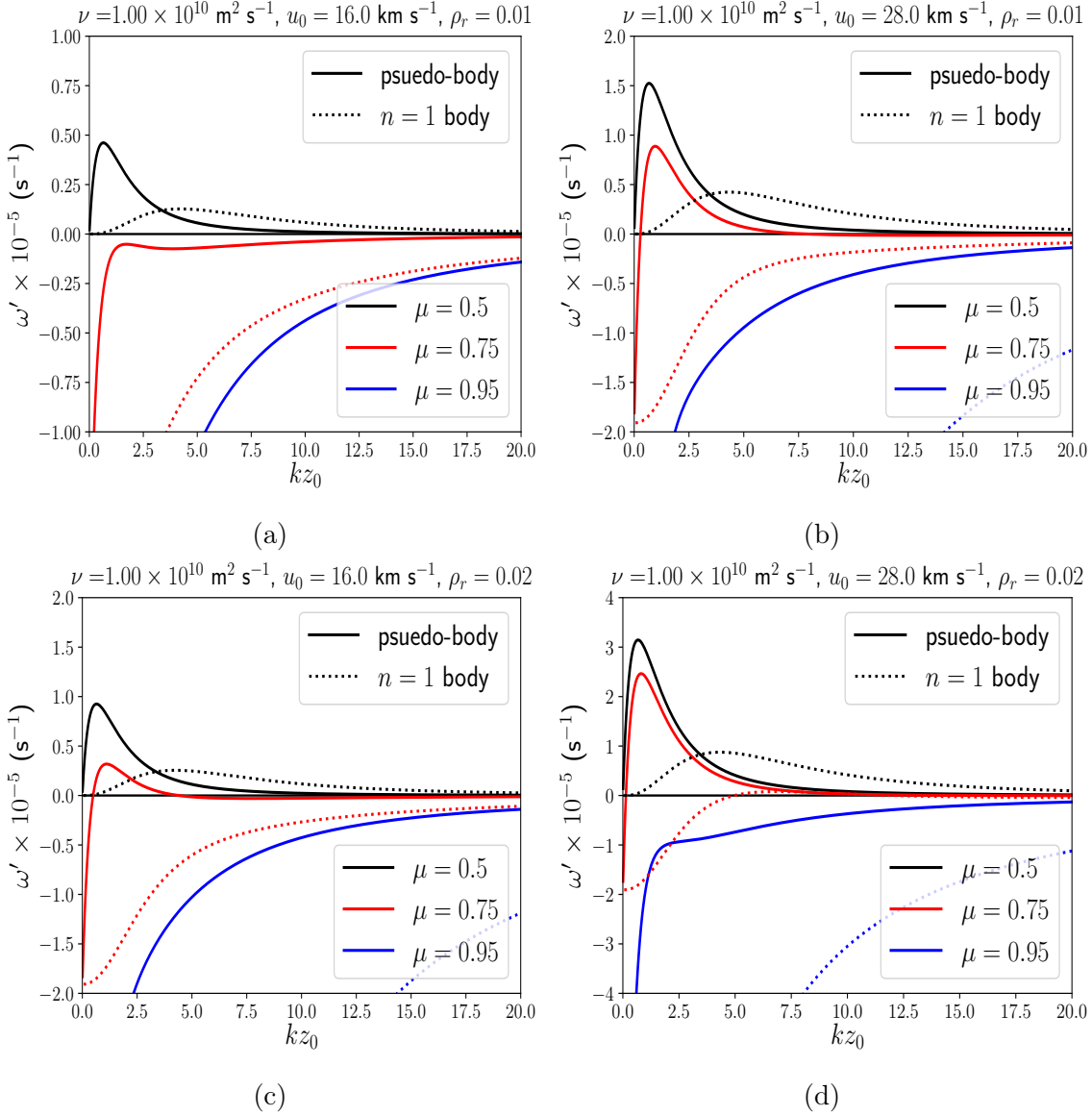


Fig. 6.5 Variation of the imaginary part of the frequency,  $\omega'$ , for pseudo-body (—) and  $n = 1$  ( $\cdot \cdot$ ) body mode with respect to dimensionless wave-number,  $kz_0$ . We fix the wavenumber at  $k = 5 \times 10^{-6} \text{ m}^{-1}$  with the slabwidth varying. For each separate diagram, the background flow speed has been taken to be  $u_0 = 16.0 \text{ km s}^{-1}$  and  $u_0 = 28.0 \text{ km s}^{-1}$ , respectively. Panels (a) and (b) correspond to  $\rho_r = 0.01$ , while panels (c) and (d) to  $\rho_r = 0.02$ . All panels (a)-(d) use a viscosity coefficient of  $\nu = 10^{10} \text{ m}^2 \text{ s}^{-1}$ . Black lines denote an ionisation degree of  $\mu = 0.5$ , red and blue lines correspond to  $\mu = 0.75$  and  $\mu = 0.95$ , respectively.

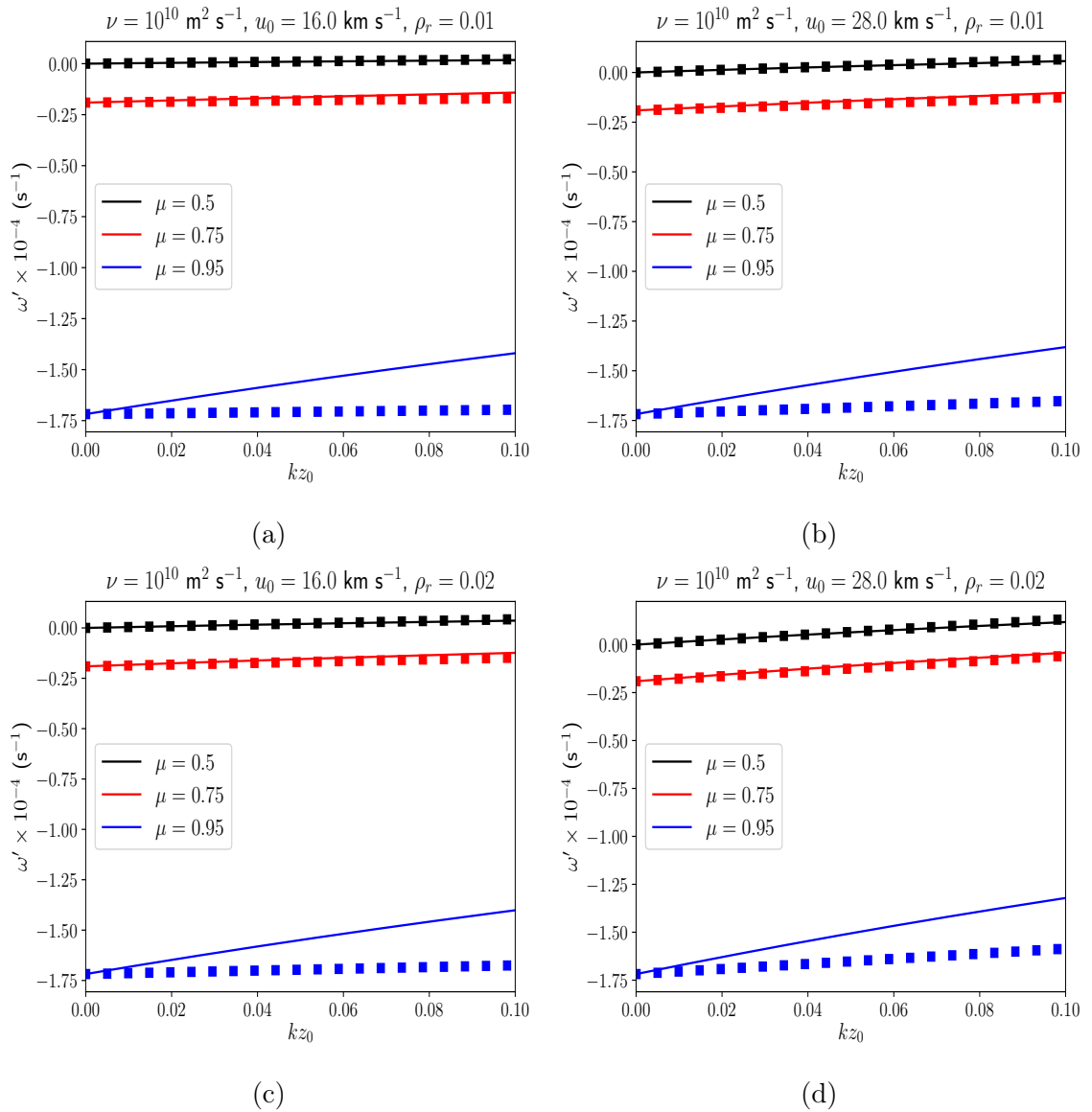


Fig. 6.6 Comparison of the variation of the imaginary part of the frequency,  $\omega'$ , with respect to dimensionless wave-number,  $kz_0$ , for the approximate analytical solution given by Eq. (6.48), shown as square markers, as compared to the numerical solution given by Eq. (6.19), shown as solid lines. All parameter values are identical to Fig. 6.5. The colours black, red and blue used for markers and lines refer to  $\mu = 0.5$ , 0.75 and 0.95, respectively.

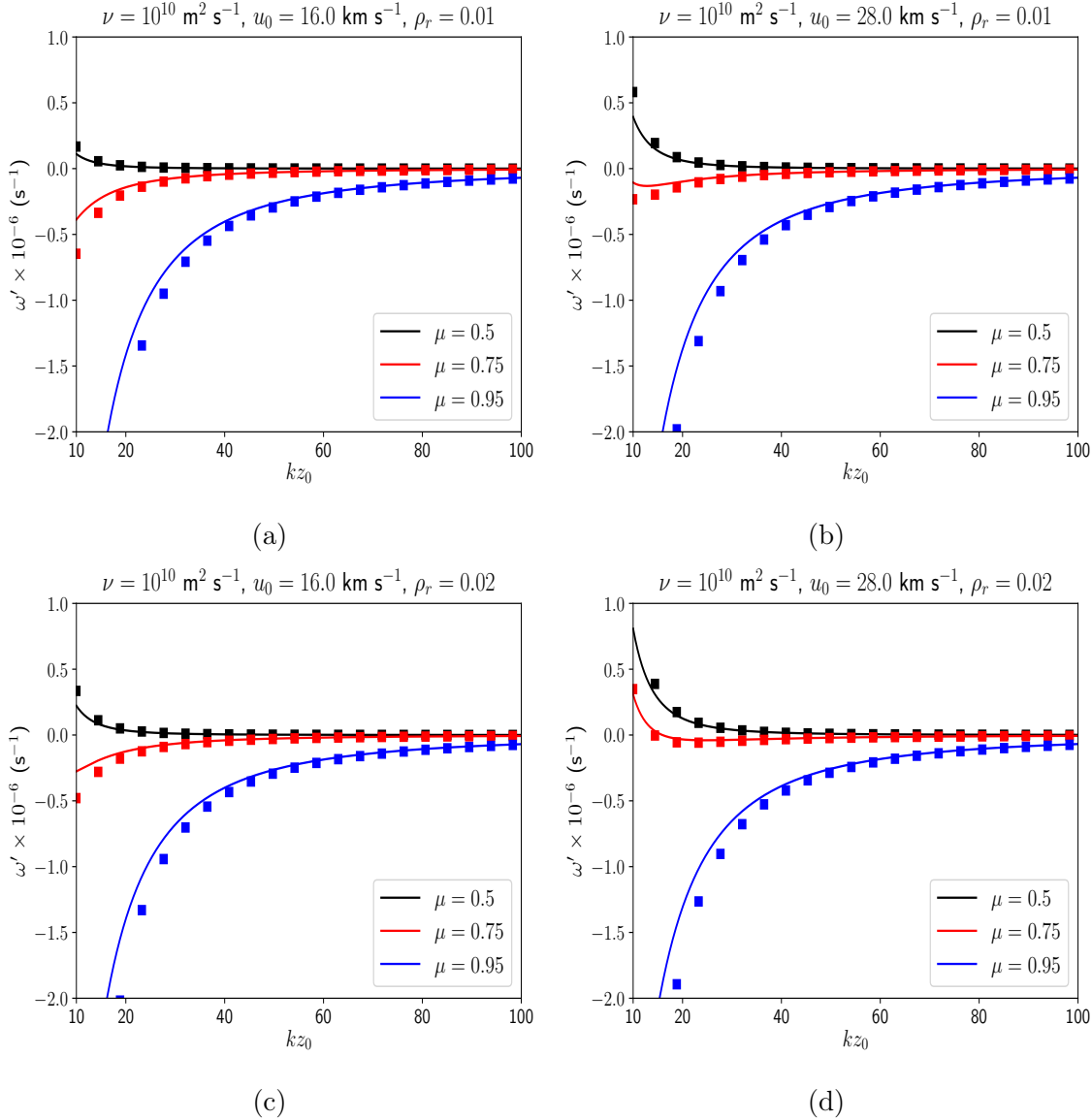


Fig. 6.7 Same as Fig. 6.6 but for the wide slab limit given by Eq. (6.52) and variation of  $kz_0$  from 10 to 100.

results confirms earlier findings that neutrals have a stabilising effect. As  $kz_0$  is increased (i.e. for larger slab sizes) both the damping and amplification of modes is reduced. When the equilibrium flow is increased to  $u_0 = 28 \text{ km s}^{-1}$  (Fig. 6.5b) modes will use the increased flow speed for additional energy and waves will become unstable much more easily. Now, the increased amount of neutrals is not enough to completely stabilise the body mode; the body mode corresponding to  $\mu = 0.75$  is stable only for very a thin slab. For an even larger concentration of neutrals ( $\mu = 0.95$ ), both the body and pseudo-body mode are damped. Comparing the results obtained for the two flow values we can observe that the amplification rate increases with the value of the equilibrium flow.

When the density contrast between the prominence and corona is increased the qualitative behaviour of modes in the fully ionised case does not change, however,

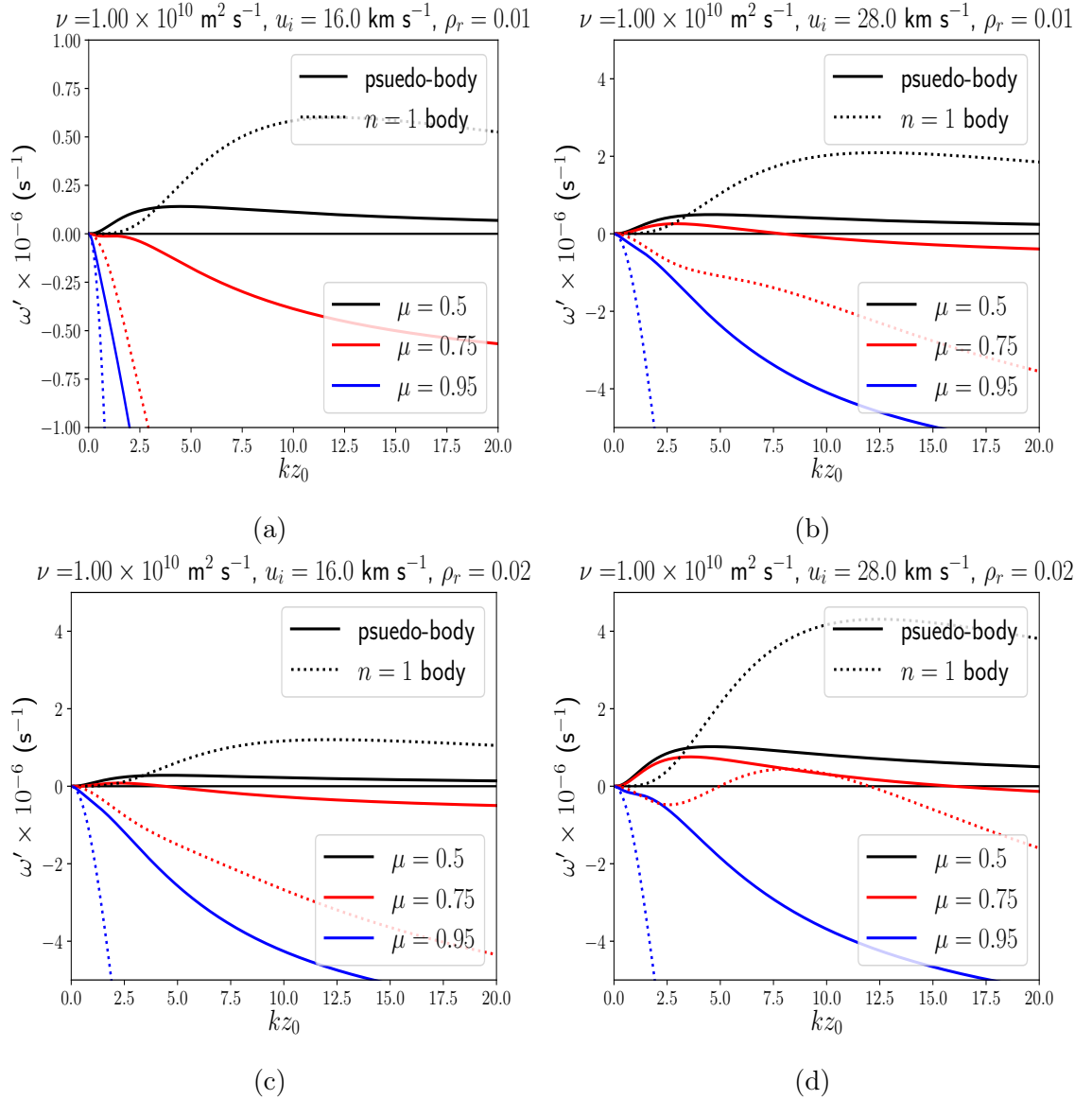


Fig. 6.8 Same as Fig. 6.5, but with the width of the slab fixed at  $z_0 = 4$  Mm and the wavenumber now the varying quantity.

significant variations occur in the behaviour of the pseudo mode corresponding to  $\mu = 0.75$ . At this concentration of neutrals, the pseudo-body mode remains stable only for large wavelengths after which it becomes unstable. For a value of  $kz_0 \approx 4$ , the mode becomes stable again (see Fig. 6.5c). This latter effect is attributed to both dispersion and the density ratio. We can see in the wide slab limit the critical flow speed given by Eq. (6.53) is proportional to  $kz_0/\rho_r$ . If we use this limit as a guide we find by inputting the parameters of  $\rho_r = 0.02$ ,  $\mu = 0.75$  and  $kz_0 = 10$  that the critical flow speed is  $u_{0c} = 23.1 \text{ km s}^{-1}$ . Therefore with a flow velocity of  $u_0 = 16 \text{ km s}^{-1}$ , the flow velocity is not large enough for instability in the wide slab limit.

Finally, when the equilibrium flow is increased the pseudo-body mode corresponding to an ionisation degree of 0.75 stays stable only for very large wavelengths. The  $n = 1$  body modes becomes unstable for a given value of  $kz_0$ . These results confirms

our finding that an increased flow speed is generating instability in modes. The peak amplification rate is seen to be at around  $kz_0 \approx 1$  in Fig. 6.5d for  $\mu = 0.5$  (fully ionised) in which  $\omega' \approx 0.3 \times 10^{-4} \text{ s}^{-1}$  that gives an amplification time-scale of  $\sim 3 \times 10^4 \text{ s}$ .

When the magnetic slab width is kept constant (Fig. 6.8) the variation of the imaginary part of frequency is investigated between the limits of long and short wavelength. All figures reveal that the most unstable/damped regime appears in the short wavelength approximation, although these will eventually tend to zero. The body mode appears to be the most affected by this increase in the wave-number. This is most likely due to the fact that the length scale on which dissipation acts becomes smaller and therefore dissipation becomes more important. For short wavelengths, all rates tend to zero. Mathematically this is expected, as in wide slab limit ( $kz_0 \gg 1$ ) given by Eq. (6.41),  $\omega' \propto 1/(kz_0)^2$ , and therefore will decrease to zero as  $kz_0 \rightarrow \infty$ . Similar to the previous case, the amplification rate for  $\mu = 0.5$  increases by a factor of two when the flow speed is increased. The maximum of the amplification rate occurs at larger wavelengths, once the concentration of neutrals is increased. Similar enhancement of the damping/amplification rate can be observed when the density contrast is increased. However, the time-scales of the instabilities seem to be far too large, being approximately  $\sim 10^6 \text{ s}$ . The damping rate can be of at least an order of magnitude larger for  $\mu = 0.95$  and, as such, the neutrals can cause damping of waves on realistic time-scales.

## 6.5 Summary and Discussion

In this chapter, we studied the effect of partial ionisation on the dissipative instability (negative energy wave) that occurs for surface waves within a magnetic prominence slab suspended in a viscous corona.

We derived the dispersion relation for this model and were able to find an approximate form for the imaginary part of the frequency using a Taylor expansion around the ideal solution, due to our assumption that both the viscous and magnetic Reynolds numbers were large. We, then, took the slender slab limit of Eq. (6.18) to find approximate frequencies for the slow sausage wave. This in turn was then used to find the critical flow speed,  $u_{0c}$ , given by Eq. (6.49), at which modes would no longer be damped but actually grow in amplitude. It was found that in this case the instability could occur for the backward propagating slow sausage wave at the tube speed, which in the prominence plasma we considered was about  $14 \text{ km s}^{-1}$ . If, however, the Cowling resistivity was included this would increase the threshold for instability. The threshold was found to increase further still if more neutral atoms were present in the prominence, this is due to the increasing importance of the Cowling resistivity when more neutrals are present. Plotting the imaginary part

of the frequency as a function of both the flow speed and the ionisation fraction  $\mu$ , it was found, however, that the damping and amplification rate would mean the time-scale of these processes would be on the order of  $\sim 10^6$  s.

The slender slab limit is rather restrictive, however, so a numerical solution to Eq. (6.18) was required so that the sign and value of the imaginary part of the frequency could be attained for a greater range of  $kz_0$ . The full numerical solution was plotted in both Figs. 6.5 and 6.8 holding the wave number,  $k$ , constant and then the slab width,  $2z_0$  constant, respectively. It was found that  $\omega'$  could indeed be larger than  $10^{-7} \text{ s}^{-1}$  and even on the order of  $10^{-5} \text{ s}^{-1}$  for a completely ionised plasma at  $kz_0 \approx 2.0$ . On increasing the ionisation degree the peak amplification rate was lowered and with  $\mu = 0.95$  no amplification would occur.



# Chapter 7

## Resonant Flow Instabilities in the Two-Fluid Slab

### 7.1 Introduction

The temperature of the solar atmosphere can vary from around 4000 K in the photosphere and chromosphere to over 1 MK in the corona. The plasma is mainly composed of Hydrogen and, as such, the corona will almost certainly be a fully ionised plasma. However, in photospheric and chromospheric structures where the temperatures are much lower the plasma may be partially ionised. In chapter 5 we considered a partially ionised prominence plasma but in the single fluid approximation where the frequency of the collisions between the ions and neutrals was assumed to be much larger than the frequency of the waves. The main contribution from the neutrals was assumed to be in the Cowling resistivity term in the induction equation. The single fluid approximation clearly does not account for the collisions between the neutrals and ions in the momentum equations of the respective species.

The Sun is a highly dynamical object and for that reason it is in a continual state of flux. Many phenomena in the solar atmosphere exhibit flows. Flows in a fully ionised plasma can lead to the Kelvin-Helmholtz instability, however, flows must usually be higher than the mean square of the Alfvén speed for the instability to occur, when the flow is parallel to the magnetic field (see e.g. [Chandrasekhar, 1961](#)). However, the situation can be slightly different in a multi-fluid plasma. The neutrals cannot feel the force exerted by the magnetic field and as such different physics is at play.

[Watson \*et al.\* \(2004\)](#) studied the Kelvin-Helmholtz instability at the interface between two incompressible and weakly ionised plasma layers. It was found that the ion-neutral collisions do not inhibit the instability of the neutrals for velocity shears below the Alfvén speed. [Soler \*et al.\* \(2012\)](#) studied the Kelvin-Helmholtz instability at the interface of two compressible plasma layers. In contrast to the incompressible

case, it was found that the Kelvin-Helmholtz instability in the neutrals was rather dependent on the plasma parameters, finding that if the density contrast was high between the two layers the neutrals were more unstable and the KHI was present for velocity shears below the Alfvén speed. [Hendrix and Keppens \(2014\)](#) studied the KHI in a numerical model of a fluid with both neutral and dust particles as constituents. It was found that the dust particles reduced the growth rate of the instability, especially for small-wavelengths.

Many chromospheric structures can be modelled as in a slab or cylindrical geometry. [Soler \*et al.\* \(2013\)](#) considered the case of a fully collisional two fluid plasma, modelled in a cylindrical coordinate system. They studied the propagation of the waves in such a system, finding the appearance of cut-off regions for specific collision frequencies and ion and neutral density ratios. [Soler \*et al.\* \(2013\)](#) studied the KHI in an incompressible flux tube, finding again that the KHI would occur for any flow shear and for a high collisions between ions and neutrals. [Ballai \*et al.\* \(2017b\)](#) studied the KHI in an incompressible prominence plume modelled as a two fluid plasma slab. It was found that the neutrals would always be unstable, if a low collisional frequency was taken.

None of these cases above (or otherwise) have studied a compressible plasma slab. In this section we investigate the effect of flow and collisions between neutrals on the stability of the ion and neutral plasma. We derive the governing equations and a dispersion relation for this case. We firstly take the incompressible limit of the dispersion relation and then consider the limit of a highly collisional plasma to first order and the sign of the imaginary part of the frequency. We then take the collision-less limit and finally the highly collisional limit.

## 7.2 Linearised Two Fluid MHD Equations and Governing Equation

We consider a collisional two-fluid plasma consisting of both ion and neutral species in a Cartesian coordinate system, governed by Eqs. (1.31)-(1.37). The equilibrium background plasma is embedded within a constant magnetic field in the  $x$ -direction i.e.  $\mathbf{B} = (B_0, 0, 0)$ . There are equal constant background flows for both the ions and neutrals. i.e.  $\mathbf{v}_{i0} = (u, 0, 0)$  and  $\mathbf{v}_{n0} = (u, 0, 0)$  and we neglect any form of dissipation. The background pressure for both the ion and neutral species is considered to be constant in all directions, as is the density and thus the temperature due to the ideal gas law. We linearise Eqs. (1.31)-(1.37) around this background plasma and from now on denote neutral and ion quantities with subscript ‘ $n$ ’ and ‘ $i$ ’ respectively, and use ‘ $\prime$ ’ to denote perturbed quantities and conversely quantities without this are

background quantities (Soler *et al.*, 2012):

$$\frac{D\rho'_i}{Dt} + \rho_{i0}\nabla \cdot \mathbf{v}'_i = 0, \quad (7.1)$$

$$\frac{D\rho'_n}{Dt} + \rho_n\nabla \cdot \mathbf{v}'_n = 0, \quad (7.2)$$

$$\rho_i \frac{D\mathbf{v}'_i}{Dt} = -\nabla P'_T + \frac{1}{\mu}(\mathbf{B} \cdot \nabla)\mathbf{B}' - \rho_n\nu_{in}(\mathbf{v}'_i - \mathbf{v}'_n), \quad (7.3)$$

$$\rho_n \frac{D\mathbf{v}'_n}{Dt} = -\nabla p'_n + \rho_n\nu_{in}(\mathbf{v}'_i - \mathbf{v}'_n), \quad (7.4)$$

$$\frac{D\mathbf{B}'}{Dt} = (\mathbf{B} \cdot \nabla)\mathbf{v}'_i - \mathbf{B}(\nabla \cdot \mathbf{v}'_i), \quad (7.5)$$

$$\frac{DP'_T}{Dt} + \gamma p_i(\nabla \cdot \mathbf{v}'_i) - \frac{1}{\mu} \frac{D(\mathbf{B} \cdot \mathbf{B}')}{Dt} = 0, \quad (7.6)$$

$$\frac{Dp'_n}{Dt} + \gamma p_n(\nabla \cdot \mathbf{v}'_n) = 0. \quad (7.7)$$

Here,  $\nu_{in}$  is the collisional frequency between ions and neutrals,  $\rho'_i$ ,  $p'_i$  and  $\mathbf{v}'_i = (v'_{xl}, v'_{yl}, v'_{zl})$  are the perturbed density, pressure and velocity field,  $\rho_l$ ,  $p_l$  and  $\mathbf{v}_l$  are the background density, pressure and velocity field, where  $l = n, i$ ,  $\mathbf{B}' = (B_x, B_y, B_z)$  and  $\mathbf{B} = (B_0, 0, 0)$  are the perturbed and background magnetic field. We have also introduced the *total pressure* (ion gas plus magnetic),  $P'_T = p'_i + \mathbf{B}' \cdot \mathbf{B}/\mu$  and the material derivative (this is the same when the background velocity fields are identical),

$$\frac{D}{Dt} = \frac{\partial}{\partial t} + u \frac{\partial}{\partial x}.$$

We now assume that perturbations have the form  $f' = \widehat{f}(z) \exp(i(kx - \omega t))$ , where we have assumed there is no variation in the y-direction and so the Alfvén wave decouples from the system and we therefore do not study the perturbations in the y-direction. Eqs. (7.1)-(7.7) then form two coupled second order differential equations for  $P'_T$  and  $p'_n$ . Detailed derivations of these are left for Appendix B.

$$\frac{d^2 \widehat{P}_T(z)}{dz^2} - M_i^2 \widehat{P}_T(z) = q_i \widehat{p}_n(z), \quad (7.8)$$

where

$$M_i^2 = -\frac{(\Omega^2 - k_x^2 v_A^2 + i\Omega\chi v_{in})}{\tilde{D}_T(c_{si}^2 + v_A^2)} \left( \tilde{\Omega}^2 - k^2 c_{si}^2 \frac{\tilde{\Omega}^2 - k^2 v_A^2}{(\Omega^2 - k_x^2 v_A^2 + i\Omega\chi v_{in})} \right), \quad (7.9)$$

and

$$q_i = \frac{i\Omega v_{in}}{D_n c_{sn}^2} \left( D_n - \frac{c_{sn}^2 k^2 v_A^2}{(c_{si}^2 + v_A^2) \tilde{D}_T} \left( \tilde{\Omega}^2 - \frac{\Omega^2 \chi v_{in}^2}{D_n} \right) \right). \quad (7.10)$$

$$\frac{d^2 \widehat{p}_n(z)}{dz^2} - M_n^2 \widehat{p}_n(z) = q_n \widehat{P}_T(z), \quad (7.11)$$

$$M_n^2 = -\frac{\left( \Omega^2 + i\Omega v_{in} - c_{sn}^2 k^2 \left( 1 - \frac{\Omega^2 \chi v_{in}^2 v_A^2}{\tilde{D}_T D_n (c_{si}^2 + v_A^2)} \right) \right)}{c_{sn}^2}, \quad q_n = i\Omega \frac{\chi v_{in} \tilde{\Omega}^2}{(c_{si}^2 + v_A^2) \tilde{D}_T}. \quad (7.12)$$

Here we have defined the Doppler shifted frequency,  $\Omega = \omega - ku$ , the *ion sound speed*,  $c_{si} = (\gamma p_i / \rho_i)^{1/2}$ , the *neutral sound speed*,  $c_{sn} = (\gamma p_n / \rho_n)^{1/2}$  and the *Alfvén speed*,  $v_A = (B_0^2 / \mu_0 \rho_i)$ , along with :

$$\tilde{D}_A = \tilde{\Omega}^2 - k^2 v_A^2, \quad \tilde{D}_{si} = \tilde{\Omega}^2 - k^2 c_{si}^2, \quad \tilde{D}_T = \tilde{\Omega}^2 - k^2 c_T^2, \quad D_n = \Omega^2 + i\Omega v_{in}, \quad (7.13)$$

where  $c_T = c_{si} v_A / (c_{si}^2 + v_A^2)^{1/2}$  is the *tube speed* and

$$\tilde{\Omega}^2 = \Omega^2 \left( 1 + \frac{i\chi v_{in}}{\Omega + i v_{in}} \right), \quad (7.14)$$

is the modified frequency (Kumar and Roberts, 2003 or Soler *et al.*, 2013). We now have obtained two coupled second order ODEs for  $\widehat{P}_T(z)$  and  $\widehat{p}_n(z)$ , respectively. These govern the dynamics of plane linear waves in a homogeneous two fluid system.

For completeness we also present the equations in their *Hein-Lust* form. We use the fact that

$$\boldsymbol{\xi}_i = \frac{\mathbf{v}'_i}{-i\Omega}, \quad \boldsymbol{\xi}_n = \frac{\mathbf{v}'_n}{-i\Omega},$$

where,  $\boldsymbol{\xi}_l = (\widehat{\xi}_{xl}(z), \widehat{\xi}_{yl}(z), \widehat{\xi}_{zl}(z)) \exp(i(kx - \omega t))$ , where  $l = n, i$ . We then use equations (B.17) and (B.16) to form the two following equations

$$\frac{d\widehat{P}_T(z)}{dz} = \rho_i \left( \Omega^2 - k_x^2 v_A^2 + i\Omega\chi v_{in} \right) \widehat{\xi}_{zi}(z) - i\Omega \rho_n v_{in} \widehat{\xi}_{zn}(z), \quad (7.15)$$

$$\frac{d\widehat{p}_n(z)}{dz} = \rho_n \Omega (\Omega + i\nu_{in}) \widehat{\xi}_{zn}(z) - i\rho_n \nu_{in} \Omega \widehat{\xi}_{zi}(z). \quad (7.16)$$

Using equations (B.23) and (B.26) we find

$$\rho_i (c_{si}^2 + v_A^2) \widetilde{D}_T \frac{d\widehat{\xi}_{zi}(z)}{dz} = -\widetilde{D}_{si} \widehat{P}_T(z) + \frac{i\nu_{in}}{\Omega + i\nu_{in}} c_{si}^2 k^2 \widehat{p}_n(z), \quad (7.17)$$

$$\begin{aligned} \rho_n \rho_i c_{sn}^2 \widetilde{D}_T (c_{si}^2 + v_A^2) \frac{d\widehat{\xi}_{zn}(z)}{dz} &= \frac{i\nu_{in}}{\Omega + i\nu_{in}} \rho_n c_{sn}^2 c_{si}^2 k^2 \widehat{P}_T(z) \\ &\quad - \widehat{p}_n(z) \left( \rho_i (c_{si}^2 + v_A^2) \widetilde{D}_T \left( 1 - \frac{k^2 c_{sn}^2}{D_n} \right) + \rho_n \frac{k^2 c_{sn}^2 \nu_{in}^2}{(\Omega + i\nu_{in})^2} \right). \end{aligned} \quad (7.18)$$

### 7.3 Differential Equations and Solutions

Eqs. (7.8) and (7.11) can be combined together to form a fourth order differential equation for  $p_n$ :

$$\frac{d^4 \widehat{p}_n(z)}{dz^4} - (M_i^2 + M_n^2) \frac{d^2 \widehat{p}_n(z)}{dz^2} + (M_i^2 M_n^2 - q_i q_n) \widehat{p}_n(z) = 0. \quad (7.19)$$

Eq. (7.19) has constant coefficients and, as such, has exponential solutions in general, which are:

$$\widehat{p}_n(z) = C_1 e^{R_1 z} + C_2 e^{-R_1 z} + C_3 e^{R_2 z} + C_4 e^{-R_2 z}. \quad (7.20)$$

Here,

$$R_1 = \left( \frac{M_i^2 + M_n^2 + \left( (M_i^2 + M_n^2)^2 - 4(M_i^2 M_n^2 - q_i q_n) \right)^{1/2}}{2} \right)^{1/2}, \quad (7.21)$$

$$R_2 = \left( \frac{M_i^2 + M_n^2 - \left( (M_i^2 + M_n^2)^2 - 4(M_i^2 M_n^2 - q_i q_n) \right)^{1/2}}{2} \right)^{1/2}, \quad (7.22)$$

$$\widehat{P}_T(z) = N_1 \left( C_1 e^{R_1 z} + C_2 e^{-R_1 z} \right) + N_2 \left( C_3 e^{R_2 z} + C_4 e^{-R_2 z} \right). \quad (7.23)$$

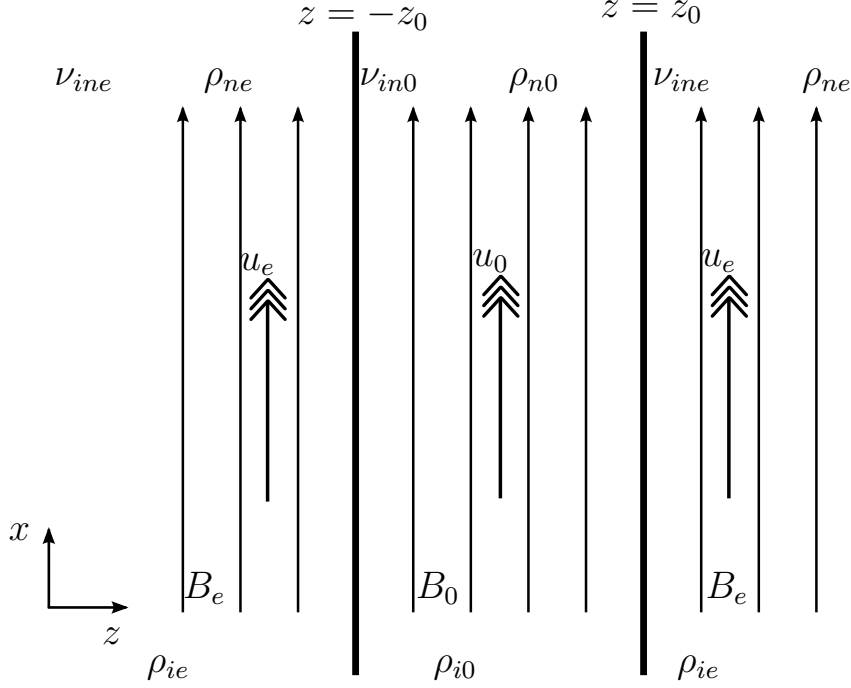


Fig. 7.1 The equilibrium configuration for the magnetic slab and its surrounding magnetic environment.

To apply boundary conditions we also need to obtain the velocity components (for ions and neutrals) perpendicular to the interface, which are given by

$$\frac{\widehat{v}_{zi}(z)}{-i\Omega} = \Psi_1(C_1 e^{R_1 z} - C_2 e^{-R_1 z}) + \Psi_2(C_3 e^{R_2 z} - C_4 e^{-R_2 z}), \quad (7.24)$$

$$\frac{\widehat{v}_{zn}(z)}{-i\Omega} = \Phi_1(C_1 e^{R_1 z} - C_2 e^{-R_1 z}) + \Phi_2(C_3 e^{R_2 z} - C_4 e^{-R_2 z}). \quad (7.25)$$

Here,

$$N_{1,2} = \frac{R_{1,2}^2 - M_n^2}{q_n}, \quad \Psi_{1,2} = \frac{R_{1,2} \left( N_{1,2} + \frac{i\Omega v_{in}}{D_n} \right)}{\rho_i \tilde{D}_A}, \quad (7.26)$$

$$\Phi_{1,2} = \frac{R_{1,2} \left( \frac{i\Omega \chi v_{in} N_{1,2}}{\tilde{D}_A} + 1 - \frac{\Omega^2 \chi v_{in}^2}{\tilde{D}_A D_n} \right)}{\rho_n D_n}. \quad (7.27)$$

## 7.4 Derivation of Dispersion Relation

We now wish to derive the dispersion relation for a slab environment. The slab environment (shown in Fig. 7.1) is set up as follows:

- Slab width is  $2z_0$ .

- Slab boundaries within  $-z_0 < z < z_0$ .
- Background characteristic speeds and temperatures for ions,

$$T_i(z), c_{si}(z), v_A(z), c_T(z), u_i(z) = \begin{cases} T_{ie}, & c_{ie}, & v_{Ae}, & c_{Te}, & u_e & z > z_0, \\ T_{i0}, & c_{i0}, & v_{A0}, & c_{T0}, & u_0, & z_0 > z > -z_0, \\ T_{ie}, & c_{ie}, & v_{Ae}, & c_{Te}, & u_e & z < -z_0, \end{cases} \quad (7.28)$$

- Background typical speeds and temperatures for the neutrals,

$$T_n(z), c_{sn}(z), v_A(z), c_T(z), u_n(z) = \begin{cases} T_{ne}, & c_{ne}, & 0, & 0, & u_e, & z > z_0, \\ T_{n0}, & c_{n0}, & 0, & 0, & u_0, & z_0 > z > -z_0, \\ T_{ne}, & c_{ne}, & 0, & 0, & u_e & z < -z_0, \end{cases} \quad (7.29)$$

- We have boundary conditions that perturbations are finite as  $z \rightarrow \pm\infty$ , thus the solutions outside the slab become, for  $z < -z_0$

$$\widehat{p}_n(z) = A_1 e^{R_{1e}(z+z_0)} + A_3 e^{R_{3e}(z+z_0)}, \quad (7.30)$$

for  $z > z_0$

$$\widehat{p}_n(z) = A_{10} e^{-R_{1e}(z-z_0)} + A_{12} e^{-R_{3e}(z-z_0)}, \quad (7.31)$$

for  $z_0 > z > -z_0$

$$\widehat{p}_n(z) = A_5 \cosh(R_{10}z) + A_6 \sinh(R_{10}z) + A_7 \cosh(R_{30}z) + A_8 \sinh(R_{30}z). \quad (7.32)$$

- The next boundary conditions are the continuity of  $P'_T$ ,  $p'_n$ ,  $v'_{zi}/i\Omega$  and  $v'_{zn}/i\Omega$  at  $z = -z_0, z_0$ . The first of these two boundary conditions can be found by integrating Eqs. (7.3) and (7.4) across both interfaces at  $z = -z_0$  and  $z = z_0$ , respectively (see e.g. [Díaz et al., 2012](#)). The second two boundary conditions come from the kinematic condition.

Using these boundary conditions, we can now write an  $8 \times 8$  matrix that gives us the dispersion relation for the problem:

$$\begin{pmatrix} 1 & 1 & C_1 & -S_1 & C_2 & -S_2 & 0 & 0 \\ 0 & 0 & C_1 & S_1 & C_2 & S_2 & 1 & 1 \\ N_{1e} & N_{2e} & N_{10}C_1 & -N_{10}S_1 & N_{20}C_2 & -N_{20}S_2 & 0 & 0 \\ 0 & 0 & N_{10}C_1 & N_{10}S_1 & N_{20}C_2 & N_{20}S_2 & N_{1e} & N_{2e} \\ \Psi_{1e} & \Psi_{2e} & -\Psi_{10}S_1 & \Psi_{10}C_1 & -\Psi_{20}S_2 & \Psi_{20}C_2 & 0 & 0 \\ 0 & 0 & \Psi_{10}S_1 & \Psi_{10}C_1 & \Psi_{20}S_2 & \Psi_{20}C_2 & -\Psi_{1e} & -\Psi_{2e} \\ \Phi_{1e} & \Phi_{2e} & -\Phi_{10}S_1 & \Phi_{10}C_1 & -\Phi_{20}S_2 & \Phi_{20}C_2 & 0 & 0 \\ 0 & 0 & \Phi_{10}S_1 & \Phi_{10}C_1 & \Phi_{20}S_2 & \Phi_{20}C_2 & -\Phi_{1e} & -\Phi_{2e} \end{pmatrix} \begin{pmatrix} A_1 \\ A_3 \\ A_5 \\ A_6 \\ A_7 \\ A_8 \\ A_{10} \\ A_{12} \end{pmatrix} = 0, \quad (7.33)$$

Performing two simple row operations, we have

$$\begin{pmatrix} 1 & 1 & 2C_1 & 0 & 2C_2 & 0 & 1 & 1 \\ -1 & -1 & 0 & 2S_1 & 0 & 2S_2 & 1 & 1 \\ N_{1e} & N_{2e} & 2N_{10}C_1 & 0 & 2N_{20}C_2 & 0 & N_{1e} & N_{2e} \\ -N_{1e} & -N_{2e} & 0 & 2N_{10}S_1 & 0 & 2N_{20}S_2 & N_{1e} & N_{2e} \\ \Psi_{1e} & \Psi_{2e} & 0 & 2\Psi_{10}C_1 & 0 & 2\Psi_{20}C_2 & -\Psi_{1e} & -\Psi_{2e} \\ -\Psi_{1e} & -\Psi_{2e} & 2\Psi_{10}S_1 & 0 & 2\Psi_{20}S_2 & 0 & -\Psi_{1e} & -\Psi_{2e} \\ \Phi_{1e} & \Phi_{2e} & 0 & 2\Phi_{10}C_1 & 0 & 2\Phi_{20}C_2 & -\Phi_{1e} & -\Phi_{2e} \\ -\Phi_{1e} & -\Phi_{2e} & 2\Phi_{10}S_1 & 0 & 2\Phi_{20}S_2 & 0 & -\Phi_{1e} & -\Phi_{2e} \end{pmatrix} \begin{pmatrix} A_1 \\ A_3 \\ A_5 \\ A_6 \\ A_7 \\ A_8 \\ A_{10} \\ A_{12} \end{pmatrix} = 0, \quad (7.34)$$

We now add Columns 7 and 8 to columns 1 and 2, respectively

$$\begin{pmatrix} 2 & 2 & 2C_1 & 0 & 2C_2 & 0 & 1 & 1 \\ 0 & 0 & 0 & 2S_1 & 0 & 2S_2 & 1 & 1 \\ 2N_{1e} & 2N_{2e} & 2N_{10}C_1 & 0 & 2N_{20}C_2 & 0 & N_{1e} & N_{2e} \\ 0 & 0 & 0 & 2N_{10}S_1 & 0 & 2N_{20}S_2 & N_{1e} & N_{2e} \\ 0 & 0 & 0 & 2\Psi_{10}C_1 & 0 & 2\Psi_{20}C_2 & -\Psi_{1e} & -\Psi_{2e} \\ -2\Psi_{1e} & -2\Psi_{2e} & 2\Psi_{10}S_1 & 0 & 2\Psi_{20}S_2 & 0 & -\Psi_{1e} & -\Psi_{2e} \\ 0 & 0 & 0 & 2\Phi_{10}C_1 & 0 & 2\Phi_{20}C_2 & -\Phi_{1e} & -\Phi_{2e} \\ -2\Phi_{1e} & -2\Phi_{2e} & 2\Phi_{10}S_1 & 0 & 2\Phi_{20}S_2 & 0 & -\Phi_{1e} & -\Phi_{2e} \end{pmatrix} \begin{pmatrix} A_1 \\ A_3 \\ A_5 \\ A_6 \\ A_7 \\ A_8 \\ A_{10} \\ A_{12} \end{pmatrix} = 0. \quad (7.35)$$

We now minus columns 1 and 2 from columns 7 and 8 multiplied by two, respectively, resulting in:

$$\begin{pmatrix} 2 & 2 & 2C_1 & 0 & 2C_2 & 0 & 0 & 0 \\ 0 & 0 & 0 & 2S_1 & 0 & 2S_2 & 2 & 2 \\ 2N_{1e} & 2N_{2e} & 2N_{10}C_1 & 0 & 2N_{20}C_2 & 0 & 0 & 0 \\ 0 & 0 & 0 & 2N_{10}S_1 & 0 & 2N_{20}S_2 & 2N_{1e} & 2N_{2e} \\ 0 & 0 & 0 & 2\Psi_{10}C_1 & 0 & 2\Psi_{20}C_2 & -2\Psi_{1e} & -2\Psi_{2e} \\ -2\Psi_{1e} & -2\Psi_{2e} & 2\Psi_{10}S_1 & 0 & 2\Psi_{20}S_2 & 0 & 0 & 0 \\ 0 & 0 & 0 & 2\Phi_{10}C_1 & 0 & 2\Phi_{20}C_2 & -2\Phi_{1e} & -2\Phi_{2e} \\ -2\Phi_{1e} & -2\Phi_{2e} & 2\Phi_{10}S_1 & 0 & 2\Phi_{20}S_2 & 0 & 0 & 0 \end{pmatrix} \begin{pmatrix} A_1 \\ A_3 \\ A_5 \\ A_6 \\ A_7 \\ A_8 \\ A_{10} \\ A_{12} \end{pmatrix} = 0. \quad (7.36)$$

Factoring out all the multiples of 2 and then switching columns 4 and 5

$$\begin{pmatrix} 1 & 1 & C_1 & C_2 & 0 & 0 & 0 & 0 \\ 0 & 0 & 0 & 0 & S_1 & S_2 & 1 & 1 \\ N_{1e} & N_{2e} & N_{10}C_1 & N_{20}C_2 & 0 & 0 & 0 & 0 \\ 0 & 0 & 0 & 0 & N_{10}S_1 & N_{20}S_2 & N_{1e} & N_{2e} \\ 0 & 0 & 0 & 0 & \Psi_{10}C_1 & \Psi_{20}C_2 & -\Psi_{1e} & -\Psi_{2e} \\ -\Psi_{1e} & -\Psi_{2e} & \Psi_{10}S_1 & \Psi_{20}S_2 & 0 & 0 & 0 & 0 \\ 0 & 0 & 0 & 0 & \Phi_{10}C_1 & \Phi_{20}C_2 & -\Phi_{1e} & -\Phi_{2e} \\ -\Phi_{1e} & -\Phi_{2e} & \Phi_{10}S_1 & \Phi_{20}S_2 & 0 & 0 & 0 & 0 \end{pmatrix} \begin{pmatrix} A_1 \\ A_3 \\ A_5 \\ A_6 \\ A_7 \\ A_8 \\ A_{10} \\ A_{12} \end{pmatrix} = 0. \quad (7.37)$$

We now swap rows to find

$$\begin{pmatrix} 1 & 1 & C_1 & C_2 & 0 & 0 & 0 & 0 \\ N_{1e} & N_{2e} & N_{10}C_1 & N_{20}C_2 & 0 & 0 & 0 & 0 \\ -\Psi_{1e} & -\Psi_{2e} & \Psi_{10}S_1 & \Psi_{20}S_2 & 0 & 0 & 0 & 0 \\ -\Phi_{1e} & -\Phi_{2e} & \Phi_{10}S_1 & \Phi_{20}S_2 & 0 & 0 & 0 & 0 \\ 0 & 0 & 0 & 0 & S_1 & S_2 & 1 & 1 \\ 0 & 0 & 0 & 0 & N_{10}S_1 & N_{20}S_2 & N_{1e} & N_{2e} \\ 0 & 0 & 0 & 0 & \Psi_{10}C_1 & \Psi_{20}C_2 & -\Psi_{1e} & -\Psi_{2e} \\ 0 & 0 & 0 & 0 & \Phi_{10}C_1 & \Phi_{20}C_2 & -\Phi_{1e} & -\Phi_{2e} \end{pmatrix} \begin{pmatrix} A_1 \\ A_3 \\ A_5 \\ A_6 \\ A_7 \\ A_8 \\ A_{10} \\ A_{12} \end{pmatrix} = 0. \quad (7.38)$$

Here,

$$S_{1,2} \equiv \sinh(R_{1,20}z_0), \quad C_{1,2} \equiv \cosh(R_{1,20}z_0). \quad (7.39)$$

For non-trivial solutions the determinant of this matrix must be equal to zero also. However, due to its structure the determinant of Eq. 7.38 is just the determinant of the two following matrices multiplied together and, therefore, must also be equated to zero:

$$\begin{vmatrix} 1 & 1 & C_1 & C_2 \\ N_{1e} & N_{2e} & N_{10}C_1 & N_{20}C_2 \\ -\Psi_{1e} & -\Psi_{2e} & \Psi_{10}S_1 & \Psi_{20}S_2 \\ -\Phi_{1e} & -\Phi_{2e} & \Phi_{10}S_1 & \Phi_{20}S_2 \end{vmatrix} = 0, \quad (7.40)$$

and

$$\begin{vmatrix} S_1 & S_2 & 1 & 1 \\ N_{10}S_1 & N_{20}S_2 & N_{1e} & N_{2e} \\ \Psi_{10}C_1 & \Psi_{20}C_2 & -\Psi_{1e} & -\Psi_{2e} \\ \Phi_{10}C_1 & \Phi_{20}C_2 & -\Phi_{1e} & -\Phi_{2e} \end{vmatrix} = 0. \quad (7.41)$$

Eq. (7.40) represents the symmetric *sausage* oscillations of the slab and Eq. (7.41) represents asymmetric *kink* oscillation of the magnetic slab. When Eqs. (7.40) and

(7.41) are expanded out, we find that

$$\begin{aligned}
& \left\{ \begin{array}{c} \tanh(R_{20}z_0) \\ \coth(R_{20}z_0) \end{array} \right\} \left\{ \begin{array}{c} \tanh(R_{10}z_0) \\ \coth(R_{10}z_0) \end{array} \right\} (\Psi_{20}\Phi_{10} - \Psi_{10}\Phi_{20})(N_{1e} - N_{2e}) \\
& + \left\{ \begin{array}{c} \tanh(R_{10}z_0) \\ \coth(R_{10}z_0) \end{array} \right\} [N_{1e}(\Psi_{2e}\Phi_{10} - \Psi_{10}\Phi_{2e}) + N_{2e}(\Psi_{10}\Phi_{1e} - \Psi_{1e}\Phi_{10}) \\
& \quad + N_{20}(\Phi_{10}(\Psi_{1e} - \Psi_{2e}) - \Psi_{10}(\Phi_{1e} - \Phi_{2e}))] \\
& + \left\{ \begin{array}{c} \tanh(R_{20}z_0) \\ \coth(R_{20}z_0) \end{array} \right\} [N_{1e}(\Psi_{20}\Phi_{2e} - \Psi_{2e}\Phi_{20}) + N_{2e}(\Psi_{1e}\Phi_{20} - \Phi_{1e}\Psi_{20}) \\
& \quad + N_{10}(\Psi_{20}(\Phi_{1e} - \Phi_{2e}) - \Phi_{20}(\Psi_{1e} - \Psi_{2e}))] \\
& + (N_{10} - N_{20})(\Psi_{2e}\Phi_{1e} - \Phi_{2e}\Psi_{1e}) = 0.
\end{aligned} \tag{7.42}$$

## 7.5 Incompressible Limit

We now study the incompressible limit applied to the two fluid slab dispersion relation (7.42), that is  $c_{i0} \rightarrow \infty$ ,  $c_{ie} \rightarrow \infty$ ,  $c_{n0} \rightarrow \infty$  and  $c_{ne} \rightarrow \infty$ . After a significant amount of algebra the dispersion relation for the incompressible limit is given for both the sausage and kink mode is obtained

$$\begin{aligned}
& \left( \frac{\left\{ \begin{array}{c} \tanh(kz_0) \\ \coth(kz_0) \end{array} \right\}}{\rho_{i0}\tilde{D}_{A0}} + \frac{1}{\rho_{ie}\tilde{D}_{Ae}} \right) \left( \frac{\left\{ \begin{array}{c} \tanh(kz_0) \\ \coth(kz_0) \end{array} \right\}}{\rho_{n0}D_{n0}} + \frac{1}{\rho_{ne}D_{ne}} \right) \\
& + \frac{\left\{ \begin{array}{c} \tanh(kz_0) \\ \coth(kz_0) \end{array} \right\}}{\rho_{i0}\rho_{ie}\tilde{D}_{A0}\tilde{D}_{Ae}} \left( \frac{i\Omega_0\nu_{in0}}{D_{n0}} - \frac{i\Omega_e\nu_{ine}}{D_{ne}} \right)^2 = 0.
\end{aligned} \tag{7.43}$$

Here, the subscripts  $e$  and  $0$  refer to quantities evaluated in either the external or internal plasma, for example  $\Omega_e = \omega - ku_e$  etc. Eq. (7.43) is essentially the same as the equation derived for the incompressible two fluid slab in Ballai *et al.* (2017b) and, indeed, very similar to the dispersion relation derived in Martínez-Gómez *et al.* (2015) for the incompressible two fluid cylinder. We write Eq. (7.43) slightly differently to Ballai *et al.* (2017b), however, as it is more useful for the highly collisional limit that follows.

### 7.5.1 Highly Collisional Limit

Eq. (7.43) is transcendental and can only be solved, to the best of our knowledge, numerically. We can, however, take the physically appropriate limit of high collisional frequency, where we assume  $\Omega_0/\nu_{in0} \ll 1$  and  $\Omega_e/\nu_{ine} \ll 1$  and both these quantities

are of approximately the same order. This can be justified by using the approximation for  $\nu_{in}$  given by Eq. (2.32). Using parameters taken from Zaqqarashvili *et al.* (2011) for the mass of neutron and proton and typical values for a chromospheric plasma with  $T = 10^4$  K and hydrogen ion and neutral number densities of  $2.3 \times 10^{10} \text{ cm}^{-3}$  and  $1.2 \times 10^{10} \text{ cm}^{-3}$  gives a collisional frequency of  $\nu_{in} \sim 11 \text{ s}^{-1}$ . Wave periods observed in the solar atmosphere can range from 1000 s to 10 s so that taking  $\Omega/\nu_{in} \ll 1$  is clearly justified here.

Applying this limit to Eq. (7.43) and neglecting terms of order  $(\Omega/\nu_{in})^2$  and higher we find the dispersion relation can be approximated as

$$D(\omega, k) = D_0(\omega, k) + iD_1(\omega, k) = 0, \quad (7.44)$$

where

$$D_0(\omega, k) = D_{01}D_{02}, \quad (7.45)$$

with

$$D_{01} = \left( \rho_{ie} \begin{Bmatrix} \tanh(kz_0) \\ \coth(kz_0) \end{Bmatrix} \tilde{D}_{Ae} + \rho_{i0} \tilde{D}_{A0} \right), \quad (7.46)$$

$$D_{02} = \left( \frac{\begin{Bmatrix} \tanh(kz_0) \\ \coth(kz_0) \end{Bmatrix}}{\rho_{n0} \Omega_0^2} + \frac{1}{\rho_{ne} \Omega_e^2} \frac{\Omega_e \nu_{in0}}{\Omega_0 \nu_{ine}} \right), \quad (7.47)$$

and

$$D_1(\omega, k) = -\frac{\Omega_0}{\nu_{in0}} D_{02} D_{11} - \frac{\Omega_e}{\nu_{ine}} D_{01} D_{12} - \frac{\Omega_0}{\nu_{in0}} \begin{Bmatrix} \tanh(kz_0) \\ \coth(kz_0) \end{Bmatrix} \left( 1 - \frac{\Omega_e \nu_{in0}}{\Omega_0 \nu_{ine}} \right)^2, \quad (7.48)$$

with

$$\begin{aligned} D_{11} = & \rho_{ie} \begin{Bmatrix} \tanh(kz_0) \\ \coth(kz_0) \end{Bmatrix} \check{D}_{Ae} + \rho_{i0} D_{A0} \\ & + \frac{\Omega_e \nu_{in0}}{\Omega_0 \nu_{ine}} \left( \rho_{ie} \begin{Bmatrix} \tanh(kz_0) \\ \coth(kz_0) \end{Bmatrix} D_{Ae} + \rho_{i0} \check{D}_{A0} \right), \end{aligned} \quad (7.49)$$

$$D_{12} = \left( \frac{\begin{Bmatrix} \tanh(kz_0) \\ \coth(kz_0) \end{Bmatrix}}{\rho_{n0}\Omega_0^2} + \frac{1}{\rho_{ne}\Omega_e^2} \right). \quad (7.50)$$

Here,

$$\check{D}_{Al} = \Omega_l^2(1 + \chi_l) - k^2 v_{Al}^2, \quad D_{Al} = \Omega_l^2 - k^2 v_{Al}^2, \quad l = 0, e. \quad (7.51)$$

The purpose of this expansion is to find both the damping rates of the modes due to the collisions between the neutrals and ions and whether there is a possibility of instabilities arising due to the presence of the background flow. We therefore suppose that  $\omega = \omega_0 + i\omega'$ , where  $\omega' \ll \omega_0$ . Next, we expand Eq. (7.44) around  $\omega_0$ , where  $\omega_0$  is the solution to  $D_0(\omega_0, k) = 0$  so that the imaginary part of the frequency can be approximated as

$$\omega' = -\frac{D_1(\omega_0, k)}{\partial D_0(\omega_0, k)/\partial \omega}. \quad (7.52)$$

We note that we can also use other simple perturbation methods to find  $\omega'$  as the next order correction.

We now study the two separate roots of the equation  $D_0(\omega_0, k) = 0$ , independently, to determine the value of  $\omega'$ . Studying the root given by  $D_{01}(\omega_0, k) = 0$  we have the solution

$$\omega_0 = \frac{u_e \tilde{\rho}_e \begin{Bmatrix} \tanh(kz_0) \\ \coth(kz_0) \end{Bmatrix} + \tilde{\rho}_0 u_0}{\tilde{\rho}_e \begin{Bmatrix} \tanh(kz_0) \\ \coth(kz_0) \end{Bmatrix} + \tilde{\rho}_0} k \pm k \frac{\left( \tilde{\rho}_e \tilde{\rho}_0 \begin{Bmatrix} \tanh(kz_0) \\ \coth(kz_0) \end{Bmatrix} (v_{KH}^2 - u_D^2) \right)^{1/2}}{\tilde{\rho}_e \begin{Bmatrix} \tanh(kz_0) \\ \coth(kz_0) \end{Bmatrix} + \tilde{\rho}_0}. \quad (7.53)$$

Here,  $\tilde{\rho}_l = \rho_{il} + \rho_{nl}$  ( $l = 0, e$ ) and

$$v_{KH}^2 = \frac{\left( \tilde{\rho}_e \begin{Bmatrix} \tanh(kz_0) \\ \coth(kz_0) \end{Bmatrix} \tilde{v}_{Ae}^2 + \tilde{\rho}_0 \tilde{v}_{A0}^2 \right) \left( \tilde{\rho}_e \begin{Bmatrix} \tanh(kz_0) \\ \coth(kz_0) \end{Bmatrix} + \tilde{\rho}_0 \right)}{\tilde{\rho}_e \tilde{\rho}_0 \begin{Bmatrix} \tanh(kz_0) \\ \coth(kz_0) \end{Bmatrix}}. \quad (7.54)$$

Here  $v_{Al} = v_{Al}/(1 + \chi_l)^{1/2}$  is the *total* Alfvén speed (the Alfvén speed given by  $B_l^2/\mu_0(\tilde{\rho}_l)$ ). The imaginary part of the frequency,  $\omega'$ , can then be written (using the

fact  $D_{01}(\omega_0, k) = 0$ ), i.e.

$$\omega' = -\frac{1}{v_{ine}} \frac{\left( \left\{ \begin{array}{c} \tanh(kz_0) \\ \coth(kz_0) \end{array} \right\} \rho_{ne} \Omega_{e0}^2 + \rho_{n0} \Omega_{00}^2 \right)^2}{2 \left( \tilde{\rho}_e \left\{ \begin{array}{c} \tanh(kz_0) \\ \coth(kz_0) \end{array} \right\} \Omega_{e0} + \tilde{\rho}_0 \Omega_{00} \right) D_{020}}, \quad (7.55)$$

Here,

$$D_{020} = \left( \left\{ \begin{array}{c} \tanh(kz_0) \\ \coth(kz_0) \end{array} \right\} \rho_{ne} \Omega_{e0} + \rho_{n0} \Omega_{00} \frac{v_{in0}}{v_{ine}} \right). \quad (7.56)$$

The numerator of Eq. (7.55) is always positive and we are thus left to determine the sign of the denominator. We, firstly, have

$$\tilde{\rho}_e \left\{ \begin{array}{c} \tanh(kz_0) \\ \coth(kz_0) \end{array} \right\} \Omega_{e0} + \tilde{\rho}_0 \Omega_{00} = \pm k \left( \tilde{\rho}_e \tilde{\rho}_0 \left\{ \begin{array}{c} \tanh(kz_0) \\ \coth(kz_0) \end{array} \right\} \left( v_{KH}^2 - u_D^2 \right) \right)^{1/2}, \quad (7.57)$$

and secondly,

$$D_{020} = \frac{k v_{in0} \rho_{n0}}{v_{ine} \left( \left\{ \begin{array}{c} \tanh(kz_0) \\ \coth(kz_0) \end{array} \right\} + \tilde{\rho}_r \right)} \left[ u_D \left( \kappa \tilde{\rho}_r - \left\{ \begin{array}{c} \tanh(kz_0) \\ \coth(kz_0) \end{array} \right\} \right) \pm (1 + \kappa) \left( \tilde{\rho}_r \left\{ \begin{array}{c} \tanh(kz_0) \\ \coth(kz_0) \end{array} \right\} \left( v_{KH}^2 - u_D^2 \right) \right)^{1/2} \right], \quad (7.58)$$

where we have defined

$$\kappa = \frac{\left\{ \begin{array}{c} \tanh(kz_0) \\ \coth(kz_0) \end{array} \right\} \rho_{ne} v_{ine}}{\rho_{n0} v_{in0}}, \quad u_D = u_0 - u_e. \quad (7.59)$$

The first term in the denominator is just dependent on whether the wave is a backward or forward propagating wave, so therefore has the sign that complements that, i.e. negative for backward and positive for forward propagation. The second term is not so simple. When there is no shearing flow i.e.  $u_D = 0$ , the sign of the second term is negative and therefore waves are damped. However, there will be a flow speed when Eq. (7.56) does change sign, and thus so does the sign of Eq. (7.55). The fact that Eq. (7.56) equals to zero is interesting as it indicates that  $D_{02} = 0$  (Eq. (7.47)) and this therefore shows a resonant interaction between the modes given by Eq. (7.47) and Eq. (7.46). Equating Eq. (7.58) to zero, we find the critical flow

speed is given by:

$$u_D^2 = v_{KH}^2 \Xi^2, \quad \Xi^2 = \frac{(1 + \kappa)^2 \tilde{\rho}_r \left\{ \begin{array}{c} \tanh(kz_0) \\ \coth(kz_0) \end{array} \right\}}{\left( \tilde{\rho}_r + \left\{ \begin{array}{c} \tanh(kz_0) \\ \coth(kz_0) \end{array} \right\} \right) \left( \left\{ \begin{array}{c} \tanh(kz_0) \\ \coth(kz_0) \end{array} \right\} + \kappa^2 \tilde{\rho}_r \right)}. \quad (7.60)$$

Here,  $\rho_r = \tilde{\rho}_0/\tilde{\rho}_e$ . A requirement for this sign change to happen for flow values less than that of the Kelvin-Helmholtz instability requires that  $\Xi < 1$ . With some simple algebra we can prove that this is exactly the case:

$$\Xi^2 = 1 - \Gamma, \quad (7.61)$$

$$\Gamma = \frac{\left( \left\{ \begin{array}{c} \tanh(kz_0) \\ \coth(kz_0) \end{array} \right\} - \tilde{\rho}_r \kappa \right)^2}{\left( \tilde{\rho}_r + \left\{ \begin{array}{c} \tanh(kz_0) \\ \coth(kz_0) \end{array} \right\} \right) \left( \tilde{\rho}_r \kappa + \left\{ \begin{array}{c} \tanh(kz_0) \\ \coth(kz_0) \end{array} \right\} \right)}. \quad (7.62)$$

Here, we have used the definition of  $\kappa$  defined by Eq. (7.59). Thus,  $\Gamma$  is a completely positive quantity and therefore  $\Xi \leq 1$ . The speed at which this sign change occurs is given as a fraction of the Kelvin-Helmholtz threshold velocity:

$$u_D = \pm v_{KH} \Xi. \quad (7.63)$$

As the perturbation method actually breaks down around these points, we leave analysis until the next numerical solutions sub-section. We have in fact found the flow speeds required in which the frequencies for the eigen-frequencies of both Eqs. (7.46) and (7.47) are equal.

We now consider the case for the second root of Eq. (7.45), that is  $D_{02}(\omega_0, k) = 0$ . Again, expanding the dispersion relation around  $\omega_0$  we find that the real part is given as

$$\omega_0 = k \frac{u_e \kappa + u_0}{1 + \kappa}. \quad (7.64)$$

The imaginary part of the frequency can then be approximated as

$$\omega' = \frac{u_D^2 k^2 \kappa \left( \frac{\kappa v_{ine}}{v_{in0}} + 1 \right) (u_D^2 \Upsilon - v_{KH}^2 \Xi^2)}{v_{ine} (1 + \kappa)^3 (u_D^2 - v_{KH}^2 \Xi^2)}. \quad (7.65)$$

Here,

$$\Upsilon = \left( 1 - \frac{\left\{ \begin{array}{c} \tanh(kz_0) \\ \coth(kz_0) \end{array} \right\} \left( \frac{\kappa v_{ine}}{v_{in0}} + 1 \right) \chi_e}{(1 + \chi_e) \left( \left\{ \begin{array}{c} \tanh(kz_0) \\ \coth(kz_0) \end{array} \right\} + \tilde{\rho}_r \kappa^2 \right)} \right). \quad (7.66)$$

The sign of  $\omega'$ , given by Eq. (7.65), is clearly positive when there is a flow present and therefore this mode of oscillation is always unstable. This agrees well with the result given in Soler *et al.* (2013) that an instability in the plasma occurs due to the shear flow and the presence of the neutrals.

## 7.5.2 Numerical solutions

Figs. 7.2-7.5 plot the variation of the real and imaginary parts of the dimensionless frequency,  $\omega/kv_K$ , with respect to the dimensionless flow parameter,  $u_0/v_{KH}$ , for the approximations given by Eqs. (7.53), (7.55), (7.65) and (7.65) where the kink frequency,  $kv_K$ , is given as,

$$v_K = \left( \frac{\tilde{\rho}_e \tilde{v}_{Ae}^2 + \tilde{\rho}_0 \tilde{v}_{A0}^2}{\tilde{\rho}_e + \tilde{\rho}_0} \right)^{1/2}.$$

Also plotted in the same figures as solid ( $kz_0 = 0.1$ ) and dashed ( $kz_0 = 1$ ) black lines are the numerical solutions to Eq. (7.43) that correspond to the specific approximation. The blue circles correspond to the approximation when  $kz_0 = 1$  and the orange squares the approximation when  $kz_0 = 0.1$ . In the the lower right hand panels only the full numerical solutions are plotted, to demonstrate the avoided crossings and the resonance that occurs around these points.

Fig. 7.2 is plotted for a situation in which the external plasma is cooler and less dense than the internal plasma. Using Eq. (1.30) as a rough guide for ionisation fractions, we choose  $\chi_e = 3$  so that there are three times as many neutral atoms than there are ions. As the internal plasma is hotter, we choose  $\chi_0 = 0.1$  so that, for this plasma, there are ten times as many ions as there are neutrals meaning the plasma is almost completely ionised. The dimensionless collisional frequency,  $v_{in0}/kv_K = 100$ , is chosen so the effective collision time,  $1/v_{in0}$ , between the ion and neutral species is 100 times less than the kink period,  $1/kv_K$ .

Fig. 7.2a plots the solution of the kink approximation given by Eqs. (7.64) and (7.65), whilst Figs. 7.2b and c are plotted for the forward (positive sign) and backward (negative sign) propagating kink approximations given by Eqs. (7.53) and (7.55), respectively. The green lines represent the the dimensionless speeds  $u_0/v_{KH} = \Xi$  at which a singularity occurs in our perturbation methods, the solutions are not

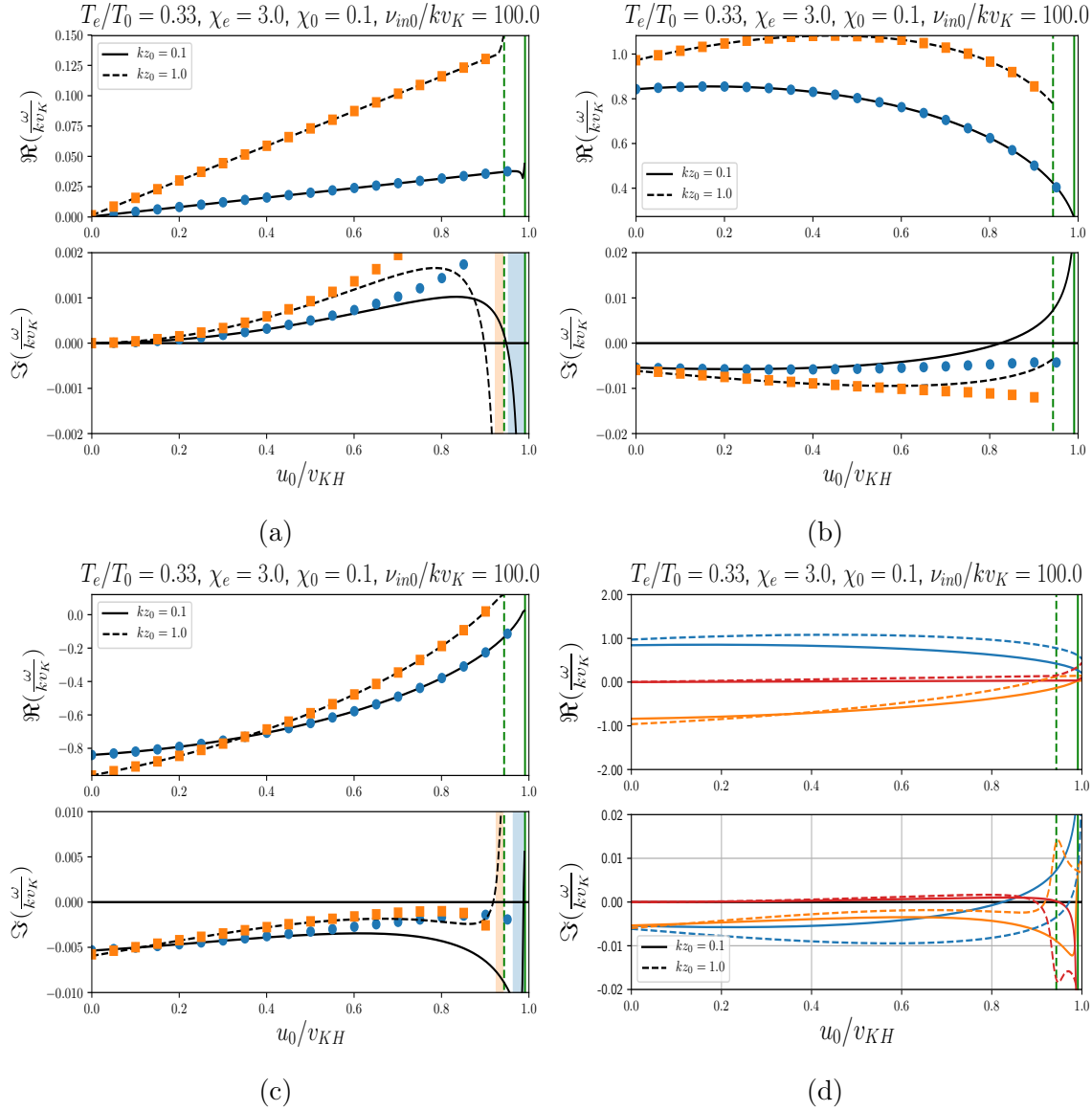


Fig. 7.2 Variation of the real,  $\Re(\omega/kv_K)$ , and imaginary,  $\Im(\omega/kv_K)$ , parts of the dimensionless frequency,  $\omega/kv_K$ , for the kink mode (*coth*) with respect to the dimensionless flow parameter,  $u_0/v_{KH}$ , for the parameters  $T_e/T_0 = 0.33$ ,  $\chi_e = 3$ ,  $\chi_0 = 0.1$  and  $\nu_{in0}/kv_K = 100$  (a) the approximation given by Eqs. (7.64) and (7.65) with the corresponding kink solution of Eq. (7.43) as a comparison (b) the approximation given by the positive sign of Eq. (7.53) and Eq. (7.55) with the corresponding kink solution (7.43) (c) the same as (b) but for the negative solution of Eq. (7.53). The blue circles and orange boxes correspond to the approximation when  $k_{z0} = 0.1$  and  $k_{z0} = 1$ , respectively, and the black solid and dashed lines correspond to the full numerical solutions when  $k_{z0} = 0.1$  and  $k_{z0} = 1$ , respectively (d) the full numerical solutions of Eq. (7.43) for the backward (orange lines) and forward (blue) propagating kink and the neutral (red) modes for with solid lines for  $k_{z0} = 0.1$  and dashed lines for  $k_{z0} = 1$ . In all panels the green solid and dashed lines indicate the speed  $u_0/v_{KH} = \Xi$  when  $k_{z0} = 0.1$  and  $k_{z0} = 1$ , respectively.

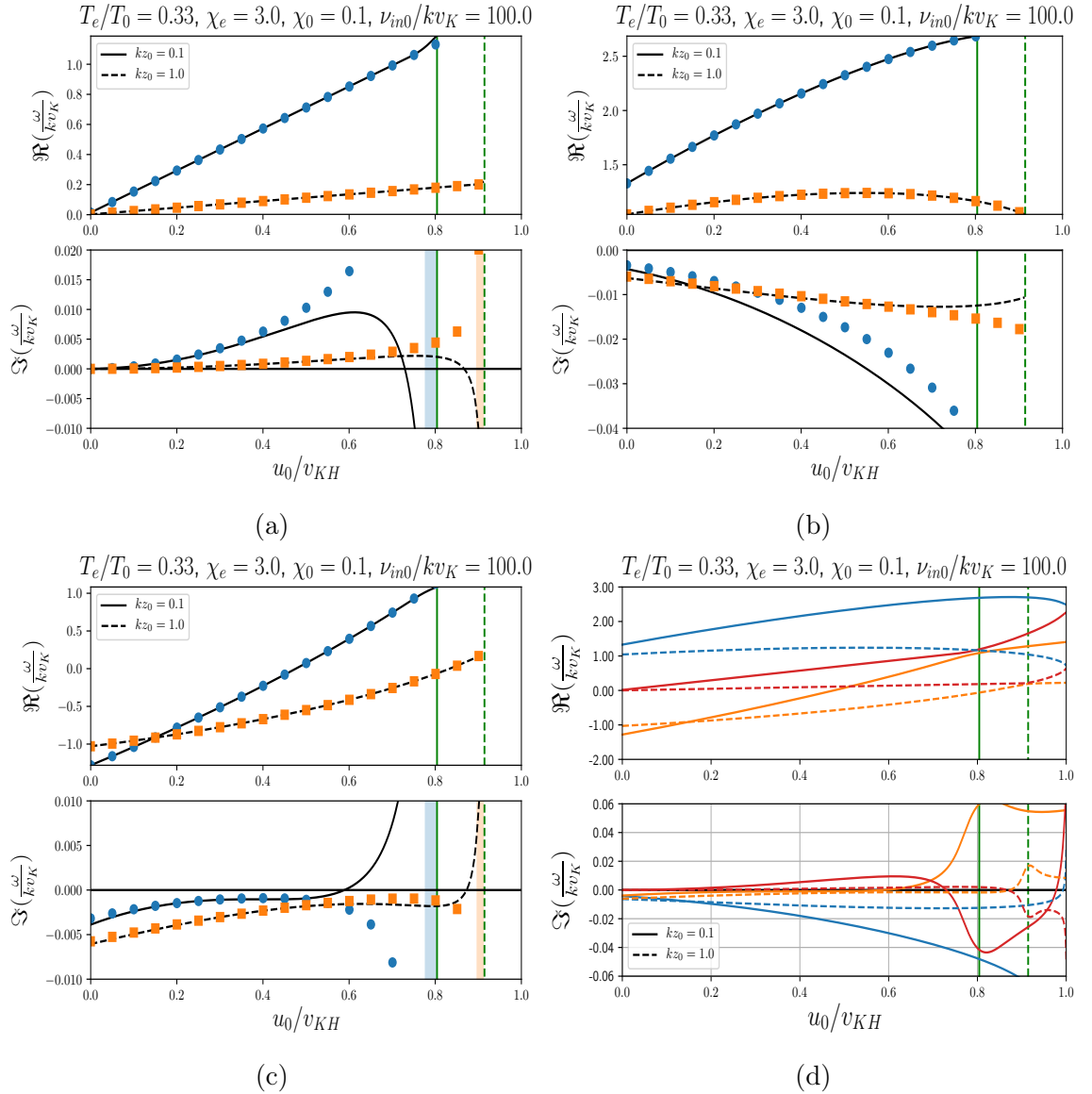


Fig. 7.3 Same as Fig. 7.2 but for the sausage (tanh) mode.

computed any further after this point. Also noted are regions, blue for  $k_{z0} = 0.1$  and orange for  $k_{z0} = 1$ , where the approximation has a larger than 10% total error compared to the numerical solution. Evidently, by studying Figs. 7.2a-c we see that the approximations are very good, particularly for the real part of the solution, up until  $u_0/v_{KH} \approx \Xi$ . The approximation for the forward (positive sign) propagating kink mode (shown in Fig. 7.2b) never has a higher than 10% error, as there is no singularity in the perturbation method for this particular mode. The modes shown in Figs. 7.2a and c reach exactly the same real dimensionless frequency value when  $u_0/v_{KH} = \Xi$ , at which point the singularity is reached and the approximation breaks down.

In Fig. 7.2d we plot only the full numerical solutions. The red lines correspond to the neutral mode of Fig. 7.2a, the blue lines the forward propagating kink mode of Fig. 7.2b and the orange lines the backward propagating mode of Fig. 7.2. Plotted

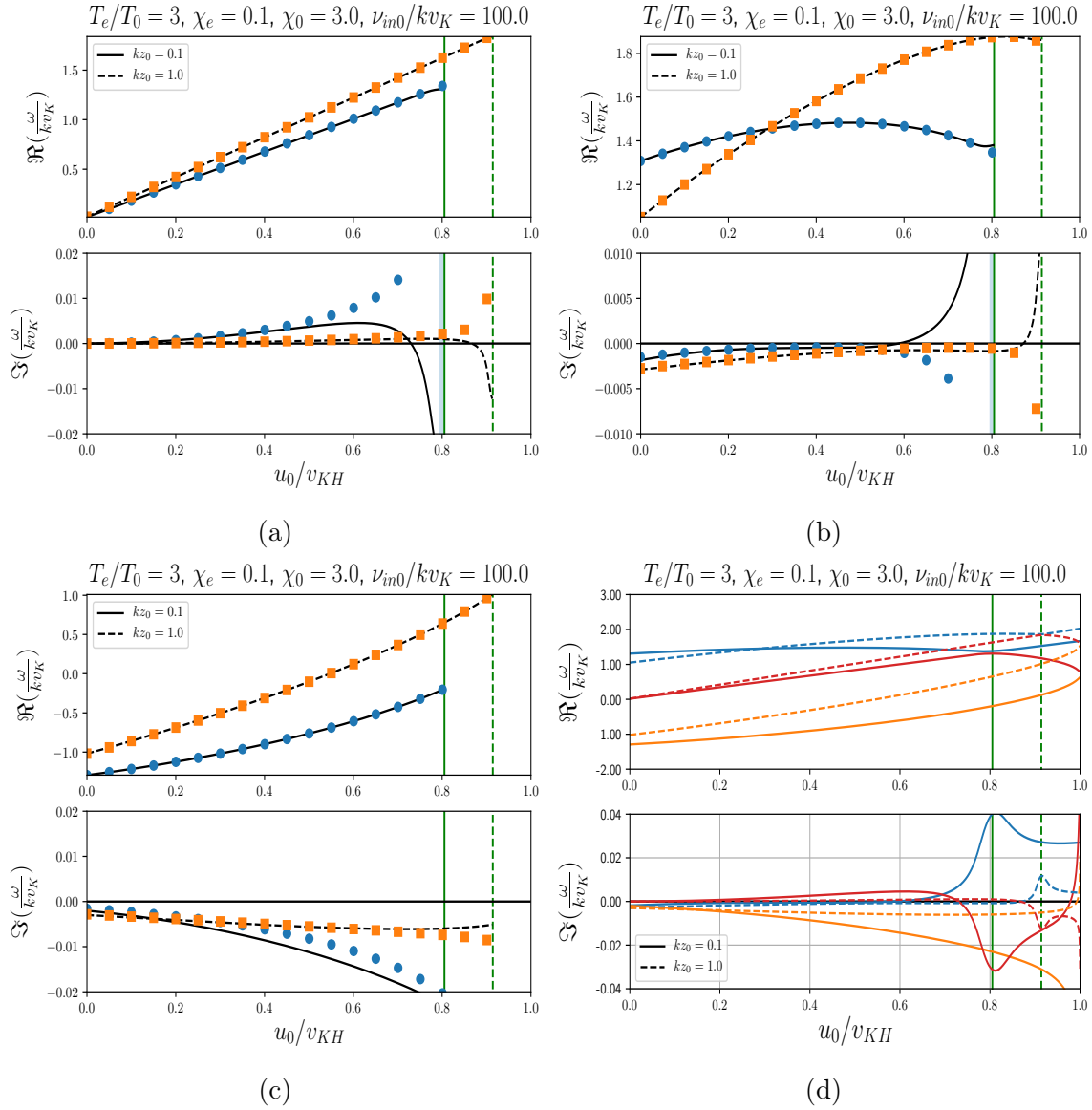


Fig. 7.4 Same as Fig. 7.2 but for the dimensionless parameters  $T_e/T_0 = 3$ ,  $\chi_e = 0.1$ ,  $\chi_0 = 3$  and  $\nu_{in0}/kv_K = 100$ .

in green are the vertical lines where  $u_0/v_{KH} = \Xi$ , solid for  $k_{z0} = 0.1$  and dashed for  $k_{z0} = 1$ . At these vertical lines, the real parts of the dimensionless frequency of neutral mode and backward propagating kink mode approach and avoid each other. The imaginary part of the frequency for the solution coloured orange then reaches a positive peak. When  $k_{z0} = 0.1$ , the time-scale of amplification is approximately 16 times greater than the kink mode period as  $\Im(\omega/kv_K) \approx 0.06$ . When  $k_{z0} = 1$ , the time-scale of amplification is slightly larger, being approximately 50 times greater than the kink period, as  $\Im(\omega/kv_K) \approx 0.02$ .

Fig. 7.3 is plotted for the same parameters as Fig. 7.2 but for the sausage solutions of Eqs. (7.43), (7.53), (7.55), (7.64) and (7.65). Figs. 7.3a-c confirm that the approximations given by Eqs. (7.53), (7.55), (7.64) and (7.65) are indeed very good. The green vertical lines show that the dimensionless flow speed at which the

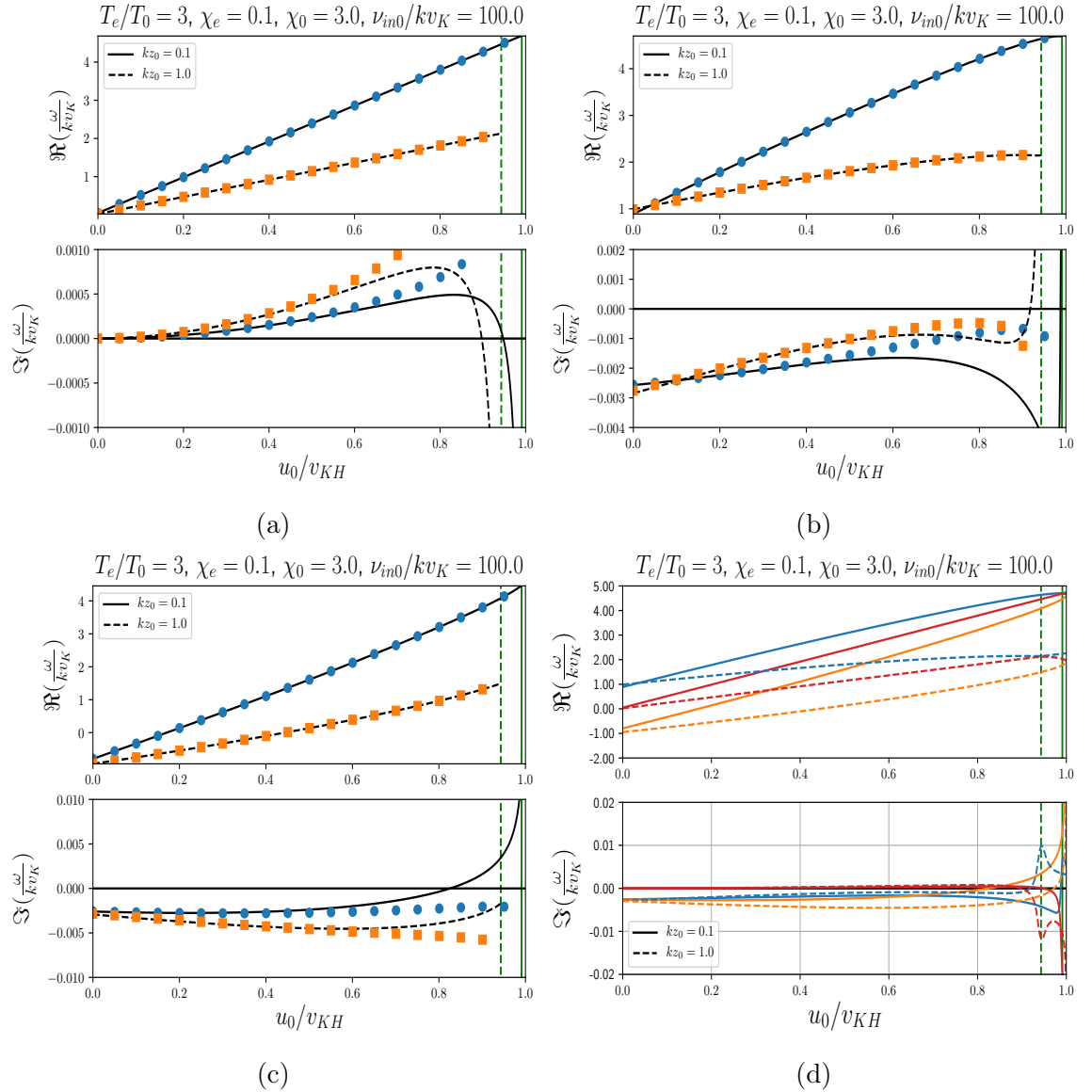


Fig. 7.5 Same as Fig. 7.3 but for the dimensionless parameters  $T_e/T_0 = 3$ ,  $\chi_e = 0.1$ ,  $\chi_0 = 3$  and  $\nu_{in0}/kv_K = 100$ .

perturbation method breaks down ( $u_0/v_{KH} = \Xi$ ) has increased for both  $k_{z0} = 0.1$  and  $k_{z0} = 1$ . When  $k_{z0} = 1$ , we have  $\Xi \approx 1$  so that the instability practically occurs at the Kelvin-Helmholtz threshold velocity, as confirmed by Fig. 7.3d. When  $k_{z0} = 1$  the value of  $\Xi$  is decreased, and when  $u_0/v_{KH} = \Xi$  the real parts of the dimensionless frequencies of the neutral (red) and forward propagating (blue) modes come very close and avoid each. At their closest approach there is a positive peak in the imaginary part of the dimensionless frequency of the forward propagating sausage mode. The time-scale of amplification is approximately 100 times greater than the sausage mode period, as  $\Im(\omega/kv_K) \approx 0.01$ .

Fig. 7.4 is evaluated for a situation in which the external plasma is three times hotter than the plasma within the slab. We, therefore choose,  $\chi_e = 0.1$  and  $\chi_0 = 3$ . Again the internal collisional time-scale is 100 times less than the kink period,  $1/\nu_K$ .

Fig. 7.4a is plotted for the kink approximation given by Eq. (7.64) and (7.65), whilst Figs. 7.2b and c are plotted for the forward (positive sign) and backward (negative sign) propagating kink approximations, respectively, given by Eqs. (7.53) and (7.55). As compared to Fig. 7.2 we see, by comparing the positions of the green vertical lines in each figure, that the solution breaks down for lower fractions of the Kelvin-Helmholtz threshold, as  $\Xi$  is less in this situation. Interestingly, the green vertical lines are in the same position as for sausage modes shown in Fig. 7.3. We again see a very good agreement between the analytical approximations and the numerical solutions by studying Figs. 7.4a-c. Again, in Fig. 7.4, at the vertical green lines where the analytical solutions breaks down, the real part of the dimensionless frequencies of the neutral (red) and forward propagating kink (blue) modes approach and avoid one another. At their closest approach, there are large peaks and troughs in the dimensionless imaginary part of the frequency. When  $kz_0 = 0.1$ , the shortest time-scale of amplification is approximately 25 times greater than the kink mode period i.e.  $\Im(\omega/kv_K) \approx 0.04$ . When  $kz_0 = 1$ , the shortest time-scale of amplification is slightly greater, being approximately 100 times greater than the kink period i.e.  $\Im(\omega/kv_K) \approx 0.01$ .

Fig. 7.5 is plotted for the same parameters as in Fig. 7.4 but for the sausage solutions of Eqs. (7.43), (7.53), (7.55), (7.64) and (7.65). By studying Figs. 7.5a-c, it is, again, confirmed that the analytical approximations are quite accurate. The speeds at which the approximations break down are identical to those in Fig. 7.2, and are quite close to the Kelvin-Helmholtz threshold, particularly when  $kz_0 = 0.1$ . When  $kz_0 = 1$  the real part of the dimensionless frequencies of the neutral (red) and forward propagating kink (blue) modes approach and avoid one another. At their closest approach, there are large peaks and troughs in the dimensionless imaginary part of the frequencies, respectively. The shortest time-scale of the amplification is approximately 100 times greater than the kink period i.e.  $\Im(\omega/kv_K) \approx 0.01$ .

The evidence from Figs. 7.2-7.5 indicates that there is a resonant interaction between the neutral mode and either the backward or forward propagating modes of the single fluid incompressible slab. This resonant interaction can lead to reasonable time-scales for the amplification of the modes. For example, the lowest amplification period was found for the sausage mode shown in Fig. 7.3. The period was only 16 times longer than the kink period i.e. a wave with a period of 10 seconds would increase in magnitude by a factor of  $\exp(1)$  in 160 seconds. This is a very reasonable time-scale for most solar phenomena.

## 7.6 Collision-less limit

In this section, we study the collision-less limit, that is  $v_{in} \ll \Omega$ . This is a fairly restrictive limit as it assumes that the waves must be of a high frequency, given

that the collisional frequency is about  $\sim 11 \text{ s}^{-1}$  in the Chromosphere, as stated before. However, it is useful as it gives a physical insight into the problem. We must also note that this approximation will only be valid as long as the frequencies of the oscillations are still much larger than the frequency of the collisions between electrons and ions, if not we can no longer treat the electrons and ions as a single fluid (see e.g. [Zaqarashvili et al., 2011](#)).

We start by expanding both  $M_i^2$  and  $M_n^2$  around the small parameter  $v_{in}/\Omega \ll 1$ .

$$M_i^2 \approx \hat{M}_i^2 - \frac{i\Omega v_{in} \chi \Omega^2 (\Omega^2 - 2k^2 c_T^2)}{(c_i^2 + v_A^2) \hat{D}_T^2} + O(v_{in}^2), \quad (7.67)$$

$$M_n^2 \approx \hat{M}_n^2 - \frac{i\Omega v_{in}}{c_n^2} + O(v_{in}^2). \quad (7.68)$$

Here,

$$\hat{M}_i^2 = -\frac{\hat{D}_A \hat{D}_{si}}{(c_i^2 + v_A^2) \hat{D}_T}, \quad \hat{D}_A = \Omega^2 - k^2 v_A^2, \quad \hat{D}_{si} = \Omega^2 - k^2 c_i^2, \quad (7.69)$$

$$\hat{D}_T = \Omega^2 - k^2 c_T^2, \quad \hat{M}_n^2 = -\frac{(\Omega^2 - k^2 c_n^2)}{c_n^2}. \quad (7.70)$$

We can now expand  $R_1$  and  $R_2$  using Eqs. (7.67) and (7.68) and as such we obtain

$$R_1 \approx \hat{M}_i - \frac{i\Omega v_{in} \chi \Omega^2 (\Omega^2 - 2k^2 c_T^2)}{2(c_i^2 + v_A^2) \hat{D}_T^2 \hat{M}_i^2} + O(v_{in}^2) \quad (7.71)$$

and

$$R_2 \approx \hat{M}_n - \frac{i\Omega v_{in}}{2c_n^2 \hat{M}_n^2}. \quad (7.72)$$

Now, we assess the orders of  $N_1$  and  $N_2$

$$N_1 \approx \frac{M_i^2 - M_n^2}{q_n} = O(\Omega/v_{in}), \quad N_2 \approx O(v_{in}/\Omega). \quad (7.73)$$

This means that, in Eq. (7.42), any terms multiplied by  $N_2$  can be neglected as they are two orders of magnitude smaller. The parameters  $\Psi_1$ ,  $\Psi_2$ ,  $\Phi_1$  and  $\Phi_2$  are also expanded and their orders calculated

$$\Psi_1 = O(\Omega/v_{in}), \quad \Psi_2 = O(v_{in}/\Omega), \quad \Phi_1 = O(1), \quad \Phi_2 = O(1). \quad (7.74)$$

These are only comparisons in order between each of the quantities. We neglect terms that are  $O(v_{in}^2)$  different in size and obtain

$$\left( N_{10}\Psi_{1e} + \left\{ \begin{array}{c} T_1 \\ C_1 \end{array} \right\} N_{1e}\Psi_{10} \right) \left( \Phi_{2e} + \left\{ \begin{array}{c} T_2 \\ C_2 \end{array} \right\} \Phi_{20} \right) \approx 0, \quad (7.75)$$

$$\frac{M_{i0}^2 - M_{n0}^2}{q_{n0}} \frac{M_{ie}^2 - M_{ne}^2}{q_{ne}} \left( \frac{R_{1e}}{\rho_{ie}D_{Ae}} + \frac{R_{10}}{\rho_{i0}D_{A0}} \left\{ \begin{array}{c} T_1 \\ C_1 \end{array} \right\} \right) \left( \frac{R_{2e}}{\rho_{ne}D_{ne}} + \frac{R_{20}}{\rho_{n0}D_{n0}} \left\{ \begin{array}{c} T_2 \\ C_2 \end{array} \right\} \right) \approx 0. \quad (7.76)$$

We now expand around  $v_{in}$  to find

$$F(\omega, k) \approx F_R(\omega, k) + F_I(\omega, k) = 0, \quad (7.77)$$

where

$$F_R(\omega, k) = F_{R1}(\omega, k)F_{R2}(\omega, k), \quad F_I(\omega, k) = F_{R1}(\omega, k)F_{I2}(\omega, k) + F_{R2}(\omega, k)F_{I1}(\omega, k). \quad (7.78)$$

Here,

$$F_{R1} = \left( \left\{ \begin{array}{c} \tanh \\ \coth \end{array} \right\} (\hat{M}_{i0}z_0) \frac{\hat{M}_{i0}}{\rho_{i0}\hat{D}_{A0}} + \frac{\hat{M}_{ie}}{\rho_{ie}\hat{D}_{Ae}} \right) \quad (7.79)$$

$$F_{R2} = \left( \frac{\hat{M}_{ne}\Omega_0^2}{\rho_{ne}} + \left\{ \begin{array}{c} \tanh \\ \coth \end{array} \right\} (\hat{M}_{n0}z_0) \frac{\hat{M}_{n0}\Omega_e^2}{\rho_{n0}} \right) \quad (7.80)$$

and

$$\begin{aligned} F_{I1} = & \frac{i\Omega_0\chi_0v_{in0}}{2\rho_{i0}\hat{D}_{T0}\hat{D}_{A0}^2\hat{D}_{si0}} \left( 1 - \left\{ \begin{array}{c} \tanh^2 \\ \coth^2 \end{array} \right\} (\hat{M}_{i0}z_0) \right) \hat{M}_{i0}^2z_0\Omega_0^2 (\Omega_0^2 - 2k^2c_{T0}^2) \\ & - \frac{i\Omega_0\chi_0v_{in0}}{2\rho_{i0}\hat{D}_{T0}\hat{D}_{A0}^2\hat{D}_{si0}} \left\{ \begin{array}{c} \tanh \\ \coth \end{array} \right\} (\hat{M}_{i0}z_0)\hat{M}_{i0}\hat{D}_{mc0} \\ & - \frac{i\Omega_e\chi_e v_{ine}\hat{D}_{mce}}{2\hat{D}_{Ae}\hat{D}_{Te}\hat{D}_{sie}} \frac{\hat{M}_{ie}}{\rho_{ie}\hat{D}_{Ae}} \end{aligned} \quad (7.81)$$

and

$$\begin{aligned}
F_{I2} = & \left\{ \begin{array}{c} \tanh \\ \coth \end{array} \right\} \left( \hat{M}_{n0} z_0 \right) \left( i\Omega_e \nu_{ine} + \frac{i\Omega_e^2 \Omega_0 \nu_{in0}}{2\hat{D}_{sn0}} \right) \frac{\hat{M}_{n0}}{\rho_{n0}} \\
& + \left( 1 - \left\{ \begin{array}{c} \tanh^2 \\ \coth^2 \end{array} \right\} \left( \hat{M}_{n0} z_0 \right) \right) \hat{M}_{n0} z_0 \frac{i\Omega_0 \nu_{in0}}{2\hat{D}_{sn0}} \frac{\hat{M}_{n0} \Omega_e^2}{\rho_{n0}} \\
& + \frac{\hat{M}_{ne}}{\rho_{ne}} \left( i\Omega_0 \nu_{in0} + \frac{i\Omega_0^2 \Omega_e \nu_{ine}}{2\hat{D}_{sne}} \right).
\end{aligned} \tag{7.82}$$

We can see from Equations (7.79)-(7.82), we have two separate branches of this dispersion relation. If we set  $\nu_{in0} = \nu_{ine} = 0$  we see that these two branches correspond to the dispersion relation of waves in the ion fluid (Eq. 7.79) and another dispersion relation governing the waves in the neutral fluid (Eq. 7.80) decoupled from each other due to there being no collisions between the ions and neutrals, thus they behave as two separate fluids.

The first solution considered is the case where  $F_{R1}(\omega_1, k) = 0$ . The solutions to this are interpreted as the kink and sausage modes in a medium where the ions and neutrals do not collide. Eq. (7.79) is the dispersion relation derived in [Nakariakov and Roberts \(1995\)](#) and, as such, this case has been studied extensively and we therefore do not discuss it here. We next consider the neutral root of Eq. (7.78), given by  $F_{R2} = 0$

$$\frac{\hat{M}_{ne} \Omega_0^2}{\rho_{ne}} + \left\{ \begin{array}{c} \tanh \\ \coth \end{array} \right\} \left( \hat{M}_{n0} z_0 \right) \frac{\hat{M}_{n0} \Omega_e^2}{\rho_{n0}} = 0. \tag{7.83}$$

Eq. (7.83) describes the modes of oscillation of neutrals in a slab geometry with steady flows within and outside of the slab. If we take the incompressible limit of Eq. (7.83), we simplify to the dispersion relation in the collision-less limit given by [Ballai \*et al.\* \(2017a\)](#) which has solutions for the frequency given as

$$\omega = \frac{u_0 \rho_{n0} + u_e \left\{ \begin{array}{c} \tanh \\ \coth \end{array} \right\} (k z_0) \rho_{ne}}{\rho_{n0} + \left\{ \begin{array}{c} \tanh \\ \coth \end{array} \right\} (k z_0) \rho_{ne}} k \pm i k u_D \frac{\left( \left\{ \begin{array}{c} \tanh \\ \coth \end{array} \right\} (k z_0) \frac{\rho_{ne}}{\rho_{n0}} \right)^{1/2}}{1 + \left\{ \begin{array}{c} \tanh \\ \coth \end{array} \right\} (k z_0) \frac{\rho_{ne}}{\rho_{n0}}}. \tag{7.84}$$

Clearly, in the incompressible limit, the modes described in Eq. (7.84) are unstable as long as a shear flow exists between the slab and its environment. It must be noted that this result was found in [Ballai \*et al.\* \(2017b\)](#) and has been discussed there. A similar result was, again, shown for the case of a shear flow at a single interface in [Soler \*et al.\* \(2012\)](#). The incompressible case has been fully discussed so it is neglected here and we prefer to acknowledge it.

Returning to Eq. (7.83), we can of course see there are two branches, the kink and sausage modes. Immediately evident is that neither branch has solutions unless a shear flow is present. To study the modes that arise from this root analytically, we take the slender slab limit ( $kz_0 \rightarrow 0$ ) of both the sausage and kink modes, respectively. In this limit, the sausage mode branch tends to

$$\frac{\hat{M}_{ne}\Omega_0^2}{\rho_{ne}} + \frac{\hat{M}_{n0}^2 z_0 \Omega_e^2}{\rho_{n0}} = 0. \quad (7.85)$$

Following a simple perturbation procedure, we find that the solution to Eq. (7.85) for the frequency  $\omega$  can be approximated as

$$\omega \approx u_0 k \pm i u_D k (kz_0)^{1/2} \left( \frac{\rho_{ne}}{\rho_{n0}} \right)^{1/2} \left( \frac{c_{ne}}{(c_{ne}^2 - u_D^2)^{1/2}} \right)^{1/2}. \quad (7.86)$$

In the same limit, the kink mode reduces to

$$\frac{\hat{M}_{ne}\Omega_0^2}{\rho_{ne}} z_0 + \frac{\Omega_e^2}{\rho_{n0}} = 0. \quad (7.87)$$

Again, following a simple perturbation procedure, we find that the solution to Eq. (7.87) can be approximated in this limit as

$$\omega \approx u_e k \pm i u_D k (kz_0)^{1/2} \left( \frac{\rho_{n0}}{\rho_{ne}} \right)^{1/2}. \quad (7.88)$$

Firstly, it is obvious from Eqs. (7.86) and (7.88) that both the solutions cannot exist without a background flow present within the system. Secondly, both modes are unstable if there is a shear flow between the layers i.e.  $u_D \neq 0$ . This result agrees with the conclusions of Soler *et al.* (2012) and Ballai *et al.* (2017b), where it was found that in the collision-less limit the neutral species are always Kelvin-Helmholtz unstable. We could, in fact, take the incompressible limit of the neutral root of Eq. (7.78) but we choose not to as it has been sufficiently studied in the aforementioned investigations.

## 7.7 Highly Collisional Limit

Many of the cases considered in the previous sections are good indicators of the physics present in the study of these partially ionised plasmas, however they are fairly restrictive and are not what is generally observed in prominence plasmas. We therefore opt for the limit of high collisional frequency again, that is  $\Omega_l \ll \nu_{inl}$ .

Applying this limit to Eq. (7.42), we obtain two separate branches

$$f(\omega, k) = f_0(\omega, k)f_1(\omega, k) = 0, \quad (7.89)$$

$$f_0(\omega, k) = \left\{ \begin{array}{l} \tanh \\ \coth \end{array} \right\} \left( \check{M}_{0z0} \right) \frac{\check{M}_0}{\check{D}_{A0}\check{\rho}_0} + \frac{\check{M}_e}{\check{D}_{Ae}\check{\rho}_e}, \quad (7.90)$$

$$f_1(\omega, k) = \frac{\zeta_0}{v_{in0}\Omega_0\rho_{n0}} + \frac{\zeta_e}{v_{ine}\Omega_e\rho_{ne}}. \quad (7.91)$$

Here,

$$\zeta_l^2 = -\frac{i\Omega_l v_{inl}(1 + \chi_l)^2(\tilde{c}_l^2 + \tilde{v}_{Al}^2)\check{D}_{Tl}}{c_{nl}^2(c_{il}^2 + v_{Al}^2)\check{D}_{Tl}}, \quad (7.92)$$

where,

$$\check{D}_{Al} = \Omega_l^2 - k^2\tilde{v}_{Al}^2, \quad \check{D}_{sl} = \Omega_l^2 - k^2\tilde{c}_l^2, \quad \tilde{c}_l^2 = \frac{c_{nl}^2\chi_l + c_{il}^2}{1 + \chi_l}, \quad (7.93)$$

$$\check{D}_{Tl} = \Omega_l^2 - k^2\tilde{c}_{Tl}^2, \quad \tilde{c}_{Tl}^2 = \frac{\tilde{c}_l^2\tilde{v}_{Al}^2}{(\tilde{c}_l^2 + \tilde{v}_{Al}^2)}, \quad (7.94)$$

$$\check{M}_l^2 = -\frac{\check{D}_{Al}\check{D}_{sl}}{(\tilde{c}_l^2 + \tilde{v}_{Al}^2)\check{D}_{Tl}}, \quad \check{D}_{Tl} = \Omega_l^2(1 + \chi_l) - k^2c_{Tl}^2. \quad (7.95)$$

The first root given by Eq. (7.90) portrays the fact that the neutrals and ions are colliding so often that they just behave as one fluid and so we recover the classic case of a single fluid plasma slab derived in [Edwin and Roberts \(1982\)](#) as is expected. However, the next root, given by Eq. (7.91), is more interesting. It is similar in structure to Eq. (7.47) and arises due solely to the presence of the flow, as with no flow shear this equation has no solutions. We therefore suspect that similar to incompressible case where we have shown there is an instability associated with the flow that occurs for lower flow shears than those required for the Kelvin-Helmholtz instability. To show its similarity in structure to Eq. (7.47) we rewrite Eq. (7.91) in the following form

$$\omega = \frac{u_0 + \tau u_e}{1 + \tau}k, \quad \tau = \frac{\zeta_0 v_{ine}\rho_{ne}}{\zeta_e v_{in0}\rho_{n0}}. \quad (7.96)$$

This has a very similar structure to Eq. (7.47), however the terms  $\zeta_0$  and  $\zeta_e$  occur due to the compressibility of the plasma. Both Eqs. (7.91) and (7.96) show some interesting features. Firstly, for a real solution to Eq. (7.91),  $\Omega_0$  and  $\Omega_e$  must have

different signs, otherwise no solution can exist. For real solutions we also require that

$$\text{sign} \left( \Omega_e \check{D}_{Te} \check{D}_{T0} \right) = \text{sign} \left( \Omega_0 \check{D}_{T0} \check{D}_{Te} \right). \quad (7.97)$$

Eq. (7.91) can be expanded to form a fifth order polynomial for the frequency:

$$X \Omega_0 \left( \Omega_e^2 - k^2 \check{c}_{Te}^2 \right) \left( \Omega_0^2 - k^2 \frac{c_{T0}^2}{1 + \chi_0} \right) = \Omega_e \left( \Omega_0^2 - k^2 \check{c}_{T0}^2 \right) \left( \Omega_e^2 - k^2 \frac{c_{Te}^2}{(1 + \chi_e)} \right) \quad (7.98)$$

where

$$X = \frac{(1 + \chi_e)^3 \check{\rho}_0^2 \chi_0^2 \nu_{in0} c_{n0}^2 (\check{c}_e^2 + \check{v}_{Ae}^2)(c_{i0}^2 + v_{A0}^2)}{(1 + \chi_0)^3 \check{\rho}_e^2 \chi_e^2 \nu_{ine} c_{ne}^2 (\check{c}_0^2 + \check{v}_{A0}^2)(c_{se}^2 + v_{Ae}^2)} \quad (7.99)$$

This polynomial is still generally insoluble being a fifth order polynomial but is easy to solve numerically. The roots of this polynomial must be substituted back into Eq. (7.91) to validate whether they satisfy it, as spurious roots may have been introduced by squaring terms. In Figs. 7.6a-d, we have plotted the solution to Eq. (7.91) as well as the solution to Eq. (7.38), both in the limit as  $kz_0 \rightarrow \infty$ , to compare the validity of the approximation. Also plotted are the bounds  $\check{c}_{Te}$ ,  $c_{Te}/\sqrt{1 + \chi_e}$ ,  $R_1 = (u_0 - \check{c}_{T0})/\check{v}_{A0}$  and  $R_2 = (u_0 - c_{T0}/\sqrt{1 + \chi_0})/\check{v}_{A0}$ , to which the modes asymptote or cannot exist beyond. This has been plotted for several different values of the temperature ratio,  $T_e/T_0$  and ionisation ratios  $\chi_e$  and  $\chi_0$  that would mimic plasmas in the chromosphere. We also take a value of  $\nu_{in0}/k\check{v}_{A0} = 1000$ , in this case the Alfvén frequency  $k\check{v}_{A0}$  is 1000 times larger than the collisional frequency  $\nu_{in0}$ . The plasma-beta value is set at  $\beta = 0.1$  to model the solar atmosphere. Immediately it is evident that there exist unstable modes for flow speeds that lie below the single fluid Alfvén speed,  $\check{v}_{A0}$ . Also interesting are the magnitudes of the positive imaginary part of the frequencies. The imaginary parts are only one order of magnitude smaller than the dimensionless frequency, meaning the time scale of the instability will only be one order of magnitude larger than the period of the wave, which is a realistic time-scale. The instability appears to occur within the region where the real part of the phase speed of the wave is

$$\max \left( u_0 - \check{c}_{T0}, \frac{c_{Te}}{\sqrt{1 + \chi_e}} \right) < \frac{\omega}{k} < \min \left( u_0 - \frac{c_{T0}}{\sqrt{1 + \chi_0}}, \check{c}_{Te} \right),$$

and exists when the two permitted solutions couple to one another for the solution Eq. (7.90).

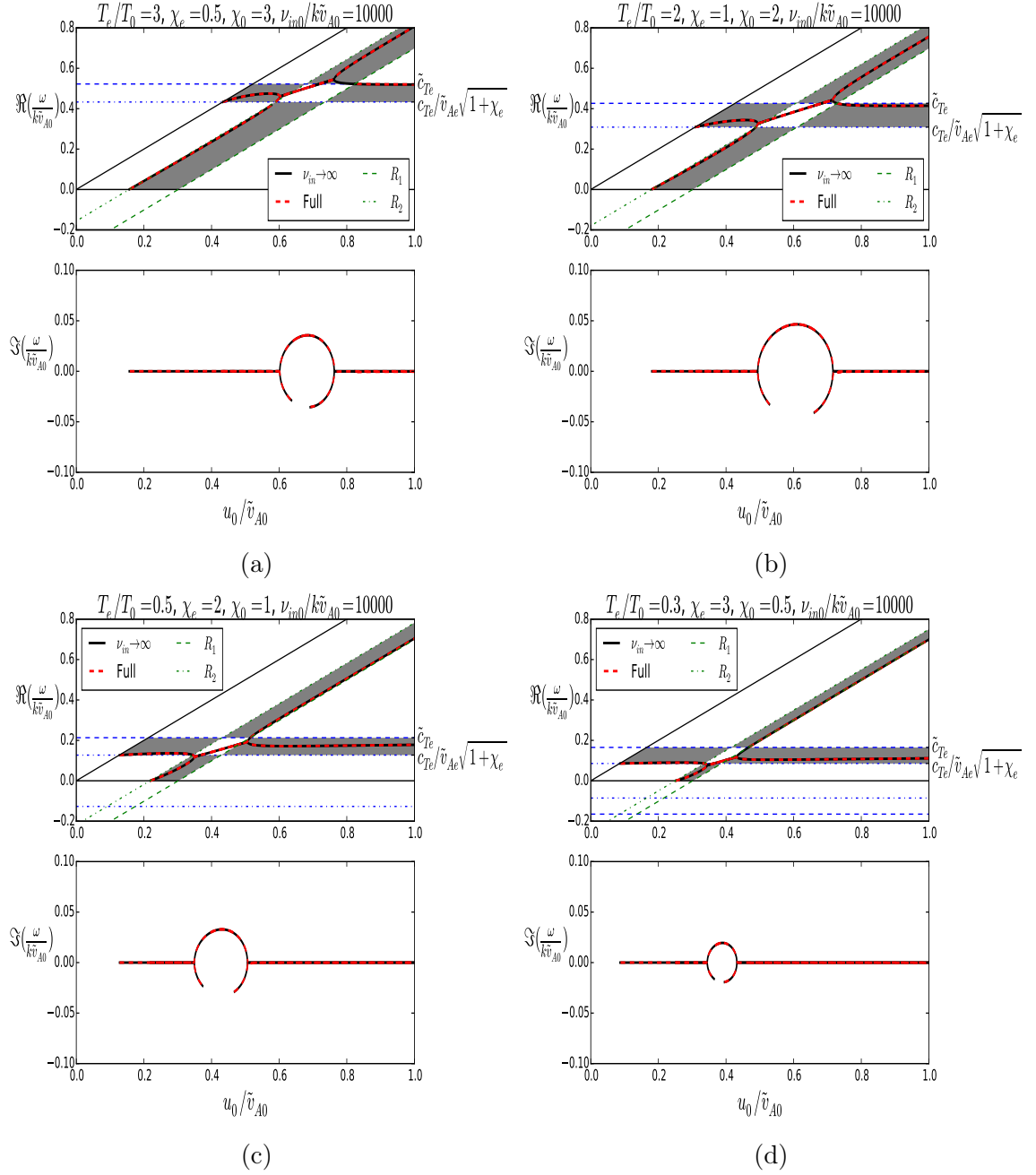


Fig. 7.6 The real and imaginary parts of the solution of Eq. (7.91), plotted as black solid lines, for increasing dimensionless flow speed,  $u_0/\tilde{v}_{A0}$  on the  $x$ -axis. The red dashed lines are the solutions to Eq. (7.41) but with  $kz_0 \rightarrow \infty$  i.e. a single interface. The two black lines not within the grey regions represent the line of  $\Re(\omega/k\tilde{v}_{A0}) = u_0/\tilde{v}_{A0}$  and 0, where solutions to Eq. (7.91) do not exist. Noted are the lines firstly, in blue,  $\tilde{c}_{Te}/\tilde{v}_{Ae}\sqrt{1+\chi_e}$  and  $c_{Te}/\tilde{v}_{Ae}\sqrt{1+\chi_e}$  and secondly, in green,  $u_0/\tilde{v}_{A0} - \tilde{c}_{T0}/\tilde{v}_{A0}$  and  $u_0/\tilde{v}_{A0} - c_{T0}/\tilde{v}_{A0}\sqrt{1+\chi_0}$ , where the grey regions are the only regions where real solutions can exist.

## 7.8 Turbulent plumes

Soler *et al.* (2012) studied the Kelvin-Helmholtz instability in turbulent plumes. In the article, they only considered the geometry of a single interface and neglected to study the effect of the plume width. By varying the mode's wavelength in comparison to the slab width ( $kz_0$ ) and flow speed, we study the flow speeds an instability can occur in a turbulent plume by solving Eqs. (7.40) and (7.41) numerically. For our model of the plume we first of all assume that both the internal and external plasmas are thermally coupled ( $T_{ne} = T_{ie}$ ,  $T_{n0} = T_{i0}$ ) so that, by the ideal gas law, both have the same ion and neutral sound speeds i.e.  $c_{ne} = c_{ie}$  and  $c_{n0} = c_{i0}$ . We also assume that the magnetic fields within the slab and outside the slab are equal that is  $B_0 = B_e$ , the temperature ratio between the external and interior medium is  $T_0/T_e = 10.0$  and the total density ratio is  $\tilde{\rho}_e/\tilde{\rho}_0 = 10$ . The ratio of the sound speed to the *total* Alfvén speed (the Alfvén speed calculated with the density of both the ion and neutral fluids),  $\tilde{v}_{Ae}$ , in the external medium is  $c_{ie}/\tilde{v}_{Ae} = \sqrt{0.1}$ , and this ratio is the same in the internal medium  $\tilde{c}_e/\tilde{v}_{Ae} = \sqrt{0.1}$ . The width of the slab is taken to be  $2z_0 = 5 \times 10^5$  m and we take  $v_{ine}z_0/\tilde{v}_{Ae} = 1000$  as we are not changing the slab width but are, rather, changing the wavelength/wave-number. For the ratio of neutrals to ions, we take  $\chi_e = 1.0$  so that there are the same number of ions as neutrals and we take  $\chi_0 = 0.05$  so that the internal hotter plasma is almost fully ionised.

Fig. 7.7 plots the backward propagating slow-wave solutions for dimensionless frequency,  $\omega/k\tilde{v}_{Ae}$ , of Eq. (7.41) varying with dimensionless wave-number,  $kz_0$ , for the parameters given above (as the slab width is kept constant we are actually varying the wave-number,  $k$ ). Figs. 7.7a,b and c are plotted for  $u_0/\tilde{v}_{Ae} = 0, 0.6$  and  $1.2$  respectively. The black lines correspond to the solutions to Eq. (7.41), whereas the red lines are the solutions obtained by solving the ‘coth’ solution of Eq. (7.90), i.e. the case where the ion and neutral plasma act as one medium. Fig. 7.7a is the solution for the static case,  $u_0/\tilde{v}_{Ae} = 0$ . Due to the high collisional frequency we can see how similar the real parts of the solutions to Eq. (7.41) are to the solution of Eq. (7.90). However, for low values of  $kz_0$ , the solutions do not match and the full two fluid solutions pass through the line  $-\tilde{c}_{T0}$ , the maximum value of the solutions of Eq. (7.90). Interestingly we see far more significant damping for the full two fluid solutions as they pass this value, dropping as  $kz_0$  tends toward zero.

Fig. 7.7b is plotted for  $u_0/\tilde{v}_{Ae} = 0.6$ . In this figure, three panels have been included; the middle panel shows the real part of the solution to Eq. (7.41) with the same modes as considered in Fig. 7.7a, again it is clear that the single fluid model represents these modes well, except when  $kz_0$  nears zero. The upper panel shows another solution exist when a flow is introduced to the system, with dimensionless frequency just above  $c_{Te}/v_{Ae}\sqrt{1 + \chi_e}$ . This mode is a result of the highly collisional

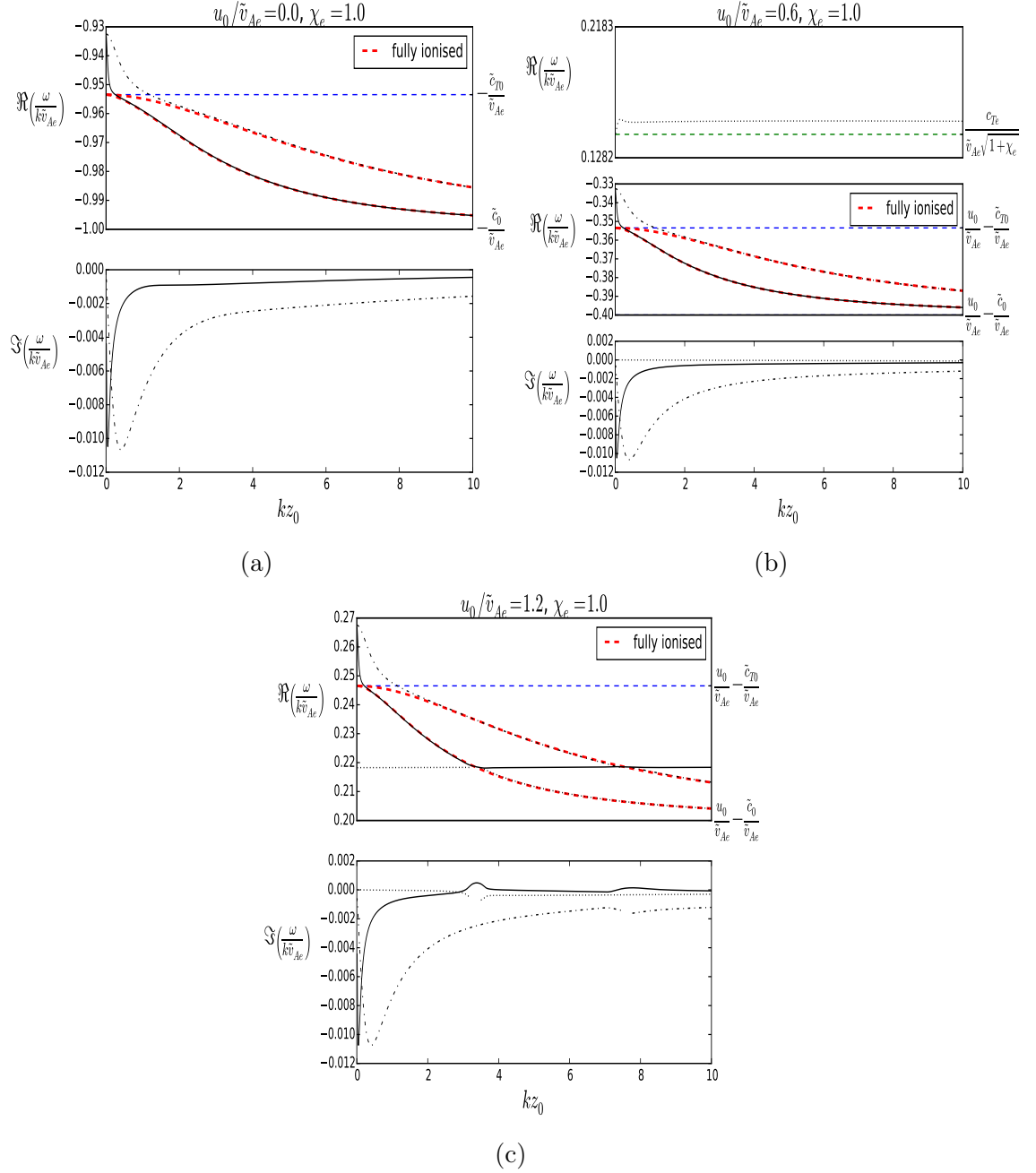


Fig. 7.7 The dimensionless solutions (real and imaginary parts) of Eq. (7.41),  $\omega/k\tilde{v}_{Ae}$ , for varying dimensionless horizontal wave-number,  $kz_0$ , for parameters:  $\nu_{ine}z_0/\tilde{v}_{Ae} = 1000$ ,  $\chi_e = 1.0$ ,  $\chi_0 = 0.05$ ,  $\tilde{c}_e^2/\tilde{v}_{Ae}^2 = 0.1$ ,  $T_0/T_e = 10.0$ ,  $2z_0 = 5 \times 10^5$  km. To explore the effect of flow on the modes the dimensionless flow parameter is set at  $u_0/\tilde{v}_{Ae} = 0.0, 0.6$  and  $1.2$  in panels (a), (b) and (c). Also, plotted are two of the solutions to Eq. (7.90), for the kink mode, which are red-dashed lines. Note the lines  $u_0/\tilde{v}_{Ae} - \tilde{c}_{T0}/\tilde{v}_{Ae}$  and  $u_0/\tilde{v}_{Ae} - \tilde{c}_0/\tilde{v}_{Ae}$ . In panel (b) the real part of the solution has been split into two regions to demonstrate that another mode exists that is solely due to the shear in flow.

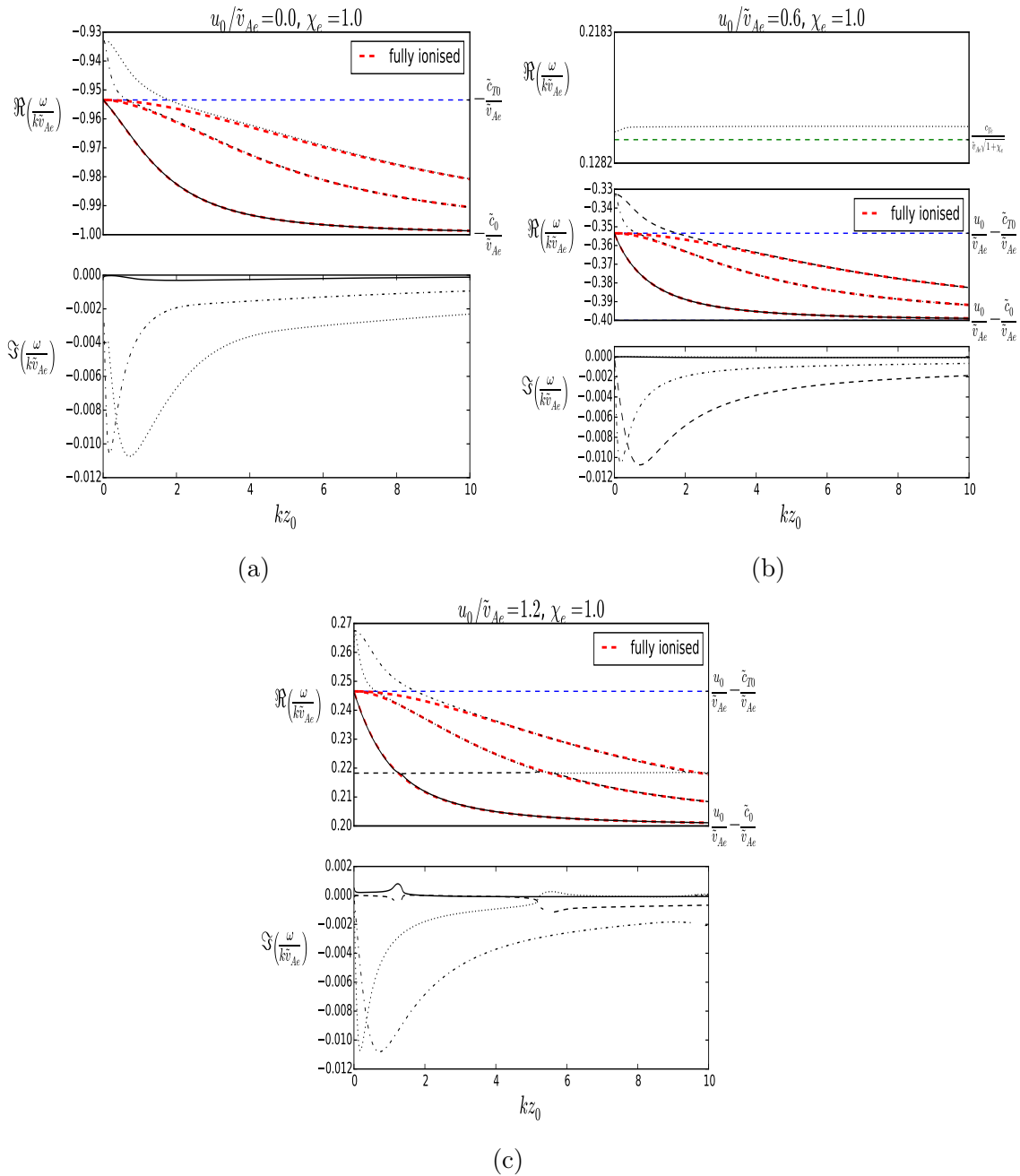


Fig. 7.8 Same as Fig. 7.7 but for the solution to Eq. (7.40). The red dashed lines are the three solutions to Eq. (7.90) but for the sausage mode.

limit given by Eq. (7.91) and, again, only exists due to the presence of the shear in flow and is somewhat akin to the neutral mode discussed for the incompressible case. Fig. 7.7c is plotted similarly but for  $u_0/\tilde{v}_{Ae} = 1.2$ . We can see in the upper panel that, again, the single fluid solution is a very good approximation for the modes but again, as  $kz_0$  nears zero, the modes cross the  $\Re(\omega/k\tilde{v}_{Ae}) = u_0/\tilde{v}_{Ae} - \tilde{c}_{T0}/\tilde{v}_{Ae}$  line. However, there is also the same mode, due to the flow, that was seen in Fig. 7.7b and one observes that this mode cuts through the two slow modes mentioned previously. What actually is seen are the two solution paths avoiding each other and we can see a large peak in the positive imaginary part of one of the modes, indicated by the black solid line. Further on, as  $kz_0$  increases, this interaction occurs once again but with the second slow mode and there is a peak in the positive imaginary part of the dimensionless frequency again. This can be viewed as similar to the instability considered in the incompressible case, where it was found that the crossings (the real parts of the frequencies became very close) of the modes, that existed because of the flow, caused a large peak in the positive imaginary part of the frequency, akin to resonance.

Fig. 7.8 is for the exact same parameters as Fig. 7.7 but for the solution of Eq. (7.40) instead i.e. the symmetric sausage modes. Fig. 7.8a is plotted for  $u_0/\tilde{v}_{Ae} = 0$ , for three of the backward propagating slow body waves. Firstly we note that the ‘pseudo-body’ mode (black solid line) that was mentioned in Chapter 5 is present here, as well as two of the proper slow sausage body modes. What we note about this mode is that, as  $kz_0 \rightarrow 0$ , the fully ionised solution, given by the sausage mode solution to Eq. (7.90), is practically the same. However, for the two proper body modes, just as for the kink mode in Fig. 7.7, the approximation by Eq. (7.90) becomes worse as  $kz_0 \rightarrow 0$  and the solutions pass through the line  $-\tilde{c}_{T0}/\tilde{v}_{Ae}$ .

Fig. 7.8b is plotted for  $u_0/\tilde{v}_{Ae} = 0.6$ . The modes of Fig. 7.8a are pushed up the  $\Re(\omega/k\tilde{v}_{Ae})$  axis by 0.6. The upper panel shows the mode that exists due to the shear flow, just as in Fig. 7.7b. None of the modes here are unstable and are only damped, again with greatest damping for the body modes as they pass through and beyond the line  $u_0/\tilde{v}_{Ae} - \tilde{c}_{T0}/\tilde{v}_{Ae}$  line. Fig. 7.8c is plotted for  $u_0/\tilde{v}_{Ae} = 1.2$ . One can see that again the mode that exist due to the flow interacts with all the slow body modes and at these points there are peaks in the positive imaginary part of the frequency.

## 7.9 Summary and Discussion

In this Chapter, we have studied the effect of flow on the oscillations in a two fluid collisional plasma slab. We derived two second order ODE’s that coupled the total (magnetic + ion-gas) pressure,  $P_T$ , to the neutral pressure,  $p_n$ , Eqs. (7.8) and (7.11), respectively. Combining these two equations resulted in a fourth order differential equation for  $p'_n$ , given by Eq. (7.19). Using appropriate boundary conditions and

the solutions to Eq. (7.19) we derived the full dispersion relation for a two fluid collisional plasma slab with constant background flows, which was found to be split into separate modes: the kink and sausage waves.

Firstly, in Section 6.5, the incompressible limit was analysed, along with the highly collisional limit. It was found that two distinct solutions existed: the first was the solution for an incompressible plasma slab, where the two fluids were acting as one fluid due to the neutrals and ions colliding so frequently; the second was a mode that was due solely to the presence of the flow and neutral fluid. The second, neutral mode, was found to always be growing in amplitude over time regardless of the flow velocity, which agreed with the results in Soler *et al.* (2012). It was found that the magnitude of this instability grew with increasing velocity shear and, for lower collisional frequencies, the time-scale of this instability could be one order of magnitude longer than the time-scale of the perturbation. However, it must be noted that increasing the collisional frequency with respect to the perturbation frequency would make the time-scale larger and potentially insignificant. It was also found that there are flow speeds at which the approximation for the correction to the frequency breaks down. These are always below the Kelvin-Helmholtz threshold velocity of the single fluid dispersion relation, Eq. (7.46). Solving the full Eq. (7.43), it was also found that the flow speeds at which the approximation breaks down occurred, matched the flow speeds when the ‘neutral flow mode’, given by Eq. (7.47), resonantly interacted with the mode given by Eq. (7.46) and a large peak in the positive imaginary part of the frequency was found. This resonance between the two modes appears not to have been documented in other studies of the incompressible two-fluid slab or cylinder with a background flow and could be responsible for instabilities that occur for background flows lower than the Kelvin-Helmholtz threshold velocity, in the parts of the solar atmosphere where the plasma is partially ionised.

Next the collision-less limit was taken and it was found that the dispersion relation reduced to two separate roots, one governing the neutral fluid and one governing waves in the ion plasma. It was confirmed that, by taking the slender slab limit of the neutral root, the neutral fluid was always KHI unstable to a shear flow (see e.g. Soler *et al.*, 2013 or Martínez-Gómez *et al.*, 2015).

The last part of the chapter was concerned with the more realistic situation of highly collisional plasmas which are more likely for the wave periods observed. The highly collisional limit of Eq. (7.42) was taken and two separate roots were found: the first being the case where the ions and neutrals act as one single fluid and returned the dispersion relation derived in Edwin and Roberts (1982); the second was a root that only has solutions when there is a flow shear and was shown to be very similar to the mode given by Eq. (7.47). Using this limit it was found that one solution could not exist until  $u_0 = c_{Te}/\sqrt{1 + \chi_e}$  and the other until  $u_0 = c_{T0}/\sqrt{1 + \chi_0}$ .

These modes two modes could then couple together and an instability was found to occur. Significantly the flow speeds required are sub-Alfvénic.

Finally, the full Eqs. (7.41) and (7.40) were solved numerically for parameters similar to that of turbulent plumes. It was found that the single fluid dispersion relation was a very good approximation for the slow body modes in both the kink and sausage cases apart from when the dimensionless wave-number was low. One of the modes given by Eq. (7.91) was shown to exist when a flow was introduced and a semi-resonant interaction between this mode and the body modes was found to occur when the real parts of the frequency neared became close, with the imaginary part becoming orders of magnitude larger around these crossings. This occurred for flow speeds 1.2 times larger than the single fluid Alfvén speed of the interior of the plasma slab,  $\tilde{v}_{A0}$ , which may be too fast as compared to turbulent plumes flow speeds of around  $30 \text{ km s}^{-1}$ . However, in both the sausage and kink modes the growth rate of the instability was approximately two to three orders of magnitude lower than the frequency of the perturbation. Therefore this would only be significant for higher frequency perturbations in the sense of turbulent plumes which have a life time of  $\sim 870 \text{ s}$ .



# Chapter 8

## Conclusion

### 8.1 Overview of the thesis

The over-arching study in this thesis was of oscillations in the solar atmosphere. The thesis was split into two main parts: the first studying magneto-acoustic gravity oscillations in the stratified solar atmosphere and then, secondly, flow instabilities in partially ionised plasmas in the solar atmosphere, where special attention was given to prominence plasmas.

Chapter 3 was based on work from the published paper [Mather and Erdélyi \(2016\)](#). In Chapter 3, the equilibrium background for a plasma stratified by gravity, with a constant embedded magnetic field parallel with the gravitational field, was introduced. Solutions were found for a new variable not yet considered,  $\Theta = p_1/\rho$ , namely the pressure perturbation divided by the background density. A dispersion relation for standing waves was derived with the limiting case of small wavelength taken also. The dispersion relation was then solved for two distinct models of the solar atmosphere i.e. the lower solar atmosphere and the corona, respectively.

Chapter 4 was based on the second part of the published paper [Mather and Erdélyi \(2016\)](#). Chapter 4 extended the investigation of Chapter 3 by connecting two separate plasmas across a discontinuity in density/pressure, where a highly transcendental dispersion relation for standing modes was found. Two different solar atmospheric situations were studied: a transition from the photosphere/low chromosphere to the high chromosphere; a sharp transition from the lower solar atmosphere to the corona where the discontinuity was used to model the jump in the density and temperature of the transition region. The energy density of the waves was studied in both layers to determine their properties and where the energy was trapped. The conclusion for the first model was that energy was trapped mostly in the the lower region and only for the acoustic modes was there any energy distributed in the upper layer. For the second model, all the energy was seen to be trapped

in on of the separate layers, with some sharing of total energy between the layers around the avoided crossings.

Chapter 5 took the study of MAG waves in a slightly different direction, the effect of a constant flow on MAG waves at a tangential magnetic interface was investigated, with a dispersion relation governing the propagation of waves derived. The cold plasma and small wavelength limits were taken of this dispersion relation. Cut-off regions where waves cannot propagate were found and these regions changed depending on the value of the flow parameter. The dispersion relation was solved numerically for specific background parameters chosen to model the solar atmosphere and interior. The cut-off curves led to the disappearance of the fast wave as the value of the bulk flow was increased. The flow was also found to lead to the reversal in direction of surface waves which could lead to negative energy wave instabilities.

Chapter 6 introduced the next part of the thesis, the study of partially ionised plasmas. In this chapter, a background equilibrium was established for a magnetic plasma slab embedded in an external magnetised plasma. The external plasma was considered as the fully ionised corona but non-ideal as Braginskii's viscosity tensor [Braginskii \(1965\)](#) was included for dissipation. The internal plasma was partially ionised prominence plasma, with Cowling's resistive term in the induction equation. Perturbing around this background a dispersion relation was found and the dissipative instability was studied. It was found that negative energy wave instabilities existed in the fully ionised prominence and only flow speeds of approximately  $10 \text{ km s}^{-1}$  were required, although the time-scales for these were possibly too large to be relevant. When there were more neutrals the instability could only occur at higher flow velocities.

Chapter 7, just like Chapter 6, considered a partially ionised plasma slab but both internal and external plasmas were fully collisional, although other two fluid effects were neglected. The basic governing equations and dispersion relations were derived and limits such as the incompressible, collision-less and highly collisional limits were taken. It was confirmed, as in previous studies, the neutrals are always KHI unstable when there is a flow shear between separate layers, in both the incompressible and collision-less limits. This is not the case when the plasma is compressible. Also, confirmed in both the incompressible and compressible cases (turbulent plumes), were the existence of resonant interactions between neutral flow modes and the modes when both the neutral and ion fluids were acting as one fluid, in the highly collisional limit.

## 8.2 Summary of Results

### 8.2.1 Chapter 3

Chapter 3 introduced the basic equilibrium and governing equations for a plasma stratified by gravity embedded with a magnetic field parallel to the gravitational field, the so-called vertical field model. A new variable, never before considered, was introduced,  $\Theta = p_1/\rho_0$ , that was used to derive a fourth order differential equation, Eq. (3.25), that was then solved by the Fröbenius method in terms of Fröbenius series solutions. Ultimately, these were written in terms of hypergeometric functions. With the simple algebraic relations of the horizontal and vertical velocities with respect to  $\Theta$ , these two velocity components were written in terms of hypergeometric functions as in the previous works of Zhugzhda (1979), Wang (1986). The importance of the hypergeometric functions are that they have been well studied and have well defined asymptotic expansions, most of which can be found in Luke (1975).

Using the derived solutions for  $v_z$  and  $v_x$  a single-layer model was derived, using perfectly reflecting boundary conditions at the base and ceiling. The result was a highly transcendental dispersion equation given only as the determinant of a matrix by Eq. (3.29). However, a simple short horizontal wavelength limit was able to be taken, using well known properties of the Pochhammer function. This resulted in the disappearance of the fast mode (see e.g. Roberts, 2006 or Hague and Erdélyi, 2016). The dispersion relation, Eq. (3.33), acquired was also transcendental, comprised of hypergeometric functions. By using well known asymptotic expansions of these functions, the low and high beta limits were taken. It was found for the low beta limit that the slow mode degenerates into a vertically propagating sound wave trapped, as harmonics, within the cavity. The high plasma-beta limit revealed that at low frequencies, i.e. the low harmonics, the modes were of a more gravitational nature but for the higher harmonics, with higher frequencies, became essentially magnetic slow modes. The dispersion relation, Eq. (3.37) was found to be in full agreement with that obtained in Hasan and Christensen-Dalsgaard (1992), however, their equation was derived directly from the governing equation, not from the full dispersion relation.

Having investigated the analytic limiting forms of the dispersion relation, two separate single layer models, approximating different models and regions of the solar atmosphere, were studied. Eq. (3.29) was numerically solved with dimensionless parameters for both models. The first model considered approximated a coronal plasma, with a low plasma beta value at the base decreasing with height. By solving the dispersion relation the dispersion diagram was plotted in Figs. 3.2a-d. The internal and magnetic energy densities of the modes were compared, making use of the colour bar, and it was found that the slow and fast mode were distinct

and separated. However, at avoided crossings, the notion of fast or slow modes does not make sense due to the equal distribution of internal and magnetic energy densities of the mode. The second model described a plasma changing from the high plasma-beta of the photosphere to the low plasma-beta of the chromosphere. Solutions were plotted in Fig. 3.3 with a colour bar representing the proportion of internal and gravitational energy densities compared to the magnetic energy density. The plasma at the base had, initially, a very high plasma-beta value so that modes were separated into acoustic ‘fast’ modes and magnetic/gravity ‘slow’ modes. Near the Brunt-Väisälä frequency, the slow modes were more gravitational in nature but for higher frequencies the slow modes were mostly magnetic, mimicking the small-wavelength results. Again, around avoided crossings, the modes could not be distinguished due to the equal distribution of the separate energy densities.

### 8.2.2 Chapter 4

Chapter 4 followed on from the study of the single layer plasma of Chapter 3. Using the solutions derived in Chapter 3, a general two layer model was initialised in which there was a jump in temperature across a discontinuity between the lower and upper layers, which were bounded by perfectly reflecting barriers at the bottom and top respectively. The dispersion relation, Eq. (4.4), was given by the determinant of an  $8 \times 8$  matrix and thus it was numerically solved. Several models have considered multilayer models before in this geometry (see e.g. [Scheuer and Thomas, 1981](#), [Yelles Chaouche and Abdelatif, 2005](#)). The model considered here was bounded above so that acoustic modes would be trapped, not just magnetic modes.

The first numerical model was analogous to the temperature jump between the photosphere/low chromosphere and the high chromosphere, bounded above and below by the solar interior and transition region respectively. With a typical value of  $7.9 \text{ km s}^{-1}$  for the sound speed in the photosphere, it was found that eigen-frequencies lay within the 3-minute and 5-minute oscillation range, as shown by Fig. 4.3. By studying the wave energy density it was found that the wave energy would be trapped mainly in the photosphere/chromosphere (see Fig. 4.4d). This is due to the increasing Alfvén speed of the system that acts to reflect the magnetic energy, as could be seen in Figs. 4.5b and c. However, for the modes of acoustic nature, the energy distribution was shared more evenly between the layers. This is due to the sound speed being constant as well as the temperature discontinuity only being fairly small and as such waves incident on this surface are not so readily reflected. This can be noted in Figs. 4.5a and d. Modes with frequencies near/under the Brunt-Vaisala frequency were found to have most energy trapped within the lower layer.

The second numerical model considered a two layer plasma: the upper layer a coronal plasma and the lower layer a lower solar atmospheric plasma. The discontinu-

ity between the layers was considered as a factor of 400 increase in the temperature i.e. a transition to coronal temperatures. By plotting the dispersion diagram in Fig. 4.14 and the proportion of energy in the lower layer compared to the total energy in both layers, it was found that modes were either trapped within the upper or lower layers (see Fig. 4.15). This is obvious physically as the large density discontinuity acts as a physical barrier to reflect waves incident on the surface. There could, however, be an even amount of energy between both layers at avoided crossings, showing the inherent coupling between them. This coupling is important as it would allow wave energy to leak from one layer to another.

### 8.2.3 Chapter 5

The focus of Chapter 5 shifted away from the two layer model of the vertical field, to the study of the effect of flow on MAG surface waves (see Miles and Roberts, 1992) at a tangential magnetic discontinuity. The situation described in this chapter is important for situations such as the meridional flow of the solar surface or the stronger flow regions of Evershed flow above sunspot canopies.

The dispersion relation derived was highly transcendental so was solved numerically but some interesting limits were taken. The incompressible limit permitted a very simple second order polynomial for the phase speed of the wave that had solutions given by Eq. (5.38). In this situation, the Kelvin-Helmholtz was possible but for flow speeds greater than the Alfvén speed. Fig. 5.2 showed that the critical flow speed for the instability was increased by the inclusion of gravity.

By taking the limit of small wavelength, gravity was essentially neglected and returned Eq. (5.42) as the dispersion relation. This was highly transcendental and as such the cold plasma limit was taken to remove the fast wave, which resulted in a fourth order polynomial for the Doppler shifted frequency, Eq. (5.43). However, two further approximations were taken using a perturbation method, the limit of small flow and small density ratio. The first approximation showed that the slow wave phase speed was just below the sound speed of the lower medium and the correction due to the flow increased the phase speed of both the forward and backward propagating waves. Thus, a meridional flow of  $0.2 \text{ km s}^{-1}$ , with a sound speed of  $\sim 7 \text{ km s}^{-1}$  giving  $u_e/c_{se} \approx 0.03$ , would likely have little effect on the wave propagation of the slow surface wave. The small density ratio approximation allowed the analysis to cover larger flow speeds. Fig. 5.4 showed that both the backward and forward propagating slow modes were affected linearly by the flow, with the backward propagating mode actually changing direction for flow speeds near the sound speed. This could be interesting for the observation of waves in Evershed flows as the observed phase speeds may not correlate to the actual phase speed of the wave.

Finally, the dispersion relation, Eq. (5.33), was solved numerically and plotted in Figs. 5.5-5.8. The backward and forward propagating modes were plotted in all these figures. With the flow parameter set to zero, the modes found in Miles and Roberts (1992) were returned. By steadily increasing the flow parameter the forward propagating modes were seen to barely increase in phase speed and could exist for only a small range of dimensionless wavelengths. The backward propagating modes, whilst existing for a smaller set of dimensionless wavelengths than previously, were accelerated and even changed their direction of propagation. This change in direction could be important for stability due to the negative energy wave instability being able to occur if dissipative processes are present or the interaction between positive and negative energy waves of the system (Ryutova, 1988). The fast modes from Fig. 5.6 were also seen not to exist if the flow parameter was too large and did not propagate. Evidenced in all the figures was the coupling of backward and forward propagating modes at which point the Kelvin-Helmholtz instability occurs. This instability always occurs for super Alfvénic speeds as can be seen in all of Figs. 5.5-5.8.

Evershed flows in sunspots can reach up to  $6 \text{ km s}^{-1}$ . Applying this to Figure 5.6 and taking  $c_{se} = 7 \text{ km s}^{-1}$  and  $u_e = 6 \text{ km s}^{-1}$  and thus  $u_e/c_{se} = 0.86$ , it can be seen from Figures 5.6 and 5.8 that this flow speed is high enough for the backward-propagating waves to reverse their direction of propagation. Thus, some running penumbral waves (RPW) may become negative energy waves. This change in direction of propagation may also have implications on the interpretation of observations of RPWs, as some may have very slow phase speed because they may be backward-propagating surface waves, affected by a flow.

## 8.2.4 Chapter 6

Chapter 6 shifted the focus from fully ionised plasmas towards partially ionised plasmas. The main focus of this chapter was the study of the dissipative instability due to a constant background flow, closely related to the negative energy wave instability, in a partially ionised prominence plasma slab surrounded by a viscous corona.

Firstly the background equilibrium was introduced. The external coronal plasma was static but viscous, using the approximation for a strong magnetic field derived by Braginskii (1965) (see also Hollweg, 1985). The internal prominence plasma had a constant background flow and was treated as a single fluid with partial ionisation in the Cowling resistive term. Perturbing around these backgrounds resulted in the dispersion relation given by Eq. (6.15). The slender slab limit was then taken, which revealed that two surface modes were possible for the sausage modes one propagating at the external sound speed and the other propagating at the internal tube speed

but modified linearly by the background flow. Two modes were revealed for the kink modes, one propagating at the external Alfvén speed and another at the external tube speed.

Taking into consideration the slender-slab limit, the dissipative instability was now investigated. The negative energy wave instability was considered first. When the sign of the frequency of a wave changes that wave can become unstable to a negative energy wave instability. The Cowling resistivity was therefore neglected and it was found that the sausage mode propagating at the internal tube speed, in the slender slab limit, would be the only mode that would likely change from a backward to forward propagating wave for flow speeds that were not too large. The other modes, having approximately coronal background phase speeds, would likely have phase speeds too large for actual physical flows to reverse the direction of propagation.

The dissipative instability was then considered for the case of a prominence plasma slab, surrounded by a coronal plasma. As the coronal plasma was much hotter and much less dense an approximation for the imaginary part of the frequency was taken, given by Eq. (6.48). It was found that this changed sign for flow speeds greater than the internal tube speed, shown by Eq. (6.49), and at the tube speed if the resistive term was neglected. As the resistive term became larger due to the increase in the proportion of neutrals, the speed at which the dissipative instability occurred became larger (see Fig. 6.3). The incompressible case was also compared to the compressible case. In the incompressible case the flow required would have to be larger than the Alfvén speed (Eq. (6.50)). However, there were values of the ionisation degree which were large enough for the onset of the instability to be lower for the incompressible case than the compressible case. The value for the growth rate of the instability was very small, however, with a time-scale of  $\sim 10^6$  s.

Due to the large time-scale of this instability in the slender slab limit, the dispersion relation, Eq. (6.15), was solved numerically and plotted in Figs. 6.5-6.8, for varying wave number,  $k$ , and varying slab width,  $2z_0$ , respectively, to see how these affected the time-scales of the instability. When holding the wave-number constant at  $k = 5 \times 10^{-6} \text{ m}^{-1}$ , it was found that the largest amplification rate occurred for the pseudo-body mode at around  $kz_0 \approx 1$  with an amplification rate of approximately  $5 \times 10^{-5} \text{ s}^{-1}$  seen for  $u_0 = 28 \text{ km s}^{-1}$  and  $\rho_r = 0.02$ . The addition of neutrals served to inhibit this negative energy wave instability and, indeed, by progressively increasing the ionisation degree,  $\mu$ , the magnitude of the damping rate increased. When the slab width was held constant, the body mode experienced the highest amplification rate, with a maximum in Fig. 6.8d of approximately  $\omega' \approx 5 \times 10^{-6} \text{ s}^{-1}$ .

### 8.2.5 Chapter 7

After approximating a partially ionised plasma as a single fluid in Chapter 6, Chapter 7 sought to investigate the effect of the collisions between ion and neutral species on the stability of a two fluid magnetic slab with a constant background flow.

Firstly, two coupled second order ODE's were derived for the neutral pressure,  $p_n$ , and the total pressure,  $P_T$ , given by Eqs. (7.11) and (7.8) respectively. These were found to be very similar to the equations derived by Soler *et al.* (2013) but for a Cartesian coordinate system rather than a cylindrical one and with a constant background flow. These equations were then formed into a fourth order differential equation that governed the two fluid system given by Eq. (7.19). With the appropriate boundary conditions a dispersion relation was found, Eq. (7.38). This was shown to reduce down into the sausage and kink branches given by Eqs. (7.40) and (7.41), respectively.

The next part of the chapter studied the incompressible limit of Eq. (7.42), which was found to reduce to Eq. (7.43) in agreement with Ballai *et al.* (2017a) and similar to the equation derived for a cylindrical coordinate system in Martínez-Gómez *et al.* (2015). The highly collisional limit of Eq. (7.43) ( $\omega/\nu_{in} \ll 1$ ) was taken and as a result, two separate branches were found in the zeroth order approximation. The first branch corresponded to the solution when the neutral and ion fluids are acting as a single fluid. The second branch existed due to the neutral fluid and the background flow. By studying the correction to the frequency of the mode, the neutral flow was confirmed to be unstable regardless of how high the collisional frequency was. The corrections to both Eqs. (7.46) and (7.47) showed the interesting feature that at certain flow speeds the frequencies of the zeroth order approximations would be equal. The flow speeds for this to occur were found to always be lower than those for the Kelvin-Helmholtz instability of Eq. (7.46)

To investigate the case where the two branches had equal frequency, Eq. (7.43) was solved numerically for both the sausage and kink modes for a dimensionless model in which the external plasma was cooler than the internal plasma and another in which the internal plasma was cooler than the external plasma. The dimensionless phase speed was plotted as a function of the dimensionless flow parameter,  $u_0/\nu_{KH}$ , in Fig. 7.4d. At the flow speeds where the frequencies of the two branches were equal, the real parts of the phase speeds avoided one another and there was a sharp rise in the magnitude of the imaginary part of the dimensionless frequency, suggesting a resonant interaction between the neutral flow mode and the 'single fluid' kink mode. This suggests that instabilities with realistic growth time-scales can exist for flow speeds less than those required for the Kelvin-Helmholtz instability. For example, for the case of a cooler interior shown in Fig. 7.4d it was found, for the kink mode, that this instability would occur at  $u_0 \approx 0.8\nu_{KH}$  for  $kz_0 = 0.1$  or  $u_0 \approx 0.93\nu_{KH}$  for

$kz_0 = 1.0$ , although we must bear in mind the Kelvin-Helmholtz threshold velocity becomes very large for thinner slabs. The smallest amplification time-scale was found to be approximately only 16 times longer than the kink period.

Moving on from the incompressible limit, the collision-less limit of Eq. (7.42) was taken. The zeroth order approximation resulted in two separate branches where the ion and neutral fluids do not collide and, as such, are treated as separate fluids, given by Eqs. (7.79) and (7.80) respectively. By taking the slender slab limit of Eq. (7.80), the neutral fluid was found to always be unstable to the Kelvin-Helmholtz instability, mimicking the results of [Martínez-Gómez \*et al.\* \(2015\)](#) and [Ballai \*et al.\* \(2017b\)](#) for the incompressible case and [Soler \*et al.\* \(2012\)](#) for the compressible case. The importance of this is that it shows that the presence of neutrals may cause partially ionised plasmas to be more unstable to flow instabilities as they are not affected by the magnetic field and as such it cannot inhibit the KHI in the neutrals.

The collision-less limit is a good means of easily seeing the physics of the problem. However, as the collisional frequency between ions and neutrals is usually much higher than the frequencies of waves usually observed on the Sun, it is not a very useful limit for actual physical quantities. Therefore the highly collisional limit was taken next. Two separate branches were found, much like for the incompressible case. The first branch portrayed the case in which the two fluids are acting as a single fluid and is exactly the same as for the single fluid case given in [Nakariakov and Roberts \(1995\)](#). The second branch was found to exist only when a flow and neutrals are included in the system, much like Eq. (7.47). It was found that for real solutions to Eq. (7.91) that cut-offs existed bounded given by the condition of Eq. (7.97). The modes satisfying Eq. (7.91) were found and plotted varying with increasing flow parameter,  $u_0/\tilde{v}_{A0}$ , in Fig. 7.6 with the solutions to Eq. (7.42) as  $kz_0 \rightarrow 0$  plotted over these. Both solutions showed great agreement. An instability was even seen to occur when the flow was large enough that they coupled together. The growth rate of this instability was only an one order of magnitude less than the frequency of the perturbation, suggesting that it would likely occur on a realistic time-scale. This, however, needs further investigation.

The last part of the chapter focussed on turbulent plumes within prominences. The plasma chosen to be studied was cooler in the external plasma and hotter in the internal plasma. The modes studied in both the kink and sausage cases were the backward propagating body modes that propagate at phase speeds between the internal tube speed and internal sound speed. It was found that for both the kink and sausage branches, that the body modes were almost identical to those if the plasma was fully ionised, however there was a difference if the modes were near the phase speed of  $-\tilde{c}_{T0}$ , where the two fluid modes passed through this and tended towards the value  $-c_{T0}/\sqrt{1 + \chi_0}$ , where there occurred significant damping near this point (shown by Figs. 7.8a and 7.8a). However, one of the sausage modes,

that related to the pseudo body mode mentioned in Chapter 6, tended toward the  $-\tilde{c}_{T0}$ . The flow was then increased and a new mode appeared with phase speed in between  $c_{Te}/\sqrt{1+\chi_e}$  and  $\tilde{c}_{Te}$  (see Figs. 7.7b and 7.8b). When the flow was sufficient that the body modes passed through this mode, there was a resonant interaction between them, in which the imaginary part of the frequency increased to around  $\omega/k\tilde{v}_{Ae} \approx 0.001$  at its peak (see Figs. 7.7c and 7.8c).

### 8.3 Further Work

This thesis covered a wide range of different topics and as such there are still many unanswered questions.

Chapters 3 and 4 investigated the MAG modes in a vertical field, with the two separate models of an interface between the low chromosphere and high chromosphere and an interface between the lower solar atmosphere and the corona. A further study would be a three-layer model in which the lower layer is the photosphere/low chromosphere, the middle layer is the high chromosphere and the upper layer as the coronal plasma. The benefit of this model would be the lower temperature jump from the chromosphere to the corona and as such more wave energy may be able to penetrate through the interface. The possibility of standing modes developing in this intermediate layer may also be an interesting consequence of the model. The other issue with this model is that the magnetic field does not decrease with height (preserving the solenoidal condition). Realistically as one moves out further from the Sun the magnetic field strength decreases and as such the corona transitions from a low beta plasma to high beta plasma. Therefore a spherical model may be a more physical representation.

The models investigated in Chapter 5 approximated different regions of the lower solar atmosphere, specifically the lower solar chromosphere and photospheric plasmas. An interesting study, in keeping with the theme of partially ionised plasmas of the last two chapters, would be to consider the two layers as partially ionised themselves. This would obviously complicate the situation but the stability of the MAG surface waves could be studied. Chapter 7 established that flows in collisional plasmas can cause instabilities and it would be interesting to see what the effect of gravity was on either stabilising or destabilising the two fluid modes, if there is any effect at all

Eq. (5.12) is completely general for an arbitrary flow that varies in the vertical direction, therefore one could investigate a situation where the flow speed decreases descending in the lower layer. This would bring the possibility of resonant absorption and could also lead to the trapping of waves.

In Chapter 6 we found evidence of a negative energy type dissipative instability that may occur in a prominence slab situation, with the presence of neutrals acting to stabilise this situation in the Cowling resistive term. In the analysis, only waves

propagating parallel to the magnetic field were considered. Therefore it would be interesting to investigate the effect of a non-zero wave-number in the  $y$ - direction, which would then lead naturally on to the investigation in cylindrical co-ordinates.

Another consideration would be to investigate the kink slow body modes of the same situation, and find whether the instability is more pronounced. This could then lead onto the cylindrical situation, in which the sausage, kink and even the fluting modes could be considered.

Chapter 7, specifically, opened up many questions. It was found that in both the incompressible and compressible cases, there were modes that were solely due to the presence of neutrals and the background flow and that a semi-resonant interaction could occur between these modes and the usual modes of oscillation of a magnetic slab. There was only a brief analysis of these, particularly in the compressible case. A more complete study could be undertaken, in which the collisional frequency between the neutrals and ions is lowered, for example, which would likely result in higher growth rates for the instability.

Another solar situation that could be studied would be the case of solar prominence threads, much like the study in the incompressible case investigated by [Martínez-Gómez \*et al.\* \(2015\)](#).

The direction of propagation of the waves would be another interesting avenue to proceed down. By having a non-zero  $k_y$  value, the effect of the angle between the wave vector and the magnetic field on the instabilities as well as the modes themselves could be investigated. This would then lead nicely on to the cylindrical coordinate system, following on from the work in [Soler \*et al.\* \(2013\)](#).



# References

- Abdelatif, T. E., 1990, “Magneto-atmospheric waves”, *Solar Phys.*, **129**, 201–219. [DOI], [ADS].
- Alfvén, H., 1942, “Existence of Electromagnetic-Hydrodynamic Waves”, *Nature*, **150**, 405–406. [DOI], [ADS].
- Andries, J. and Goossens, M., 2001, “Kelvin-Helmholtz instabilities and resonant flow instabilities for a coronal plume model with plasma pressure”, *Astron. Astrophys.*, **368**, 1083–1094. [DOI], [ADS].
- Andries, J., Tirry, W. J. and Goossens, M., 2000, “Modified Kelvin-Helmholtz Instabilities and Resonant Flow Instabilities in a One-dimensional Coronal Plume Model: Results for Plasma  $\beta=0$ ”, *Astrophys. J.*, **531**, 561–570. [DOI], [ADS].
- Athay, R. G. (Ed.), 1976, *The solar chromosphere and corona: Quiet sun*, Astrophysics and Space Science Library, 53. [DOI], [ADS].
- Ballai, I., Oliver, R. and Alexandrou, M., 2015, “Dissipative instability in partially ionised prominence plasmas”, *Astron. Astrophys.*, **577**, A82. [DOI], [ADS], [arXiv:1503.07917 [astro-ph.SR]].
- Ballai, I., Pinter, B., Oliver, R. and Alexandrou, M., 2017a, “Dissipative instability in a partially ionised prominence plasma slab”, *Astron. Astrophys.*, pp. 1–2.
- Ballai, I., Pinter, B., Oliver, R. and Alexandrou, M., 2017b, “Dissipative instability in a partially ionised prominence slab”, *ArXiv e-prints*. [ADS], [arXiv:1703.07452 [astro-ph.SR]].
- Banerjee, D., Hasan, S. S. and Christensen-Dalsgaard, J., 1995, “The Influence of a Vertical Magnetic Field on Oscillations in an Isothermal Stratified Atmosphere. II.”, *Astrophys. J.*, **451**, 825. [DOI], [ADS].
- Bender, C.M. and Orszag, S.A., 1978, *Advanced Mathematical Methods for Scientists and Engineers*, International series in pure and applied mathematics, McGraw-Hill URL: <https://books.google.co.uk/books?id=SCFQPgAACAAJ>.
- Berger, T. E., Shine, R. A., Slater, G. L. et al., 2008, “Hinode SOT Observations of Solar Quiescent Prominence Dynamics”, *Astrophys. J. Lett.*, **676**, L89. [DOI], [ADS].
- Berger, T. E., Slater, G., Hurlburt, N. et al., 2010, “Quiescent Prominence Dynamics Observed with the Hinode Solar Optical Telescope. I. Turbulent Upflow Plumes”, *Astrophys. J.*, **716**, 1288–1307. [DOI], [ADS].
- Braginskii, S. I., 1965, “Transport Processes in a Plasma”, *Reviews of Plasma Physics*, **1**, 205. [ADS].
- Bray, R. J. and Loughhead, R. E., 1974, *The solar chromosphere*. [ADS].
- Cairns, R. A., 1979, “The role of negative energy waves in some instabilities of parallel flows”, *J. Fluid Mech.*, **92**, 1–14. [DOI], [ADS].
- Cally, P. S., 2001, “Note on an Exact Solution for Magnetoatmospheric Waves”, *Astrophys. J.*, **548**, 473–481. [DOI], [ADS].
- Chandrasekhar, S., 1961, *Hydrodynamic and hydromagnetic stability*. [ADS].
- Christensen-Dalsgaard, Jørgen, 1997, “Lecture Notes on Stellar Oscillations”.
- Cirigliano, D., Vial, J.-C. and Rovira, M., 2004, “Prominence corona transition region plasma diagnostics from SOHO observations”, *Solar Phys.*, **223**, 95–118. [DOI], [ADS].

- Cowling, T. G., 1941, “The non-radial oscillations of polytropic stars”, *Mon. Not. Roy. Astron. Soc.*, **101**, 367. [ADS].
- Díaz, A. J., Soler, R. and Ballester, J. L., 2012, “Rayleigh-Taylor Instability in Partially Ionized Compressible Plasmas”, *Astrophys. J.*, **754**, 41. [DOI], [ADS].
- Dorotovic, I., Erdélyi, R., Freij, N., Karlovsky, V. and Marquez, I., 2014, “Standing sausage waves in photospheric magnetic waveguides”, *Astron. Astrophys.*, **563**, A12. [DOI], [ADS], [arXiv:1210.6476 astro-ph.SR].
- Edwin, P. M. and Roberts, B., 1982, “Wave propagation in a magnetically structured atmosphere. III - The slab in a magnetic environment”, *Solar Phys.*, **76**, 239–259. [DOI], [ADS].
- Edwin, P. M. and Roberts, B., 1983, “Wave propagation in a magnetic cylinder”, *Solar Phys.*, **88**, 179–191. [DOI], [ADS].
- Engvold, O., 1998, “Observations of Filament Structure and Dynamics (Review)”, in *IAU Colloq. 167: New Perspectives on Solar Prominences*, (Eds.) Webb, D. F., Schmieder, B., Rust, D. M., Astronomical Society of the Pacific Conference Series, 150, [ADS].
- Erdélyi, R., 1996, *Resonant Absorption of MHD Waves in Visco-Resistive Plasmas: Applications to the Solar Atmosphere*, Ph.D. thesis, Ph.D thesis, K. U.Leuven, Leuven, Belgium., (1996). [ADS].
- Erdélyi, R., 2006a, “Magnetic seismology of the lower solar atmosphere”, in *Proceedings of SOHO 18/GONG 2006/HELAS I, Beyond the spherical Sun*, ESA Special Publication, 624, [ADS].
- Erdélyi, R., 2006b, “Magnetic coupling of waves and oscillations in the lower solar atmosphere: can the tail wag the dog?”, *Philosophical Transactions of the Royal Society of London Series A*, **364**, 351–381. [DOI], [ADS].
- Erdélyi, R. and Fedun, V., 2006, “Sausage MHD Waves in Incompressible Flux Tubes with Twisted Magnetic Fields”, *Solar Phys.*, **238**, 41–59. [DOI], [ADS].
- Erdélyi, R. and Fedun, V., 2007a, “Are There Alfvén Waves in the Solar Atmosphere?”, *Science*, **318**, 1572. [DOI], [ADS].
- Erdélyi, R. and Fedun, V., 2007b, “Linear MHD Sausage Waves in Compressible Magnetically Twisted Flux Tubes”, *Solar Phys.*, **246**, 101–118. [DOI], [ADS].
- Erdélyi, R. and Goossens, M., 1995, “Resonant absorption of Alfvén waves in coronal loops in visco-resistive MHD”, *Astron. Astrophys.*, **294**, 575–586. [ADS].
- Erdélyi, R. and Mather, J. F., 2017, “Effects of Steady Flow on Magnetoacoustic-Gravity Surface Waves: I. The Weak Field Case”, *Solar Phys.*, **292**, 26. [DOI], [ADS].
- Erdélyi, R. and Taroyan, Y., 2003, “MHD resonant flow instability in the magnetotail”, in *Solar Wind Ten*, (Eds.) Velli, M., Bruno, R., Malara, F., Bucci, B., American Institute of Physics Conference Series, 679, [DOI], [ADS].
- Evershed, J., 1909, “Radial movement in sun-spots”, *Mon. Not. Roy. Astron. Soc.*, **69**, 454. [DOI], [ADS].
- Ferraro, C. A. and Plumpton, C., 1958, “Hydromagnetic Waves in a Horizontally Stratified Atmosphere. V.”, *Astrophys. J.*, **127**, 459. [DOI], [ADS].
- Gibson, S. E., Kucera, T. A., Rastawicki, D. et al., 2010, “Three-dimensional Morphology of a Coronal Prominence Cavity”, *Astrophys. J.*, **724**, 1133–1146. [DOI], [ADS].
- Goedbloed, J. P., Keppens, R. and Poedts, S., 2010, *Advanced Magnetohydrodynamics*. [ADS].
- Goedbloed, J. P. H. and Poedts, S., 2004, *Principles of Magnetohydrodynamics*. [ADS].
- Goossens, M., Ruderman, M. S. and Hollweg, J. V., 1995, “Dissipative MHD solutions for resonant Alfvén waves in 1-dimensional magnetic flux tubes”, *Solar Phys.*, **157**, 75–102. [DOI], [ADS].
- Goossens, M., Erdélyi, R. and Ruderman, M. S., 2011, “Resonant MHD Waves in the Solar Atmosphere”, *Space Sci. Rev.*, **158**, 289–338. [DOI], [ADS].

- Hague, A. and Erdélyi, R., 2016, “Buoyancy-driven Magnetohydrodynamic Waves”, *Astrophys. J.*, **828**, 88. [DOI], [ADS].
- Hasan, S. S. and Banerjee, D. (Eds.), 2007, *Kodai School on Solar Physics*, American Institute of Physics Conference Series, 919. [ADS].
- Hasan, S. S. and Christensen-Dalsgaard, J., 1992, “The influence of a vertical magnetic field on oscillations in an isothermal stratified atmosphere”, *Astrophys. J.*, **396**, 311–332. [DOI], [ADS].
- Heinzel, P. and Anzer, U., 2006, “On the Fine Structure of Solar Filaments”, *Astrophys. J. Lett.*, **643**, L65–L68. [DOI], [ADS].
- Hendrix, T. and Keppens, R., 2014, “Effect of dust on Kelvin-Helmholtz instabilities”, *Astron. Astrophys.*, **562**, A114. [DOI], [ADS], [arXiv:1401.6774].
- Heyvaerts, J. and Priest, E. R., 1983, “Coronal heating by phase-mixed shear Alfvén waves”, *Astron. Astrophys.*, **117**, 220–234. [ADS].
- Hillier, A., Berger, T., Isobe, H. and Shibata, K., 2012, “Numerical Simulations of the Magnetic Rayleigh-Taylor Instability in the Kippenhahn-Schlüter Prominence Model. I. Formation of Upflows”, *Astrophys. J.*, **746**, 120. [DOI], [ADS].
- Hollweg, J. V., 1985, “Viscosity in a magnetized plasma - Physical interpretation”, *J. Geophys. Res.*, **90**, 7620–7622. [DOI], [ADS].
- Jess, D. B., Mathioudakis, M., Erdélyi, R., Crockett, P. J., Keenan, F. P. and Christian, D. J., 2009, “Alfvén Waves in the Lower Solar Atmosphere”, *Science*, **323**, 1582. [DOI], [ADS], [arXiv:0903.3546 [astro-ph.SR]].
- Joarder, P. S., Nakariakov, V. M. and Roberts, B., 1997, “A Manifestation of Negative Energy Waves in the Solar Atmosphere”, *Solar Phys.*, **176**, 285–297. [DOI], [ADS].
- Kelvinsong, 2015, accessed: 2015-01-01. License: Creative Commons Attribution-ShareAlike 3.0 Unported.
- Khodachenko, M. L., Arber, T. D., Rucker, H. O. and Hanslmeier, A., 2004, “Collisional and viscous damping of MHD waves in partially ionized plasmas of the solar atmosphere”, *Astron. Astrophys.*, **422**, 1073–1084. [DOI], [ADS].
- Klimchuk, J. A., 2006, “On Solving the Coronal Heating Problem”, *Solar Phys.*, **234**, 41–77. [DOI], [ADS], [astro-ph/0511841].
- Kumar, N. and Roberts, B., 2003, “ION-Neutral Collisions Effect on MHD Surface Waves”, *Solar Phys.*, **214**, 241–266. [DOI], [ADS].
- Leighton, R. B., 1960, in *Aerodynamic Phenomena in Stellar Atmospheres*, (Ed.) Thomas, R. N., IAU Symposium, 12, [ADS].
- Leroy, B. and Schwartz, S. J., 1982, “Propagation of waves in an atmosphere in the presence of a magnetic field. V - The theory of magneto-acoustic-gravity oscillations. VI - Application of magneto-acoustic-gravity mode theory to the solar atmosphere”, *Astron. Astrophys.*, **112**, 84–103. [ADS].
- Lin, C.-H., Banerjee, D., Doyle, J. G. and O’Shea, E., 2005a, “The extent of 3-min oscillations in regions other than sunspot plumes”, *Astron. Astrophys.*, **444**, 585–592. [DOI], [ADS].
- Lin, Y., 2011, “Filament Thread-like Structures and Their Small-amplitude Oscillations”, *Space Sci. Rev.*, **158**, 237–266. [DOI], [ADS].
- Lin, Y., Engvold, O., Rouppe van der Voort, L., Wiik, J. E. and Berger, T. E., 2005b, “Thin Threads of Solar Filaments”, *Solar Phys.*, **226**, 239–254. [DOI], [ADS].
- Luke, Yudell Leo, 1975, *Mathematical functions and their approximations*.
- Luna, M. and Karpen, J., 2012, “Large-amplitude Longitudinal Oscillations in a Solar Filament”, *Astrophys. J. Lett.*, **750**, L1. [DOI], [ADS], [arXiv:1203.5027 [astro-ph.SR]].

- Luna, M., Díaz, A. J. and Karpen, J., 2012, “The Effects of Magnetic-field Geometry on Longitudinal Oscillations of Solar Prominences”, *Astrophys. J.*, **757**, 98. [DOI], [ADS], [arXiv:1207.6358 [astro-ph.SR]].
- Luna, M., Knizhnik, K., Muglach, K., Karpen, J., Gilbert, H., Kucera, T. A. and Uritsky, V., 2014, “Observations and Implications of Large-amplitude Longitudinal Oscillations in a Solar Filament”, *Astrophys. J.*, **785**, 79. [DOI], [ADS], [arXiv:1403.0381 [astro-ph.SR]].
- Martínez-Gómez, D., Soler, R. and Terradas, J., 2015, “Onset of the Kelvin-Helmholtz instability in partially ionized magnetic flux tubes”, *Astron. Astrophys.*, **578**, A104. [DOI], [ADS], [arXiv:1504.05379 [astro-ph.SR]].
- Mather, J. F. and Erdélyi, R., 2016, “Magneto-Acoustic Waves in a Gravitationally Stratified Magnetized Plasma: Eigen-Solutions and their Applications to the Solar Atmosphere”, *Astrophys. J.*, **822**, 116. [DOI], [ADS].
- Mathioudakis, M., Jess, D. B. and Erdélyi, R., 2013, “Alfvén Waves in the Solar Atmosphere. From Theory to Observations”, *Space Sci. Rev.*, **175**, 1–27. [DOI], [ADS], [arXiv:1210.3625 [astro-ph.SR]].
- Miles, A. J. and Roberts, B., 1992, “Magnetoacoustic-gravity surface waves. I - Constant Alfvén speed”, *Solar Phys.*, **141**, 205–234. [DOI], [ADS].
- Miles, A. J., Allen, H. R. and Roberts, B., 1992, “Magnetoacoustic-gravity surface waves. II - Uniform magnetic field”, *Solar Phys.*, **141**, 235–251. [DOI], [ADS].
- Montesinos, B. and Thomas, J. H., 1997, “The Evershed effect in sunspots as a siphon flow along a magnetic flux tube”, *Nature*, **390**, 485. [DOI], [ADS].
- Moreno-Inertis, F. and Spruit, H. C., 1989, “Stability of sunspots to convective motions. I - Adiabatic instability”, *Astrophys. J.*, **342**, 1158–1171. [DOI], [ADS].
- Nakariakov, V. M. and Roberts, B., 1995, “Magnetosonic Waves in Structured Atmospheres with Steady Flows, I”, *Solar Phys.*, **159**, 213–228. [DOI], [ADS].
- Okamoto, T. J., Tsuneta, S., Berger, T. E. et al., 2007, “Coronal Transverse Magnetohydrodynamic Waves in a Solar Prominence”, *Science*, **318**, 1577. [DOI], [ADS], [arXiv:0801.1958].
- Parenti, S., 2014, “Solar Prominences: Observations”, *Living Reviews in Solar Physics*, **11**, 1. [DOI], [ADS].
- Parnell, C. E. and De Moortel, I., 2012, “A contemporary view of coronal heating”, *Philosophical Transactions of the Royal Society of London Series A*, **370**, 3217–3240. [DOI], [ADS], [arXiv:1206.6097 [astro-ph.SR]].
- Pintér, B. and Erdélyi, R., 2011, “Effects of Magnetic Fields in the Solar Atmosphere on Global Oscillations”, *Space Sci. Rev.*, **158**, 471–504. [DOI], [ADS].
- Priest, E., 2014, *Magnetohydrodynamics of the Sun*, by Eric Priest, Cambridge, UK: Cambridge University Press, 2014. [ADS].
- Reale, F., 2010, “Coronal Loops: Observations and Modeling of Confined Plasma”, *Living Reviews in Solar Physics*, **7**, 5. [DOI], [ADS], [arXiv:1010.5927 [astro-ph.SR]].
- Roberts, B., 1981a, “Wave propagation in a magnetically structured atmosphere. I - Surface waves at a magnetic interface.”, *Solar Phys.*, **69**, 27–38. [DOI], [ADS].
- Roberts, B., 1981b, “Wave Propagation in a Magnetically Structured Atmosphere - Part Two - Waves in a Magnetic Slab”, *Solar Phys.*, **69**, 39–56. [DOI], [ADS].
- Roberts, B., 2006, “Slow magnetohydrodynamic waves in the solar atmosphere”, *Royal Society of London Philosophical Transactions Series A*, **364**, 447–460. [DOI], [ADS].
- Ruderman, M. S., 2005, “Comment on “Slow nonlinear waves in magnetic flux tubes” [Phys. Plasmas **11**, 2256 (2004)]”, *Physics of Plasmas*, **12**(3), 034701. [DOI], [http://dx.doi.org/10.1063/1.1856931]URL: <http://dx.doi.org/10.1063/1.1856931>.

- Ruderman, M. S. and Wright, A. N., 1998, “Excitation of resonant Alfvén waves in the magnetosphere by negative energy surface waves on the magnetopause”, *J. Geophys. Res.*, **103**, 26 573–26 584. [DOI], [ADS].
- Ruderman, M. S., Verwichte, E., Erdélyi, R. and Goossens, M., 1996, “Dissipative instability of the MHD tangential discontinuity in magnetized plasmas with anisotropic viscosity and thermal conductivity”, *J. Plasma Phys.*, **56**, 285–306. [DOI], [ADS].
- Ruzdjak, V. and Tandberg-Hanssen, E. (Eds.), 1990, *Dynamics of quiescent prominences; Proceedings of the 117th Colloquium of IAU, Hvar, Yugoslavia, Sept. 25-29, 1989*, Lecture Notes in Physics, Berlin Springer Verlag, 363. [DOI], [ADS].
- Ryutova, M., Berger, T., Frank, Z., Tarbell, T. and Title, A., 2010, “Observation of Plasma Instabilities in Quiescent Prominences”, *Solar Phys.*, **267**, 75–94. [DOI], [ADS].
- Ryutova, M. P., 1988, “Negative energy waves in a plasma with structured magnetic fields”, *Zhurnal Eksperimentalnoi i Teoreticheskoi Fiziki*, **94**, 138–151. [ADS].
- Scheuer, M. A. and Thomas, J. H., 1981, “Umbral oscillations as resonant modes of magneto-atmospheric waves”, *Solar Phys.*, **71**, 21–38. [DOI], [ADS].
- Schlichenmaier, R. and Schmidt, W., 2000, “Flow geometry in a sunspot penumbra”, *Astron. Astrophys.*, **358**, 1122–1132. [ADS].
- Schmieder, B., Malherbe, J. M., Mein, P. and Tandberg-Hanssen, E., 1984, “Dynamics of solar filaments. III - Analysis of steady flows in H-alpha and C IV lines”, *Astron. Astrophys.*, **136**, 81–88. [ADS].
- Schmit, D. J. and Gibson, S., 2013, “Diagnosing the Prominence-Cavity Connection”, *Astrophys. J.*, **770**, 35. [DOI], [ADS], [arXiv:1304.7595 [astro-ph.SR]].
- Schwartz, S. J. and Leroy, B., 1982, “Propagation of Waves in an Atmosphere in the Presence of a Magnetic Field - Part Six - Application of Magneto-Acoustic Mode Theory to the Solar Atmosphere”, *Astron. Astrophys.*, **112**, 93. [ADS].
- Soler, R., Díaz, A. J., Ballester, J. L. and Goossens, M., 2012, “Kelvin-Helmholtz Instability in Partially Ionized Compressible Plasmas”, *Astrophys. J.*, **749**, 163. [DOI], [ADS], [arXiv:1202.4274 [astro-ph.SR]].
- Soler, R., Díaz, A. J., Ballester, J. L. and Goossens, M., 2013, “Effect of partial ionization on wave propagation in solar magnetic flux tubes”, *Astron. Astrophys.*, **551**, A86. [DOI], [ADS], [arXiv:1301.5214 [astro-ph.SR]].
- St. John, C. E., 1913, “Radial Motion in Sun-Spots”, *Astrophys. J.*, **37**, 322. [DOI], [ADS].
- Taroyan, Y. and Erdélyi, R., 2002, “Resonant and Kelvin-Helmholtz instabilities on the magnetopause”, *Physics of Plasmas*, **9**, 3121–3129. [DOI], [ADS].
- Thomson, W., 1871, “XLVI. Hydrokinetic solutions and observations”, *Philosophical Magazine Series 4*, **42**(281), 362–377. [DOI].
- Tirry, W. J., Cadez, V. M., Erdelyi, R. and Goossens, M., 1998, “Resonant flow instability of MHD surface waves”, *Astron. Astrophys.*, **332**, 786–794. [ADS].
- Trehan, S. K. and Uberoi, M. S., 1972, “Magnetically Distorted Polytropes: Structure and Radial Oscillations”, *Astrophys. J.*, **175**, 161. [DOI], [ADS].
- Vernazza, J. E., Avrett, E. H. and Loeser, R., 1981, “Structure of the solar chromosphere. III - Models of the EUV brightness components of the quiet-sun”, *Astrophys. J. Suppl.*, **45**, 635–725. [DOI], [ADS].
- Verwichte, E., Nakariakov, V. M. and Cooper, F. C., 2005, “Transverse waves in a post-flare supra-arcade”, *Astron. Astrophys.*, **430**(3), L65–L68. [DOI]URL: <https://doi.org/10.1051/0004-6361:200400133>.
- Vigeesh, G., Jackiewicz, J. and Steiner, O., 2017, “Internal Gravity Waves in the Magnetized Solar Atmosphere. I. Magnetic Field Effects”, *Astrophys. J.*, **835**, 148. [DOI], [ADS], [arXiv:1612.04729 [astro-ph.SR]].

- Wang, J.-x., 1986, “On the propagation of magneto-acoustic-gravity waves”, *Chinese Astron. Astrophys.*, **10**, 291–297. [DOI], [ADS].
- Watson, C., Zweibel, E. G., Heitsch, F. and Churchwell, E., 2004, “Kelvin-Helmholtz Instability in a Weakly Ionized Medium”, *Astrophys. J.*, **608**, 274–281. [DOI], [ADS], [astro-ph/0401243].
- Xia, C., Keppens, R., Antolin, P. and Porth, O., 2014, “Simulating the in Situ Condensation Process of Solar Prominences”, *Astrophys. J. Lett.*, **792**, L38. [DOI], [ADS], [arXiv:1408.4249 [astro-ph.SR]].
- Yelles Chaouche, L. and Abdelatif, T. E., 2005, “MAG Waves in Sunspots Umbrae: Slow Waves Leaking to the Corona”, *Solar Phys.*, **229**, 255–271. [DOI], [ADS].
- Zaqarashvili, T. V., Khodachenko, M. L. and Rucker, H. O., 2011, “Magnetohydrodynamic waves in solar partially ionized plasmas: two-fluid approach”, *Astron. Astrophys.*, **529**, A82. [DOI], [ADS], [arXiv:1101.3913 [astro-ph.SR]].
- Zhugzhda, Y. D., 1979, “Magnetogravity waves in an isothermal conductive atmosphere”, *Soviet Astron.*, **23**, 42. [ADS].
- Zhugzhda, Y. D. and Goossens, M., 2001, “Hidden problems of thin-flux-tube approximation”, *Astron. Astrophys.*, **377**, 330–342. [DOI], [ADS].

# Appendix A

## Chapter 3 Derivations

The hypergeometric functions that comprise the solution of Eq. (3.25) are written in the following form, for ease of use,

$$\begin{aligned}
 {}_2F_3 \left[ \begin{matrix} \frac{1}{2} - iq_z + K, \frac{1}{2} + iq_z + K; \\ 1 + 2K, \frac{3}{2} - iq_0 + K, \frac{3}{2} + iq_0 + K \end{matrix} \middle| -\psi^2 \right] &= {}_2F_3 \left[ \begin{matrix} a_{11}, a_{12}; \\ b_{11}, b_{12}, b_{13} \end{matrix} \middle| -\psi^2 \right], \\
 {}_2F_3 \left[ \begin{matrix} \frac{1}{2} + iq_z - K, \frac{1}{2} - iq_z - K; \\ 1 - 2K, \frac{3}{2} - iq_0 - K, \frac{3}{2} + iq_0 - K \end{matrix} \middle| -\psi^2 \right] &= {}_2F_3 \left[ \begin{matrix} a_{21}, a_{22}; \\ b_{21}, b_{22}, b_{23} \end{matrix} \middle| -\psi^2 \right], \\
 {}_2F_3 \left[ \begin{matrix} iq_0 - iq_z, iq_0 + iq_z; \\ 1 + 2iq_0, \frac{1}{2} + iq_0 + K, \frac{1}{2} + iq_0 - K \end{matrix} \middle| -\psi^2 \right] &= {}_2F_3 \left[ \begin{matrix} a_{31}, a_{32}; \\ b_{31}, b_{32}, b_{33} \end{matrix} \middle| -\psi^2 \right], \\
 {}_2F_3 \left[ \begin{matrix} -iq_z - iq_0, iq_z - iq_0; \\ 1 - 2iq_0, \frac{1}{2} - iq_0 + K, \frac{1}{2} - iq_0 - K \end{matrix} \middle| -\psi^2 \right] &= {}_2F_3 \left[ \begin{matrix} a_{41}, a_{42}; \\ b_{41}, b_{42}, b_{43} \end{matrix} \middle| -\psi^2 \right].
 \end{aligned}$$

The derivation of the solutions of  $\widehat{v}_x$  and  $\widehat{v}_z$  follows below.

The derivative (with respect to  $\psi^2$ ) of an arbitrary hypergeometric function ( ${}_2F_3$ ) multiplied by a power function is given as:

$$\frac{d}{d\psi^2} \left( \psi^{\mu_j} \sum_{n=0}^{\infty} \frac{(a)_n (b)_n (-\psi^2)^n}{(c)_n (d)_n (e)_n n!} \right) = \psi^{\mu_j-2} \sum_{n=0}^{\infty} \frac{(a)_n (b)_n (-\psi^2)^n}{(c)_n (d)_n (e)_n n!} \left( \frac{\mu_j}{2} + n \right),$$

$$\frac{d^2}{d(\psi^2)^2} \left( \psi^{\mu_j} \sum_{n=0}^{\infty} \frac{(a)_n (b)_n (-\psi^2)^n}{(c)_n (d)_n (e)_n n!} \right) = \psi^{\mu_j-4} \sum_{n=0}^{\infty} \frac{(a)_n (b)_n (-\psi^2)^n}{(c)_n (d)_n (e)_n n!} \left( \frac{\mu_j}{2} + n \right) \left( \frac{\mu_j}{2} + n - 1 \right),$$

where  $j = 1, 2, 3$  or  $4$  and

$$\mu_1 = 2K, \quad \mu_2 = -2K, \quad \mu_3 = -1 + i2q_0, \quad \mu_4 = -1 - i2q_0.$$

The derivatives of  $z$  can be written in terms of derivatives of  $\psi^2$ ,

$$\frac{d}{dz} = \frac{\partial \psi^2}{\partial z} \frac{d}{d\psi^2} = -\frac{\psi^2}{H} \frac{d}{d\psi^2}, \quad \frac{d^2}{dz^2} = \frac{\psi^2}{H^2} \frac{d}{d\psi^2} + \frac{\psi^4}{H^2} \frac{d^2}{d(\psi^2)^2}.$$

Eq. (3.22) shows  $\widehat{v}_x$  in terms of derivatives of  $\Theta$ . Writing this in terms of derivatives with respect to  $\psi^2$  and some dimensionless variables,

$$\widehat{v}_x = \frac{\omega}{k_x(\omega^2 - N^2)} \frac{1}{H^2} \left( \psi^4 \frac{d^2}{d(\psi^2)^2} + 2\psi^2 \frac{d}{d\psi^2} + \frac{\widehat{\sigma}^2}{\gamma} \Theta \right). \quad (\text{A.1})$$

For the solutions corresponding to  $\mu_{(1,2)} = \pm 2K$  (1 refers to positive sign and 2 refers to negative sign, respectively),  $\widehat{v}_x$  can be written,

$$\widehat{v}_x^{(1,2)} = \psi^{\pm 2K} \sum_{n=0}^{\infty} \frac{(a_{(1,2)1})_n (a_{(1,2)2})_n (-\psi^2)^n}{(b_{(1,2)1})_n (b_{(1,2)2})_n (b_{(1,2)3})_n n!} \left( \frac{\widehat{\sigma}^2}{\gamma} + (n \pm K)(n + 1 \pm K) \right).$$

In both cases the  $n$ -th term of the Pochhammer symbols  $(b_{(1,2)2})_n$  and  $(b_{(1,2)3})_n$  are such that their product is

$$\begin{aligned} (b_{(1,2)2} + (n - 1))(b_{(1,2)3} + (n - 1)) &= \left( \frac{1}{2} - iq_0 \pm K + n \right) \left( \frac{1}{2} + iq_0 \pm K + n \right) \\ &= \left( \frac{\widehat{\sigma}^2}{\gamma} + (n \pm K)(n + 1 \pm K) \right). \end{aligned}$$

It is then clear that the numerator and denominators of the  $n$ -th terms cancel and the result is,

$$\widehat{v}_x^{(1,2)} = \left( K^2 \pm K + \frac{\widehat{\sigma}^2}{\gamma} \right) \psi^{\pm 2K} \sum_{n=0}^{\infty} \frac{(a_{(1,2)1})_n (a_{(1,2)2})_n (-\psi^2)^n}{(b_{(1,2)1})_n (b_{(1,2)2} - 1)_n (b_{(1,2)3} - 1)_n n!}.$$

Therefore, the type the type 1 and 2 solutions, for  $\widehat{v}_x$ , can be written as single hypergeometric functions. Considering now the solutions corresponding to  $\mu_{(3,4)} = -1 \pm i2q_0$  (3 refers to positive sign and 4 refers to negative sign respectively),  $\widehat{v}_x$  can be written,

$$\begin{aligned} \widehat{v}_x^{(3,4)} &= \psi^{-1 \pm 2iq_0} \sum_{n=0}^{\infty} \frac{(a_{(3,4)1})_n (a_{(3,4)2})_n (-\psi^2)^n}{(b_{(3,4)1})_n (b_{(3,4)2})_n (b_{(3,4)3})_n n!} \left( \frac{\widehat{\sigma}^2}{\gamma} + \left( n - \frac{1}{2} \pm iq_0 \right) \left( n + \frac{1}{2} \pm iq_0 \right) \right) \\ &= \psi^{-1 \pm 2iq_0} \sum_{n=0}^{\infty} \frac{(a_{(3,4)1})_n (a_{(3,4)2})_n (-\psi^2)^n}{(b_{(3,4)1})_n (b_{(3,4)2})_n (b_{(3,4)3})_n n!} (n \pm 2iq_0) \\ &= \psi^{1 \pm 2iq_0} \frac{(-a_{(3,4)1} a_{(3,4)2})}{(b_{(3,4)1} b_{(3,4)2} b_{(3,4)3})} \sum_{n=0}^{\infty} \frac{(a_{(3,4)1} + 1)_n (a_{(3,4)2} + 1)_n (-\psi^2)^n (n + 1)}{(b_{(3,4)1} + 1)_n (b_{(3,4)2} + 1)_n (b_{(3,4)3} + 1)_n (n + 1)!} (n + 1 \pm 2iq_0) \\ &= \psi^{1 \pm 2iq_0} \frac{(-a_{(3,4)1} a_{(3,4)2})}{(b_{(3,4)1} b_{(3,4)2} b_{(3,4)3})} \sum_{n=0}^{\infty} \frac{(a_{(3,4)1} + 1)_n (a_{(3,4)2} + 1)_n (-\psi^2)^n}{(b_{(3,4)1} + 1)_n (b_{(3,4)2} + 1)_n (b_{(3,4)3} + 1)_n n!} (n + 1 \pm 2iq_0) \end{aligned}$$

As the  $n$ -th term of the Pochhammer symbol  $(b_{(3,4)1} + 1)_n$  is given as  $(1 \pm 2iq_0 + n)$  and this is the same as the numerator, it is therefore possible to write,

$$\widehat{v}_x^{(3,4)} = \psi^{1 \pm 2iq_0} \frac{(-a_{(3,4)1} a_{(3,4)2})}{(b_{(3,4)2} b_{(3,4)3})} \sum_{n=0}^{\infty} \frac{(a_{(3,4)1} + 1)_n (a_{(3,4)2} + 1)_n (-\psi^2)^n}{(b_{(3,4)1} + 1)_n (b_{(3,4)2} + 1)_n (b_{(3,4)3} + 1)_n n!}.$$

Again, the type 3 and 4 solutions, for  $\widehat{v}_x$ , can be written as single hypergeometric functions multiplied by a power function. It is interesting to note that these solutions for the type 1,2,3 and 4 solutions are exactly the same as derived in Zhugzhda (1979). We can therefore write,

$$\begin{aligned} \widehat{v}_x &= C_1 \psi^{2K} S^{(1)} {}_2F_3 \left[ \begin{matrix} a_{11}, a_{12}; \\ b_{11}, b_{12} - 1, b_{13} - 1 \end{matrix} \middle| -\psi^2 \right] \\ &+ C_2 \psi^{-2K} S^{(2)} {}_2F_3 \left[ \begin{matrix} a_{21}, a_{22}; \\ b_{21}, b_{22} - 1, b_{23} - 1 \end{matrix} \middle| -\psi^2 \right] \\ &- C_3 \psi^{1+2iq_0} S^{(3)} {}_2F_3 \left[ \begin{matrix} a_{31} + 1, a_{32} + 1; \\ b_{31}, b_{32} + 1, b_{33} + 1 \end{matrix} \middle| -\psi^2 \right] \\ &- C_4 \psi^{1-2iq_0} S^{(4)} {}_2F_3 \left[ \begin{matrix} a_{41} + 1, a_{42} + 1; \\ b_{41}, b_{42} + 1, b_{43} + 1 \end{matrix} \middle| -\psi^2 \right] \\ &= \sum_{j=1}^4 C_j \widehat{v}_x^{(j)}, \end{aligned} \tag{A.2}$$

noting the factor

$$\frac{\omega}{k_x(\omega^2 - N^2)} \frac{1}{H^2}$$

has been merged into the constants of integration and that,

$$S^{(1)} = K^2 + K + \frac{\widehat{\sigma}^2}{\gamma}, \quad S^{(2)} = K^2 - K + \frac{\widehat{\sigma}^2}{\gamma}, \quad S^{(3)} = \frac{a_{31}a_{32}}{b_{32}b_{33}}, \quad S^{(4)} = \frac{a_{41}a_{42}}{b_{42}b_{43}}.$$

These solutions correspond to exactly to those derived in Zhugzhda (1979) and Cally (2001). Having found the solution for  $\widehat{v}_x$  completely it is prudent to find the solution for  $\widehat{v}_z$  in the simplest possible terms. Transforming to the variable  $\psi^2$  and dimensionless quantities, Eq. (3.21) becomes,

$$\widehat{v}_z = \frac{i\omega}{\omega^2 - N^2} \frac{1}{H} \left( \psi^2 \Theta' + N^2 \Theta \right). \tag{A.3}$$

It is then possible to write for each  $\mu_j$ ,

$$\begin{aligned} \widehat{v}_z^{(j)} &= \psi^{\mu_j} \sum_{n=0}^{\infty} \frac{(a_j)_n (b_j)_n (-\psi^2)^n}{(c_j)_n (d_j)_n (e_j)_n n!} \left( \frac{\mu_j}{2} + n + \widehat{N}^2 \right) \\ &= \left( \frac{\mu_j}{2} + \widehat{N}^2 \right) \psi^{\mu_j} \sum_{n=0}^{\infty} \frac{(a_j)_n (b_j)_n \left( \frac{\mu_j}{2} + \widehat{N}^2 + 1 \right)_n (-\psi^2)^n}{(c_j)_n (d_j)_n (e_j)_n \left( \frac{\mu_j}{2} + \widehat{N}^2 \right)_n n!}. \end{aligned}$$

The solutions for  $\widehat{v}_z$  in terms of hypergeometric functions is then,

$$\widehat{v}_z = iK \left[ \begin{array}{l} C_1 \psi^{2K} R^{(1)} {}_3F_4 \left[ \begin{array}{l} a_{11}, a_{12}, a_{13}; \\ b_{11}, b_{12}, b_{13}, b_{14} \end{array} \middle| -\psi^2 \right] \\ + C_2 \psi^{-2K} R^{(2)} {}_3F_4 \left[ \begin{array}{l} a_{21}, a_{22}, a_{23}; \\ b_{21}, b_{22}, b_{23}, b_{24} \end{array} \middle| -\psi^2 \right] \\ + C_3 \psi^{-1+2iq_0} R^{(3)} {}_3F_4 \left[ \begin{array}{l} a_{31}, a_{32}, a_{33}; \\ b_{31}, b_{32}, b_{33}, b_{34} \end{array} \middle| -\psi^2 \right] \\ + C_4 \psi^{-1-2iq_0} R^{(4)} {}_3F_4 \left[ \begin{array}{l} a_{41}, a_{42}, a_{43}; \\ b_{41}, b_{42}, b_{43}, b_{44} \end{array} \middle| -\psi^2 \right] \end{array} \right] \quad (\text{A.4})$$

where,

$$R^{(1)} = \widehat{N}^2 + K, \quad R^{(2)} = \widehat{N}^2 - K, \quad R^{(3)} = \widehat{N}^2 - \frac{1}{2} + iq_0, \quad R^{(4)} = \widehat{N}^2 - \frac{1}{2} - iq_0,$$

$$a_{13} = R^{(1)} + 1, \quad a_{23} = R^{(2)} + 1, \quad a_{33} = R^{(3)} + 1, \quad a_{43} = R^{(4)} + 1,$$

$$b_{13} = R^{(1)}, \quad b_{23} = R^{(2)}, \quad b_{33} = R^{(3)}, \quad b_{43} = R^{(4)}.$$

# Appendix B

## Chapter 7 Derivations

We Fourier decompose in the  $x$ -direction and in time,  $t$ , for Eq. (7.1)-(7.7) and 6 equations are formed (in fact there are eight but the mass continuity equations decouple from the other equations):

$$-i\rho_i\Omega\widehat{v}_{xi} = -ik\widehat{P}_T + ik\frac{B_0}{\mu}B_x - \rho_n v_{in}(\widehat{v}_{xi} - \widehat{v}_{xn}), \quad (\text{B.1})$$

$$-i\rho_n\Omega\widehat{v}_{xn} = -ik\widehat{p}_n + \rho_n v_{in}(\widehat{v}_{xi} - \widehat{v}_{xn}), \quad (\text{B.2})$$

$$-i\rho_i\Omega\widehat{v}_{zi} = -\frac{d\widehat{P}_T}{dz} + ik\frac{B_0}{\mu}B_z - \rho_n v_{in}(\widehat{v}_{zi} - \widehat{v}_{zn}), \quad (\text{B.3})$$

$$-i\rho_n\Omega\widehat{v}_{zn} = -\frac{d\widehat{p}_n}{dz} + \rho_n v_{in}(\widehat{v}_{zi} - \widehat{v}_{zn}), \quad (\text{B.4})$$

$$-i\Omega B_x = -B_0 \frac{d\widehat{v}_{zi}}{dz}, \quad (\text{B.5})$$

$$-i\Omega B_z = ikB_0\widehat{v}_{zi}, \quad (\text{B.6})$$

$$-i\Omega\widehat{P}_T + \rho_i \left( c_{si}^2 + v_A^2 \right) \frac{d\widehat{v}_{zi}}{dz} = -ik\rho_i c_{si}^2 \widehat{v}_{xi}, \quad (\text{B.7})$$

$$-i\Omega\widehat{p}_n + \rho_n c_{sn}^2 \widehat{v}_{zn} = -ik\rho_n c_{sn}^2 \widehat{v}_{xn}. \quad (\text{B.8})$$

Where we have defined the Doppler shifted frequency as  $\Omega = \omega - ku$ .

$$\begin{aligned} \frac{\Omega}{kc_{si}^2} \left( -i\Omega\widehat{P}_T + \rho_i \left( c_{si}^2 + v_A^2 \right) \frac{d\widehat{v}_{zi}}{dz} \right) &= -ik\widehat{P}_T + \rho_i \frac{v_A^2 k}{\Omega} \frac{d\widehat{v}_{zi}}{dz} \\ &\quad - i \frac{\chi v_{in}}{kc_{si}^2} \left( -i\Omega\widehat{P}_T + \rho_i \left( c_{si}^2 + v_A^2 \right) \frac{d\widehat{v}_{zi}}{dz} \right) + \rho_n v_{in} \widehat{v}_{xn}, \end{aligned} \quad (\text{B.9})$$

Where we have defined the ratio of neutrals to ions as  $\chi = \rho_n/\rho_i$ . Rearranging Eq. (B.9) results in the following relation:

$$\begin{aligned} -i\Omega\widehat{P}_T \left( \Omega^2 - k^2 c_{si}^2 + i\Omega\chi v_{in} \right) &= -\rho_i \left( c_{si}^2 + v_A^2 \right) \frac{d\widehat{v}_{zi}}{dz} \left( \Omega^2 - k^2 c_T^2 + i\Omega\chi v_{in} \right) \\ &\quad + \rho_n \widehat{v}_{xn} v_{in} \Omega k c_{si}^2. \end{aligned} \quad (\text{B.10})$$

We now define:

$$\acute{D}_{si} = \Omega^2 - k^2 c_{si}^2 + i\Omega\chi v_{in}, \quad \acute{D}_T = \Omega^2 - k^2 c_T^2 + i\Omega\chi v_{in}, \quad (\text{B.11})$$

and thus rewrite Eq. (B.10) as

$$-i\Omega\widehat{P}_T \acute{D}_{si} = -\rho_i (c_{si}^2 + v_A^2) \acute{D}_T \frac{d\widehat{v}_{zi}}{dz} + \rho_n \widehat{v}_{xn} v_{in} \Omega k c_{si}^2. \quad (\text{B.12})$$

Using Eq. (B.8) we finally rewrite Eq. (B.12) as:

$$-i\Omega\widehat{P}_T \acute{D}_{si} = -\rho_i (c_{si}^2 + v_A^2) \acute{D}_T \frac{d\widehat{v}_{zi}}{dz} + i\Omega v_{in} \frac{c_{si}^2}{c_{sn}^2} \left( -i\Omega\widehat{p}_n + \rho_n c_{sn}^2 \widehat{v}_{zn} \right). \quad (\text{B.13})$$

By symmetry of the problem we have

$$-i\Omega\widehat{p}_n D_{sn} = -\rho_n c_{sn}^2 D_n \widehat{v}_{zn} + i\Omega\chi v_{in} \frac{c_{sn}^2}{c_{si}^2} \left( -i\Omega\widehat{P}_T + \rho_i \left( c_{si}^2 + v_A^2 \right) \frac{d\widehat{v}_{zi}}{dz} \right), \quad (\text{B.14})$$

in which we have defined

$$D_n = \Omega^2 + i\Omega v_{in}, \quad D_{sn} = \Omega^2 - k^2 c_{sn}^2 + i\Omega v_{in}. \quad (\text{B.15})$$

From Eqs. (B.3) and (B.4), respectively, we have:

$$\rho_i \left( \Omega^2 - k_x^2 v_A^2 + i\Omega\chi v_{in} \right) \widehat{v}_{zi} = -i\Omega \frac{d\widehat{P}_T}{dz} + i\Omega \rho_n v_{in} \widehat{v}_{zn}, \quad (\text{B.16})$$

$$\rho_n D_n \widehat{v}_{zn} = -i\Omega \frac{d\widehat{p}_n}{dz} + i\Omega \rho_n v_{in} \widehat{v}_{zi}. \quad (\text{B.17})$$

We substitute Eq. (B.14) into Eq. (B.13) to obtain

$$\begin{aligned}
-i\Omega\widehat{P}_T\dot{D}_{si} &= -\rho_i(c_{si}^2 + v_A^2)\dot{D}_T\frac{d\widehat{v}_{zi}}{dz} \\
&+ i\Omega v_{in}\frac{c_{si}^2}{D_n c_{sn}^2}\left(-i\Omega\widehat{p}_n D_n + i\Omega\widehat{p}_n D_{sn}\right. \\
&\quad \left.+ i\Omega\chi v_{in}\frac{c_{sn}^2}{c_{si}^2}\left(-i\Omega\widehat{P}_T + \rho_i(c_{si}^2 + v_A^2)\frac{d\widehat{v}_{zi}}{dz}\right)\right)
\end{aligned} \tag{B.18}$$

$$\begin{aligned}
-i\Omega\widehat{P}_T\dot{D}_{si}D_n &= -\rho_i(c_{si}^2 + v_A^2)\dot{D}_T D_n\frac{d\widehat{v}_{zi}}{dz} \\
&+ i\Omega v_{in}\frac{c_{si}^2}{c_{sn}^2}\left(-i\Omega\widehat{p}_n k^2 c_{sn}^2 + i\Omega\chi v_{in}\frac{c_{sn}^2}{c_{si}^2}\left(-i\Omega\widehat{P}_T + \rho_i(c_{si}^2 + v_A^2)\frac{d\widehat{v}_{zi}}{dz}\right)\right),
\end{aligned} \tag{B.19}$$

$$-i\Omega\widehat{P}_T\left(\dot{D}_{si}D_n + \Omega^2\chi v_{in}^2\right) = -\rho_i(c_{si}^2 + v_A^2)\left(\dot{D}_T D_n + \Omega^2\chi v_{in}^2\right)\frac{d\widehat{v}_{zi}}{dz} - i\Omega\widehat{p}_n i\Omega v_{in} c_{si}^2 k^2. \tag{B.20}$$

Now

$$\begin{aligned}
\dot{D}_{si}D_n + \Omega^2\chi v_{in}^2 &= \left(\Omega^2 - k^2 c_{si}^2 + i\Omega\chi v_{in}\right)\left(\Omega^2 + i\Omega v_{in}\right) + \Omega^2\chi v_{in}^2 \\
&= \Omega^2(D_n + i\Omega\chi v_{in}) - k^2 c_{si}^2 D_n,
\end{aligned} \tag{B.21}$$

and

$$\begin{aligned}
\dot{D}_T D_n + \Omega^2\chi v_{in}^2 &= \left(\Omega^2 - k^2 c_T^2 + i\Omega\chi v_{in}\right)\left(\Omega^2 + i\Omega v_{in}\right) + \Omega^2\chi v_{in}^2 \\
&= \Omega^2(D_n + i\Omega\chi v_{in}) - k^2 c_T^2 D_n.
\end{aligned} \tag{B.22}$$

We can then write Equation (B.20) as (dividing through by  $D_n$ )

$$-i\Omega\widehat{P}_T\tilde{D}_{si} = -\rho_i(c_{si}^2 + v_A^2)\tilde{D}_T\frac{d\widehat{v}_{zi}}{dz} - i\Omega\widehat{p}_n\frac{i\Omega v_{in}c_{si}^2 k^2}{D_n} \tag{B.23}$$

We now redefine,

$$\tilde{D}_{si} = \tilde{\Omega}^2 - k^2 c_{si}^2, \quad \tilde{D}_T = \tilde{\Omega}^2 - k^2 c_T^2, \tag{B.24}$$

as well as defining,

$$\tilde{\Omega}^2 = \Omega^2 \left( 1 + \frac{i\chi v_{in}}{\Omega + iv_{in}} \right). \quad (\text{B.25})$$

We can now substitute the relation for  $\frac{d\widehat{v}_{zi}}{dz}$  from equation (B.23) into Equation (B.14) to obtain

$$\widehat{p}_n \left( D_{sn} + \frac{\Omega^2 \chi v_{in}^2 c_{sn}^2 k^2}{\tilde{D}_T D_n} \right) = -\rho_n c_{sn}^2 D_n \widehat{v}_{zn} - i\Omega \widehat{P}_T \frac{i\Omega \chi v_{in} c_{sn}^2 c_{si}^2 k^2}{(c_{si}^2 + v_A^2) \tilde{D}_T}. \quad (\text{B.26})$$

We now eliminate  $\widehat{v}_{zn}$  from equation (B.16)

$$\rho_i \tilde{D}_A \widehat{v}_{zi} = -i\Omega \frac{d\widehat{P}_T}{dz} - i\Omega \frac{d\widehat{p}_n}{dz} \frac{i\Omega v_{in}}{D_n}. \quad (\text{B.27})$$

Where we define

$$\tilde{D}_A = \tilde{\Omega}^2 - k^2 v_A^2. \quad (\text{B.28})$$

We now eliminate  $\widehat{v}_{zi}$  from equation (B.17)

$$\rho_n D_n \widehat{v}_{zn} = -i\Omega \frac{d\widehat{p}_n}{dz} \left( 1 - \frac{\Omega^2 \chi v_{in}^2}{\tilde{D}_A D_n} \right) - i\Omega \frac{d\widehat{P}_T}{dz} \frac{i\Omega \chi v_{in}}{\tilde{D}_A}. \quad (\text{B.29})$$

We now differentiate and substitute Equation (B.16) in equation (B.23) to obtain

$$-i\Omega \widehat{P}_T \tilde{D}_{si} = -\left( c_{si}^2 + v_A^2 \right) \tilde{D}_T \left( \frac{-i\Omega \frac{d^2 \widehat{P}_T}{dz^2} + i\Omega \rho_n v_{in} \widehat{v}_{zn}}{(\Omega^2 - k_x^2 v_A^2 + i\Omega \chi v_{in})} \right) - i\Omega \widehat{p}_n \frac{i\Omega v_{in} c_{si}^2 k^2}{D_n}. \quad (\text{B.30})$$

Substituting Eq. (B.26) into Eq. (B.30) and performing some simple algebraic manipulations we find a second order ODE for the variable  $\widehat{P}_T$  that is couple to  $\widehat{p}_n$ :

$$\frac{d^2 \widehat{P}_T}{dz^2} - M_i^2 \widehat{P}_T = q_i \widehat{p}_n, \quad (\text{B.31})$$

where

$$M_i^2 = -\frac{(\Omega^2 - k_x^2 v_A^2 + i\Omega \chi v_{in})}{\tilde{D}_T (c_{si}^2 + v_A^2)} \left( \tilde{\Omega}^2 - k_c^2 c_i^2 \frac{\tilde{\Omega}^2 - k^2 v_A^2}{(\Omega^2 - k_x^2 v_A^2 + i\Omega \chi v_{in})} \right) \quad (\text{B.32})$$

and

$$q_i = \frac{i\Omega v_{in}}{D_n c_{sn}^2} \left( D_n - \frac{c_{sn}^2 k^2 v_A^2}{(c_{si}^2 + v_A^2) \tilde{D}_T} \left( \tilde{\Omega}^2 - \frac{\Omega^2 \chi v_{in}^2}{D_n} \right) \right). \quad (\text{B.33})$$

We now find an equation for  $\widehat{p}_n$ . We substitute Eq. (B.17) into Eq. (B.26) to obtain

$$\begin{aligned} -i\Omega \widehat{p}_n \left( D_{sn} + \frac{\Omega^2 \chi v_{in}^2 c_{sn}^2 k^2}{\tilde{D}_T D_n} \right) &= -c_{sn}^2 \left( -i\Omega \frac{d^2 \widehat{p}_n}{dz^2} + i\Omega \rho_n v_{in} \frac{d\widehat{v}_{zi}}{dz} \right) \\ &\quad - i\Omega \widehat{P}_T \frac{i\Omega \chi v_{in} c_{sn}^2 c_{si}^2 k^2}{(c_{si}^2 + v_A^2) \tilde{D}_T}. \end{aligned} \quad (\text{B.34})$$

Substituting Eq. (B.23) for  $\frac{d\widehat{v}_{zi}}{dz}$  into Eq. (B.34) and performing some simple algebra a second order ODE with respect to  $\widehat{p}_n$  that couples to  $\widehat{P}_T$  is found:

$$\frac{d^2 \widehat{p}_n}{dz^2} - \widehat{p}_n M_n^2 = q_n \widehat{P}_T, \quad (\text{B.35})$$

$$M_n^2 = -\frac{\left( \Omega^2 + i\Omega v_{in} - c_{sn}^2 k^2 \left( 1 - \frac{\Omega^2 \chi v_{in}^2 v_A^2}{\tilde{D}_T D_n (c_{si}^2 + v_A^2)} \right) \right)}{c_{sn}^2}, \quad q_n = i\Omega \frac{\chi v_{in} \tilde{\Omega}^2}{(c_{si}^2 + v_A^2) \tilde{D}_T}. \quad (\text{B.36})$$

We now have obtained two coupled Second order ODE's for  $\widehat{P}_T$  and  $\widehat{p}_n$  respectively. These govern the dynamics of plane waves in such a system.